INFORMATION TO USERS

This manuscript has been reproduced from the microfilm master. UMI films the text directly from the original or copy submitted. Thus, some thesis and dissertation copies are in typewriter face, while others may be from any type of computer printer.

The quality of this reproduction is dependent upon the quality of the copy submitted. Broken or indistinct print, colored or poor quality illustrations and photographs, print bleedthrough, substandard margins, and improper alignment can adversely affect reproduction.

In the unlikely event that the author did not send UMI a complete manuscript and there are missing pages, these will be noted. Also, if unauthorized copyright material had to be removed, a note will indicate the deletion.

Oversize materials (e.g., maps, drawings, charts) are reproduced by sectioning the original, beginning at the upper left-hand corner and continuing from left to right in equal sections with small overlaps.

Photographs included in the original manuscript have been reproduced xerographically in this copy. Higher quality 6" x 9" black and white photographic prints are available for any photographs or illustrations appearing in this copy for an additional charge. Contact UMI directly to order.

ProQuest Information and Learning
300 North Zeeb Road, Ann Arbor, MI 48106-1346 USA
800-521-0600

Electrodeposition of Ag and Tl on Platinum Single Crystals Covered with Iodine.

by

Miguel M. Labayen de Inza
B.Sc., Universidad Autónoma de Madrid, (Spain), 1996

A Dissertation Submitted in Partial Fulfilment of the
Requirements for the Degree of

DOCTOR OF PHILOSOPHY

in the Department of Chemistry

We accept this dissertation as conforming
to the required standard

Dr. D.A. Harrington, Supervisor (Department of Chemistry)

Dr. W.J. Balfour, Departmental Member (Department of Chemistry)

Dr. T.E. Gough, Departmental Member (Department of Chemistry)

Dr. R.K. Keeler, Outside Member (Department of Physics and Astronomy)

Dr. J. Lipkowski (Department of Chemistry and Biochemistry, University of Guelph, Guelph, Canada)

© Miguel M. Labayen de Inza, 2002
University of Victoria

All rights reserved. This dissertation may not be reproduced in whole or in part, by photocopying or other means, without the permission of the author.

Surpervisor: Dr. D.A. Harrington.

ABSTRACT

The electrodeposition of Ag and Tl on Pt single crystal surfaces covered with iodine has been investigated, focusing on the study of the electrodeposited Pt(111)(3 x 3)-AgI structure. These crystals were prepared under atmospheric or ultra high-vacuum conditions. Multiple techniques were used for characterization: traditional electrochemical methods, A.C. impedance, LEED, Auger spectroscopy, thermal desorption spectroscopy and contact angle measurements.

The surface compound Pt(111)(3 x 3)-AgI is formed during the first electrodeposition peak of Ag^+ on Pt(111)($\sqrt{7}$ x $\sqrt{7}$)R19.1°-I. The crystallographic structure of this compound was determined using tensor LEED analysis. Using stepped single crystals with (111) terraces, it was found that there is a correlation between the charge of this peak and the length of the terrace. Terraces are more reactive than steps, and ordered structures are only found for terraces wider than about 10 Å. The long-range order is associated with the directional nature of the Ag-I bonds.

Cohesive and formation thermodynamic parameters of the Pt(111)(3 x 3)-AgI are calculated using a thermodynamic sequence. Two of the steps: electrodeposition of Ag on Pt(111)($\sqrt{7}$ x $\sqrt{7}$)R19.1°-I and desorption of iodine are studied in more detail. The thermodynamic parameters calculated are partly explained by the metallic character of the Pt-Ag bond, and the covalent character of the Ag-I bond.

A study of Tl electrodeposition on Pt(111)($\sqrt{7}$ x $\sqrt{7}$)R19.1°-I was also undertaken. Some of the features of the voltammogram are related to specific surface structures.

Examiners:

Dr. D.A. Harrington, Supervisor (Department of Chemistry)

Dr. W.J. Balfour , Departmental Member (Department of Chemistry)

Dr. T.E. Gough, Departmental Member (Department of Chemistry)

Dr. R.K. Keeler, Outside Member (Department of Physics and Astronomy)

Dr. J. Lipkowski (Department of Chemistry and Biochemistry , University of Guelph , Guelph, Canada)

TABLE OF CONTENTS

SYMBOLS

Symbol	Meaning	Units
$\langle u^2 \rangle$	Mean-square displacement	m^2
α	Contact angle. Proportionality constant.	(deg) Depends on equation
γ	Surface tension. Activity coefficient.	mJ m^{-2}
Γ	Surface excess.	mol m^{-2}
Γ_{max}	Surface excess at saturation.	mol m^{-2}
$\Delta E(\theta, 0\ K)$	Apparent activation energy dependent on θ at 0 K.	kJ, kJ mol^{-1}
$\Delta E^{\circ}(0\ K)$	Standard apparent activation energy at 0 K and 0 coverage.	kJ, kJ mol^{-1}
ΔG, ΔG°, $\Delta^{\ddagger} G$	Gibbs energy change, standard state, of activation	kJ, kJ mol^{-1}
ΔH, ΔH°, $\Delta^{\ddagger} H$	Standard enthalpy change, standard state, of activation.	kJ, kJ mol^{-1}
ΔU, ΔU°, $\Delta^{\ddagger} U$	Internal energy change, standard state, of activation.	kJ, kJ mol^{-1}
θ	Coverage	
θ_D, ν_D	Debye characteristic temperature, frequency.	K
θ_E, ν_E	Einstein characteristic temperature, frequency.	K
ν	Vibrational frequency.	cm^{-1}
σ	Charge density.	C cm^{-2}
σ^i	Excess charge density on phase i.	C cm^{-2}
σ^M	Excess charge density on the metal surface.	C cm^{-2}
$\mathcal{A}$	Surface area.	cm^{-2}
A	Helmholtz energy. Frequency factor.	kJ, kJ mol^{-1} Depends on order

Symbol	Meaning	Units
C_{dl}	Differential capacitance of the double layer.	μF, μF cm^{-2}
C_v	Heat Capacity.	J mol^{-1} K^{-1}
E	Potential. Kinetic energy of electron.	V eV
E_a	Activation energy of desorption. Apparent activation energy.	kJ, kJ mol^{-1} kJ, kJ mol^{-1}
E_A	Kinetic energy of the Auger electron.	eV
E^o	Standard potential.	V
E_p	Peak potential.	V
E_{pzc}	Potential of zero charge.	V
g	Interaction parameter. $g = 6uN_A/RT$	
G	Gibbs energy.	kJ, kJ mol^{-1}
h	Planck constant.	J s
H	Enthalpy.	kJ, kJ mol^{-1}
$I^{\ddagger}$	Iodine transition-state complex.	
j_p	Current density at peak maximum.	μA cm^{-2}
k	Boltzmann constant. Rate constant	J K^{-1} Depends on order
K	Equilibrium constant.	
μ, μ^o	Chemical potential, standard state.	kJ mol^{-1}
M	Number of sites.	
N	Number of particles.	
N_A	Avogadro's number.	mol^{-1}
P	Partial pressure of desorbed species.	
q	Molecular partition function.	
Q	Canonical partition function. Charge of a capacitor.	 μF, μF cm^{-2}

Symbol	Meaning	Units
Q_{th}	Thermal canonical partition function.	
Q_{total}	Overall canonical partition function.	
r	Total rate of a reaction.	mol m^{-2} s^{-1}
R	Molar gas constant	J mol^{-1} K^{-1}
r_p	Reliability index for each diffraction beam.	
R_p	Average reliability index or R-factor.	
R_S	Solution resistance.	Ω
S	Entropy.	J mol^{-1} K^{-1}
S_s	Excess surface entropy.	J mol^{-1} K^{-1}
τ	Surface stress.	mJ m^{-2}
u	Interaction energy.	J
U	Internal Energy.	kJ, kJ mol^{-1}
U_{int}	Mean Energy of Interaction.	kJ, kJ mol^{-1}
v	Sweep rate.	V s^{-1}
W	Weight of the configuration.	
$w_{1/2}$	Peak full width at half height.	V
Z	Impedance.	Ω

ABBREVIATIONS

Symbol	Meaning
AC	Alternating Current.
AES	Auger Electron Spectroscopy.
CV	Cyclic Voltammetry.
DC	Direct Current.
LEED	Low Energy Electron Diffraction.
MCP	Microchannel Plate.
ML	Monolayer.
NGC	Nucleation-Growth-Collision.
PZC	Point of Zero Charge.
RFA	Retarding Field Analyzer.
RHE	Reversible Hydrogen Electrode.
STM	Scanning Tunneling Microscopy.
SXS	Surface X-ray Scattering.
TSP	Titanium Sublimation Pump.
TDS	Thermal Desorption Spectroscpy.
TP	Turbomolecular Pump.
UHV	Ultra-high Vacuum.
UPD	Underpotential electrodeposition.
XAS	X-ray Absorption Spectroscopy.

LIST OF TABLES

LIST OF FIGURES

ACKNOWLEDGMENTS

I would like to express my gratitude to my supervisor, Dr. David Harrington, for all his help and guidance throughout my graduate career. I would also like to thank a former student in our group, Scott Furman. His support during the time we worked together is greatly appreciated.

A special thanks to Bob Dean; his help fixing the electronic equipment was invaluable.

DEDICATION

Para mamá y el aitacho, de vuestro hijo.

Chapter 1

Introduction.

There has been traditionally a great interest in surface electrochemistry for its technological significance, such as in energy applications, catalysis and corrosion. Many of the processes involved in those applications, e.g., underpotential electrodeposition (UPD) reactions, growth of ultra-thin films, catalytic reactions, involve submonolayer or monolayer amounts of adsorbates on surfaces. These monolayers are structurally and energetically strongly influenced by co-adsorbed anions, and especially halides such as chloride, bromide and iodide. However, the role of the specific surface interactions of these anions in the electrodeposition process is still not fully understood. Since the electrode potential is a free-energy scale, electrochemistry readily gives the thermodynamic stability of surface compounds, and a careful comparison of thermodynamic data with the structure measured by modern surface-science methods can lead to useful insights into the nature of surface bonding.

The presence of halides in a solution or on a surface has a strong influence on electrodeposition processes. This thesis is primarily concerned with a detailed analysis of the properties of two selected metal-halide surface compounds. The goal is the development of a methodology for the calculation of the different thermodynamic parameters. In particular, the cohesive and formation energies of electrodeposited metal-halide surface compounds are sought.

There is not yet a systematic study about the real nature of metal-halide adlayers. In-situ Surface X-ray Scattering (SXS) of Tl-Cl, Br and I on Au(111) and Pb-Br on Au(111)

[1.1][1.2][1.3], in-situ Scanning Tunneling Microscopy (STM) for the Cu-Cl system on Au(110) [1.4] and Au(100) [1.5] or X-ray Absorption Spectroscopy (XAS) of Cu-Cl, Br and I on Pt(111) [1.6], suggest an ionic nature of the electrodeposited metal-halide bond. For Ag electrodeposition on polycrystalline Pt covered with iodine, it was determined by changes in the oxidation potential of iodine with coverage that the deposition of iodine is predominately zerovalent [1.7][1.8].

Research is undertaken here in order to further understand the interactions in these structures. The system Pt-Ag-I is taken as a model system. There are several reasons for this choice. Historically, AgI adsorbed on Pt(111) was the first electrodeposited structure on single crystals studied by ultra-high vacuum techniques. Early studies of this system used the iodine layer as a way of protecting the surface from contaminants during transfer from solution to ultrahigh vacuum (UHV) [1.9]. As we will see below, the mechanism that takes place during the electrodeposition of Ag on Pt covered with iodine is intrinsically interesting. The Ag lifts the iodine adlayer and deposits in direct contact with the Pt surface. At the same time, interesting surface structures are formed.

Studies of silver electrodeposition on Pt in the absence of specifically-adsorbed anions have been reported for several single-crystal faces [1.10][1.11][1.12][1.13], as well as for polycrystalline Pt [1.14][1.15]. The presence of a pre-existing monolayer of iodine modifies the electrodeposition process of Ag on Pt. The electrodeposition of Ag on I-covered Pt(111) has been studied previously by Hubbard and co-workers using ex-situ surface-analytical methods [1.16][1.17][1.18][1.19][1.20] and by Itaya [1.21] using STM. The kinetics of this system have also been studied in our laboratory [1.9].

Among the different Pt-Ag-I structures, we are interested in this thesis primarily in

the study of the surface compound Pt(111)(3 x 3)-AgI. This surface compound is produced by underpotential electrodeposition of Ag^+ onto a Pt(111) surface pre-covered by a monolayer of I atoms, in the Pt(111)(√7 x √7)R19.1°-I structure [1.22][1.23][1.24]. UPD refers to the electrochemical deposition of a submonolayer of a metal on a surface of a different metal, at a potential more positive than the equilibrium potential. In other words, the deposition of an atom on the substrate metal is favored over the bulk deposition of the same atom. The cyclic voltammogram is shown in Fig. (1.1), [1.24]. The point X in this

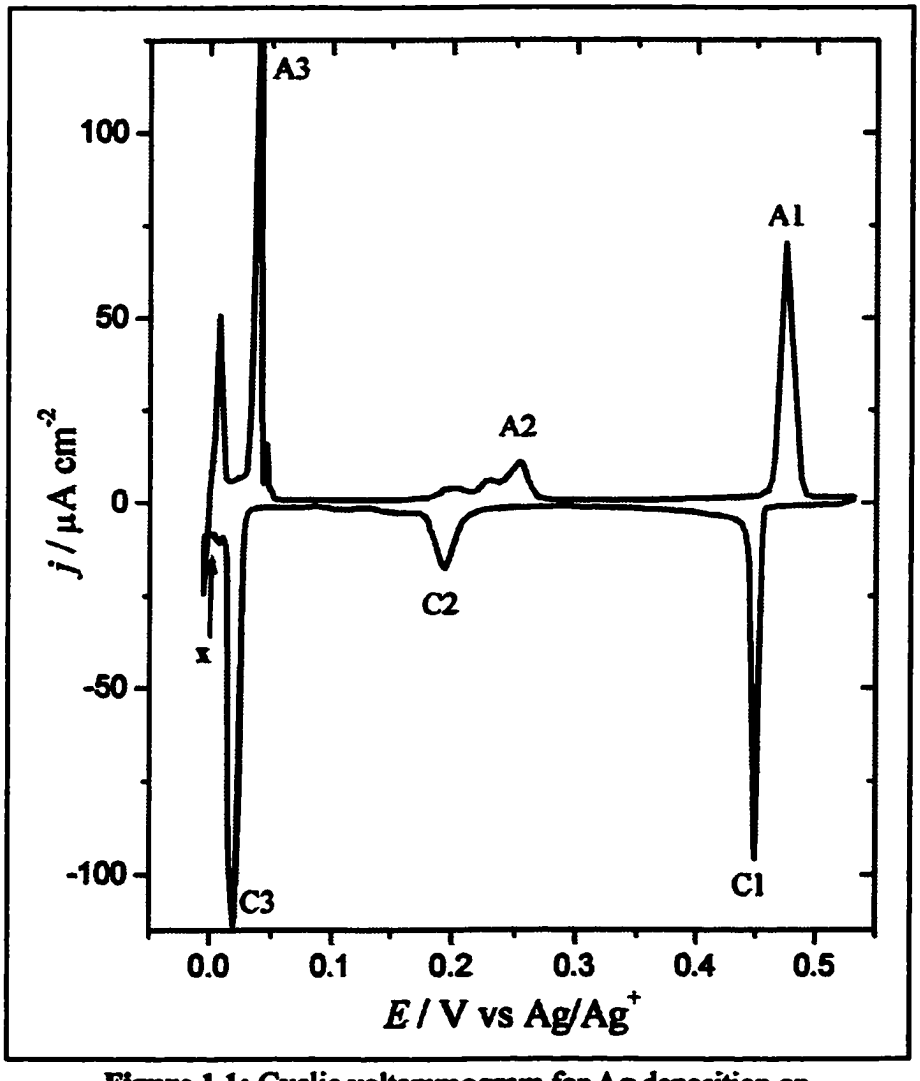

Figure 1.1: Cyclic voltammogram for Ag deposition on Pt(111)(√7 x √7)R19.1°-I. $[Ag^+]$ = 1 mM, sweep rate 5 mV s^{-1}.

figure denotes the beginning of the deposition of bulk Ag, and corresponds to the equilibrium potential $Ag|Ag^+$ under these conditions. Any silver that is deposited on the surface at a potential more positive than point X corresponds to the UPD of Ag.

The first reduction peak at + 0.448 V. vs. $Ag|Ag^+$ is production of the (3 x 3)-AgI structure via a nucleation-growth-collision mechanism (NGC) [1.9], according to the reaction:

$$I(ads,aq) + Ag^+(aq) + e^- \rightarrow AgI(ads) \qquad (1)$$

where I(ads,aq) refers to the Pt(111)($\sqrt{7}$ x $\sqrt{7}$)R19.1°-I, and AgI(ads) refers to the Pt(111)(3 x 3)-AgI structure immersed in electrolyte. The UPD peak C2 in the voltammogram corresponds to the electrodeposition of additional amounts of Ag^+ to produce the Pt(111)($\sqrt{3}$ x $\sqrt{3}$)R30°-AgI surface structure. The peak C3 corresponds with the deposition of a second monolayer of Ag [1.25]. The processes under the three cathodic peaks in the voltammogram are reversed on the positive-going sweep, with the same surface structures removed during the equivalent anodic peaks.

We calculate in chapter 3 the crystallographic structure with the exact position of the atoms of the surface [1.26]. The Pt(111)(3 x 3)-AgI structure is described as a monolayer of Ag atoms lying between a monolayer of iodine atoms and the first Pt layer. It can be represented as a slice of bulk crystalline AgI in the zinc-blende structure, sitting on the Pt surface and contracted laterally by 10%, Fig. (1.2). A more detailed analysis of this structure is given in chapter 3.

It is interesting to study the influence of the underlying Pt surface on the electrodeposition process, in the context of the known structure of the Pt(111)(3 x 3)-AgI surface compound. Chapter 4 compares the electrochemical response of different stepped

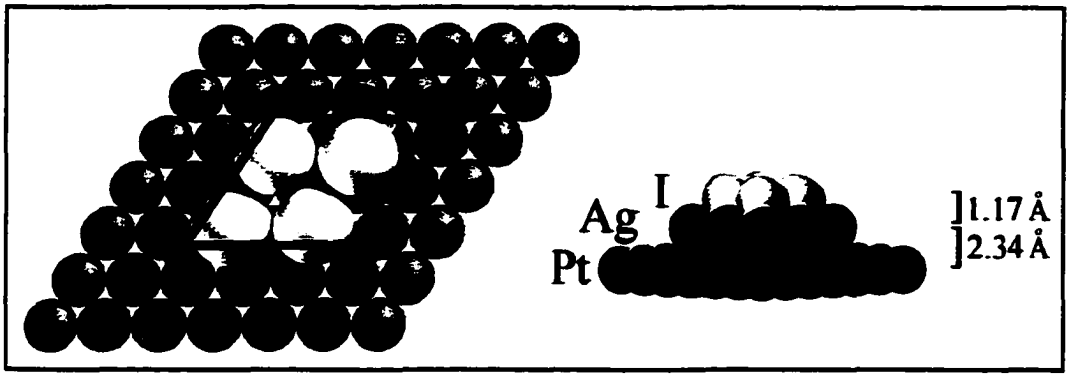

Figure 1.2: Surface structure for the Pt(111)(3 x 3)-AgI surface structure.

Pt single crystals. However, this study mostly provides qualitative information about the surface compound. In order to obtain thermodynamic parameters for Pt(111)(3 x 3)-AgI, we apply Hess' law in chapter 5 to develop a thermodynamic sequence of different reactions. The cohesive and formation energies are found from the sum of the individual components, which are measured by means of electrochemical techniques such as cyclic voltammetry and A.C. impedance. The results are complemented with standard surface analytical techniques such as Low Energy Electron Diffraction (LEED), Auger Electron Spectroscopy (AES), Thermal Desorption Spectrocopy (TDS) and measurements of contact angle and work function changes.

An important component of the sequence is calculation of the thermodynamic parameters for the removal of the Ag layer from the Pt-Ag-I surface structure. This is done electrochemically in chapter 6 from estimations of the standard potential of the electrodeposition reaction and its temperature dependence.

On the other hand, an understanding of the influence of iodine in the electrodeposition of Ag on Pt can only be accomplished with a good model of adsorption/desorption of iodine on bare Pt. This implies a knowledge of the structure and

bonding for the Pt-I system, which is studied in chapter 7.

In chapter 8 we attempt to apply the methodology developed in previous chapters to the Pt-Tl-I system. In contrast to the Ag-I bond, which is suggested to be covalent, the Tl-I bond is suggested to be of ionic nature. The comparative study of these two systems gives an important glimpse into the nature of bonding in UPD systems.

Chapter 2

Experimental

2.1. Introduction.

Iodine-covered Pt single crystal surfaces were used as the starting points for two types of experiments: (1) experiments in which the cleaning, deposition of an iodine layer, and analysis of the surface after the experiment are performed under Ultra-High Vacuum (UHV) conditions (section 2.2), and (2) electrochemical experiments in which all the steps for the cleaning of the surface and deposition of iodine are performed at atmospheric pressure (section 2.4).

Electrochemical experiments involving the use of UHV technology are a great challenge experimentally for many reasons. The crystal has to be transferred from an analytical UHV chamber to a high-pressure chamber, which is then brought to atmospheric pressure under purified argon. A custom-made electrochemical cell is introduced into the chamber and an electrochemical experiment is performed. The chamber is then pumped out again to ultra-high vacuum, and the crystal transferred back to the analysis chamber in order to perform the analysis of the surface.

These analyses are only reliable if the surface is extremely clean and well ordered. Therefore, care was taken to minimize the contamination of the surface, especially by compounds such as carbon, during all the stages of the experiment. A very low pressure must be achieved in a reasonable period of time before any UHV measurement can be obtained. This is difficult to achieve for transfer experiments after electrochemistry, due to the presence of water molecules from the solution adsorbing on the chamber surfaces. Water

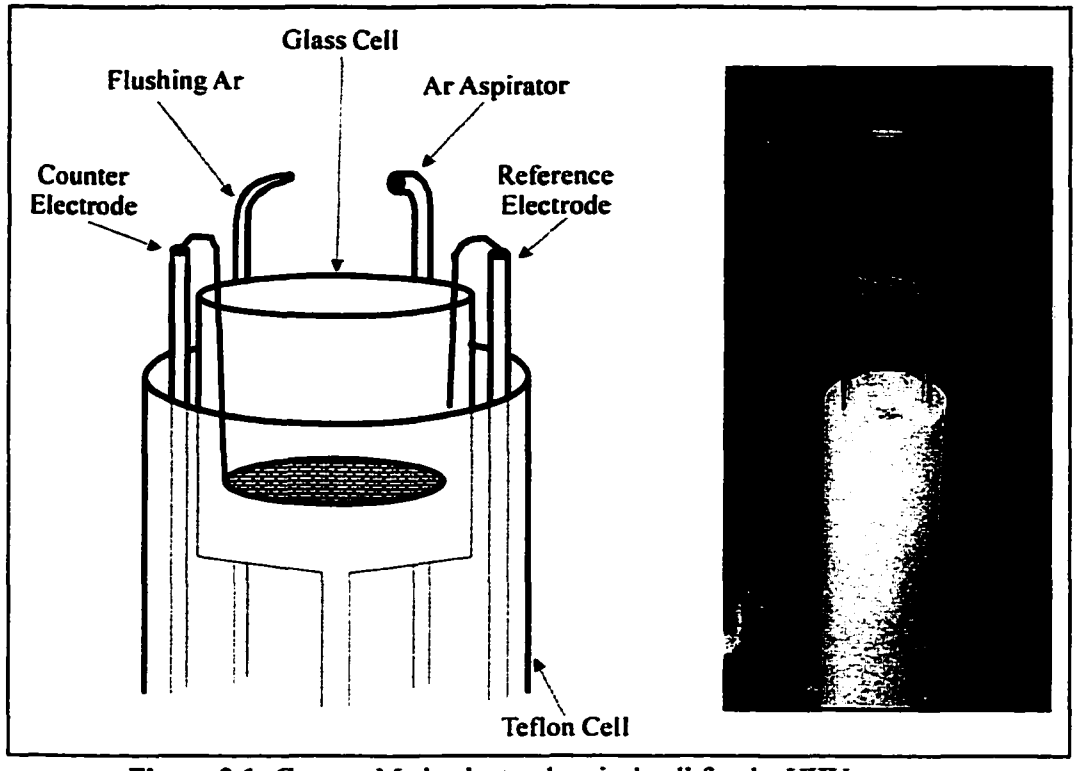

Figure 2.1: Custom-Made electrochemical cell for the UHV system.

is difficult to evacuate with the use of turbomolecular pumps, which are available in our laboratory. The main source of water contamination of the high-pressure chamber are the small droplets of electrolyte remaining on the surface after the experiment. These droplets evaporate and adsorb on the chamber surfaces during the pumpdown of the chamber. The removal of these droplets of solution before the evacuation of the chamber has been achieved with the design of a custom-made electrochemical cell, Fig. (2.1). The surface is flushed with argon and the droplets are sucked out with different glass tubes. This minimizes water residue in the chamber.

2.2. UHV System.

The UHV system in our laboratory has facilities for electrochemistry, Auger Electron Spectroscopy (AES), Low Energy Electron Diffraction (LEED), Thermal Desorption Spectroscopy (TDS) and measurements of work function changes [2.1]. The basics of the two techniques most used in this thesis, LEED and AES, are explained in the last sections of this chapter.

The pumping system is composed of three turbomolecular pumps (TP), two sorption pumps, an ion pump and a Titanium Sublimation Pump (TSP), Fig. (2.2). Contamination-free transfer of the crystal from a surface-analytical or main chamber (base pressure 1.5×10^{-10} mbar), to a high pressure chamber (base pressure 1×10^{-9} mbar) is possible. After the transfer, the high-pressure chamber can be backfilled with argon, and the electrochemical cell introduced for the electrochemical measurement.

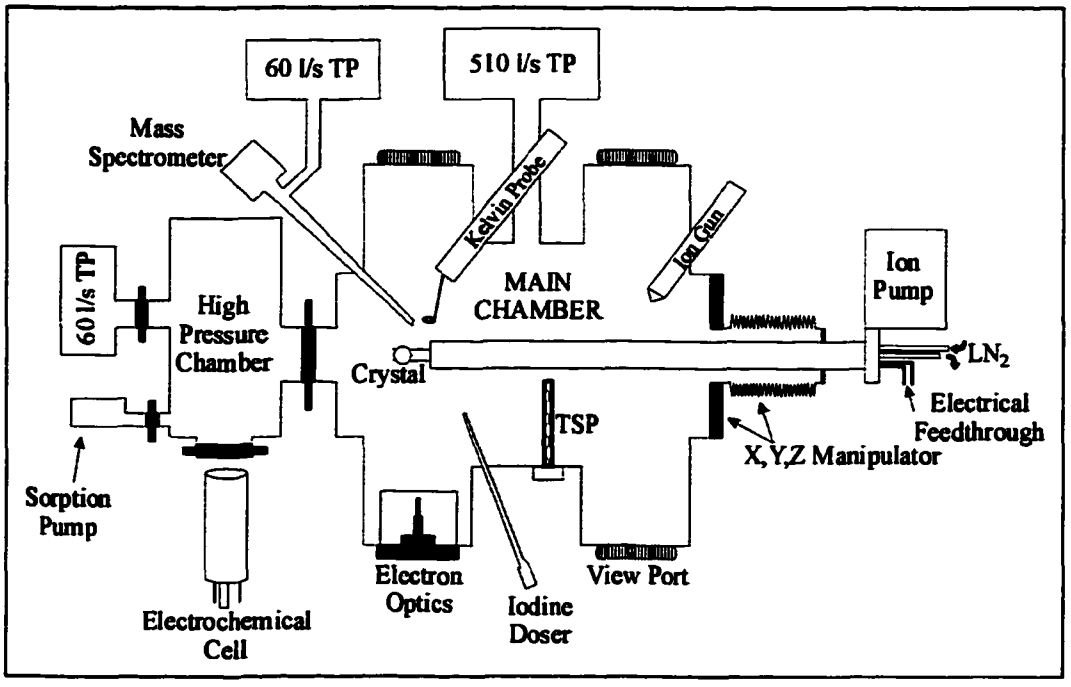

Figure 2.2: UHV system at the University of Victoria.

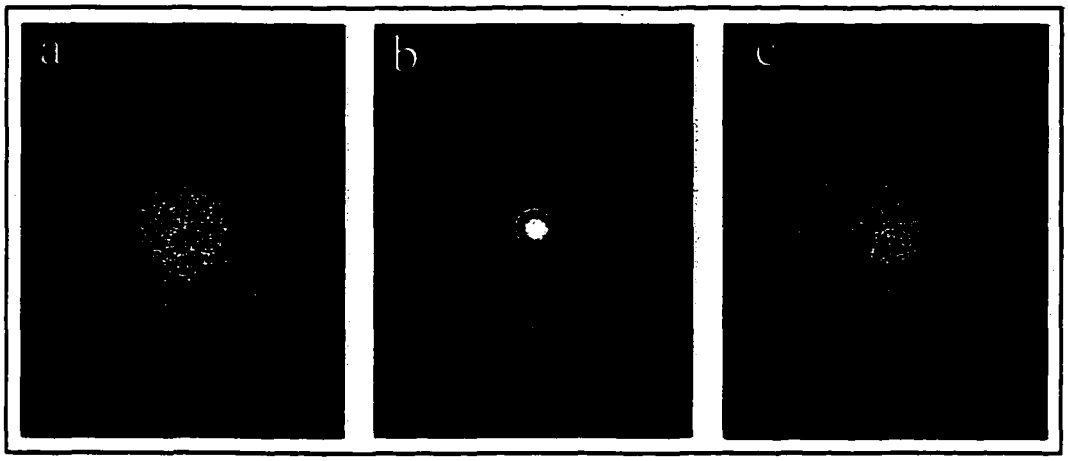

Figure 2.3: X-ray laue diffraction pattern for: a) Pt(100), b) Pt(111) and c) Pt(110).

The platinum crystal used for the UHV experiments was cut with a diamond-wafering saw from a single-crystal boule (1 cm diameter) grown by Metal Oxides and Crystals Ltd. (99.999%). After cutting, the surface was polished with successive grades of diamond paste (Beuhler Ltd.), and oriented within 0.5° of the selected plane by X-ray Laue back diffraction. Crystals with three different orientations, (111), (110) and (100), were cut and polished, although during the course of this thesis only Pt(111) single crystals were used. The surface area of the crystal used in the UHV system is 0.86 cm^2. Fig. (2.3) shows the characteristic back-Laue diffraction pattern for the three types of surfaces.

A standard ion-bombardment and annealing procedure was used to clean the crystal. Briefly, the crystal was bombarded for 5 min with Ar^+ at $3x10^{-5}$ mbar, 25 mA emission current, 3 keV beam energy and 20 μA current at the crystal. After waiting a few minutes until the pressure recovered to $9x10^{-10}$ mbar, the platinum crystal was heated resistively using an external power supply (Lambda Electronics Corp., model LK350-FMOV) at 6 K s^{-1} to 1200 K and held at 1200 K for 1 minute. The temperature was monitored with a K-

type thermocouple spot welded to the back of the crystal, connected to a custom-made temperature control unit. The crystal was then cooled to room temperature. At this point the pressure was $5x10^{-10}$ mbar. LEED and AES were used to ensure the cleanliness and order of the surface.

The iodine was deposited on the surface by passing 400 μA through an iodine doser based on a solid-state electrochemical cell using Ag_4RbI_5 electrolyte [2.2]. The clean platinum crystal was then briefly heated to 600 K at 6 K s^{-1}. During subsequent cooling, deposition was started at 500 K. The deposition ended with the crystal at 300 K. The pressure during deposition was $5x10^{-10}$ - $5x10^{-9}$ mbar. The deposition was monitored by measurement of work function changes. The iodine dosing procedure was considered acceptable when the work function change reproduced previous results in the literature, [2.1]. Fig. (2.4) shows the work function change during the deposition, which was continued

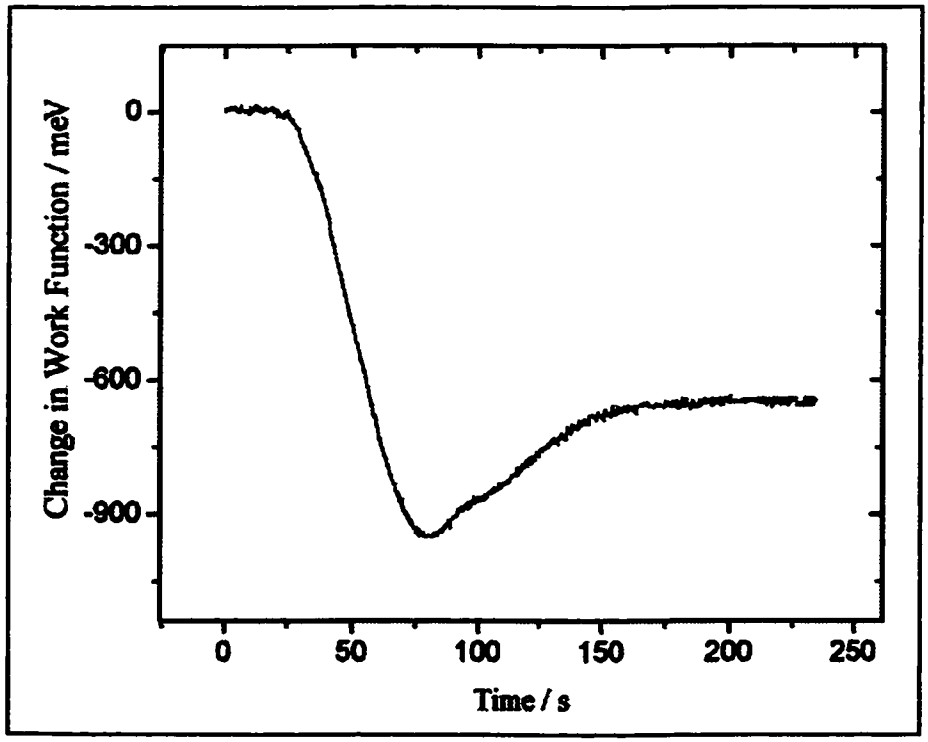

Figure 2.4: Work function change during deposition of I onto Pt(111).

until there was no further work function change.

This point is known to correspond to the formation of the saturated Pt(111)($\sqrt{7}$ x $\sqrt{7}$)R19.1°-I surface structure, with a coverage of 0.43 ML. The LEED pattern and Auger spectra were monitored again at the end of deposition to ensure the quality and cleanliness of the Pt(111)($\sqrt{7}$ x $\sqrt{7}$)R19.1°-I structure. The surface then presents a LEED pattern of good quality. However, the crystal was then heated to 400 K at 2 K s^{-1} and let cool to room temperature to make the diffraction spots of the LEED pattern even sharper, ensuring the highest quality surface structure.

After preparing the Pt(111)($\sqrt{7}$ x $\sqrt{7}$)R19.1°-I structure and transferring the crystal to the electrochemical chamber, the chamber was brought to atmospheric pressure with argon purified with a Centorr Gettering Furnace (Model 2B-20-Q). Two different types of experiments could then be performed: electrochemical experiments and measurements of the contact angle.

2.2.1. Electrochemical Experiments with Pt(111) Prepared under UHV Conditions.

Before the experiment, all glassware was cleaned with hot chromic acid and rinsed with 18 MΩ cm Millipore Q Water, wrapped in aluminum foil and left overnight in an oven. Immediately before the experiment, all glassware was rinsed with fresh electrolyte. These solutions were made with the reagents $HClO_4$ (BDH, 60%, AnalaR), H_2SO_4 (Seastar Suprapure, 98%), $AgClO_4$ (Alfa AESAR 99.9%) or Tl_2CO_3 (Alfa AESAR 99.999%). The solution and electrochemical cell were degassed for at least 1 h with high-purity argon before being introduced into the chamber.

As shown in Fig. (2.1), there is a counter and a reference electrode in the electrochemical cell. The counter electrode is a platinum mesh cleaned with chromic acid prior to the experiment. Two different types of reference electrode were used depending on the type of experiment. A 1 cm silver wire was used as the reference electrode for the experiments involving the electrodeposition of Ag. The reference electrode is then $Ag|Ag^+$ (1 mM in 0.1 M $HClO_4$), and gives the potential *vs* the potential for electrodeposition of bulk silver. This electrode was cleaned with HNO_3 and then chromic acid prior to the experiment. For the rest of the experiments a hydrogen charged 1 cm long, 0.5 mm diameter Pd wire was used as a reference electrode. The Pd was charged with hydrogen by applying a reduction current of 5 mA for 10 minutes in a 0.5 M H_2SO_4 solution. The H^+ from the solution is reduced to H, which is absorbed into the electrode. The reference electrode was then $H(Pd)/H^+$, with a measured potential of +50 mV vs the Reversible Hydrogen Electrode (RHE). RHE refers to the hydrogen electrode in the same solution as the working electrode. For convenience, the potentials in this thesis have been referred to RHE when using Pd as the reference electrode.

The crystal was put into contact with the solution at a specific potential using the hanging meniscus method, and the electrochemical experiment was then carried out. After the experiment, the meniscus was broken at a selected potential in a controlled fashion. As explained in the introduction, the remaining droplets of electrolyte on the surface were removed by flushing with argon and sucking with the different glass tubes, Fig. (2.1). The electrochemical chamber was pumped out using a molecular sieve sorption pump cooled with liquid nitrogen, and then a 60 L/s turbomolecular pump. The crystal was transferred to the main chamber, and after a few minutes the surface analysis measurements were

performed. The pressure during these measurements was never above $5x10^{-9}$ mbar. The cleanliness of the transfer was checked with AES for the presence of impurities on the surface.

As an example of the cleanliness of the transfer experiment, Fig. (2.5) shows the cyclic voltammogram of Pt(111) in H_2SO_4, which is a system especially sensitive to the presence of impurities and surface disorder. The voltammogram depicted in Fig. (2.5) reproduces results in the literature [2.3][2.4], and the AES spectra after transferring the crystal back into the main chamber shows no carbon contamination within the detection limit of the instrument.

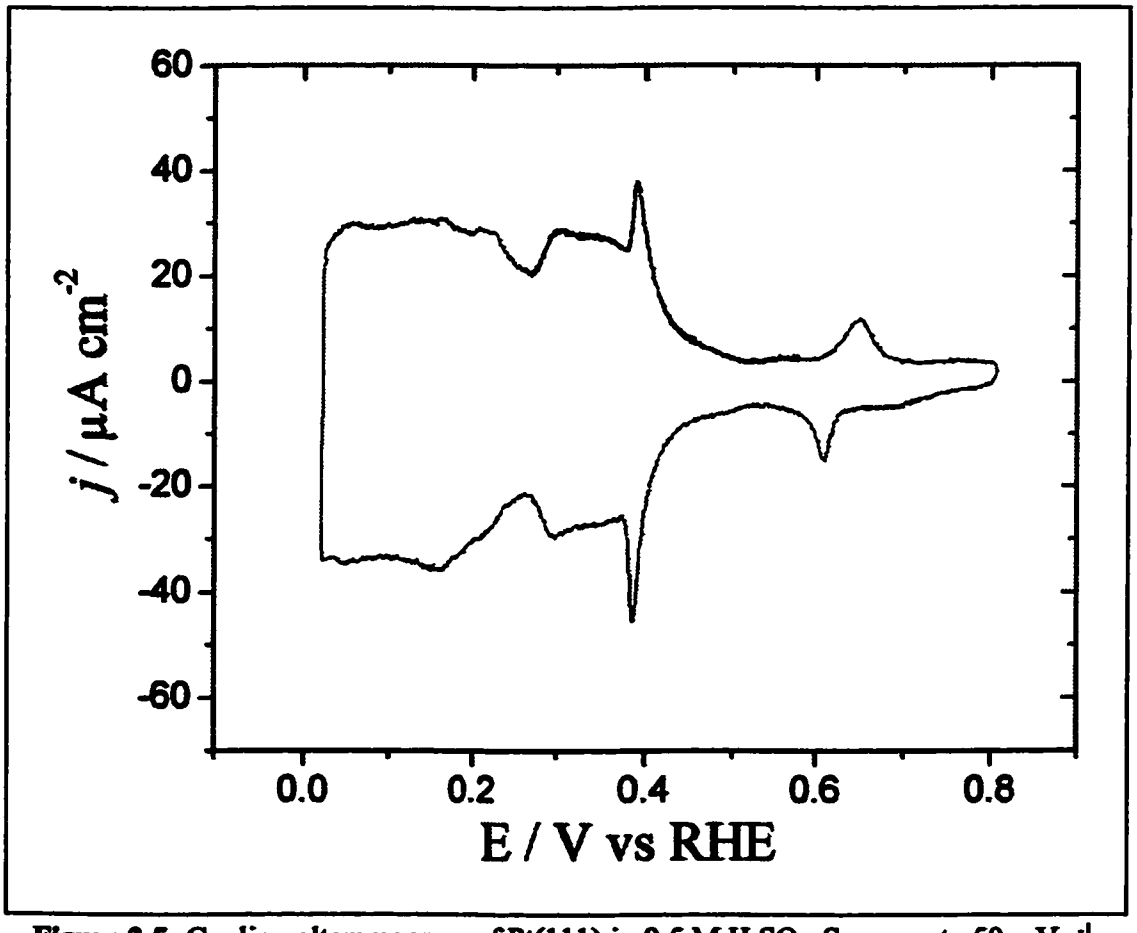

Figure 2.5: Cyclic voltammogram of Pt(111) in 0.5 M H_2SO_4. Sweep rate 50 mV s^{-1}. Initial and final potential = 0.1 V.

2.2.2. Measurements of the Contact Angle.

Measurements of contact angle were performed for surfaces prepared either under UHV conditions or in the laboratory ambient pressure. Pt(111)($\sqrt{7}$ x $\sqrt{7}$)R19.1°-I samples prepared under UHV conditions were brought to atmospheric pressure in the high pressure chamber of the UHV under high-purity argon. A droplet of electrolyte (~1μL) was put on the surface with the help of an external microsyringe attached to one of the glass tubes of the electrochemical cell. The droplet was then photographed with a Minolta SLR camera with a 55 mm macro lens attached (Micro-Nikkor), the same one used to photograph the LEED patterns. The angle was estimated from digitized and expanded images. The shape of a droplet of electrolyte on the surface shows the slight hydrophilicity of the Pt(111)($\sqrt{7}$ x $\sqrt{7}$)R19.1°-I. The large uncertainty in this result arises from the difficulty of photographing the surface in the center of our vacuum system. However, the necessity for a contamination-free measurement precludes a measurement in the laboratory ambient atmosphere.

Surfaces prepared under ambient pressure were used for measurements of the contact angle of the Pt(111)(3 x 3)-AgI structure. The crystal preparation and iodine deposition were done as described in sections 2.4.2. The Pt(111)(3 x 3)-AgI surface structure was produced electrochemically as described in chapter 1, and its quality was ensured when the peak current of the voltammogram was within 10% of the voltammogram shown in Fig. (1.1). After holding the potential at + 0.4 V vs Ag/Ag^{+}, the meniscus was broken and the crystal turned facing up. A droplet of electrolyte (~1μL) was put on the surface and photographed with the camera described above.

2.3. Electrochemical Intrumentation and Special Techniques: A.C. Impedance.

2.3.1. Potentiostats.

Five potentiostats were built during the course of this thesis in collaboration with Dr. Tom Fyles (UVic). The building process included all the stages of research, development, building and final testing.

The basic layout of the potentiostat is shown in Fig. (2.6). In order to minimize noise from wires going back and forth from the front panel, all the switches of the layout are driven by relays installed directly on the circuit board. The main operational amplifier (OP1 in Fig. (2.6)), is helped with the booster (OP2) to obtain a maximum current of 300 mA. The current through the working electrode is determined with the instrumentation amplifier (OP4) by measurements of the potential drop through an internal or external resistor, R. The current can be filtered with the selection of capacitors C of different values in parallel with the measuring resistor. The voltage of the reference electrode is measured with a voltage follower (OP3). A feature of this potentiostat is that the working electrode is at true ground.

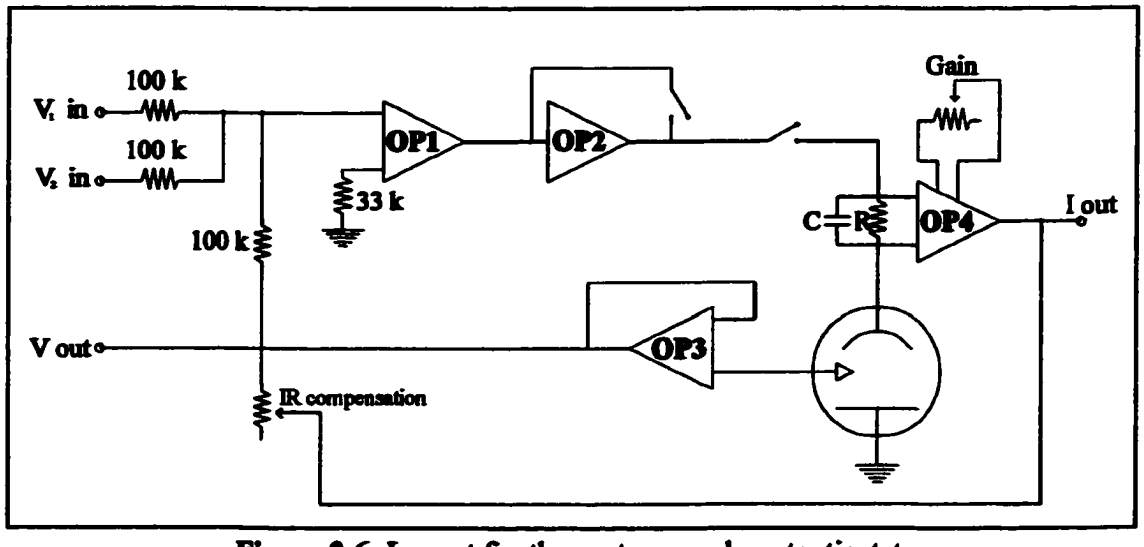

Figure 2.6: Layout for the custom-made potentiostat.

This avoids fluctuations of its potential during very fast experiments such as potential step experiments. In designs using current follower with the working electrode at virtual ground, the working electrode is not at ground during the time the amplifier takes to stabilize, usually a few microseconds. After a careful selection of the components of the potentiostats, some of the specifications are displayed in table (2.1).

Table 2.1: Specifications of the Custom-Made Potentiostats

Power Amplifier		
Compliance Voltage		15 V
Max. Current	Without Booster	10 mA
	With Booster	300 mA
Control Loop Speed (theoretical)		2.8V/μs
Rise time for potential step	1 kΩ Resistive Load	< 1μs
	- Experimental (from 0 to 0.5V.vs.RHE step in 0.5M H_2SO_4, 0.1cm^2 Pt electrode)	- 90% rise time: 2 μs - time to stabilize: 4 μs
Current Measurements		
7 Ranges: Decades (R in Fig. (2.6))	1000, 100, 10, 1mA/V, 200, 100, 10μA/V or user supplied external resistor	
6 Ranges of Filter Capacitors (C in Fig. (2.6))	0.068, 0.15, 1.5, 2.2, 4.7, 6.6μF	
3 Gain Ranges (Gain in Fig. (2.6))	x1, x10, x100	

Voltage follower accuracy	±0.1mV (±0.1%)
Nominal accuracy	±0.1%
Voltage input impedance	100 kΩ
IR Compensation	Positive Feedback

2.3.2. A.C. Voltammetry.

The technique A.C. voltammetry was used in this thesis for the calculation of the double layer capacitance, C_{dl}, for different surface structures in solution. One of the main differences between C_{dl} and a real capacitor, however, is the dependence of C_{dl} on the potential across the interface. Nevertheless, the separation of charges between the surface of the electrode and the solution is typified by the value of C_{dl} at that potential.

The simplest A.C. voltammetry technique is single frequency A.C. voltammetry. For this impedance technique, a small modulated signal (amplitude from 0.5 to 0.033 mV rms and 1 or 2 kHz frequency) was superimposed on the applied voltage for cyclic voltammetry. At the time scale of a few kHz, the only electrochemical process that responds is charging of the double layer. Therefore, the equivalent circuit of the cell can be represented as:

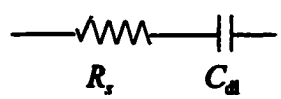

(1)

where R_s is the solution resistance. The impedance of this circuit for a frequency ω is:

$$Z = R_s + \frac{1}{i\omega C_{dl}} \qquad (2)$$

Therefore, the imaginary part of the impedance obtained with single-frequency A.C.

voltammetry is inversely proportional to C_{dl}. The imaginary and real parts of the admittance (inverse of the impedance), were measured by means of two lock-in amplifiers (Perkin Elmer 7265), which use an internal oscillator with the same frequency as the modulated signal applied to the electrode. One of the lock-in amplifiers measured the modulated current, (I lock-in amplifier), while the other measured the modulated output voltage, (E lock-in amplifier), Fig. (2.7). This second lock-in was used to correct for the error for the phase shift due to the non-ideal response of the potentiostatic control loop.

A better estimate for C_{dl} was obtained by means of multi-frequency A.C. voltammetry [2.5][2.6]. This technique was applied for measurements of C_{dl} in Chapter 8,

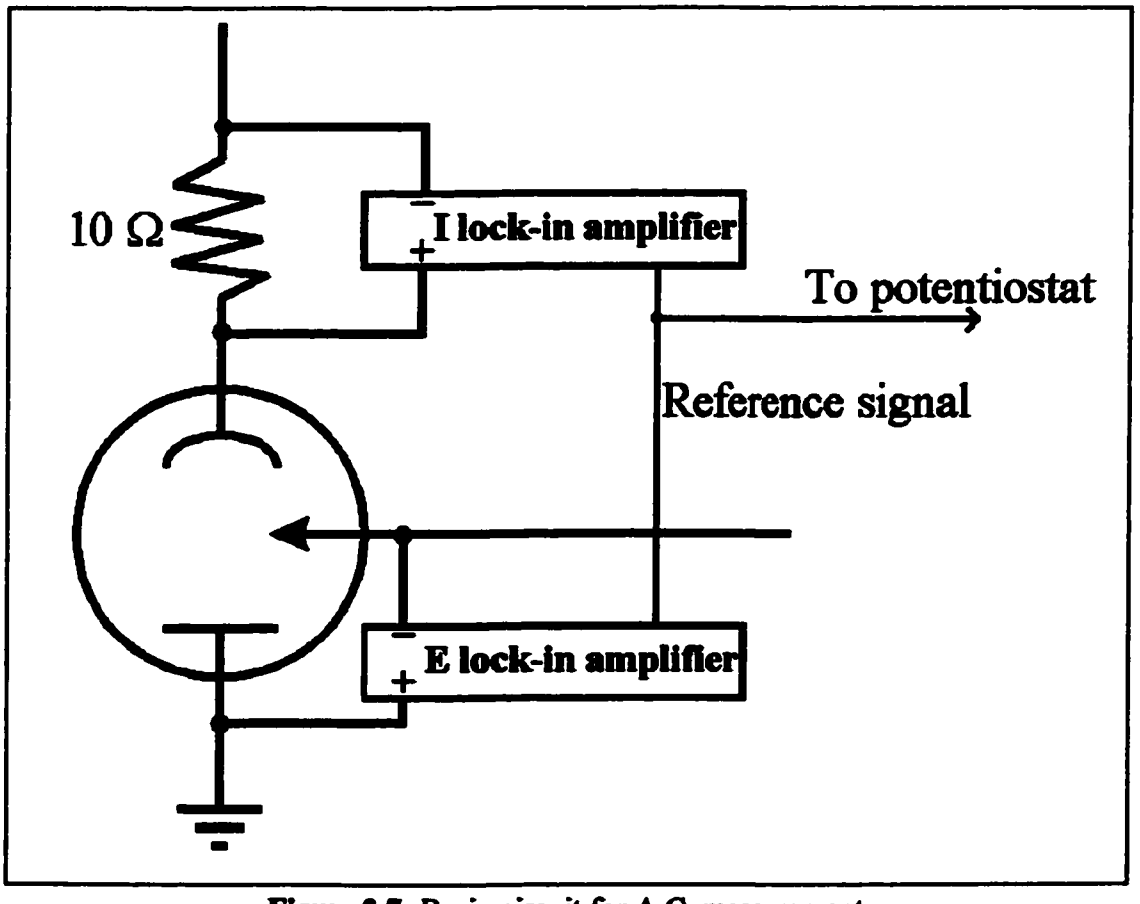

Figure 2.7: Basic circuit for A.C. measurement.

for thallium deposition on Pt(111) covered with iodine. The A.C. voltammogram was repeated for different modulation frequencies, ranging from 3 Hz to 200 kHz. The data from these voltammograms were then combined together in order to obtain the frequency response at each potential. The classical A.C. plots, i.e., Bode plot and Nyquist plots, Fig. (2.8), are obtained, and then fitted using a linear least-squares fit method with the use of the electrochemical software "Zview 2.3". For the case of Tl deposition on Pt(111)($\sqrt{7}$ x $\sqrt{7}$)R19.1°-I, Fig. (2.8), the results fitted the equivalent circuit:

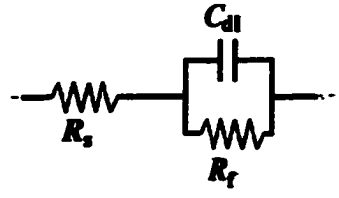

(3)

where R_f is the faradaic resistance. The value of C_{dl} is directly obtained during the fitting process.

The last A.C. technique used in this thesis for the case of silver electrodeposition on Pt(111) covered with iodine is the classical measurement of A.C. impedance. In this technique the electrode is held at a constant D.C. potential. The frequency of a superimposed modulated signal of a similar amplitude as in A.C. voltammetry was swept between 4 Hz and 2 kHz. The double layer capacitance was then obtained after combining the real and imaginary parts of the modulated output current at each potential as in A.C. voltammetry.

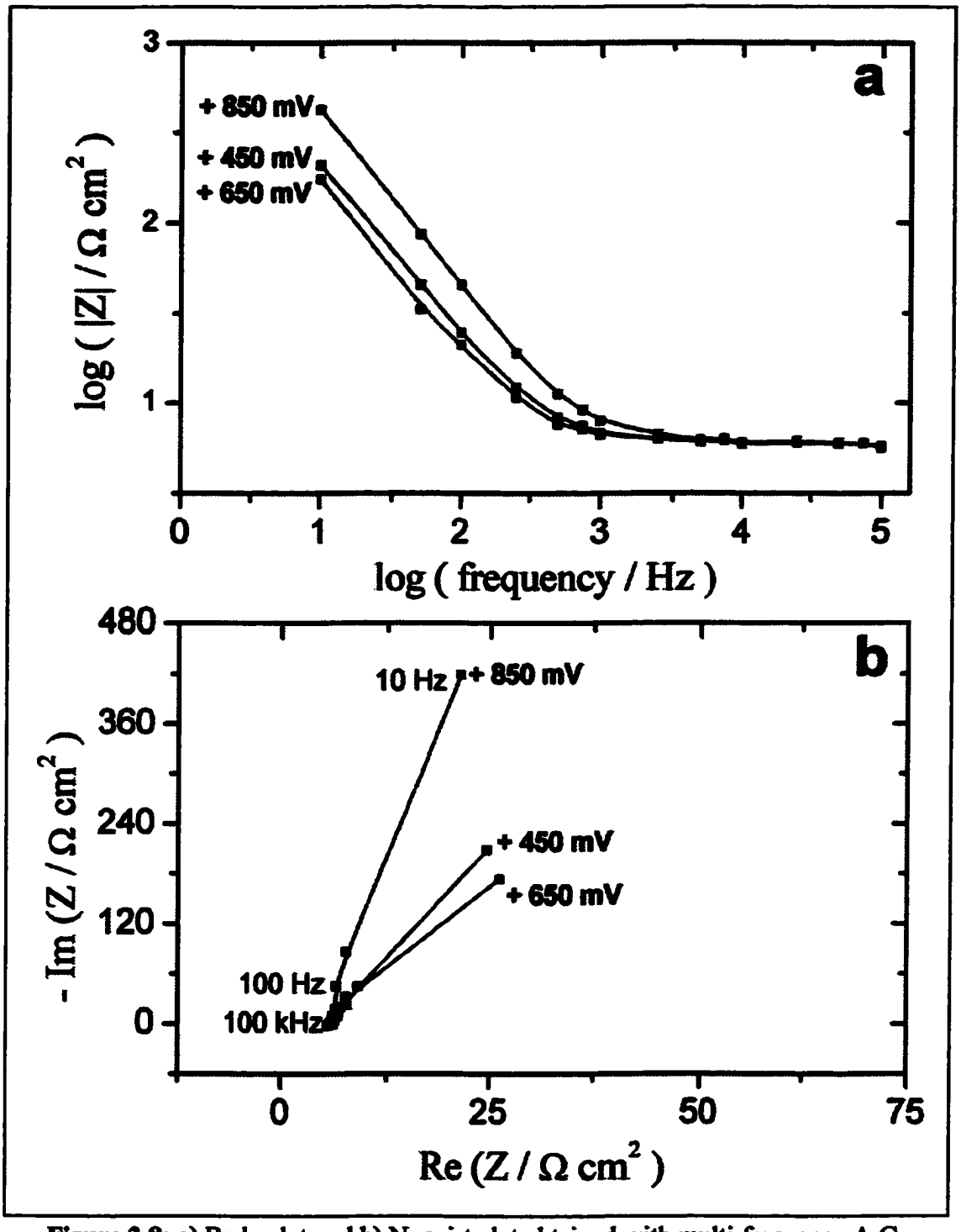

Figure 2.8: a) Bode plot and b) Nyquist plot obtained with multi-frequency A.C. voltammetry for Tl deposition on Pt(111)($\sqrt{7}$ x $\sqrt{7}$)R19.1°-I at different potentials. Note the different axes scales of the Nyquist plot to emphasize the phase angle.

2.4. Electrochemistry of Platinum Single Crystals Covered with Iodine Prepared by Flame Annealing.

In this section, all the stages of the surface preparation are performed at ambient pressure, without the use of UHV equipment. Two different types of platinum single crystals were used in this work: platinum single crystal beads and D-shaped discs.

2.4.1. Platinum Single Crystal Beads.

Unless otherwise specified, the working electrodes for the electrodeposition of Ag were oriented single crystals beads prepared and treated following Clavilier's method [2.7][2.8]. The area of these electrodes varied from 0.01 to 0.035 cm^2. These electrodes were prepared by Dr. Juan Feliu at the University of Alacant, (Spain). A conventional three-electrode glass cell was used, which was thermostatically-controlled to within 1°C. The reference electrode was RHE at the same temperature. A Pt counter electrode was used. Solutions were 0.1 M perchloric acid (Merck Suprapur) and 1 mM $AgClO_4$ (Aldrich), made up in Milli-Q water.

After heating the crystal with a flame for 1 min, the Pt(111)($\sqrt{7}$ x $\sqrt{7}$)R19.1° iodine monolayer was prepared by cooling the hot crystal in iodine vapor. The iodine crystals were warmed up at the bottom of a test tube and let cool for ten minutes before the deposition. Ten seconds after the Pt(111) crystal was removed from the flame, it was placed on top of the test tube for fifteen seconds. The Ag deposition voltammogram is very sensitive to the iodine structure, and the iodine surface was considered unacceptable if the voltammograms were not identical to those previously published [2.9], or if the first and second cycle peak heights were different by more than 10%. This surface was the starting point for the

temperature-dependence measurements.

For the study of the stepped surfaces, the clean surfaces were annealed and cooled in Ar/H_2, which is known to give well-defined stepped surfaces [2.10][2.11]. The iodine was then deposited by immersing the clean surface in 1 mM KI solution at open-circuit. Exposure to iodine vapour was not used for the study of the stepped surfaces since it leads to surface reconstruction [2.12]. In the case of Pt(111), iodide immersion is known by LEED [2.13] and STM [2.9] to give a monolayer of iodine atoms with a (3 x 3) structure. On stepped surfaces with low step densities, STM shows that this procedure gives structures which are locally (3 x 3) [2.12]. We will refer to this structure as "(3 x 3)", even though this cannot be the correct unit mesh on stepped surfaces.

It is useful to compare the measured potentials *vs* the potential for electrodeposition of bulk silver. Voltammograms for Ag electrodeposition are reported *vs* $Ag \mid Ag^+$ (1 mM in 0.1 M $HClO_4$), although for some sets of experiments they were measured *vs* RHE. The conversion used the calculated difference between these two reference electrodes, which follows from the Nernst equation and the proportionality between the entropy of reaction and $(\partial E/\partial T)_P$:

$$E_{Ag^+|Ag}(T) - E_{H^+|H_2}(T) = E^\circ_{Ag^+|Ag}(298.15\,K) + \frac{RT}{F}\ln\frac{\gamma_{Ag^+}m_{Ag^+}}{\gamma_{H^+}m_{H^-}} + \frac{\Delta_r S^\circ_{Ag^+|Ag}}{F}(T - 298.15\,K) - \frac{\Delta_r S^\circ_{H^+|1/2H_2}}{F}(T - 298.15\,K) \qquad (4)$$
$$= 0.6809\,V - (1.386\,mV\,K^{-1})(T - 298.15\,K)$$

The numerical values were obtained using data from the NBS tables [2.14], taking the activity coefficients of H^+ and Ag^+ in 0.1 M $HClO_4$ to be the same, and taking the ratio of their molalities as the experimental value of 100. The zero of the $Ag|Ag^+$ reference

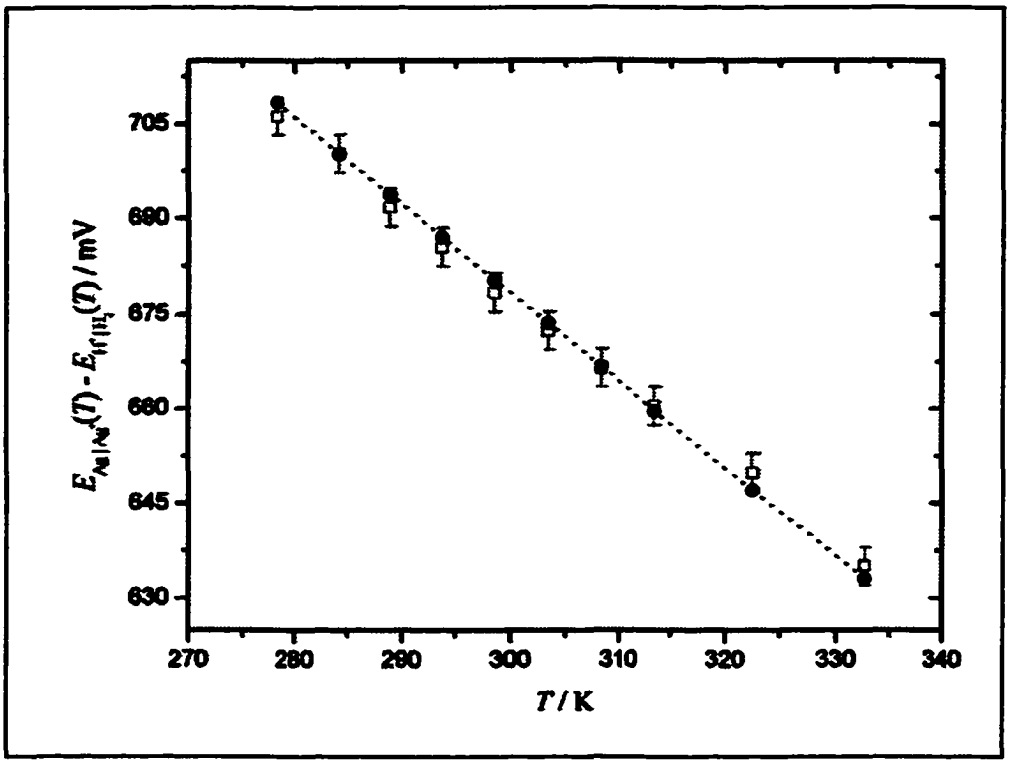

Figure 2.9: Experimental (□) and theoretical (··●··) potential of the $Ag|Ag^+$ reference electrode as a function of temperature.

electrode occurred close to the minimum in the cathodic current before the bulk Ag deposition onset (chapter 6), and this was true within 2 mV for the (111) voltammograms calculated using the above equation, Fig. (2.9).

2.4.2. Pt(111) D-shaped Single Crystals.

A Pt(111) single crystal disc was used for the electrodeposition of Tl at normal pressure. The disc (1 cm diameter, 1 mm thickness) was obtained from the same single-crystal stub as for the Pt single crystals for the use in the UHV system. It was cut in two through the diameter before polishing, giving two D-shaped like Pt(111) single crystals. A Pt wire (1 mm diameter) spot welded to the back of the crystals allows their attachment to glass rods. Before any experiment, the crystals were annealed in a bunsen flame for at least

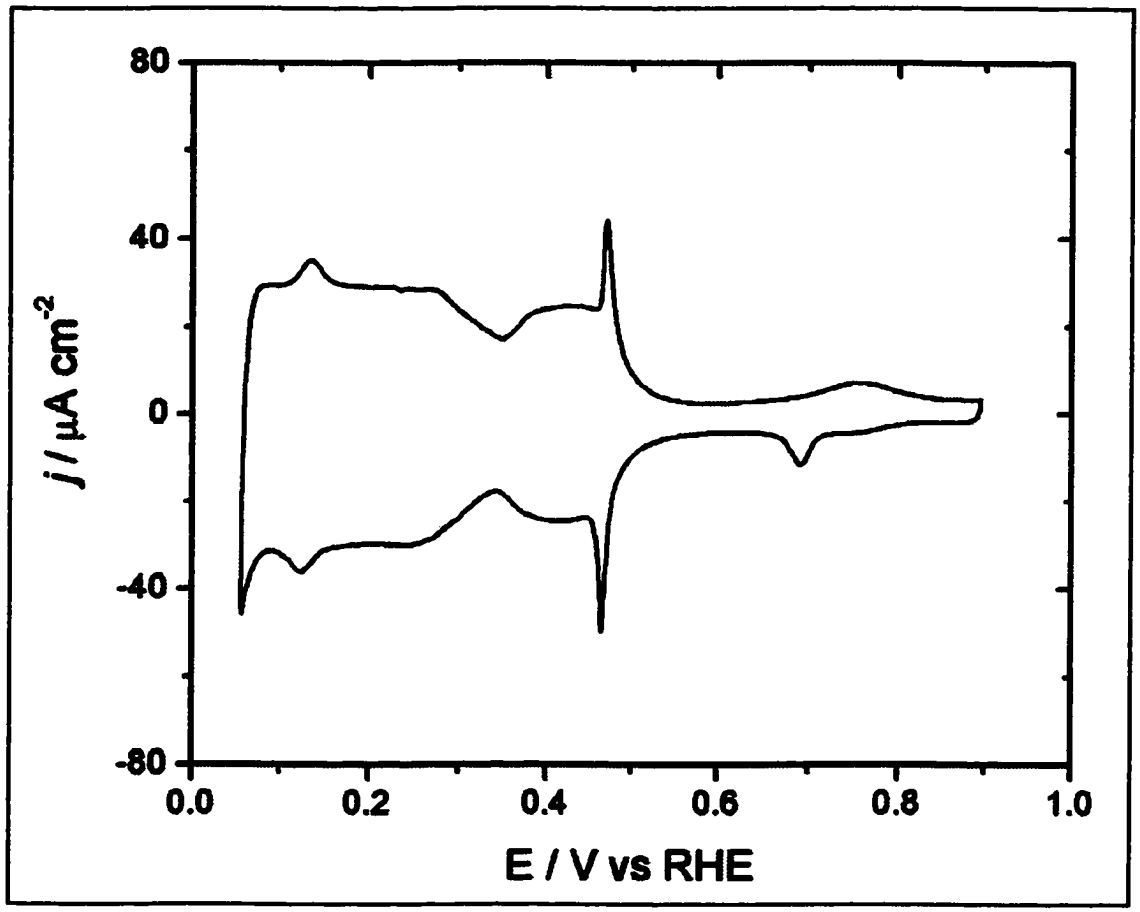

Figure 2.10: Cyclic voltammogram of Pt(111) single crystal disc in H_2SO_4 0.2 M. Sweep rate = 50 mV s^{-1}.

15 min. The iodine was deposited onto the surface in a similar fashion as with the single-crystal beads. The cyclic voltammogram in H_2SO_4 is shown in Fig. (2.10), which shows the good quality of the crystals for this type of experiment.

2.5. Low Energy Electron Diffraction (LEED).

The electron optics in our UHV system is a Retarding Field Analyzer (RFA) supplied by Omicron Vakuumphysik. The advantage of this system is that it can be used for either LEED or AES with a simple change of the control electronics.

The main feature of this analyzer is a set of three energy selection grids with a

Microchannel Plate (MCP). Behind the MCP there is a phosphorescent screen which makes the diffraction patterns visible. Between the third grid and the MCP there is a fringe-field plate. This plate corrects the path of the electrons to ensure a linear relationship between the radial distance of the electrons entering the grids, and the electrons seen on the screen. This is due to the difference in shape between the grids (hemispherical) and the MCP (flat), and results in compression of the image by a factor of two. The electron gun is located in the center of the optics. This uses a lanthanum hexaboride single-crystal filament. After being heated at 1700 K by using a filament current of ~1.1 A, the gun can produce beam currents from 0.01 to 30 μA at energies up to 3500 eV. This makes it ideal for its use in either LEED or AES[I].

LEED can be considered the equivalent of X-ray crystallography in two dimensions. According to the de Broglie relationship, the kinetic energy of the electrons, E, is related to their wavelength, λ, as:

$$\lambda \approx \sqrt{\frac{150.4\ \text{eV}\text{Å}^2}{E}} \tag{5}$$

This relationship shows that electrons with energy below 500 eV have wavelengths of the order of interatomic spacings in solids. These electrons can then diffract as if the lattice were a diffraction grating. Since at this range of energies the electrons only penetrate two or three layers into the solid, the study of the diffracted beams provides only information on the surface region. A study of the position of the diffracted beams gives information about the size and shape of the unit cell. If the spot intensities are measured as a function

---

[I] The tensor-LEED experiments described in chapter 3 were done with a Varian electron optics (RFA) provided by Dr. Keith Mitchell (University of British Columbia).

of energy, the exact position of the atoms of the outer layers of the surface may be determined by Tensor-LEED calculations. This technique will be explained in more detail in chapter 3.

A simple way to understand LEED is that, with the incident electron beam normal to the surface, a LEED photograph is a "picture" of the reciprocal lattice. If the incident electron beam is not perpendicular to the surface, the "picture" of the reciprocal lattice appears distorted. It is called a reciprocal lattice because the distance between diffraction spots is proportional to $1/a$, where a is the distance of the atoms in real space. If the unit cell of the surface is defined by the vectors a_1 and a_2, the unit cell in reciprocal space is defined with another two vectors a^*_1 and a^*_2 such as:

$$\begin{aligned} a_1 \cdot a^*_1 &= 1 \qquad a_2 \cdot a^*_2 = 1 \\ a_1 \cdot a^*_2 &= 0 \qquad a_2 \cdot a^*_1 = 0 \end{aligned} \tag{6}$$

This transformation preserves the same type of symmetry between real and reciprocal space. As an example, Fig. (2.11) shows the real lattice and LEED pattern for a Pt(111) surface, both with hexagonal symmetry.

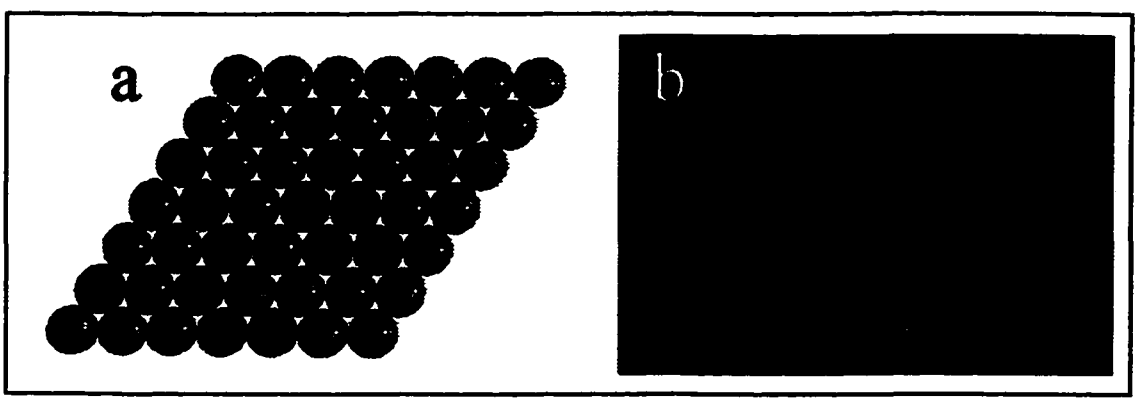

Figure 2.11: a) Ball model of a Pt(111) surface, b) LEED pattern of Pt(111). Beam energy 70 eV. 0.02 μA beam current.

2.6. Auger Electron Spectroscopy (AES).

With the same set of electron optics used in our laboratory for LEED, it is possible to perform AES experiments with a different set of control electronics. The results are, however, very different. While LEED provides information about the surface structure of the crystal, AES provides information about the composition of the elements present in the near-surface region. In Auger spectroscopy the electron yield is detected as the current impinging on the front of the MCP, i.e. the gain of the MCP is not used in this experiment.

The basic process for the production of Auger electrons is shown in Fig. (2.12). A high-energy electron ionizes an atom by ejection of a core-level electron. A beam energy of several keV is used. This is not critical, however, since it is just used to create a vacancy. Unless otherwise specified, the beam energy used in this thesis for AES is 3 keV, with a beam current of 10 μA. The vacancy is filled by another electron from a higher energy level. The excess energy can be released by either the production of photons (X-rays) or an Auger electron. The result in the latter case is a doubly ionized atom.

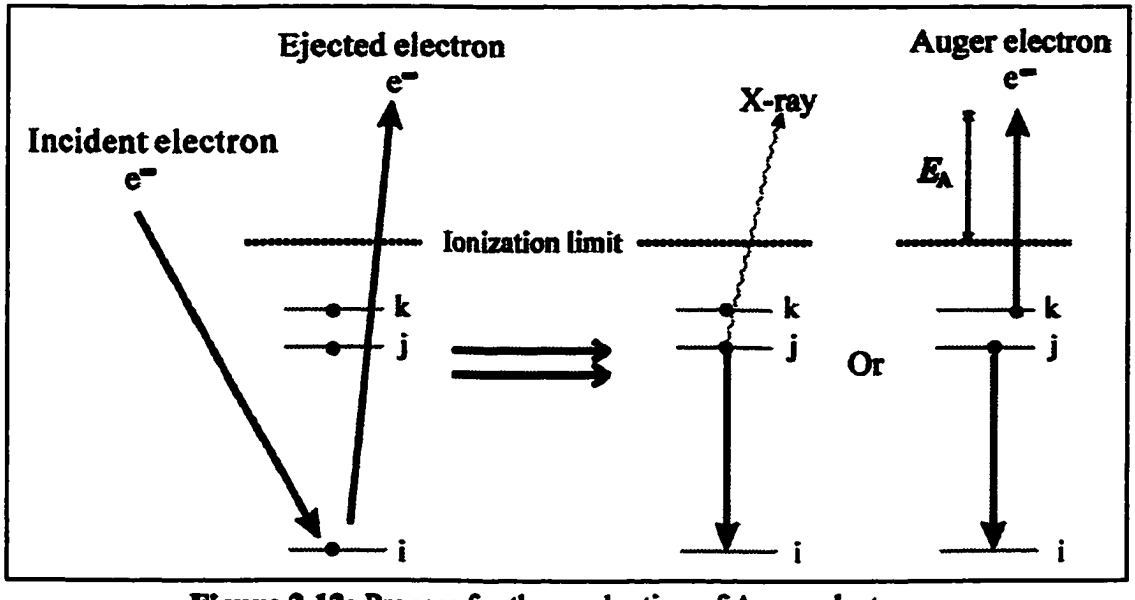

Figure 2.12: Process for the production of Auger electrons.

According to Fig. (2.12), the basic equation for the kinetic energy of the Auger electron, E_A, is:

$$E_A = E_i - E_j - E_k \tag{7}$$

where the energy of the Auger electron is characteristic of the material.

However, due to the low yield of Auger electrons compared with the total number of scattered electrons, a simple detection system is not practical. The sensitivity is increased by modulating the energy of the selector grids with a superimposed sinusoidal wave, 10Vpp and 4.7 kHz. The modulation of the voltage of the retarding grids produces a modulation of the detected current at the collector, $I(E)$. $I(E)$ is proportional to the total number of electrons passing through the grids; therefore:

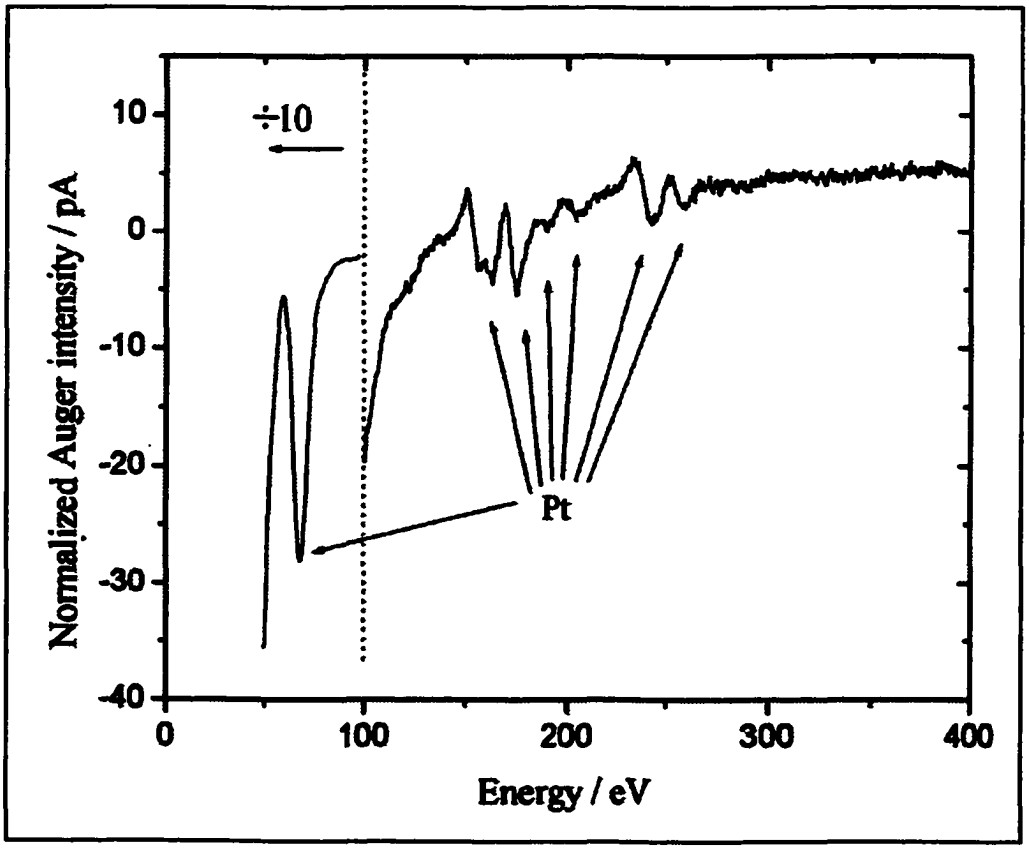

Figure 2.13: Auger spectrum of Pt(111) normalized to 10 μA ion current.

$$I(E) \propto \int_E^{\infty} N(E)\, dE$$
$$I'(E) \propto N(E) \qquad (8)$$
$$I''(E) \propto N'(E)$$

$I'(E)$ and I''(E) correspond to the first and second derivative with respect to the energy. They are measured with the help of a lock-in amplifier, using the modulation frequency as a reference. Traditionally the Auger spectra is displayed in the derivative form, $N'(E)$, which is proportional to I''(E). The main reason is to suppress the broad peak of secondary electrons in the $N(E)$ spectra. As an example, Fig. (2.13) shows the AES spectra for a clean Pt(111) surface.

Chapter 3

Surface Structure of Pt(111)(3 x 3)-AgI.

3.1. Introduction.

The surface compound Pt(111)(3 x 3)-AgI was first characterized by Hubbard [3.1][3.2][3.3]. He proposed a structure on the basis of the size and shape of the unit cell measured by LEED, the surface atomic composition measured by AES, and by analogy with the structure of solid AgI. The structure has a repeating unit mesh (2-D unit cell) with sides 832.5 pm, three times the Pt-Pt distance of 277.5 pm [3.4]. He noted that the proposed Ag and I layers of the structure were isostructural with (111) layers in solid AgI, and that it could be represented as a slice of bulk crystalline AgI with the zinc-blende structure sitting on the Pt surface, expanded laterally by 5%. The structure was composed of a monolayer of Ag atoms lying between a monolayer of iodine atoms and the first Pt layer. The Ag atoms were arbitrarily assigned to atop and two-fold bridge sites on the Pt. However, the positions of the atoms within the unit cell were not directly determined from LEED because a full intensity analysis was not performed.

3.2. Tensor LEED Analysis.

The surface technique tensor LEED is equivalent to X-ray crystallography in two dimensions. The variation of the intensity of the diffracted beams as a function of the electron energy is compared with that calculated for different proposed surface structures. These structures are chosen by a trial-and-error approach, making sure that they correspond with the symmetry defined by the diffraction pattern. The agreement is maximized by the

tensor LEED program by adjusting the atomic positions in an iterative procedure.

We have recently done, in collaboration with Dr. K. Mitchell and M. Saidy at UBC, a tensor LEED analysis for the electrodeposited Pt(111)(3 x 3)-AgI structure [3.5], together with the vapor deposited Pt(111)(√7 x √7)R19.1°-I, Pt(111)(3 x 3)-I and Pt(111)(√3 x √3)R30°-I structures [3.6]. The LEED patterns for the Pt(111)(3 x 3)-AgI as well as for the Pt(111)(√7 x √7)R19.1°-I are shown in Fig. (3.1). The experiments were done at UVic with an electron optics (RFA) provided by Dr. Mitchell. The structural analysis was done at UBC using the tensor LEED programs provided by Van Hove [3.7][3.8][3.9].

Twenty-nine different model types were investigated in the case of the Pt(111)(3 x 3)-AgI structure. Measurements of the diffracted beam intensities were made at a temperature between 298 and 302 K, and under a pressure around 4×10^{-9} mbar. Intensity-versus-energy (I(E)) curves were recorded for normal incidence using a video LEED analyzer system following standard procedures [3.10]. For example, sets of beams that are believed to be symmetrically equivalent were measured at the same time in order to ensure

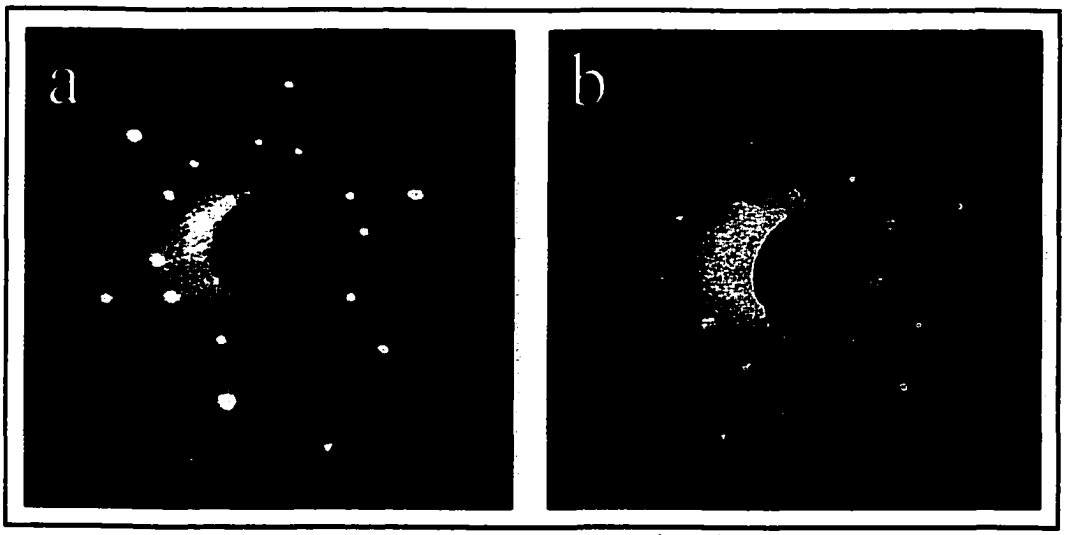

Figure 3.1: LEED pattern (97 eV) for the a) Pt(111)(√7 x √7)R19.1°-I and b) Pt(111)(3 x 3)-AgI structures.

that a close approximation to normal incidence is attained. I(E) curves were measured with appropriate beam averaging, normalization and smoothing of the symmetrically-related beams

The most relevant for this thesis is the Pt(111)(3 x 3)-AgI structure. For the analysis of the Pt(111)(3 x 3)-AgI structure, thirteen independent beams were used: (0 1), (1 0), (1 1), (0 2), (2 0), (2/3 0), (4/3 0), (0 5/3), (2/3 2/3), (2/3 1/3), (2/3 1), (1/3 1) and (4/3 1/3) (total energy range is 1350 eV). Fig. (3.2) shows the LEED pattern for the Pt(111)(3 x 3)-AgI structure, together with the notation used in this thesis for each of the beams analysed.

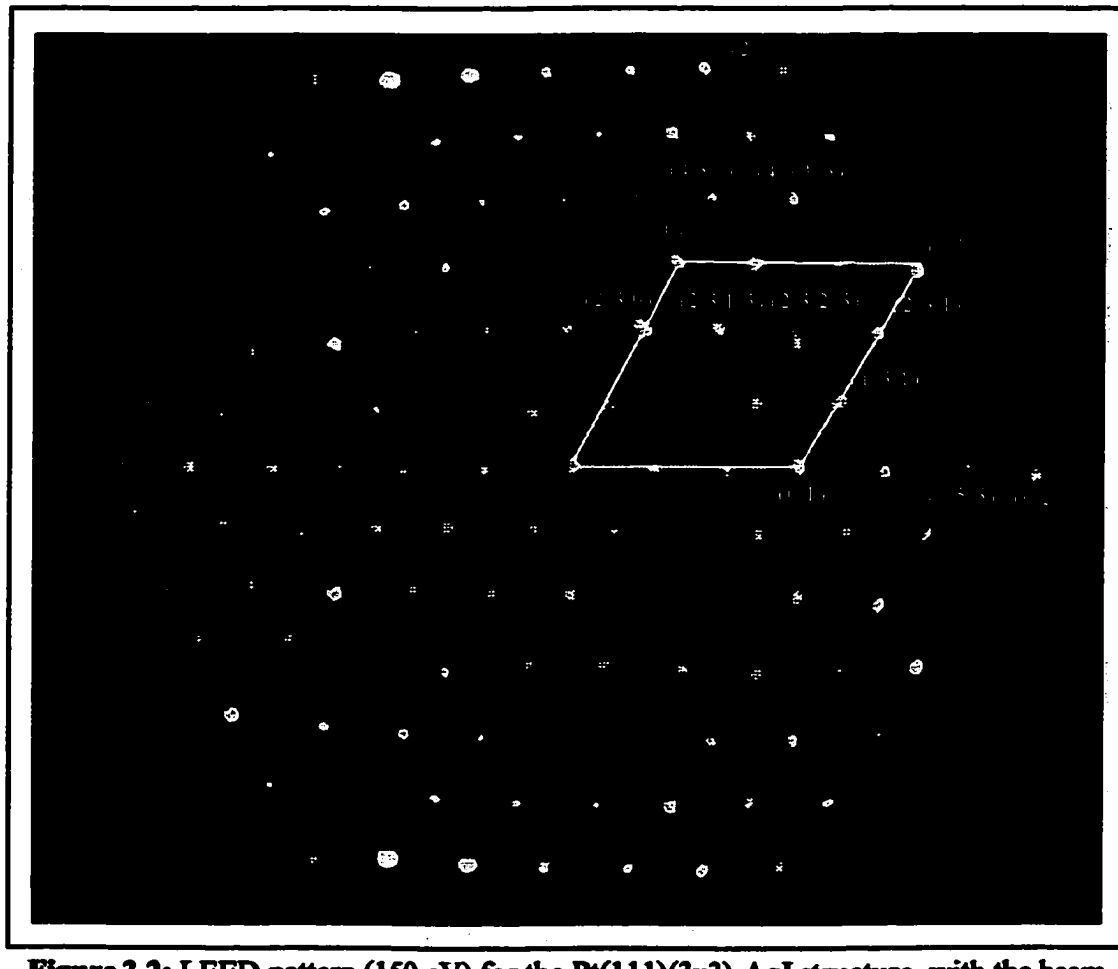

Figure 3.2: LEED pattern (150 eV) for the Pt(111)(3x3)-AgI structure, with the beam notation used for the tensor LEED measurements. (The image has been altered with the computer to show all the diffraction beams).

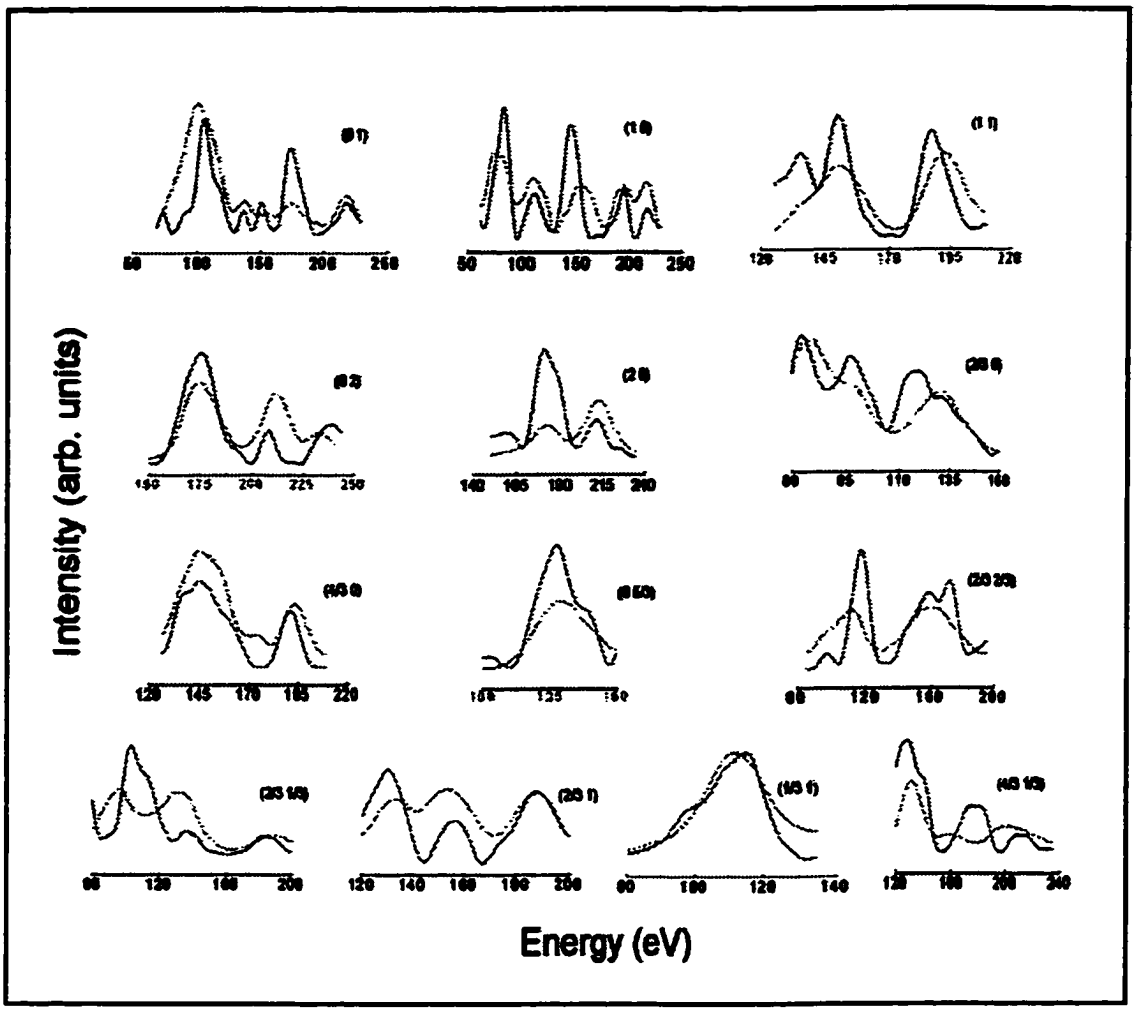

Figure 3.3: I(E) curves measured for thirteen diffracted beams (dashed lines) for normal incidence from the Pt(111)-(3x3)-AgI surface and compared with those calculated (solid lines) for the favored geometry according to the tensor LEED analysis.

Given the complexity of the preparation process, six sets of I(E) curves were measured from independently prepared surfaces, but data from a single set of measurements were used in the subsequent structural analysis. The experimental and calculated I(E) curves used for the final analysis are shown in Fig. (3.3). The reliability index or R-factor, R_p, introduced by Pendry [3.11] was used in order to compare quantitatively the experimental with the calculated I(E) curves. For each diffraction beam:

$$r_p = \frac{\int \left(Y_{calc} - Y_{exp}\right)^2 dE}{\int \left(Y_{calc}^2 - Y_{exp}^2\right) dE} \qquad (1)$$

where $Y = \frac{1}{L\left(L^{-2} + V_{oi}^2\right)}$, and $L = \frac{d \ln I}{dE}$. V_{oi} is the imaginary part of the inner potential of the "muffin-tin" approximation, used in the calculations to describe the potential of the surface. R_p is a weighted average of all the r_p factors according to their energy ranges.

The estimated R_p value for the I(E) curves in Fig. (3.3) was 0.296. Other structures gave R_p values between 0.484 and 0.843. $R_p \leq 0.2$ is considered very good agreement between experimental and calculated I(E) curves. The structure is most likely to be incorrect for $R_p \geq 0.5$ [3.12].

3.3. Pt(111)(3 x 3)-AgI Surface Structure.

With the tensor LEED technique, the crystallographic structure with the exact position of the atoms of the Pt(111)(3 x 3)-AgI surface structure was obtained. The results of these experiments confirmed the proposed structure by Hubbard, except for the location of the Ag atoms relative to the Pt substrate. The structure could be represented as a slice of bulk AgI with the zinc-blende structure contracted by 10%. We found that per unit cell, three Ag atoms are close to atop sites and one bonds on a three-fold hollow site on the Pt(111) substrate. The atomic structure for the Pt(111)($\sqrt{7}$ x $\sqrt{7}$)R19.1°-I as well as for the Pt(111)(3 x 3)-AgI are shown in Fig. (3.4). The model proposed in this work for the Pt(111)(3x3)-AgI surface has two inequivalent types of iodine atoms, and that is also the case for silver atoms, Fig. (3.4.b). The I atoms are located in sites of three-fold coordination created by the close-packed layer of Ag atoms bonded to the Pt(111) surface, with an

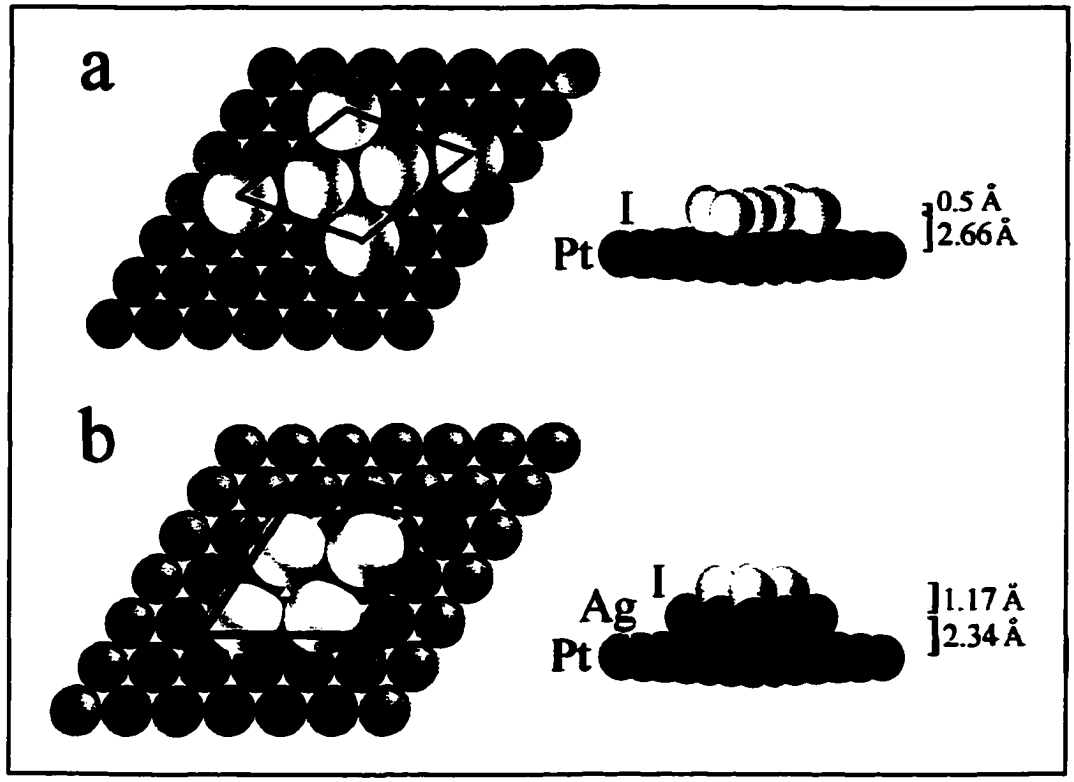

Figure 3.4: Surface structure for: a) Pt(111)($\sqrt{7}$ x $\sqrt{7}$)R19.1°-I and b) Pt(111)(3 x 3)-AgI.

average Ag-I bond distance of 2.67 Å. This distance is shorter than the Ag-I bond length in bulk AgI with the zinc blende structure (2.81 Å) [3.13]. This is expected for the lower coordination number of I (four in the bulk solid, three in the surface structure). The bond order for AgI in the Pt(111)(3 x 3)-AgI structure can be estimated according to the Brown-Altermatt method, which, using AgI bulk to parametrize a Pauling-type bond length - bond order relation, is [3.14]:

$$r = r_0 - 0.84\ \text{Å}\ \log_{10}(s) \qquad (2)$$

where r_0 is the length of a single bond and s the bond order. The bond order for AgI in the Pt(111)(3 x 3)-AgI structure is estimated as 1.46 relative to AgI in bulk.

The Ag atoms go beneath the I layer, in direct contact with the Pt atoms. Of the four

Ag atoms per unit cell, one occupies a three-fold site on Pt(111), with a Pt-Ag bond length of 2.82 Å. This bond length is close to expectation from the sum of metallic radii (2.83 Å) [3.15]. The other three Ag atoms are displaced by 0.85 Å off atop sites on the Pt(111) surface. Each of them bonds to two Pt atoms with a bond length of 3.11 Å, and to one Pt atom with a bond length of 2.48 Å, much shorter than the sum of metallic radii.

It is interesting to notice that the Ag layer is 2.34 Å above the surface Pt layer, and the I layer is 1.17 Å above the Ag layer, with no significant corrugation of either layer. On the other hand, the I layer for the Pt(111)($\sqrt{7}$ x $\sqrt{7}$)R19.1°-I structure has 0.5 Å corrugation, Fig. (3.4.a). The absence of corrugation in the Pt(111)(3x3)-AgI structure is suggestive that the Ag-I interactions are more important than the Pt-Ag interactions.

Chapter 4

Silver Electrodeposition on Pt Single Crystals Covered with Iodine.

4.1. Introduction.

It is interesting to see how the crystallography of the underlying Pt surface alters the structure and reactivity of electrodeposition processes. This chapter is a systematic study of the influence of the step density on the electrodeposition of Ag onto Pt covered with iodine. Aside from Pt(111), LEED, AES and cyclic voltammetry have been reported previously only for the iodine covered Pt(322) = 6(111) x (111) and Pt(100) [4.1][4.2] surfaces. The cyclic voltammetry on iodine covered Pt(110) has also been reported [4.3]. In this chapter, the electrodeposition of Ag on various iodine-covered Pt stepped surfaces is systematically investigated. Most of this has been previously published [4.4]

4.2. Dependence of Ag Deposition on Surface Crystallography of Surfaces Prepared by Immersion in Iodide Solutions.

Fig. (4.1) shows the voltammograms for Ag deposition on the three low-index planes of Pt, covered with iodine prepared by immersion in iodide solution. As explained in section 2.4.1., this procedure is known to give for Pt(111) a monolayer of iodine with a (3 x 3) structure. For other surfaces with low step densities it gives structures which are locally (3 x 3), which we will refer to as "(3 x3)".

The first point to note is that the peak widths are wider than for deposition on the Pt(111)($\sqrt{7}$ x $\sqrt{7}$)R19.1°-I surface (Fig. (1.1)), which may be an indication that the iodine layer prepared by immersion in iodide is less well-ordered than the iodine layer prepared

from I_2(g). The C1 and A1 peaks on the Pt(100) and Pt(111) surfaces are tentatively assigned to deposition on the respective types of terraces, with the site on the (111) terrace being more stable (C1/A1 peaks at more positive potentials). The second reduction peak (C2) is best defined on the (111) surface, is ill-defined on the (110) surface and is absent for

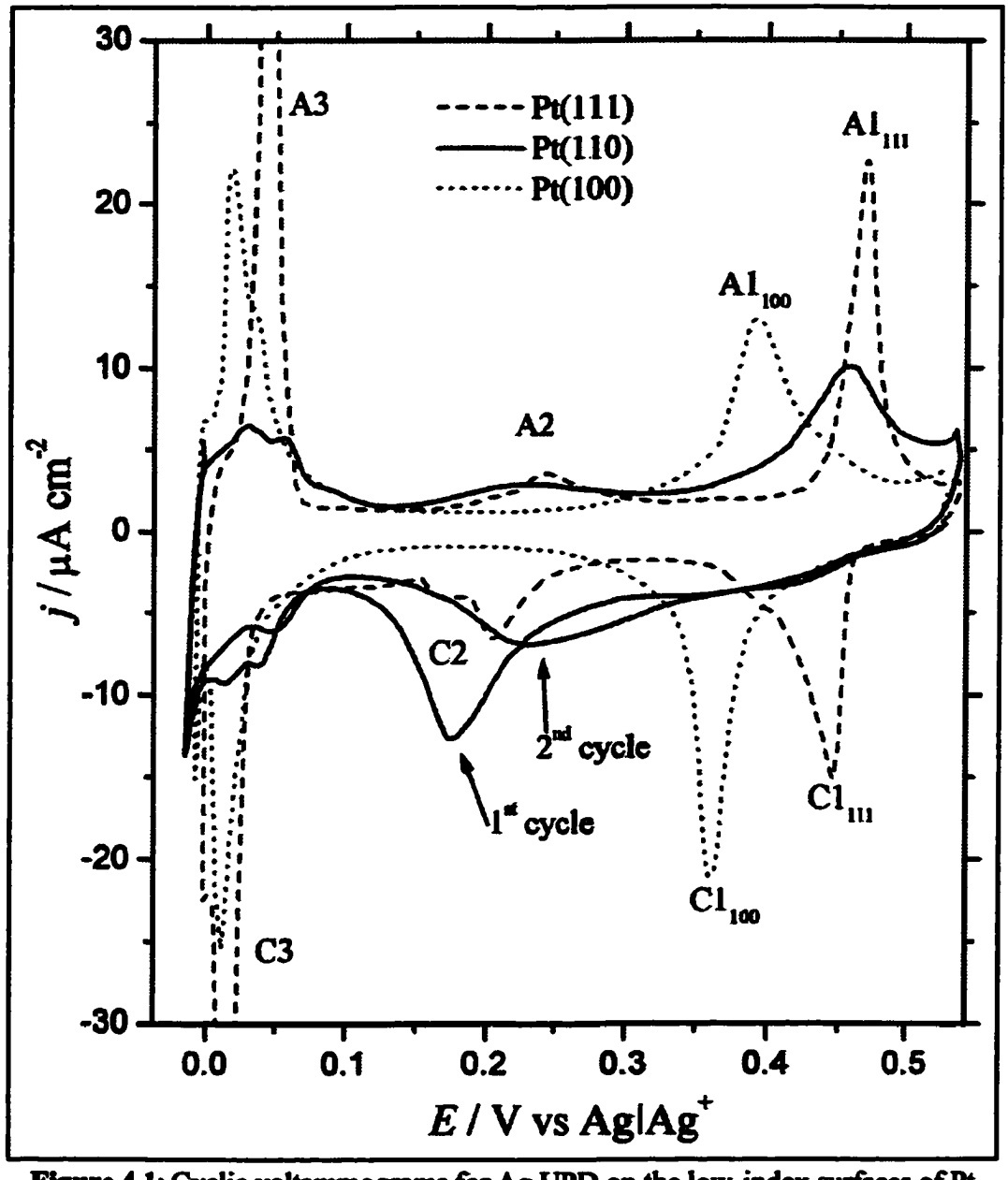

Figure 4.1: Cyclic voltammograms for Ag UPD on the low-index surfaces of Pt after immersion in KI solution. The first and second cycles for the (110) platinum surfaces are indicated. $[Ag^+] = 1$ mM, sweep rate 5 mV/s. $T = 298$ K.

the (100) surface. The third deposition peak (C3) , previously assigned to a second monolayer of Ag, is most pronounced for the (111) surface, less pronounced for the (100) surface and diminished and ill-defined for the (110) surface. For stepped surfaces, this peak merges with the bulk deposition current, and the two become indistinguishable when the terrace width is six atoms or less. For this reason, a quantitative study of this peak was not attempted.

4.2.1. First Cycle Behavior.

After immersion at + 0.60 V, the potential was first scanned to more negative potentials. Except for the (111) and (100) surfaces, this first negative-going scan on the stepped surfaces had larger charges than subsequent positive- or negative-going scans (e.g. Pt(110), Fig. (4.1)). After the first cycle, the behavior was reproducible from cycle to cycle, and anodic and cathodic charges were equal. The difference in the reduction charges for the first and second cycles increases with the step density, Fig. (4.2). The correlation with step density for the reduction charge means that edge effects or other experimental artifacts are unlikely. One possibility is the reduction of Ag^+ to give Ag at step sites. However, our second-cycle voltammograms for the 6(111) x (111) surface agree with Hubbard's voltammograms (first or subsequent cycles) [4.5], which began with well-characterized iodine layers demonstrably free of silver. Therefore it is unlikely that any silver is present on the surface at the beginning of our second cycle, particularly since the amount of silver corresponding to the excess charge would be too high, e.g, 3.3 silver atoms per step atom for the 4(111) x (100) surface. This high charge similarly precludes other reactions producing surface-adsorbed species. Reduction reactions in which both reactants and

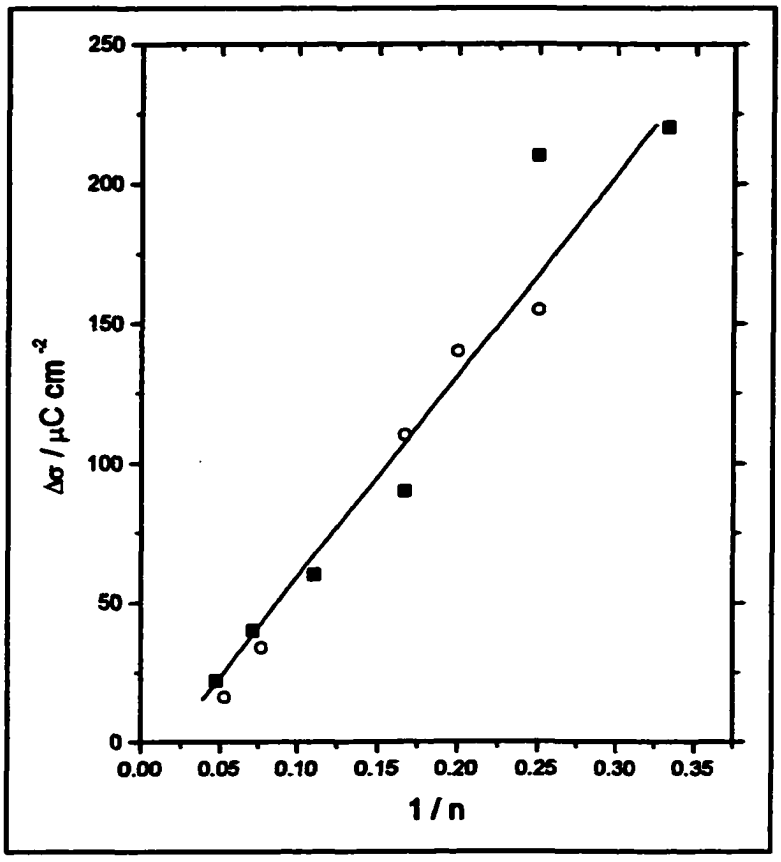

Figure 4.2: Difference in reduction charges ($\Delta\sigma$) between the first and second cycle as a function of step density ($1/n$). (■) = n(111) x (100) surfaces, and (○) = n(111) x (110).

products are solution species are unlikely to correlate with step density. The most likely process is therefore reduction of a surface species loosely-bound to steps to give a soluble product. Such a surface species could form during the open-circuit potential immersion used here, but would not form in the controlled-potential immersion used by Hubbard [4.6], which likely explains the differences in first cycle behaviors. Possible reactions are the reduction of iodine atoms or I_2 molecules to aqueous iodide (which ultimately reacts with Ag^+ in the solution), or the reduction of adsorbed oxygen to water. As explained in chapter 2, the crystals were cooled in Ar/H_2 atmosphere. This procedure is known to give well-defined stepped surfaces. Therefore, the only possible source of oxygen contamination

would be oxygen dissolved in the KI solution. It is difficult experimentally to identify the weakly-adsorbed species, and so the issue of their identity remains unresolved.

4.2.2. Stepped Platinum Surfaces.

The C1 peaks were higher and better-defined on the second cycle than on the first, with the first- and second-cycle differences larger for surfaces with higher step density. The charge in the second cycle, between the C3 peak and the positive-potential limit varies slightly with step density, but averages about 245 $\mu C\ cm^{-2}$, which agrees with the corresponding charge measured by Hubbard [4.5] for the 6(111) x (111) surface. Therefore, the following discussion of trends applies to the second-cycle behavior.

4.2.2.1. Terraces with 100 Steps.

Surfaces studied: n(111) x (100) for $n = \infty$, 21, 14, 9, 6, 4, 3, 2, i.e, (111), (11,11,10), (15, 13, 13), (544), (755), (533), (211), (311).

In this series, Fig. (4.3.a), the terraces are (111) with varying widths (n = number of atoms across the terrace) and the steps are (100) of monoatomic height. As the step density increases, the C1 peak broadens, decreases in height and moves to more negative potentials. The A1 peak behaves similarly, but the shift to more negative potentials is less pronounced. These peaks are barely distinguishable from the baseline for surfaces with terrace widths of four atoms or less, and the voltammograms for these narrow-terrace surfaces resemble the voltammogram for (110). The C2 peaks decrease in prominence similarly. As these changes occur, the flat baseline current between peaks C1 and C3, and between peaks A1 and A3 increases. This baseline current is largely Faradaic in nature, since the estimated double-

layer charging current is negligible on this scale.

4.2.2.2. Terraces with 110 Steps.

Surfaces studied: n(111) x (110) for $n = \infty$, 19, 13, 6, 5, 4, 3, 2, 0, i.e, (111), (10,10, 9), (7, 7, 6), (7, 7, 5), (3, 3, 2), (5, 5, 3), (2, 2, 1), (3, 3, 1), (1,1,0).

Despite the difference in the type of step, similar trends are seen in this series, Fig. (4.3.b) as when the steps are (100). The C1 peak broadens, decreases in height and moves to more negative potentials. The A1 peak broadens and decreases in height, but there is no significant shift to more negative potentials. For surfaces with terraces with fewer than six atoms, the voltammograms are similar to the (110) voltammograms. The C2 peak diminishes in intensity as the step density increases. As before, the charge lost as the C1 peak decreases appears in the baseline current. Indeed, the first- and second-cycle behaviors for (111) terraces are almost identical, whether the steps are of the (110) or (100) type.

4.2.2.3. Terraces with 111 Steps.

Surfaces studied: n(100) x (111) for $n = \infty$, 20, 4, 3, 2, i.e, (100), (39,1,1), (7,1,1), (5,1,1), (3,1,1).

As in the other series, the C1 and A1 peaks decrease in height as the step density increases, and for terrace widths of less than seven atoms, the voltammogram is close to that previously described for the most open surface, namely Pt(110). However, the C1 and A1 peaks do not shift in potential Fig. (4.3.c), and the broadening is less significant than for the other series.

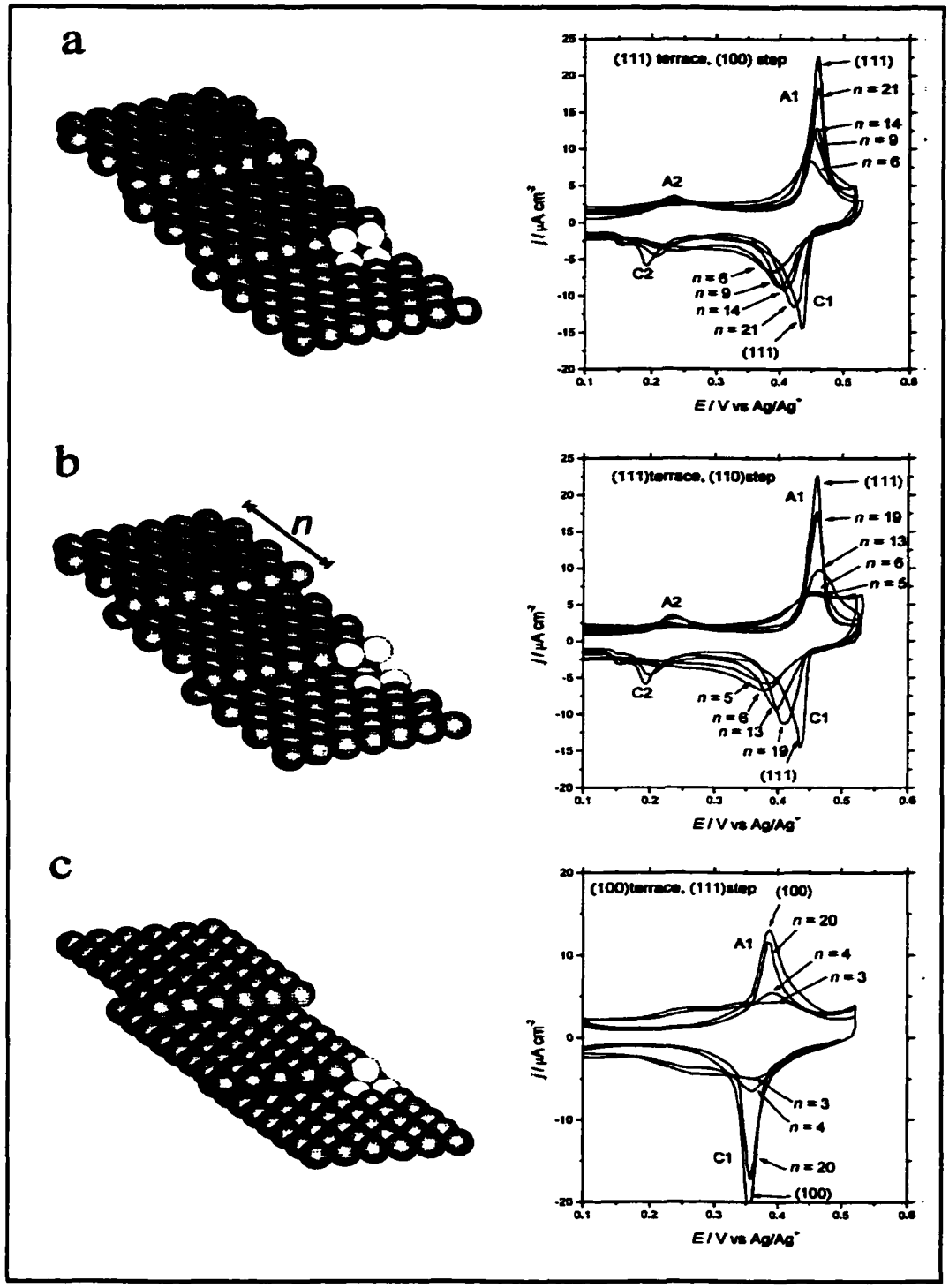

Figure 4.3: Surface models and cyclic voltammograms for Ag UPD on different Pt surfaces after immersion in KI solution, $[Ag^+]$ = 1mM, sweep rate 5 mV/s. T = 298 K: a) n(111) x (100); b) n(111) x (110) and c) n(100) x (111). (White atoms are shown to clarify the type of step).

4.2.3. Structure - Voltammetry Peak Correlations for Stepped Platinum Surfaces.

Immersion of Pt(111) into iodide solution is known to give the Pt(111)(3 x 3)-I structure [4.6]. The structure formed in the C1 peak on the iodide-immersed surface has not been characterized, but the C1 peak on the Pt(111)($\sqrt{7}$ x $\sqrt{7}$)R19.1°-I surface formed by gas-phase dosing of I_2 is known to produce Pt(111)(3 x 3)-AgI, with I:Pt and Ag:Pt ratios of 4:9 [4.7]. It is reasonable to assume that the C1 peak on the iodide-immersed surface produces the same structure. In support of this, the C1 peaks on the two surfaces occur at very similar potentials. In this thesis it is found that the C1 peak potentials on the (3 x 3)-I and ($\sqrt{7}$ x $\sqrt{7}$)R19.1°-I surfaces differed by 15 mV; a difference of ca. 25 mV is evident from examining the figures in Hubbard's work. This small difference may reflect small differences in the stability of the two iodine structures, but is unlikely to be due to very different Ag deposition structures.

For Pt(100), dosing with gas-phase I_2 produces Pt(100)($\sqrt{2}$ x $2\sqrt{2}$)R45°-I, and this surface is stable in aqueous solution at open circuit. The C1 peak on this surface produces a Pt(100)($\sqrt{2}$ x $\sqrt{2}$)R45°-AgI structure with I:Pt = Ag:Pt = 2:4 [4.1]. Unfortunately, for iodide-immersed Pt(100) neither the iodine structure nor the C1 deposition structure have been characterized. Since there appears to be no significant difference in the potentials of the C1 and C3 peaks on our iodide-immersed surfaces from those on the I_2-dosed surfaces, we assume that the Ag deposition structures are the same, although our peaks are broader and enclose a higher charge. The differences are likely related to differences in the adlayer order.

The C1 peaks are therefore assigned to production of ordered structures on the (111)

and (100) terraces, and the difference in Cl_{111} and Cl_{100} peak potentials is a reflection of the different Gibbs' energies of these structures. The decrease of the C1 and A1 peaks as the terrace widths decrease confirms that these peaks are associated with terraces. Moreover, the almost identical behavior for surfaces with (111) terraces and steps of (100) or (110) type, Figs. (4.3.a) and (4.3.b), confirms that C1 is not due to step adsorption. Ordered regions on terraces produce sharp peaks in the voltammograms. However, the deposition on steps occurs with a distribution of energies, so that the corresponding current appears in the flat baseline.

The fact that the initial deposition occurs on the terraces is surprising in view of the dogma in catalysis that step sites are the most reactive. However, this can be explained considering that the ordered structures containing iodine are more stable than the disordered structures, and so the iodine preferentially stabilizes Ag on the terraces. This is in agreement with the tensor LEED measurements in chapter 3, which show that the Ag-I angles seem to be determining the structure.

The corresponding systematic study of Ag deposition on Pt stepped surfaces in the absence of iodine has not been done. Systematic studies have been carried out for Pb UPD on gold [4.8] or Cu on platinum [4.9][4.10], and it is interesting that in those cases the voltammograms showed much more structure, and peaks could be identified with specific types of terrace and step sites. Ag UPD on bare Pt likely behaves similarly to these other metal on metal systems without strongly coadsorbed atoms. The behavior on iodine-covered surfaces is markedly different in that no peaks assignable to step sites are found, suggesting that iodine plays a special role. Other arguments can also be made that the iodine influences both the stoichiometry and structure of the Ag deposition:

A) The disappearance of the Cl and Al peaks correlates with the increasing step density and suggests that the disordering introduced by the steps alters the Gibbs energy change of the deposition. Both these peaks are well defined for surfaces with at least nine atoms on the terrace, and disappear once the terrace width becomes smaller than about five or six atoms. This suggests that these structures require a long-range order over at least 10 Å, which is about the size of one (3 x 3)-AgI unit mesh on the terrace. Whether the change in energetics is due to the sensitivity of the initial iodine layer or the product AgI or both to the presence of steps is difficult to decide experimentally.

B) Iodine adsorption structures at saturation coverage on Pt single-crystal surfaces are typically close-packed layers with interatomic distances close to twice the van der Waals

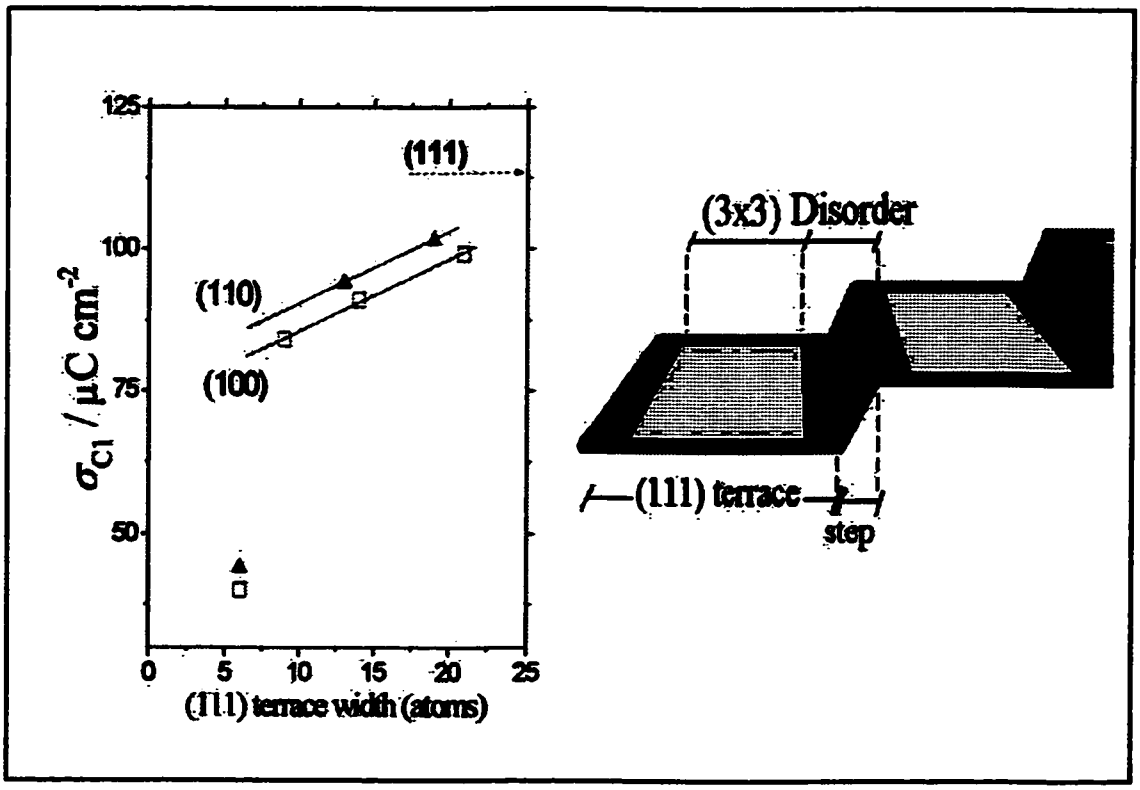

Figure 4.4: Charge density for the Cl peak for Pt(111) and stepped surfaces as a function of the (111) terrace width (*n*) for: □) *n*(111) x (100) and ▲) *n*(111) x (110) surfaces.

radius. Even across step edges, the iodine positions are close to those predicted from simply laying down a close-packed layer of iodine atoms over the step edge. That is, specific Pt-I interactions seem less important than iodine packing considerations, and this leads to a spectrum of types of surface bonding across a step edge, probably of similar energies. This region of rather ill-defined sites may persist as a disordered region in the AgI phase after deposition, since iodine packing considerations probably still play a role (iodine being larger than silver). If we assume this disordered region extends a fixed distance from a step edge in either direction, then its size may be estimated from the area of the C1 peak. Fig. (4.4) shows the charge for the C1 peak for surfaces with steps of (100) and (110) type as a function of the (111) terrace width. If the charge for the C1 peak is related to "(3x3)" ordered regions on the terrace, the difference in C1 charge between a stepped surface and the clean (111) is a measurement of the percentage of surface that is lost to the "(3x3)" region due to the disordering influence of the steps. The slope of the linear regions in Fig. (4.4) allows us to calculate that the disordered region is 2 - 2½ atoms per (100) step, and 1½ - 2 atoms per (110) step. As explained above, for surfaces with small terrace widths the approximation breaks down, and the disordered region is larger than this estimate, (see e.g. the points for $n = 6$ on Fig. (4.4)).

C) As the step density increases and the C1 peak diminishes, the silver deposition voltammograms approach the Pt(110) voltammogram. Furthermore, the Pt(110) voltammogram is very similar to the voltammogram on a Pt(111) surface which has been disordered by electrochemical cycling prior to iodine adsorption [4.11]. The voltammograms become more featureless, and there is no obvious correlation of voltammetry features with types of steps. Moreover, the charge for silver deposition between the C3 peak and the

positive potential limit remains approximately constant at 245 $\mu C\ cm^{-2}$ for all the surfaces studied. Therefore, it seems that the same amount of silver can be deposited, but that the deposition is disordered in a region around the steps. This suggests that Ag:I stoichiometry is more important than Ag:Pt, and that Ag deposition is not site specific with respect to platinum. This is verified in the tensor-LEED measurements, which show how the structure remains essentially flat despite the different types of coordination of the Ag atoms within the unit cell.

Chapter 5

Thermodynamic Calculations of AgI adsorbed on Pt(111).

5.1. Introduction.

In this chapter, we combine data from several types of experiments to find the cohesive and formation energies for the surface compound AgI(ads) which can be electrochemically deposited on a Pt(111) surface. The cohesive and formation reactions correspond respectively to:

$$AgI(ads) \rightarrow I(g) + Ag(g) \quad (1)$$

$$Ag(s) + \tfrac{1}{2}I_2(s) \rightarrow AgI(ads) \quad (2)$$

AgI(ads) refers to the Pt(111)(3 x 3)-AgI structure in vacuum, and includes Ag-I as well as Pt-Ag bonding.

Most of the thermodynamic parameters of the surface compound AgI(ads) formed in the electrochemical process above are still unknown. Therefore, with primary data from our laboratory, support data from thermodynamic tables and some thermodynamic sequences we will deduce the nature of the bonding in AgI(ads). Two steps of this sequence require more detailed discussion, which will be deferred until chapters 6 and 7. This will allow calculation of the cohesive and thermodynamic parameters of the surface compound AgI(ads). All quantities calculated are per mole of iodine.

5.2. Cohesive Enthalpy and Gibbs Energy Change of Pt(111)(3 x 3)-AgI.

The cohesive enthalpy and free energy for AgI when it is adsorbed as Pt(111)(3 x 3)-AgI are defined as the changes in these quantities in the reaction (3). As we will see in chapter 7, in principle it would be possible to study this reaction through TDS experiments.

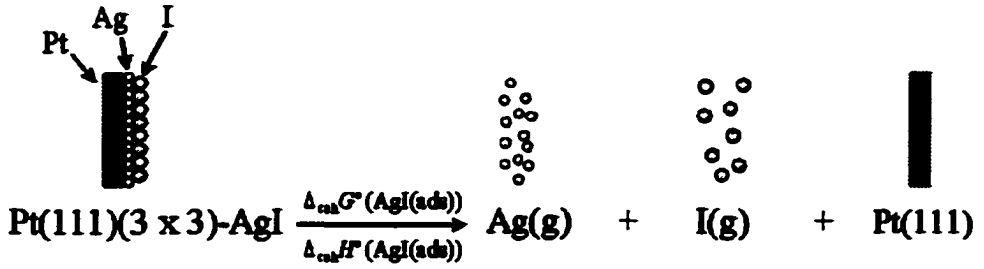

(3)

However, for Pt(111) [5.1], Pt(6(111) x (111)) [5.2] and Pt(100) [5.3], the thermal desorption of iodine overlaps with the thermal desorption of silver. The study of this system is then limited by the lack of an accurate model of desorption to account for the interactions between Ag and I. Therefore, in order to get thermodynamic information for this reaction we use the reaction scheme shown in Fig. (5.1). In this sequence, the initial structure Pt(111)(3 x 3)-AgI, or AgI, is disassembled in successive stages to finally obtain silver and iodine atoms in the gas phase. After immersion of the AgI structure into the electrolyte, the silver is removed from AgI(ads) to give solid Ag and Pt(111)($\sqrt{7}$ x $\sqrt{7}$)R19.1°-I. The sublimation stage changes the silver from solid to gas phase. The other two stages are related to the iodine. First, the emersion of the Pt(111)($\sqrt{7}$ x $\sqrt{7}$)R19.1°-I structure from the solution to vacuum; and second, the desorption in vacuum of the iodine from the surface. According to this thermodynamic sequence, we can deduce the set of equations:

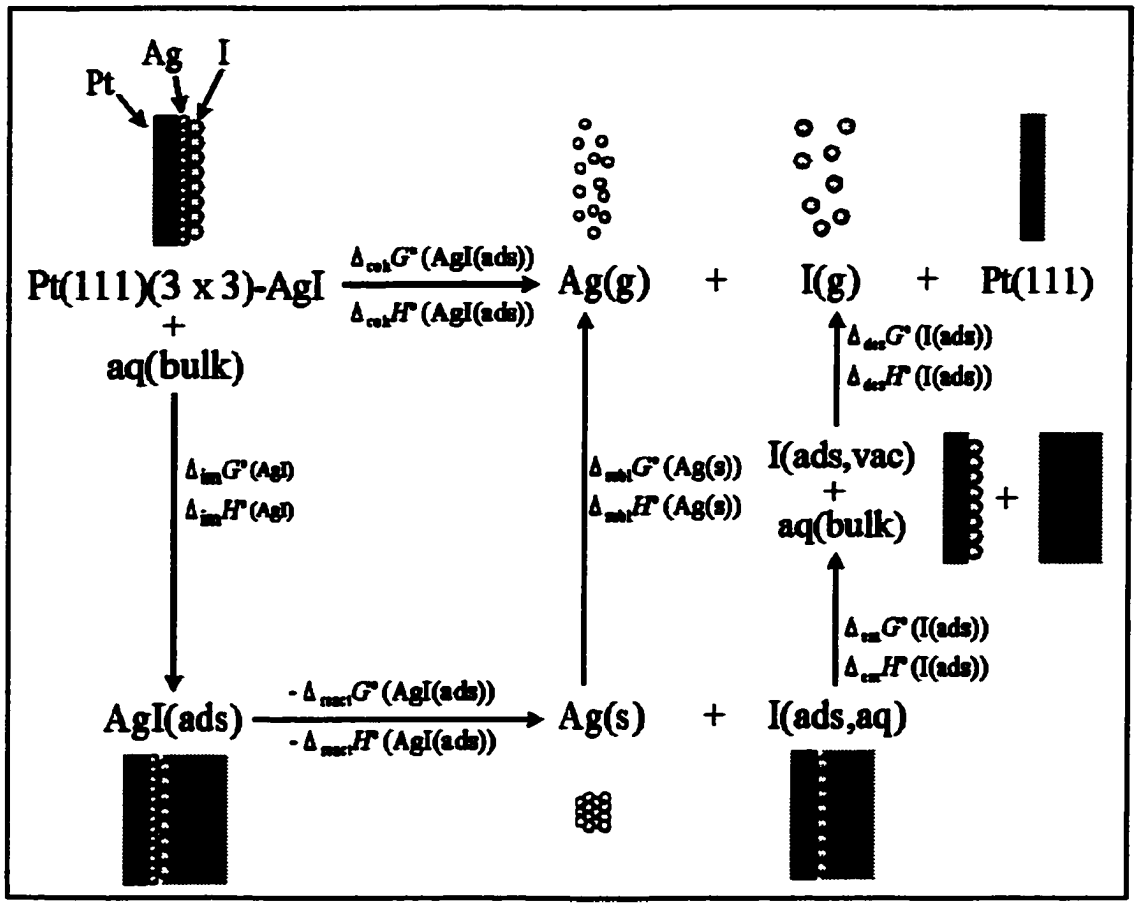

Figure 5.1: Thermodynamic sequence corresponding with the cohesion of AgI(ads). I(ads,vac) refers to the Pt(111)($\sqrt{7}$ x $\sqrt{7}$)R19.1°-I structure in vacuum, as distinct from I(ads,aq), which refers to the same structure in contact with an electrolyte solution of 0.1 M $HClO_4$ + 1 mM $AgClO_4$. $\Delta_{im}G^{\circ}$ (AgI) refers to Gibbs energy of immersion of Pt(111)(3 x 3)-AgI in vacuum, and $\Delta_{coh}G^{\circ}$ (AgI(ads)) refers to Gibbs energy of cohesion of AgI(ads). $\Delta_{react}G^{\circ}$ (AgI(ads)) is the Gibbs energy of reaction Ag(s) + I(ads,aq) → AgI(ads), $\Delta_{subl}G^{\circ}$ (Ag(s)) is the Gibbs energy of sublimation of silver, $\Delta_{em}G^{\circ}$ (I(ads)) is the Gibbs energy of emersion of I(ads,aq), and $\Delta_{des}G^{\circ}$ (I(ads) is the Gibbs energy of desorption of I(ads,vac). The notation is equivalent for the enthalpy changes of the different reactions.

$$\Delta_{coh}G^{\circ}(\mathrm{AgI(ads)}) = \Delta_{im}G^{\circ}(\mathrm{AgI}) - \Delta_{react}G^{\circ}(\mathrm{AgI(ads)}) + \Delta_{subl}G^{\circ}(\mathrm{Ag(s)}) + \Delta_{em}G^{\circ}(\mathrm{I(ads)}) + \Delta_{des}G^{\circ}(\mathrm{I(ads)}) \quad (4)$$

$$\Delta_{coh}H^{\circ}(\mathrm{AgI(ads)}) = \Delta_{im}H^{\circ}(\mathrm{AgI}) - \Delta_{react}H^{\circ}(\mathrm{AgI(ads)}) + \Delta_{subl}H^{\circ}(\mathrm{Ag(s)}) + \Delta_{em}H^{\circ}(\mathrm{I(ads)}) + \Delta_{des}H^{\circ}(\mathrm{I(ads)}) \quad (5)$$

In the following sections we calculate independently the four untabulated terms on the right-hand sides of equations (4) and (5), which sum to give the cohesive enthalpy and free energy for Pt(111)(3 x 3) - AgI structure.

5.2.1. Immersion of Pt(111)(3 x 3)-AgI into the Electrolyte.

The initial stage of the thermodynamic sequence is the immersion of the AgI structure from the vacuum into the electrolyte:

$$AgI + aq(bulk) \rightarrow AgI(ads) \quad -\Delta_{im}G^{\circ}(AgI),\ -\Delta_{im}H^{\circ}(AgI) \qquad (6)$$

aq(bulk) is the electrolyte in the bulk form, as compared with aq(gas), which is the electrolyte with its surface in contact with an atmosphere saturated of electrolyte . In practice this atmosphere is replaced by a dry inert atmosphere, without significant change in the surface tension.

In the next sections we calculate first the Gibbs energy change of immersion, and then the enthalpy change.

5.2.1.1. Calculation of the Gibbs Energy Change of Immersion, $\Delta_{im}G^{\circ}$ (AgI).

The creation of new surface in a solid or liquid can be represented as the cleavage the surface, followed by the rearrangement of the surface atoms to their new equilibrium positions. The two processes occur at the same time in a liquid, being the surface tension, γ, the work required to create a unit area of surface, A:

$$\gamma = \left(\frac{\partial G}{\partial A}\right)_{T,P} \qquad (7)$$

Since the rearrangement of the atoms on a solid surface is a slow process, γ is not a quantity directly applicable in the case of solids. In other words, it is possible to create new area in a solid by stretching the distances of the atoms of the surface. The work required to form the surface is called surface stress, τ [5.4]:

$$\tau = \gamma + A\left(\frac{\partial \gamma}{\partial A}\right)_{T,P} \tag{8}$$

In the case of liquids, the stretching term $(\partial\gamma/\partial A)_{T,P} = 0$, which is why $\tau = \gamma$. In our experiments, the surface is adsorbate-covered, no reconstruction of Pt atoms is observed in tensor-LEED, and we assume any lateral deformation of the silver and iodine atoms by the solution is small, i.e. we take $\tau = \gamma$. We will sometimes use the terms surface tension and interfacial tension synonymously.

Reaction (6) can not be studied directly since the electrolyte is in the bulk form. In order to study it, this reaction has to be divided in two stages:

$$AgI + aq(gas) \rightarrow AgI(ads) \tag{9}$$

$$aq(bulk) \rightarrow aq(gas) \tag{10}$$

According with this equation, the free energy change per unit area of equations (9) and (10) in terms of the surface tension is respectively:

$$\Delta_{r9}G^{\circ} = \gamma^{AgI(ads),aq} - \gamma^{aq,gas} - \gamma^{AgI,gas} \tag{11}$$

$$\Delta_{r10}G^{\circ} = \gamma^{aq,gas} \tag{12}$$

Adding both free energies gives the total Gibbs free energy change of immersion:

$$\Delta_{im}G^{\circ}(AgI) = \gamma^{AgI(ads),aq} - \gamma^{AgI,gas} \tag{13}$$

Measurements of the contact angle α of the electrolyte with Pt(111)(3 x 3)-AgI give

an estimate of the relationship between the different components of the surface tension at the point of contact, Fig. (5.2). According to Young's equation [5.5], the value of the surface tension of the electrolyte is related to the difference between the surface tension of Pt(111)(3 x 3)-AgI in vacuum and in solution. This is shown in equation (14):

$$\gamma^{AgI,gas} - \gamma^{AgI,aq} = \gamma^{gas,aq} \cos\alpha \qquad (14)$$

Although Young's equation applies only for systems under equilibrium conditions (drop of electrolyte under a saturated atmosphere), it is assumed that there is no significant deviation from equilibrium conditions for a drop under a dry atmosphere. This assumption is supported by the fact that the time scale of evaporation of the drop was slow, ca. 10 min. Also, the heat conductivity of the Pt crystal and support wires acts to maintain the temperature of the sample despite the evaporation of the drop.

According to this assumption, substituting Eq. (14) into Eq. (13) yields:

$$\Delta_{im}G^{\circ}(AgI) = -\gamma^{gas,aq} \cos\alpha \qquad (15)$$

Measurements of the contact angle of a ca. 1 μL droplet of electrolyte gave $\alpha = 73 \pm 5°$. Accordingly, the Pt(111)(3 x 3)-AgI structure is slightly hydrophilic (contact angle > 90°). That is, the Gibbs energy change $\Delta_{im}G^{\circ}(AgI)$ for immersion of this structure from

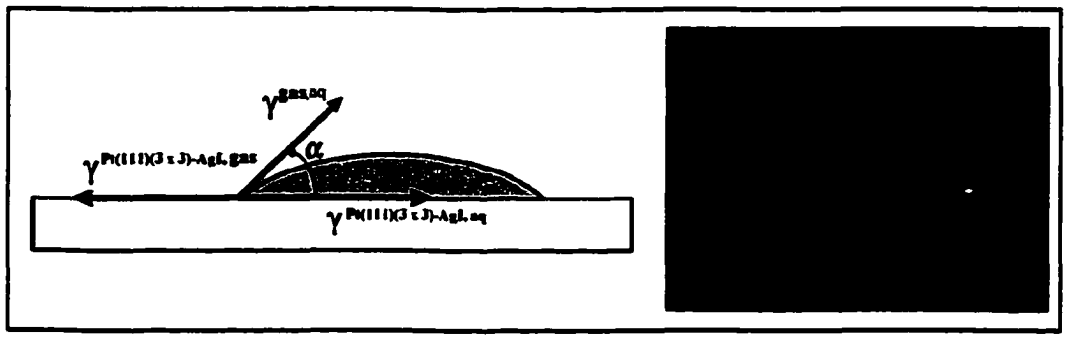

Figure 5.2: Contact angle and components of surface tension for a drop of electrolyte (1 mM $AgClO_4$, 0.1 M $HClO_4$) on a Pt(111)(3 x 3)-AgI surface.

vacuum to electrolyte is endergonic. This is because the introduction of the surface breaks the structure of the bulk electrolyte. The contact angle for H_2O and electrolyte on a Pt(111)(3 x 3)-AgI surface were also the same within the experimental error.

The surface tension of the electrolyte $\gamma^{gas,aq}$ is unknown. Hence, we approximate $\gamma^{gas,aq}$ to γ^{gas,H_2O}, which has been measured as 72.60 ± 0.01 mJ m^{-2} [5.6]. Substituting α and γ^{gas,H_2O} in equation (15) gives a value of Gibbs energy change per unit area as -21 ± 7 mJ m^{-2}. The number of moles of AgI on a Pt(111)(3 x 3)-AgI structure per unit area is 1.010 $\times 10^{-5}$ mol m^{-2}, and therefore the molar Gibbs energy change is $\Delta_{im}G^{\circ}(AgI) = -2.1 \pm 0.7$ kJ mol^{-1}.

5.2.1.2. Calculation of the Enthalpy Change of Immersion, $\Delta_{im}H^{\circ}$ (AgI).

According to equation (16), the entropy change is proportional to the change of surface tension with temperature:

$$\Delta S^{\circ} = -\left(\frac{\partial \Delta G^{\circ}}{\partial T}\right)_P \qquad (16)$$

Since the surface tension is a measurement of the free energy of the surface, substituting Eq. (15) into Eq. (16) gives the standard entropy of emersion per unit area:

$$\Delta_{im}S^{\circ}(AgI) = \left(\frac{\partial (\gamma^{gas,H_2O}\cos\alpha)}{\partial T}\right)_P \qquad (17)$$

Thus:

$$\Delta_{im}S^{\circ}(AgI) = \left(\frac{\partial \gamma^{gas,H_2O}}{\partial T}\right)_P \cos\alpha + \gamma^{gas,H_2O}\left(\frac{\partial \cos\alpha}{\partial T}\right)_P \qquad (18)$$

As seen in the next section, measurements of the contact angle for Pt(111)($\sqrt{7} \times \sqrt{7}$)R19.1°-I between 290 and 310 K suggest that it does not change within the experimental error.

Assuming similar behavior for the Pt(111)(3 x 3)-AgI structure, the term $\gamma^{gas,H_2O}(\partial\cos\alpha/\partial T)_p$ in equation (18) is less than 0.01 mJ K^{-1} m^{-2}. The temperature-dependence of the surface tension at room temperature is known [5.5], $(\partial\gamma^{gas,H_2O}/\partial T)_p = -0.153 \pm 0.005$ mJ K^{-1} m^{-2}. Therefore, equation (18) yields $\Delta_{im}S^\circ$ (AgI) = - 0.09 ± 0.02 mJ K^{-1} m^{-2}, and per mol of AgI this is $\Delta_{im}S^\circ$ (AgI) = - 9.5 ± 2 J K^{-1} mol^{-1}.

The enthalpy change of emersion at 298.15 K is then calculated from the Gibbs energy and the entropy of emersion as $\Delta_{im}H^\circ$ (AgI) = - 4.9 ± 1.3 kJ mol^{-1}.

5.2.2. Electrochemical Adsorption of Ag^+ onto Pt(111)($\sqrt{7}$ x $\sqrt{7}$)R19.1°-I.

This component of the thermodynamic sequence is the desorption of the silver from the AgI(ads) structure into silver metal:

$$AgI(ads) \rightarrow Ag(s) + I(ads, aq) \quad -\Delta_{react}G^\circ(AgI(ads)),\ -\Delta_{react}H^\circ(AgI(ads)) \qquad (19)$$

In chapter 6, we calculate electrochemically the change in Gibbs energy and then the change in enthalpy of reaction. This is done through a temperature dependence study of the reversible potential of the C1/A1 peak in the voltammogram. The thermodynamic parameters calculated are:

$\Delta_{react}G^\circ$ (AgI(ads)) = - 44.0 ± 0.3 kJ mol^{-1}.

$\Delta_{react}H^\circ$ (AgI(ads)) = - 35.5 ± 0.3 kJ mol^{-1}.

5.2.3. Sublimation of Ag(s).

The next reaction in the thermodynamic sequence is the sublimation of silver:

$$Ag(s) \rightarrow Ag(g) \qquad -\Delta_{subl}G^\circ(Ag(s)),\ \Delta_{subl}H^\circ(Ag(s)) \qquad (20)$$

According to the NBS tables [5.7], these parameters are:

$\Delta_{subl}G^{\circ}$ (Ag(s)) = + 245.6 ± 0.04 kJ mol^{-1}.

$\Delta_{subl}H^{\circ}$ (Ag(s)) = + 284.6 ± 0.04 kJ mol^{-1}.

5.2.4. Emersion of Iodine in a Pt(111)($\sqrt{7}$ x $\sqrt{7}$)R19.1°-I Structure from Solution into Vacuum.

Once the silver has been disassembled from the AgI(ads) structure, the next reaction is the removal or emersion of the solution from the I(ads,aq) structure.

$$I(ads,aq) \rightarrow I(ads,vac) + aq(bulk) \quad \Delta_{em}G^{\circ}(Ag(s)),\ \Delta_{em}H^{\circ}(Ag(s)) \qquad (21)$$

Applying the same methodology as for the calculation of $\Delta_{im}G^{\circ}$ (AgI) and $\Delta_{im}G^{\circ}$ (AgI), in the next sections we calculate first the Gibbs energy change of emersion, and then the enthalpy change.

5.2.4.1. Calculation of the Gibbs Energy Change of Emersion, $\Delta_{em}G^{\circ}$ (I(ads)).

As in the case of immersion of Pt(111)(3 x 3)-AgI, reaction (21) is divided into two reactions:

$$I(ads,aq) \rightarrow I(ads,vac) + aq(gas) \qquad (22)$$

$$aq(gas) \rightarrow aq(bulk) \qquad (23)$$

The free energy change per unit area of equations (22) and (23) in terms of the surface tension is respectively:

$$\Delta_{r22}G^{\circ} = \gamma^{aq,gas} + \gamma^{I(ads),vac} - \gamma^{I(ads),aq} \qquad (24)$$

$$\Delta_{r22}G^{\circ} = -\gamma^{aq,gas} \tag{25}$$

Adding both free energy changes gives the total Gibbs free energy change of emersion:

$$\Delta_{em}G^{\circ}(I(ads)) = \gamma^{I(ads),vac} - \gamma^{I(ads),aq} \tag{26}$$

According to Fig. (5.3), the relationship between the different components of the surface tension is:

$$\gamma^{I(ads),vac} - \gamma^{I(ads),aq} = \gamma^{gas,aq}\cos\alpha \tag{27}$$

which yields after substituting into equation (26):

$$\Delta_{em}G^{\circ}(I(ads)) = \gamma^{vac,gas}\cos\alpha \tag{28}$$

Measurements of the contact angle of a ca. 1μL droplet of electrolyte gave $\alpha = 55 \pm 5°$. This angle corresponds to a hydrophilic surface, although a slight hydrophobicity of the Pt(111)(√7 x √7)R19.1°-I structure had been deduced indirectly previously [5.8]. The contact angle does not change within the experimental error in the temperature range between 290 and 310 K. The contact angle for H_2O and electrolyte on a Pt(111)(√7 x √7)R19.1°-I surface were also the same within the experimental error. As in the case of immersion of the Pt(111)(3 x 3)-AgI structure, we approximate $\gamma^{gas,aq}$ to γ^{gas,H_2O}.

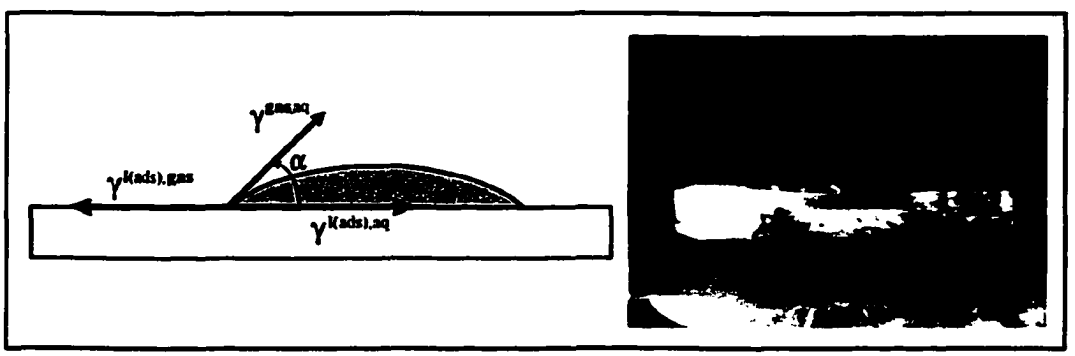

Figure 5.3: Contact angle and components of surface tension for a drop of H_2O on a Pt(111)(√7 x √7)R19.1°-I surface.

Substituting α and γ^{gas,H_2O} in equation (28) gives a value of Gibbs energy change per unit area as 41 ± 5 mJ m^{-2}. The area per mole of I(ads) on a Pt(111)(√7 x √7)R19.1°-I structure is 9.743x10^{-6} mol m^{-2}, and therefore the molar Gibbs energy change is $\Delta_{em}G^{\circ}$(I(ads)) = 4.2 ± 0.5 kJ mol^{-1}.

5.2.4.2. Calculation of the Enthalpy Change of Emersion, $\Delta_{em}H^{\circ}$(I(ads)).

According to the relationship between ΔS° and ΔG° in equation (16), the standard entropy of emersion per unit area is:

$$\Delta_{em}S^{\circ}(\text{I(ads)}) = -\left(\frac{\partial(\gamma^{gas,H_2O}\cos\alpha)}{\partial T}\right)_P \qquad (29)$$

Therefore,

$$\Delta_{em}S^{\circ}(\text{I(ads)}) = -\left(\frac{\partial\gamma^{gas,H_2O}}{\partial T}\right)_P \cos\alpha - \gamma^{gas,H_2O}\left(\frac{\partial\cos\alpha}{\partial T}\right)_P \qquad (30)$$

As explained in the previous section, measurements of the contact angle at 290, 300 and 310 K suggest that it does not change within the experimental error, making the term $\gamma^{gas,H_2O}(\partial\cos\alpha/\partial T)_P$ in equation (30) less than 0.01 mJ K^{-1} m^{-2}. Since $(\partial\gamma^{gas,H_2O}/\partial T)_p$ is known, equation (30) yields $\Delta_{em}S^{\circ}$ (I(ads)) = 0.09 ± 0.02 mJ K^{-1} m^{-2}, and per mol of iodine this is $\Delta_{em}S^{\circ}$ (I(ads)) = 9.2 ± 2 J K^{-1} mol^{-1}.

The enthalpy change of emersion at 298.15 K is obtained from the Gibbs energy and the entropy of emersion, $\Delta_{em}H^{\circ}$ (I(ads)) = 6.9 ± 0.6 kJ mol^{-1}.

5.2.5. Desorption in Vacuum of Iodine from Pt(111)(√7 x √7)R19.1°-I.

The desorption in vacuum of iodine from Pt(111) corresponds to the reaction:

$$I(ads, vac) \rightarrow I(g) \quad \Delta_{des}G^{\circ}(I(ads)),\ \Delta_{des}H^{\circ}(I(ads)) \qquad (31)$$

In chapter 7, thermal desorption experiments of iodine under UHV conditions, together with the development of a model of desorption allow calculation of $\Delta_{des}G^{\circ}$ (I(ads)) and $\Delta_{des}H^{\circ}$ (I(ads)). The parameters obtained are:

$\Delta_{des}G^{\circ}$ (I(ads)) = 170 ± 22 kJ mol^{-1}.

$\Delta_{des}H^{\circ}$ (I(ads)) = 209 ± 20 kJ mol^{-1}.

5.2.6. Cohesive Enthalpy and Gibbs Energy Change of Pt(111)(3 x 3)-AgI.

In the previous sections we have calculated all the terms in Eq. (4) and Eq. (5) for the cohesive enthalpy and Gibbs energy change of Pt(111)(3 x 3)-AgI. The question that remains is whether or not the structure I(ads,aq) obtained from the electrochemical experiments is the same as the I(ads,aq) from the contact angle measurements, since the first experiment is under potential control, while the second is at open-circuit potential. The open-circuit potential was measured in our laboratory as ca. 0.5 V vs Ag|Ag^{+}, only 50 mV more positive than the first reduction peak in the voltammogram. This potential agrees with previous results in the literature [5.9]. Therefore, it is reasonable to assume that the Pt(111)($\sqrt{7}$ x $\sqrt{7}$)R19.1°-I in solution has similar characteristics in both experiments.

Once all the terms in the right hand side of equations (4) and (5) have been calculated, we substitute them and obtain the total cohesive enthalpy and free energy for AgI adsorbed on Pt(111):

$$\Delta_{coh}G^{\circ}(\text{AgI(ads)}) = -2.1 \pm 0.7 + 44 \pm 0.3 + 245.6 \pm 0.04 + 4.2 \pm 0.5 + 170 \pm 22 = +462 \pm 24 \text{ kJ mol}^{-1} \quad (32)$$

$$\Delta_{coh}H^{\circ}(\text{AgI(ads)}) = -4.9 \pm 1.3 + 35 \pm 0.3 + 284.6 \pm 0.04 + 6.9 \pm 0.6 + 209 \pm 20 = +531 \pm 22 \text{ kJ mol}^{-1} \quad (33)$$

5.3. Formation Enthalpy and Gibbs Energy of AgI(ads).

The formation enthalpy and Gibbs energy of AgI (ads) are defined as the enthalpy and Gibbs energy of formation of AgI(ads) from its pure elements in their reference states i.e., for the reaction:

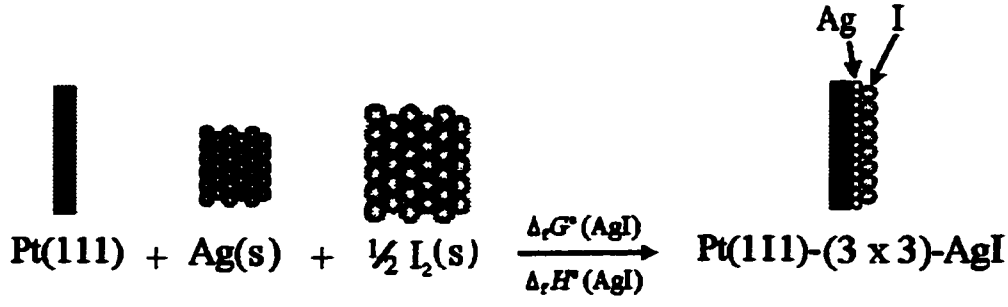

(34)

The previous method of constructing a thermodynamic sequence is then followed (see Fig. (5.4)). According to this figure:

$$\Delta_f G^{\circ}(\text{AgI(ads)}) = \Delta_f G^{\circ}(\text{I(g)}) + \Delta_{ads}G^{\circ}(\text{I(g)}) + \Delta_{im}G^{\circ}(\text{I(ads)}) + \Delta_{react}G^{\circ}(\text{AgI(ads)}) + \Delta_{cm}G^{\circ}(\text{AgI}) \quad (35)$$

$$\Delta_f H^{\circ}(\text{AgI(ads)}) = \Delta_f H^{\circ}(\text{I(g)}) + \Delta_{ads}H^{\circ}(\text{I(g)}) + \Delta_{im}H^{\circ}(\text{I(ads)}) + \Delta_{react}H^{\circ}(\text{AgI(ads)}) + \Delta_{cm}H^{\circ}(\text{AgI}) \quad (36)$$

Except for $\Delta_f G^{\circ}$(I(g)) and $\Delta_f H^{\circ}$(I(g)) (standard formation free energy change and enthalpy

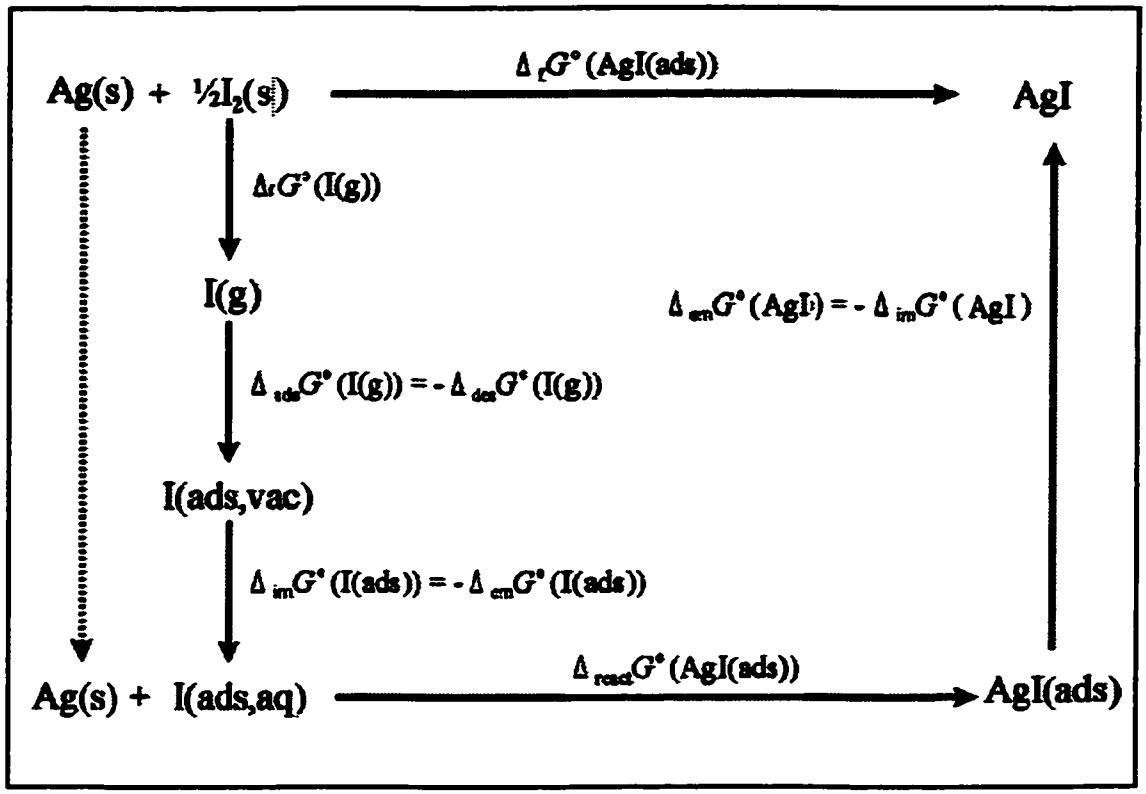

Figure 5.4: Thermodynamic cycle corresponding with the formation of Pt(111)(3 x 3)-AgI.

change of I(g)), all of the terms in the right hand side of equations (35) and (36) have been previously calculated. Their equivalences are shown in Fig. (5.4).

According to the NBS tables [5.6]:

$$\Delta_f G^\circ(\mathrm{I(g)}) = +70.250 \pm 4\cdot10^{-4}\ \mathrm{kJ\ mol^{-1}},\ \Delta_f H^\circ(\mathrm{I(g)}) = +106.838 \pm 4\cdot10^{-4}\ \mathrm{kJ\ mol^{-1}} \quad (37)$$

$\Delta_f G^\circ$(AgI(ads)) and $\Delta_f H^\circ$(AgI(ads)) are obtained by substituting back all the terms in the right hand side of equations (35) and (36):

$$\Delta_f G^\circ(\mathrm{AgI(ads)}) = 70.250 \pm 4\cdot10^{-4} - 170 \pm 22 - 4.2 \pm 0.5 - 44 \pm 0.3 + 2.1 \pm 0.7$$
$$= -146 \pm 23\ \mathrm{kJ\ mol^{-1}} \qquad (38)$$

$$\Delta_f H^\circ(\mathrm{AgI(ads)}) = 106.838 \pm 4\cdot10^{-4} - 209 \pm 20 - 6.9 \pm 0.6 - 35 \pm 0.3 + 4.9 \pm 1.3$$
$$= -139 \pm 22\ \mathrm{kJ\ mol^{-1}} \qquad (39)$$

Chapter 6

Silver Electrodeposition on Pt(111)(√7 x √7)R19.1°-I.

6.1. Introduction.

In this chapter, the UPD of silver on Pt(111)(√7 x √7)R19.1°-I and its temperature dependence are studied. Much of this has been published [6.1], and this chapter is largely excerpted from there. As shown in chapter 1, starting from a Pt(111)(√7 x √7)R19.1°-I surface structure with the iodine deposited from I_2(g) gives the cyclic voltammogram shown in Fig. (6.1), similar voltammogram as Fig. (1.1). The voltammogram shows three UPD peaks, of which C1 and C2 will be of most interest.

The reaction for the C1 peak is:

$$(\sqrt{7} \times \sqrt{7})R19.1°\text{-I(ads)} + Ag^+(aq) + e^- \rightarrow (3 \times 3)\text{-AgI(ads)} \qquad (1)$$

where the surface before the peak is fully covered with I(ads) in the (√7 x √7)R19.1°-I structure and the surface after the peak is fully covered by (3 x 3)-AgI [6.2][6.3]. The narrowness of the peaks is a reflection of the fact that the process is essentially a surface phase transition between the two ordered phases. In the limit of perfectly-ordered phases and rapid kinetics, the voltammetry peaks would be delta functions occurring at the reversible potential for the above reaction. Like solid crystals, the condensed surface phases have chemical potentials independent of the amount (coverage), and so the standard state will be taken to be the fully-covered ordered surface phase. As the reaction proceeds, islands of I(ads) are replaced by islands of AgI(ads), rather than the Ag being randomly deposited across the surface, as would occur for Langmuir isotherm kinetics. Experimental support for an island-growth model comes from LEED [6.4][6.5], where the spots for both species

are observed on emersion before the process is completed, and from the kinetics for this peak, which follow a Nucleation-Growth-Collision (NGC) (island) model [6.6].

As we will see below, the potential of the foot of the C1 and A1 peaks is

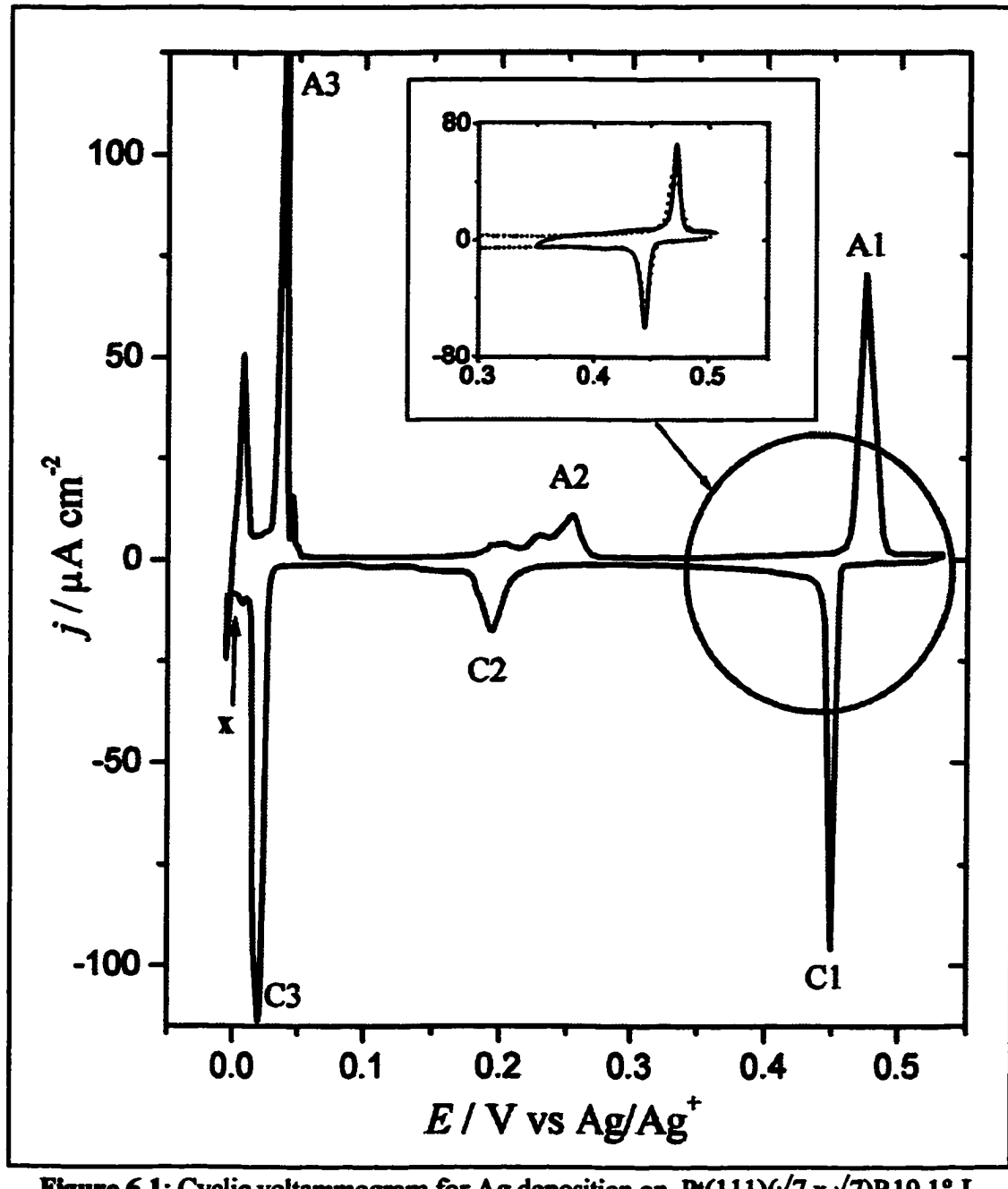

Figure 6.1: Cyclic voltammogram for Ag deposition on Pt(111)($\sqrt{7}$ x $\sqrt{7}$)R19.1°-I. [Ag^+] = 1 mM, sweep rate 5 mV s^{-1}. Insert: (.....) Steady-state voltammogram reversing the potential at + 0 V, (——) 1st cycle of the voltammogram starting at + 0.5 V and reversing at + 0.35 V.

independent of the sweep rate, which indicates that the reaction under these peaks is reversible. The hysteresis associated with the A1/C1 is assumed to correspond to an unknown nucleation overpotential [6.6], and not to the history of sweeping voltage to potentials close to the onset of bulk Ag deposition. This is depicted in the insert of Fig. (6.1), which shows the similarity between the steady-state voltammogram and the 1st cycle of the voltammogram reversing the potential between the C1 and C2 peaks.

As the reaction under the peak C1 is reversible, the temperature dependence of this peak enables the calculation of the different thermodynamic parameters for the reaction:

$$Ag(s) + I(ads) \rightarrow AgI(ads) \qquad (2)$$

where I(ads) refers to Pt(111)($\sqrt{7}$ x $\sqrt{7}$)R19.1°-I, and AgI(ads) to (3 x 3)-AgI. The parameters determined are $\Delta_{react}H^{o}$(AgI(ads)), $\Delta_{react}S^{o}$(AgI(ads)) and $\Delta_{react}G^{o}$(AgI(ads)), (standard enthalpy, entropy and Gibbs free energy changes for this reaction). These are used in the thermodynamic sequence in chapter 5 for the calculation of the cohesive and formation energies for the Pt(111)(3 x 3)-AgI surface compound.

Additionally, a limited study of the temperature dependence for the process associated with the peak C2 in Fig. (6.1) is made in section 6.3. This peak corresponds to the additional deposition of 0.4 - 0.5 ML Ag. The surface phase transition that takes place is from a fully-covered (3 x 3)-AgI structure before the peak, to a ($\sqrt{3}$ x $\sqrt{3}$)R30°-AgI structure after the peak [6.7].

6.2. Dependence on Temperature of the First Deposition Peak of Ag on Pt(111)($\sqrt{7}$ x $\sqrt{7}$)R19.1°-I.

The measured reversible potential of C1/A1 relative to an $Ag|Ag^{+}$ electrode in the

same solution is the cell potential for the reaction which is the sum of reaction (1) and the reaction $Ag \rightarrow Ag^+ + e^-$; that is:

$$Ag(s) + (\sqrt{7} \times \sqrt{7})R19.1°\text{-}I(ads) \rightarrow (3 \times 3)\text{-}AgI(ads) \quad (3)$$

which is the reaction we are interested in for the thermodynamic sequence in chapter 5. Since all species are in their standard states, the reversible potential of C1/A1 versus $Ag|Ag^+$ is $E°$ for reaction (3), and the standard entropy of this reaction can be obtained from:

$$\Delta_{react}S°(AgI(ads)) = F\left(\frac{\partial E°}{\partial T}\right)_P \quad (4)$$

where F is the Faraday constant. Therefore, the variation of the reversible potential for

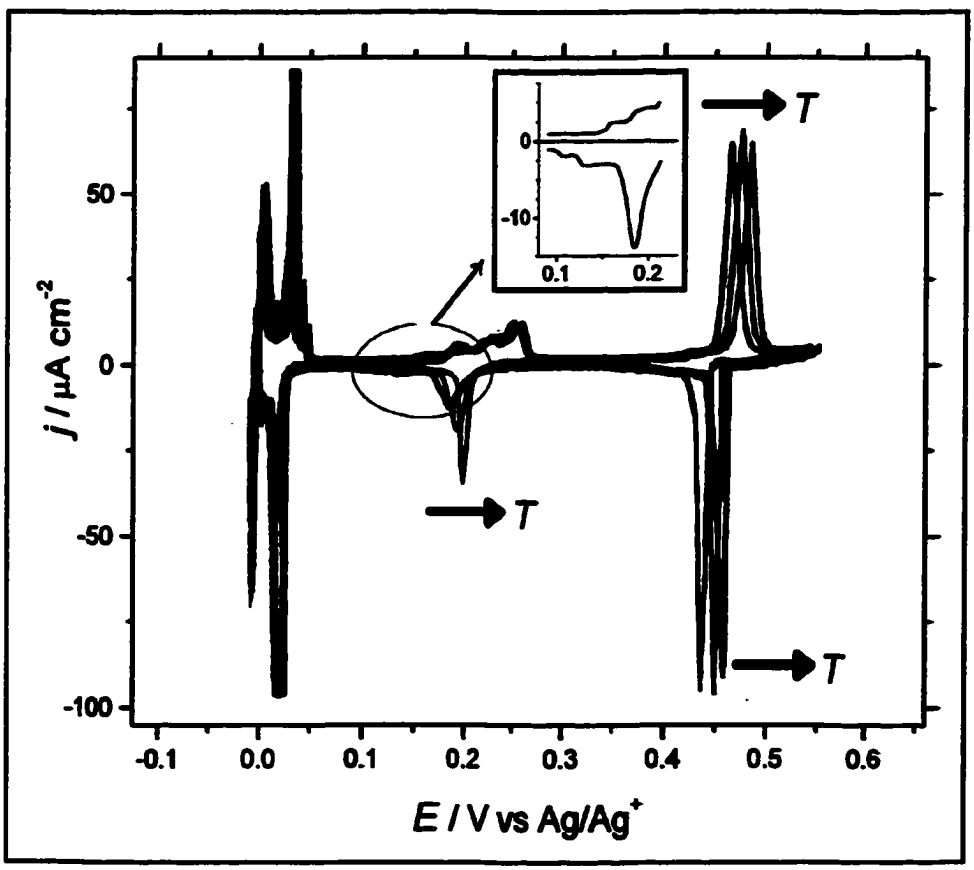

Figure 6.2: Temperature dependence for the voltammograms of Ag UPD on Pt(111)($\sqrt{7} \times \sqrt{7}$)R19.1°-I at 5, 30 and 50°C. Insert: C2 peak at 5°C. $[Ag^+]$ = 1mM, sweep rate 5 mV/s.

reaction (3) with temperature enables the calculation of the standard entropy of reaction, $\Delta_{react}S^{o}$(AgI(ads)).

6.2.1. Reversible Potential and $\Delta_{react}S^{o}$(AgI(ads)) for reaction Ag(s) + I(ads) → AgI(ads).

A series of voltammograms were run at 5°C intervals from 5°C to 50°C, with at least three runs at each temperature, Fig. (6.2). The values reported for the peak parameters are the averages of replicate runs. The peak potentials of the C1 and A1 peaks shift linearly to more positive potentials as the temperature increases, Fig. (6.3), but the separation between these two peaks is 27 ± 3 mV independent of temperature. If this shift is interpreted in

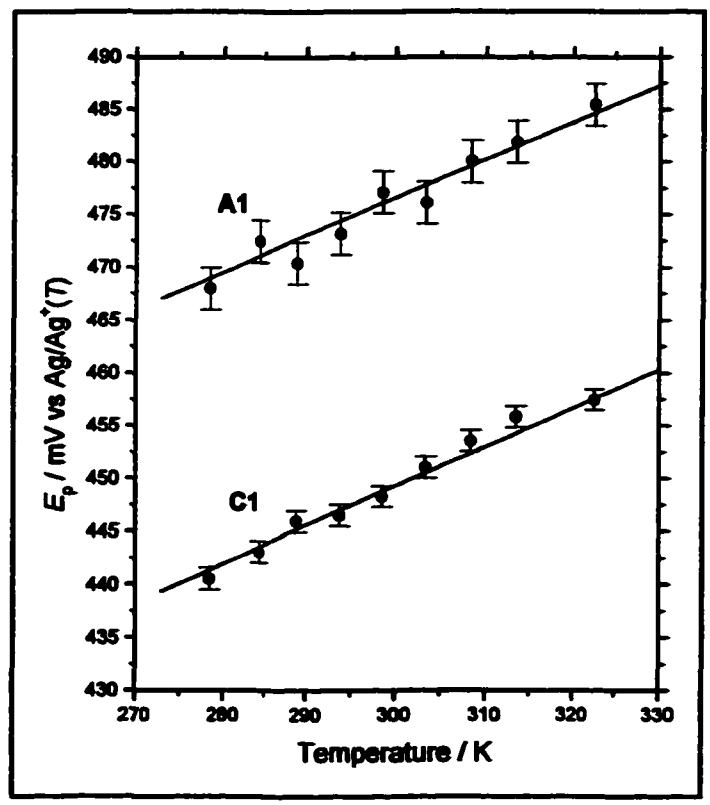

Figure 6.3: Temperature dependence of peak potentials for the first reduction (C1) and oxidation (A1) peaks of Ag UPD on Pt(111)(√7 x √7)R19.1°-I.

thermodynamic terms, it indicates that the (3 x 3) Ag-I structure becomes more stable relative to bulk silver as the temperature increases.

Over the temperature range studied, the C1 and A1 peak heights (j_p) and widths ($w_{1/2}$, full width at half height) show some variation. Some of this is due to variation in the degree of surface order, but it is anticipated that an increase in width associated with poorer surface

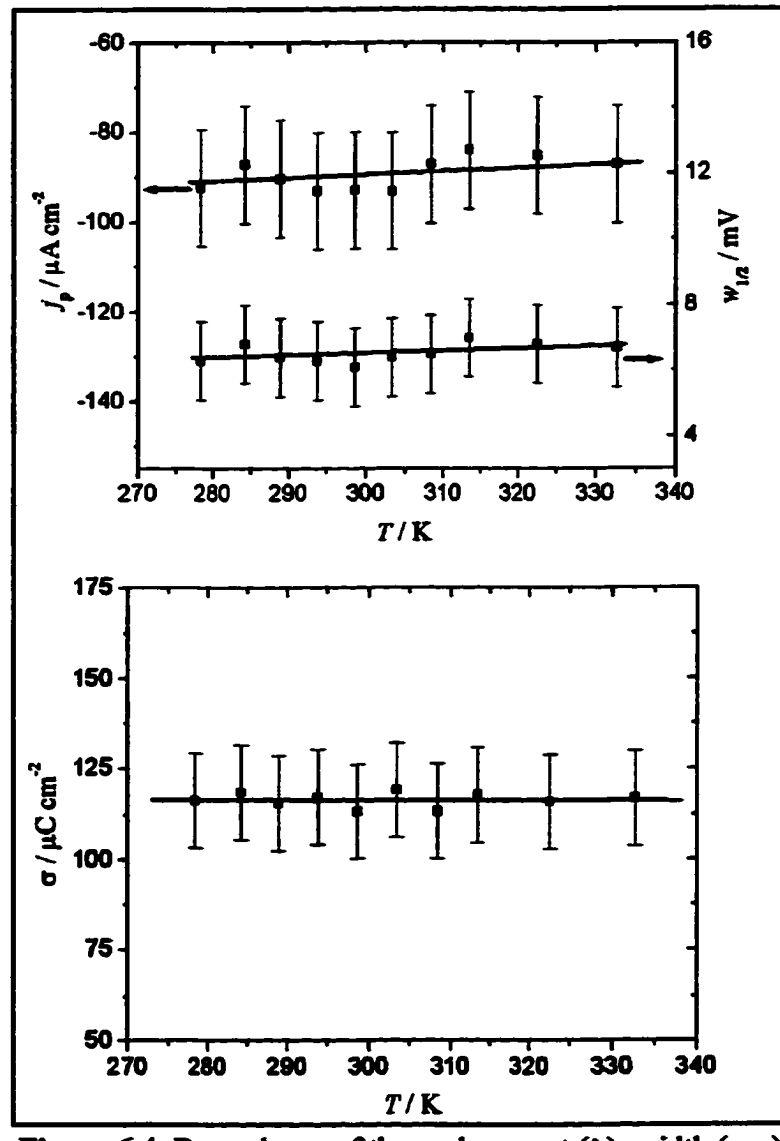

Figure 6.4: Dependence of the peak current (j_p), width ($w_{1/2}$) and charge density (σ) with temperature for the peak C1 for Ag UPD on Pt(111)(√7 x √7)R19.1°-I .

order will be compensated by a decrease in height, so that the area should vary less with surface quality. Plots of j_p versus T, $w_{1/2}$ versus T, and peak area, Fig .(6.4), estimated from the triangle formula $\sigma = j_p w_{1/2}$ *vs* T showed no significant variation of these quantities with temperature — the slopes of the regression lines were not significantly different from zero at the 95% confidence level. As expected, the areas showed less fluctuations than either the peak currents or widths.

A limited study of the kinetics was undertaken by varying the sweep rates, v, from

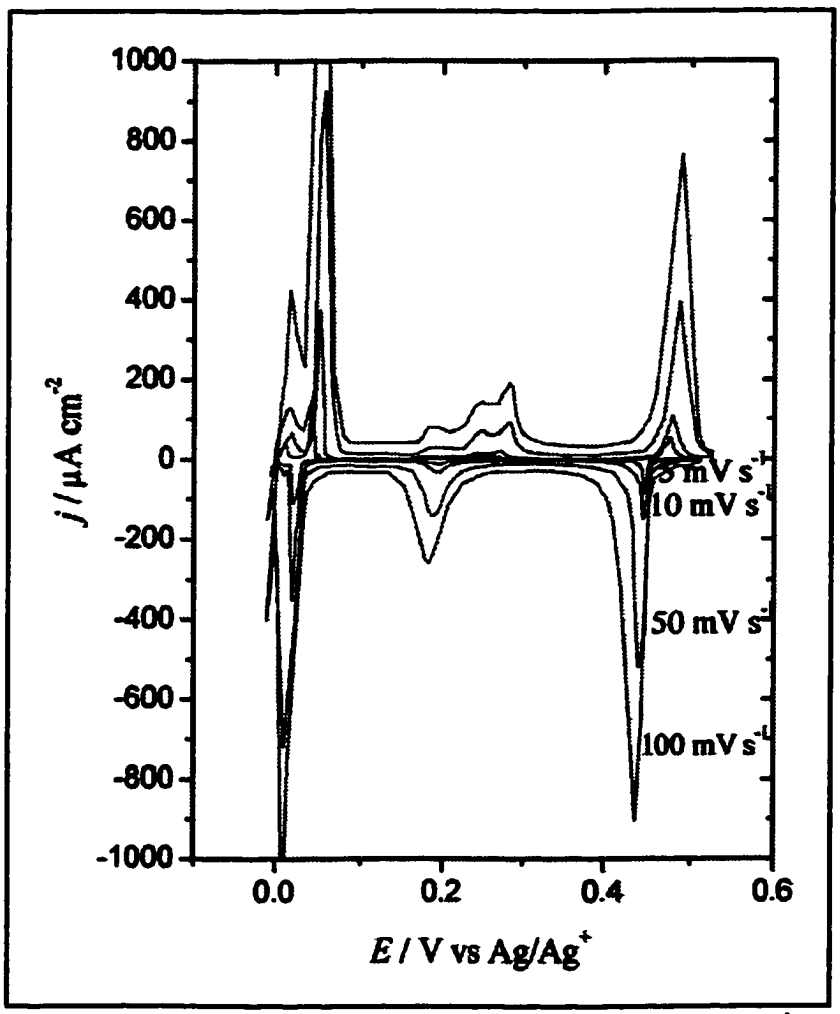

Figure 6.5: Cyclic voltammograms for Ag UPD on Pt(111)($\sqrt{7}$ x $\sqrt{7}$)R19.1°-I at different sweep rates. T = 15°C. [Ag^+] = 1mM, sweep rate 5 mV/s.

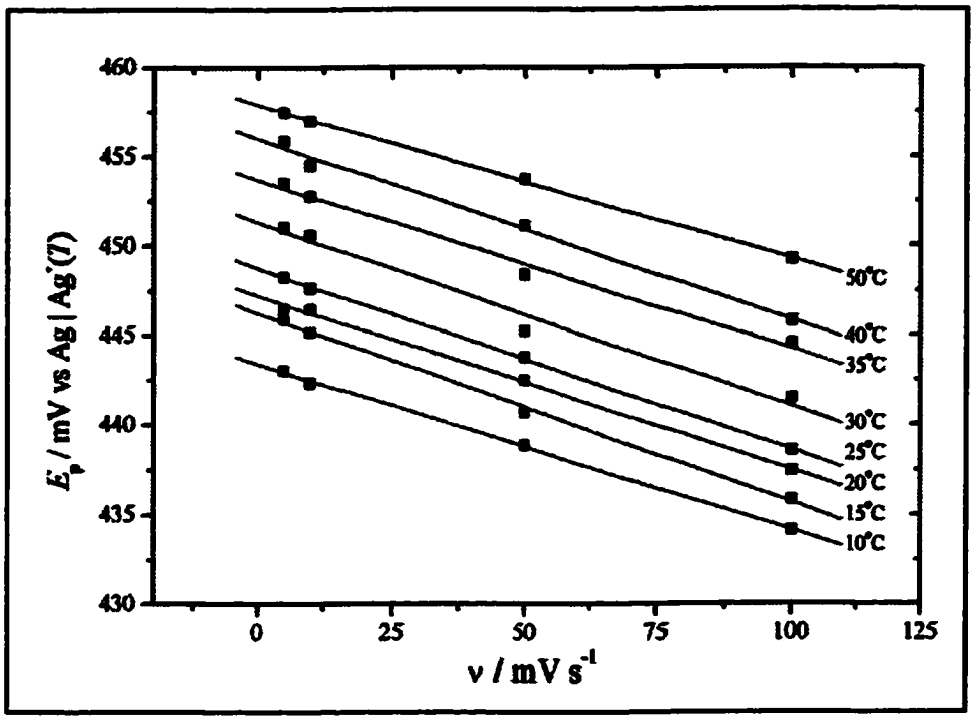

Figure 6.6: Change of peak potential of C1 peak with sweep rate at different temperatures.

5 mV s^{-1} to 100 mV s^{-1}, Fig. (6.5). At each temperature, the C1 and A1 peak potential E_p changed linearly with sweep rate, and the slopes of the E_p *vs* ν plots were 50 ms independent of temperature, Fig. (6.6). The C1 peak current varied as a power law in sweep rate, $j_p = \nu^{0.8 \pm 0.1}$, Fig. (6.7), in agreement with earlier work [6.14], and furthermore the exponent was independent of temperature.

The independence of the E_p versus ν slopes, the j_p power law exponents, and the peak shapes with temperature indicates that the mechanism and rate parameters are not changing significantly over this temperature range (about a 20% change in T or $1/T$). Therefore, the shift in the reversible potential for this reaction probably tracks the shift in peak potentials. The reversible potential must lie somewhere between the C1 and A1 peaks, and several estimates, Fig. (6.8), of the reversible potential were made:

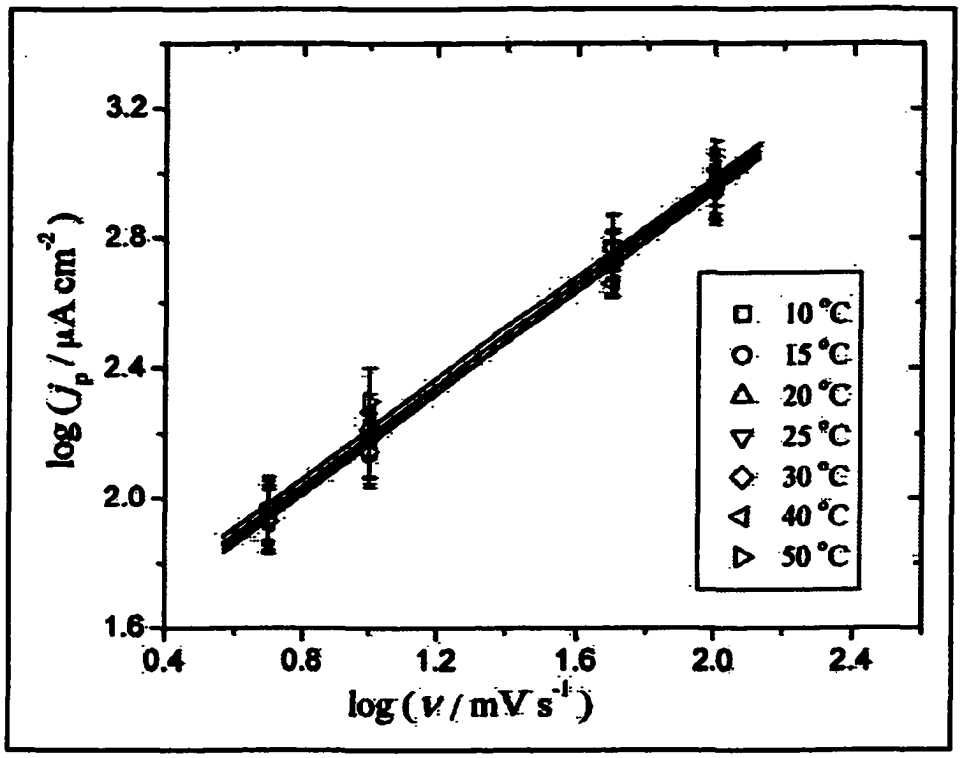

Figure 6.7: Dependence of log (j_p) with log (ν) with temperature.

(I) The average of the A1 and C1 peak potentials, under the assumption that the overpotentials at the maxima for the C1 and A1 peaks are the same.

(II) Extrapolation of the current of the reduction peak to the baseline, under the assumption that the reduction process begins at the reversible potential.

(III) Average between the extrapolation of the reduction and oxidation peaks to the baseline, under the assumption that the processes are initiated at well-defined nucleation overpotentials, and that these nucleation overpotentials are equal for the C1 and A1 processes.

The result of these three estimates is shown in Fig. (6.9).

Estimate (I) involves the potential of the A1 process at the peak maximum. The position and shape of the A1 peak were found to be very dependent on the cleanliness and

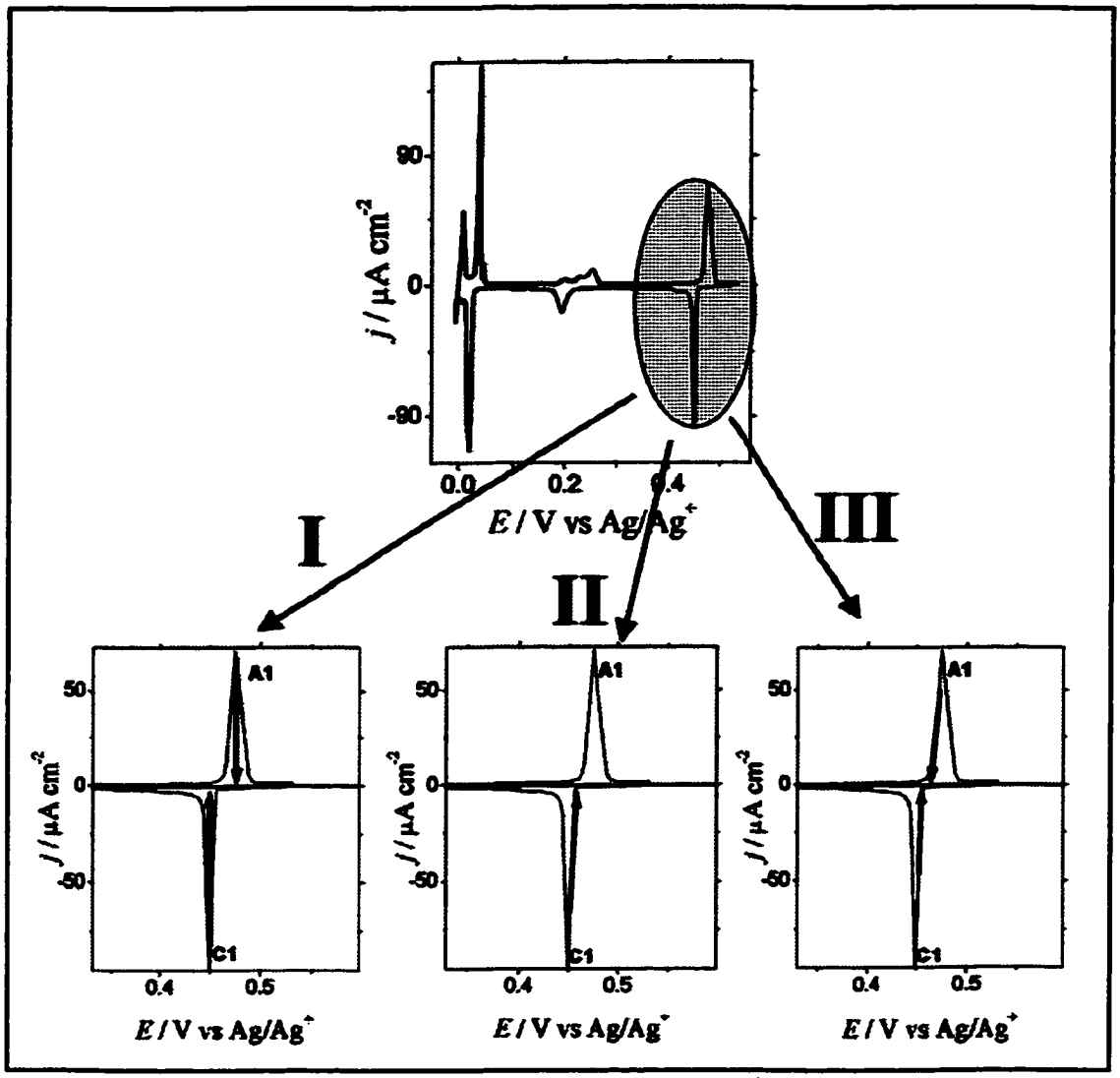

Figure 6.8: Cyclic voltammogram for Ag UPD on Pt(111)(√7 x √7)R19.1°-I showing the different estimates of the reversible potential.

condition of the surface, which introduces substantial error into this estimate. Estimate (III) also involves the shape of the A1 peak, whose initial potential was not always well defined, so that some reaction may already have occurred by the estimated A1 nucleation potential, especially at low temperatures. Indeed, some voltammograms showed that the C1 and A1 peaks initiated at approximately the same potential, suggesting that there is no significant nucleation overpotential. Therefore, the best estimation is the extrapolation of the reduction

peak to the baseline (method (II) in Fig. (6.8)). This estimate is uncomplicated by the issues of the A1 peak shape. At 25°C the E° for reaction (2) from the three estimates are (I) 462 mV, (II) 455.5 mV and (III) 457.5 mV. The $\Delta_{react}S^{\circ}$(I(ads)) calculated from the slopes are: (I) 37 ± 2 J mol^{-1} K^{-1}, (II) 30 ± 2 J mol^{-1} K^{-1} and (III) 26 ± 2 J mol^{-1} K^{-1}. Giving less weight to (I) and using the difference between estimates (II) and (III) as a measure of the systematic

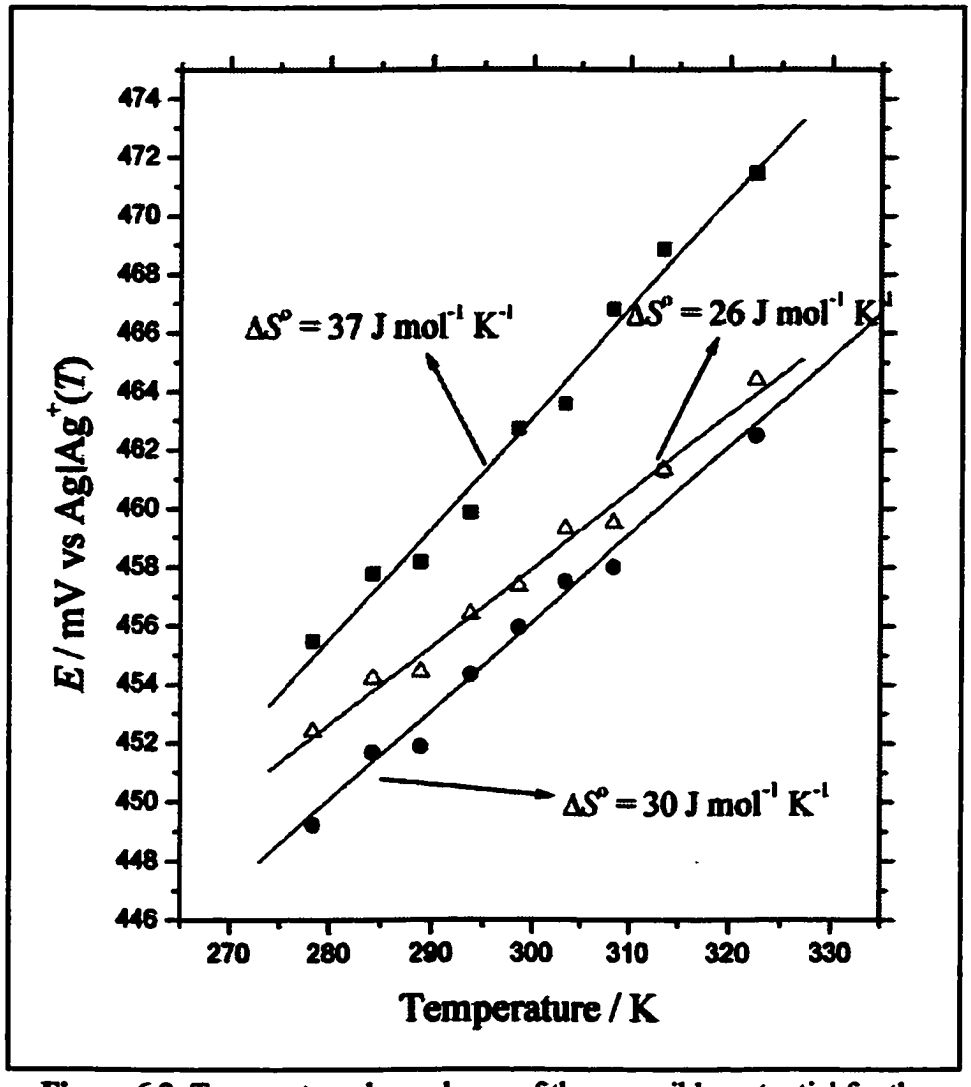

Figure 6.9: Temperature dependence of the reversible potential for the C1/A1 process. Reversible potentials estimated as: I) average of C1 and A1 peak potentials (■), II) extrapolation of the reduction peak C1 to the baseline (●), and III) average of the extrapolation for the oxidation (A1) and reduction (C1) peaks to the baseline (△).

errors, it may be conservatively estimated that $E^{\circ} = 456 \pm 3$ mV and $\Delta_{react}S^{\circ}(I(ads)) = 30 \pm 6$ J mol^{-1} K^{-1}.

6.2.1.1. $\Delta_{react}S^{\circ}$(AgI(ads)) and Double Layer.

A question that arises is whether the entropy change for reaction (3) (Ag(s) + ($\sqrt{7}$ x $\sqrt{7}$)R19.1°-I(ads) → (3 x 3)-AgI(ads)) of 30 ± 6 J mol^{-1} K^{-1} has a significant double layer component, or is mainly due to changes of the surface structure. Two different approaches are used to answer this question: estimation of the entropy change of the reaction from the entropy of the individual components, and estimation of the entropy change of the electrolyte from measurements of the double layer capacitance.

6.2.1.1.1. Entropy Change of the Surface Reaction.

The entropy change of the reaction (3) is:

$$\Delta S^{\circ} = S^{\circ}_{(3 \times 3)\text{-AgI(ads)}} - S^{\circ}_{Ag(s)} - S^{\circ}_{(\sqrt{7} \times \sqrt{7})R19.1^{\circ}\text{-I(ads)}} \qquad (5)$$

$S^{\circ}_{Ag(s)}$ is tabulated as 42.55 J mol^{-1} K^{-1} [6.8]. The other two terms in Eq. (5), $S^{\circ}_{(3 \times 3)\text{-AgI(ads)}}$ and $S^{\circ}_{(\sqrt{7} \times \sqrt{7})R19.1^{\circ}\text{-I(ads)}}$, are unknown. In chapter 3 the crystallographic structure of the surface compound (3 x 3)-AgI(ads) is calculated. It is determined that this structure resembles the structure of bulk AgI. Therefore, we approximate $S^{\circ}_{(3 \times 3)\text{-AgI(ads)}}$ to the entropy $S^{\circ}_{AgI(bulk)}$ = 115.5 J mol^{-1} K^{-1} [6.8]. We also approximate $S^{\circ}_{(\sqrt{7} \times \sqrt{7})R19.1^{\circ}\text{-I(ads)}}$ to $S^{\circ}_{Pt(bulk)}$ = 41.63 J mol^{-1} K^{-1} [6.8], since the iodine in the Pt(111)-($\sqrt{7}$ x $\sqrt{7}$)R19.1°-I(ads) surface structure follows and adapts to the corrugation of the Pt surface.

Substituting in Eq. (5) gives:

$$\Delta S^{\circ} = 115.50 \text{ J mol}^{-1} \text{ K}^{-1} - 42.55 \text{ J mol}^{-1} \text{ K}^{-1} - 41.63 \text{ J mol}^{-1} \text{ K}^{-1} = 31.32 \text{ J mol}^{-1} \text{ K}^{-1} \quad (6)$$

This entropy change is comparable to the entropy change calculated experimentally. Therefore, a rough approximation of the entropy change indicates that the entropy change of the reaction is effectively due to changes of the surface structure.

6.2.1.1.2. Entropy Change of the Electrolyte.

An estimate of the entropy change due to changes in the electrolyte in the double-layer can be calculated from measurements of the differential capacitance of the double layer, C_{dl}. The double layer capacitance for Ag electrodeposition on Pt(111) covered with iodine, Fig (6.10), was measured by Paul Saville at the University of Victoria. As explained in chapter 2, it used single frequency A.C. voltammetry at 1 kHz, as well as A.C. impedance, both techniques with a modulated potential of 0.033 mV rms oscillation amplitude. Some of the values of C_{dl} calculated with A.C. impedance are shown in Fig. (6.10). These agree with the calculated C_{dl} from single frequency A.C. voltammetry, which confirms the validity of the technique for measuring double layer capacitance.

As seen in Fig. (6.10), C_{dl} decreases from 46 $\mu F\ cm^{-2}$ to 22 $\mu F\ cm^{-2}$ during the C1 peak in the voltammogram. At + 0.38 V versus $Ag|Ag^{+}$ there is a minimum in C_{dl}. This potential might be assumed the potential of zero charge, E_{pzc}, at which the charge density on the metal surface, σ^{M}, is zero. However, the current that flows in this flat region of the voltammogram is too large to correspond just to double layer charging. This implies that at these potentials there is electrodeposition of silver and the surface and double layer structure are changing. The minimum in capacitance can not therefore be reliably assigned to the PZC. Two different estimations of E_{pzc} for a Pt(111) surface have been proposed. Based on in-situ infrared spectroscopic measurements [6.9] or "CO charge-displacement" method

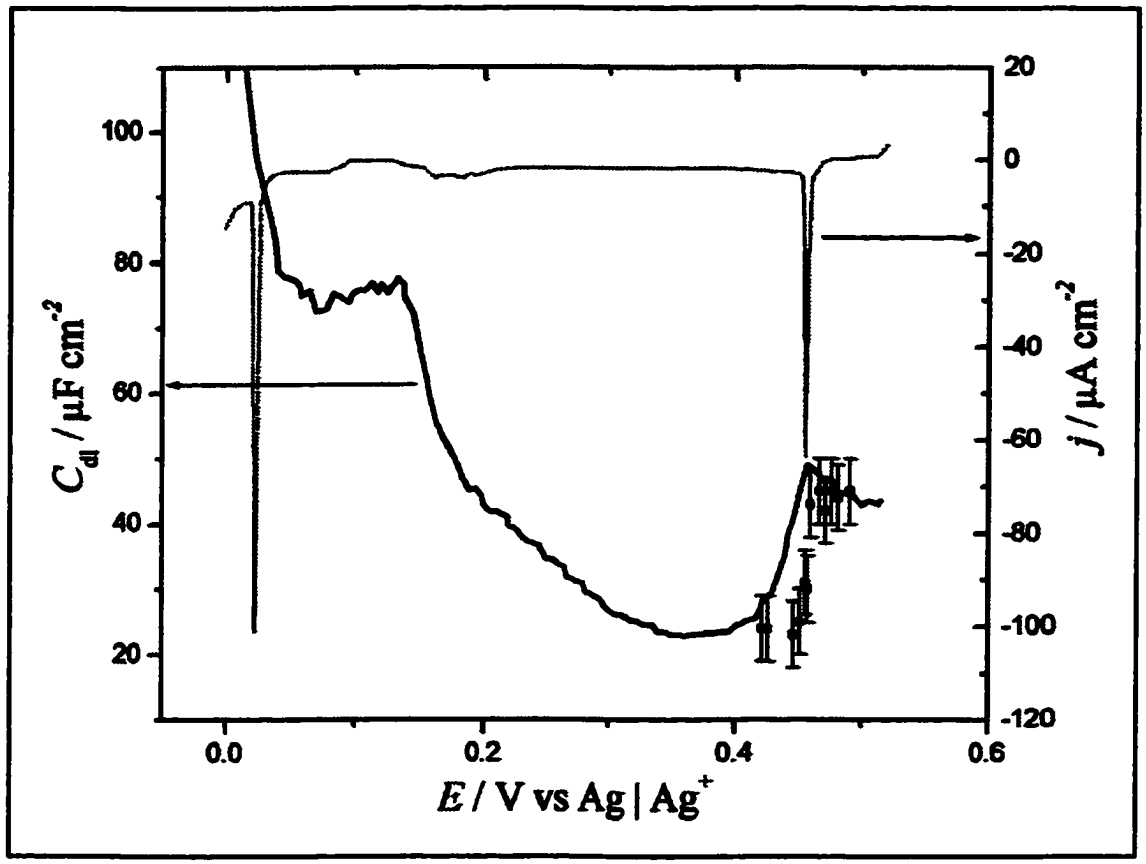

Figure 6.10: Double layer capacitance obtained with (——) A.C. voltammetry, and (■) A.C. impedance. Potential of zero charge, E_{pzc}, shown at the minimum of C_{dl}. (------) Cyclic voltammogram shown for comparison. Similar conditions as in Fig. (6.1).

[6.10] E_{pzc} is estimated at about + 0.1 V vs Ag|Ag$^+$. On the other hand, E_{pzc} is estimated at about + 0.6 V vs Ag|Ag$^+$ by measurements of the charge flowing during contact [6.11]. However, none will be correct for the present situation because adsorption affects the PZC. Since + 0.1 V is furthest from the C1 peak, it will be used to get an upper limit for the energy of the double layer.

From the plot in Fig. (6.10), and assuming E_{pzc} = + 0.1 V, we calculate first the energy component of the double layer, and then the free energy change. A comparison of both quantities gives an estimate of the change of entropy due to the double layer.

6.2.1.1.2.1. Energy Change of the Double Layer.

The differential capacitance of the double layer is defined as:

$$C_{dl} = \frac{d\sigma^M}{dE} \tag{7}$$

Rearranging terms in this equation gives:

$$d\sigma^M = C_{dl} dE \tag{8}$$

The energy of a capacitor is $dU = E\, dQ$, where Q is the charge of the capacitor. Therefore, the energy of the double layer capacitance is:

$$dU = E\, d\sigma^M \tag{9}$$

substituting Eq. (8) in Eq. (9) gives the energy stored by the double layer:

$$\Delta U = \int_{E_{pzc}}^{E} C_{dl} E dE \tag{10}$$

The energy of the double layer is then the integral of C_{dl} from Fig. (6.10) times the potential. This is shown in Fig. (6.11), assuming $E_{pzc} = +0.1$ V. According to Fig. (6.11), the energy change of the double layer from a potential before to a potential after the C1 peak in the voltammogram may be assigned conservatively as less than 1 μJ cm^{-2}.

6.2.1.1.2.2. Free Energy Change of the Double Layer.

The surface tension, γ, is related to the potential according to the electrocapillary equation:

$$d\gamma = -S_s\, dT - \sigma^M\, dE - \sum_i \Gamma_i d\mu_i \tag{11}$$

where S_s is the excess surface entropy, μ the chemical potential and Γ the surface excess or concentration per unit area on the surface of the electrode. σ^M was defined in Eq. (8) in terms of C_{dl} as:

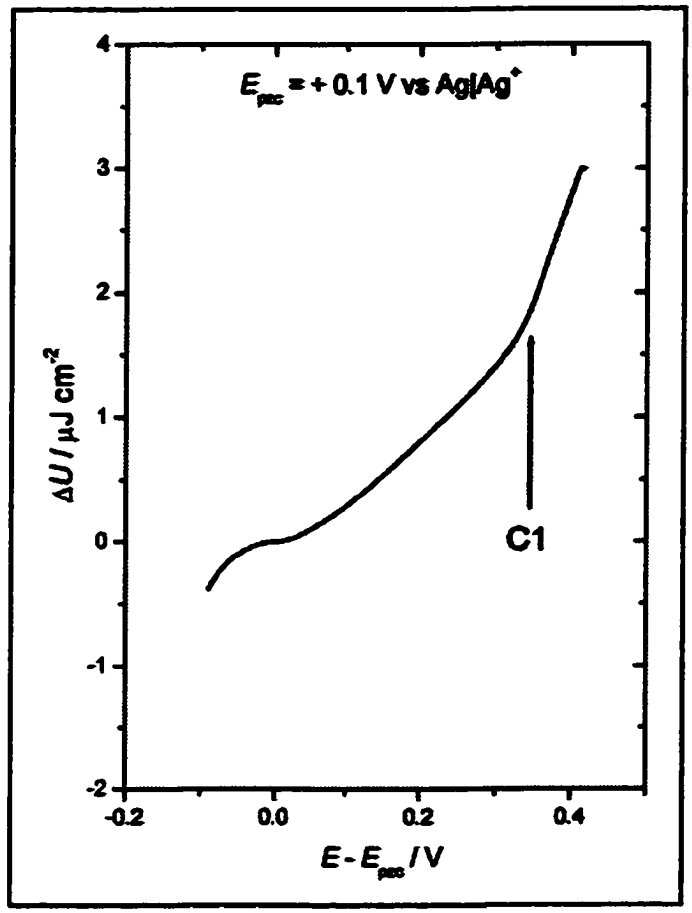

Figure 6.11: Dependence of the energy of the double layer with potential. Position of the C1 peak in the voltammogram included.

$$\sigma^M = \int_{E_{pzc}}^{E} C_{dl}\, dE \tag{12}$$

substituting in Eq. (11) yields, for constant temperature:

$$d\gamma = -\left(\int_{E_{pzc}}^{E} C_{dl}\, dE\right) dE - \sum_i \Gamma_i\, d\mu_i \tag{13}$$

Therefore, the surface tension at constant μ is obtained through double integration of C_{dl} with respect to the potential:

$$\gamma = -\left(\int\int_{E_{pzc}}^{E} C_{dl}\, dE\, dE\right)_{\mu_i} \tag{14}$$

Since γ is a measurement of the free energy per unit area, A:

$$\gamma = \left(\frac{\partial G}{\partial A}\right)_{T,P} \tag{15}$$

combining Eq. (14) and Eq. (15) gives:

$$G - G_{pzc} = -A\left(\int\int_{E_{pzc}}^{E} C_{dl}\, dE\, dE\right)_{\mu_i,T,P} \tag{16}$$

Fig. (6.12) shows the free energy change of the double layer with potential calculated from Eq. (16) assuming $E_{pzc} = +0.1$ V. Since the absolute value of the free energy of the surface at any potential is unknown, a value of $G = 0$ is assigned arbitrarily for each case at the E_{pzc} considered. According to Fig. (6.12), the free energy change before and after the C1 peak in the voltammogram changes no more than - 1 μJ cm^{-2}.

Therefore, the entropy change of the double layer is estimated as:

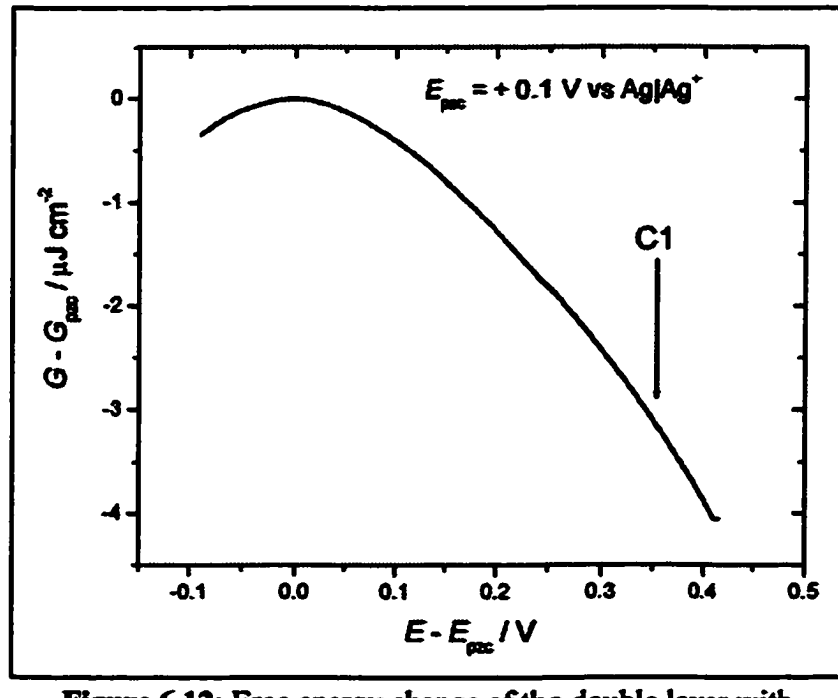

Figure 6.12: Free energy change of the double layer with potential assuming the zero at $E_{pzc} = 0$. Position of the C1 peak in the voltammogram included.

$$\Delta S = \left(\frac{\Delta H - \Delta G}{T}\right) \approx \left(\frac{1\,\mu J\,cm^{-2} - (-1\,\mu J\,cm^{-2})}{298.15\,K}\right) \approx 67 \cdot 10^{-10}\ J\,cm^{-2}\,K^{-1} \qquad (17)$$

Since the density of I atoms in a Pt(111)(3x3) structure is $8.32 \cdot 10^{-10}$ mol cm^{-2}, the entropy change is conservatively $\Delta S \approx 7$ J mol^{-1} K^{-1}. Therefore, it seems reasonable that an entropy change $\Delta_{react}S^{\circ}$(I(ads)) = 30 ± 6 J mol^{-1} K^{-1} is due primarily to the actual changes of the surface structure and not of the double layer.

This result agrees with previous calculations of the absolute entropy of the double layer for Hg measured with the laser-induced temperature jump method [6.12][6.13]. In these experiments, Hg is immersed in solutions that do not produce specific adsorption, NaF or KF, so the interface is mainly composed of H_2O molecules. A laser wavelength that avoids photoemission is chosen so that the light of the pulses is absorbed in the metal, causing an increase in temperature on the surface. Under constant charge of the electrode, the increase in temperature produces a change in the electrode potential [6.14], and the shift changes sign at potentials near the E_{pzc}. This is explained in terms of the reorientation of the dipoles of the molecules of H_2O at the interface. The excess entropy of the double layer can then be obtained through a modification of the electrocapillary equation, Eq. (8). The maximum entropy change deduced with this method due to the dipole orientation of the molecules of H_2O is less than 5 J mol^{-1} K^{-1} [6.12][6.15].

6.2.2. $\Delta_{react}G^{\circ}$(AgI(ads)) and $\Delta_{react}H^{\circ}$(AgI(ads)) for reaction Ag(s) + I(ads) → AgI(ads).

The E° at 298.15 K obtained in the previous section may be multiplied by $-F$ to give the free energy change of reaction as - 44.0 ± 0.3 kJ mol^{-1}, which corresponds with

$\Delta_{react}G°$(I(ads)) for reaction (2). Applying then the thermodynamic relation:

$$\Delta_{react}H°(\text{I(ads)}) = \Delta_{react}G°(\text{I(ads)}) + T\,\Delta_{react}S°(\text{I(ads)}) \qquad (18)$$

gives $\Delta_{react}H°(\text{I(ads)}) = -35 \pm 2$ kJ mol^{-1}

6.3. Dependence on Temperature of the Second Deposition Peak of Ag on Pt(111)(√7 x √7)R19.1°-I.

The phase transition that takes place during the C2 peak is

$$(3 \times 3)\text{-AgI(ads)} + Ag^{+}(aq) + e^{-} \rightarrow (\sqrt{3} \times \sqrt{3})R30°\text{-AgI(ads)} \qquad (19)$$

where the charge involved corresponds to the additional deposition of 0.4-0.5 ML Ag [6.7][6.5].

As shown in Fig. (6.2), the most interesting change in the voltammograms is that, unlike the C1 peak, C2 sharpens at higher temperatures. E_p shifts to higher potentials, although potential at the onset of the peak (225 mV *vs* Ag|Ag^{+}) is independent of temperature. This suggests that it is a kinetically-controlled process. The activation energy (E_a) has to be higher than for the nearly-reversible C1 process (assuming similar pre-exponential factors). If the peak maximum occurs at the same coverage independently of temperature, the current density at the peak maximum, j_p, is proportional to the rate constant for the process. Then the apparent activation energy E_a may be calculated from the slope of the Arrhenius plot log(j_p) versus T^{-1}, Fig. (6.13), as *ca.* 10 kJ mol^{-1}. This is only an apparent activation energy, since the interfacial potential difference is not constant across the plot.

The insert in Fig. (6.2) shows that at lower temperatures the peak has a tail that encloses appreciable charge. j_p is constant from 5 to 15°C, but increases exponentially at higher temperatures. The charge associated with this peak is independent of temperature,

but the presence of a tail in the voltammogram at the lower temperatures, affects the background subtraction and increases the uncertainty. Therefore, the assumption that the peak maximum occurs at the same coverage, valid at high temperatures, is violated at lower temperatures, which may explain the deviation from linearity of the Arrhenius plot at low temperatures.

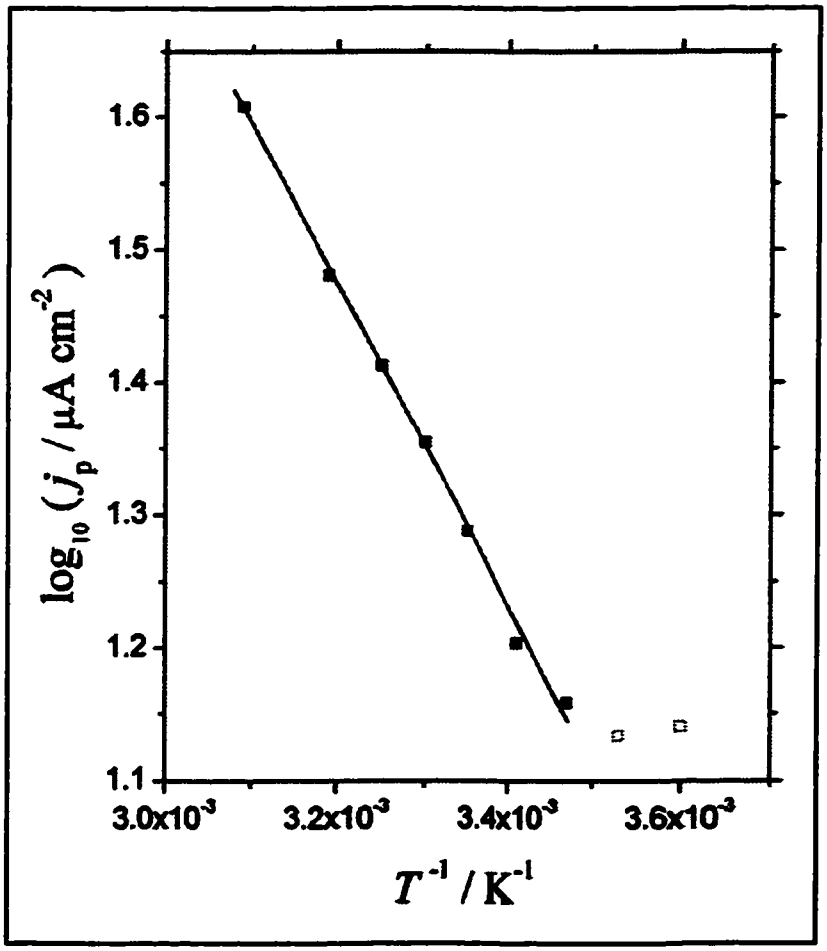

Figure 6.13: Temperature dependence of the C2 peak height. The line has a slope corresponding to an activation energy of 10 kJ mol^{-1} (□ points were excluded from the regression line).

Chapter 7

Thermal Desorption of Iodine from Pt(111)(√7 x √7)R19.1°-I.

7.1. Introduction.

One of the earliest techniques for the study of surfaces was thermal desorption spectroscopy (TDS). Briefly, the crystal is heated up to a certain temperature with a linear heating rate, usually in the range 1 - 20 K s^{-1}. This provides the adsorbed species with enough thermal energy to desorb from the surface into the gas phase. Monitoring the products of desorption with a mass spectrometer as a function of temperature gives insight into the nature, structure and energy of the adsorbed species.

Data from thermal desorption experiments of iodine from Pt(111)(√7 x √7)R19.1°-I under UHV conditions are needed to calculate the standard enthalpy change, $\Delta_{des}H^{\circ}$ (I(ads)), the entropy change, $\Delta_{des}S^{\circ}$ (I(ads)), and the Gibbs free energy change, $\Delta_{des}G^{\circ}$ (I(ads)), for the desorption in vacuum of iodine from Pt(111) at room temperature, Eq. (1).

$$\text{I(ads, vac)} \longrightarrow \text{I(g)} \qquad (1)$$

where I(ads,vac) refers to the Pt(111)(√7 x √7)R19.1°-I structure exposed to UHV. For simplicity, I(ads) is used in this chapter. As discussed in chapter 3, these thermodynamic parameters complete the cycle for the calculation of the cohesive energy of Pt-AgI.

A series of thermal desorption experiments of iodine from a Pt(111)(√7 x √7)R19.1°-I structure were performed by Scott Furman at the University of Victoria [7.1]. Fig. (7.1) shows the desorption spectra of iodine at heating rates from 3 to 15 K/s, starting from saturation coverage in a Pt(111)(√7 x √7)R19.1°-I structure.

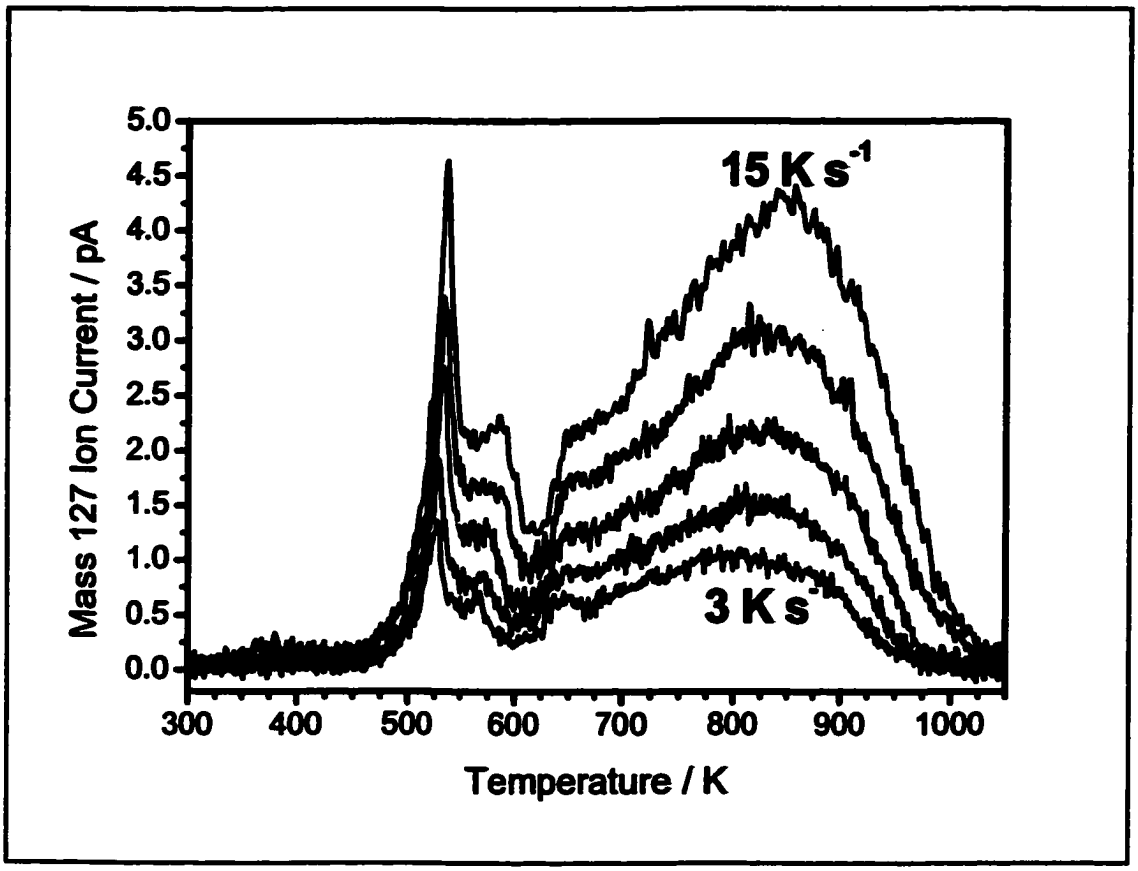

Figure 7.1: Thermal desorption spectra of iodine from Pt(111)(√7 x √7)R19.1°-I at different heating rates (3, 5, 7 10 and 15 K s^{-1}).

There are several distinctive features in the spectra in Fig. (7.1). A sharp peak at 525 - 550 K is followed by a broad peak centered at 850 K. The peaks give an indication of different phase transformations during the desorption process, which can be observed with LEED [7.1]. Thus, in the first desorption peak there is a change from the Pt(111)(√7 x √7)R19.1°-I structure to a diffuse phase. At 570 K the structure becomes Pt(111)(√3 x √3)R30°-I, and at 670 K the pattern become diffuse again. Another conclusion from these spectra is that iodine desorbing in the broad peak follows first order desorption kinetics [7.1]. However, a thermodynamic study of these processes has not yet been performed.

In this chapter, the classical interpretation of the results of the TDS experiment is

explained, together with some of its limitations, (section 7.2). In order to solve those limitations, a model is developed for the desorption of iodine from Pt(111)($\sqrt{7}$ x $\sqrt{7}$)R19.1°-I (section 7.3). Based on this model, some of the changes observed in the thermal desorption experiments in Fig. (7.1) are explained from a thermodynamic point of view. These include calculations for the enthalpy and Gibbs free energy change of desorption at absolute zero, $\Delta_{des}H^{\circ}$ (I(ads),0 K) and $\Delta_{des}G^{\circ}$ (I(ads),0 K), (section 7.5). These parameters are then used in a thermodynamic cycle for the calculation at room temperature of $\Delta_{des}H^{\circ}$ (I(ads)), $\Delta_{des}S^{\circ}$ (I(ads)) and $\Delta_{des}G^{\circ}$ (I(ads)), (section 7.6). The absolute thermodynamic parameters of the surface are obtained in the last section of this chapter, (section 7.7).

7.2. Classical Arrhenius analysis of the TDS.

According to the Arrhenius law, the rate constant of a reaction, k, is exponentially related with the reciprocal of the absolute temperature as:

$$k = A\exp\left(-\frac{E_a}{RT}\right) \tag{2}$$

where A is the frequency factor and E_a the activation energy. In a thermal desorption experiment run at the high pumping speed limit, the rate of the reaction is proportional to the partial pressure of desorbed species (P). Therefore:

$$P = \alpha f(\theta) A\exp\left(-\frac{E_a}{RT}\right) \tag{3}$$

where α is a proportionality constant which depends on the pumping system, and $f(\theta)$ a function that depends on coverage or surface concentration. According to Eq. (3), at each iodine coverage, θ, a plot of $\ln P$ versus $1/T$ gives a straight line with slope $-E_a/R$.

Fig. (7.1) shows a series of thermal desorption experiments of iodine from

Pt(111)($\sqrt{7}$ x $\sqrt{7}$)R19.1°-I [7.1]. These spectra can be integrated and converted to coverage versus temperature profiles. At 0.01 increments in coverage from 0.01 to 0.43, the rate and temperature corresponding to those coverages were determined at each heating rate. This allowed a series of graphs to be constructed for the determination of E_a using Eq. (3). A sample of those graphs is shown in Fig. (7.2). The different slopes indicate different activation energies of desorption. The variation of the activation energy with coverage is depicted in Fig. (7.3). Fig. (7.3) shows how the activation energy changes with coverage. This change is due to the interaction between the iodine atoms adsorbed on the surface. Therefore, E_a obtained has contributions from the interactions between the adsorbed atoms.

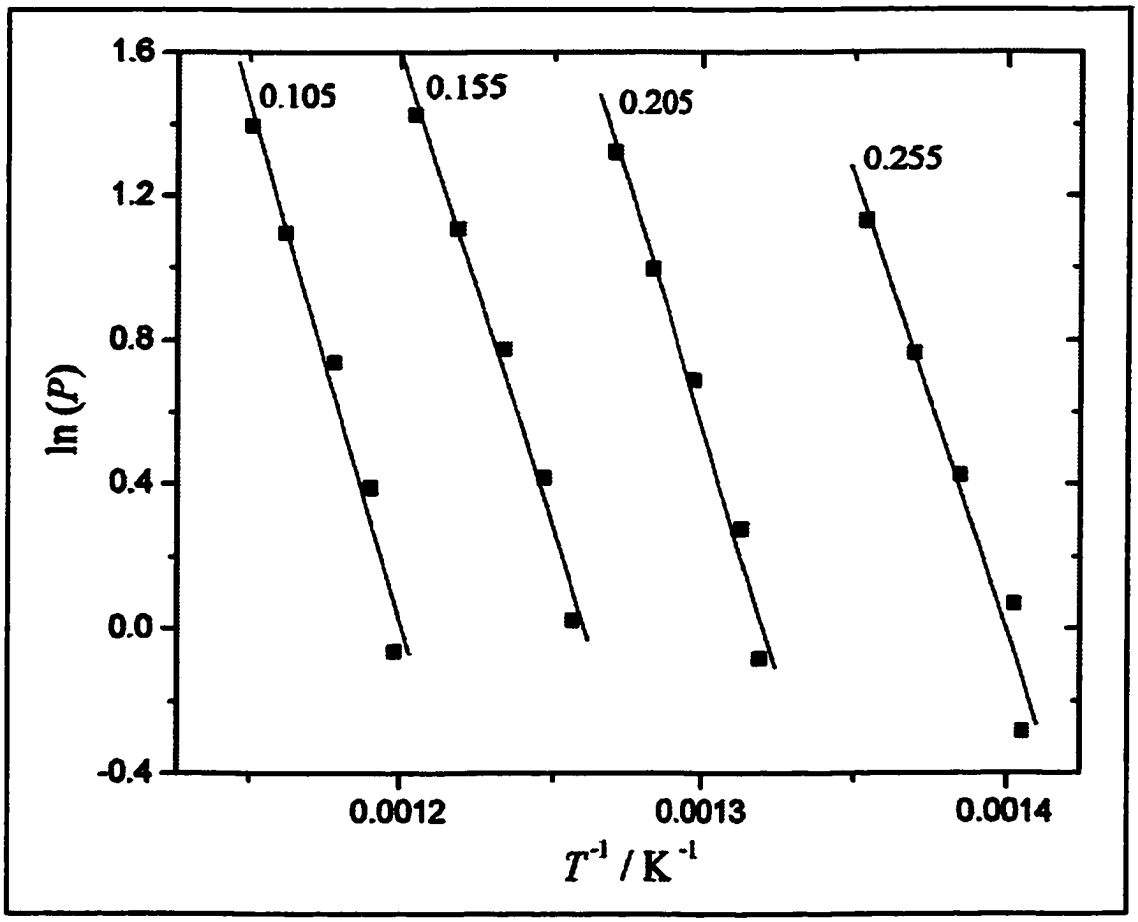

Figure 7.2: Arrhenius plot for the determination of E_a for different iodine coverages. Each line is labeled with the corresponding coverage.

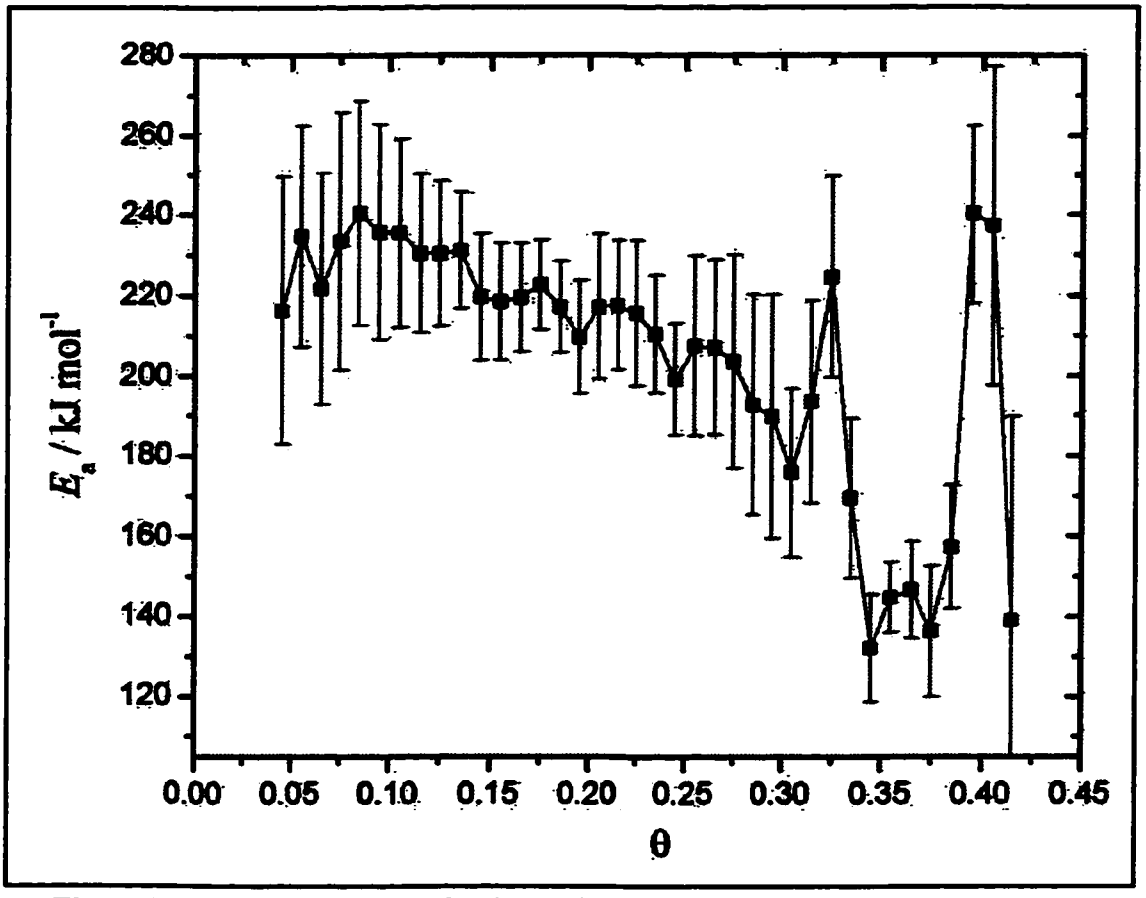

Figure 7.3: Activation energy for desorption of I from Pt(111) at each I coverage.

A limitation of this model is that experimentally, the thermal desorption of iodine from Pt(111) takes place in a temperature range from 500 to 1000 K. Over this temperature range the contribution of the vibrational energy of the adsorbed atoms in the activation energy is changing. A new model of desorption is required to account for the effect of the vibrations.

7.3. Model of Desorption.

Two main approaches have been proposed in order to reproduce thermal desorption spectra: (i) assuming a transition-state, (ii) not assuming a transition-state. The main derivation assuming a transition-state is based on the kinetic lattice-gas approximation. It accounts for vibrations and lateral interactions, adding a term for diffusion of the adsorbate on the surface [7.2][7.3][7.4]. Among approaches that not consider a transition-state there are two main derivations: one is based on the co-existence of two different phases on the surface and a 2D gas phase above. It uses irreversible thermodynamics, considering vibrations according to the harmonic oscillator and lateral interactions described according to either the "Bragg-Williams" or quasichemical approximations [7.5][7.6][7.7][7.8]. The second approach to describe TDS that does not assume a transition state is based on statistical rate theory, and considers vibrations of the adsorbates according to double harmonic oscillators [7.9][7.10].

As we will see below, we develop a model of desorption based on transition-state theory. In our model the transition-state is allowed to occupy a site on the surface, and the vibrations are treated according to the Debye and not the Einstein model of lattice vibrations.

Our model assumes that the iodine atoms pass through a transition-state before desorbing from the platinum surface, according to transition-state theory. Thus, the iodine is at quasi-equilibrium with an activated complex ($I^{\ddagger}$) before being desorbed, Eq. (4). This quasi-equilibrium is described by the equilibrium constant $K^{\ddagger}$.

$$I\,(ads) \overset{K^{\ddagger}}{\rightleftharpoons} I^{\ddagger} \longrightarrow I\,(g) \qquad (4)$$

The coverage of transition-state iodine, $\theta_{I^{\ddagger}}$, is assumed small compared with the iodine in

the adsorbed state I(ads). The validity of this approximation is tested and discussed in the following sections. The transition-state iodine does not move across the surface, and takes up only one site, the one the adsorbed atom was in.

The rate of desorption is influenced by the interactions between the iodine atoms on the surface. Only interactions between the iodine atoms in the adsorbed state are considered. The adsorbed atoms are assumed not to interact with the iodine atoms in the transition state, since each $I^{\ddagger}$ atom is assumed to be far above the site of the I(ads) from which it comes. In as much as $\theta_{I^{\ddagger}}$ is small, the interactions between iodine atoms in the transition state are also neglected. The energy of interaction between the adsorbed atoms is further assumed to be independent of the vibrational energy of the adsorbed atoms, and is assumed to follow the "Bragg-Williams" approximation. That is, the interactions are only strong enough to change the energy of the possible configurations of the particles on the surface, but all configurations are equally likely. In other words, the entropy is not affected, only the energy.

Accordingly, there is a random distribution of the atoms on the surface. However, the model of lattice vibrations considered in this chapter: Debye model, assumes island distribution of the atoms adsorbed on the surface. This difficulty can be overcome with more accurate models of lattice vibrations. However, they bring unmanageable mathematical expressions that are difficult to treat. In the next sections we see how our model is still reasonable, since the influence of the vibrations of the lattice are minimal over the range of energies considered.

Our model assumes that the activated complex has similar energy and structure to the final state iodine atoms, in accordance with Hammond's postulate [7.11], Fig. (7.4). In

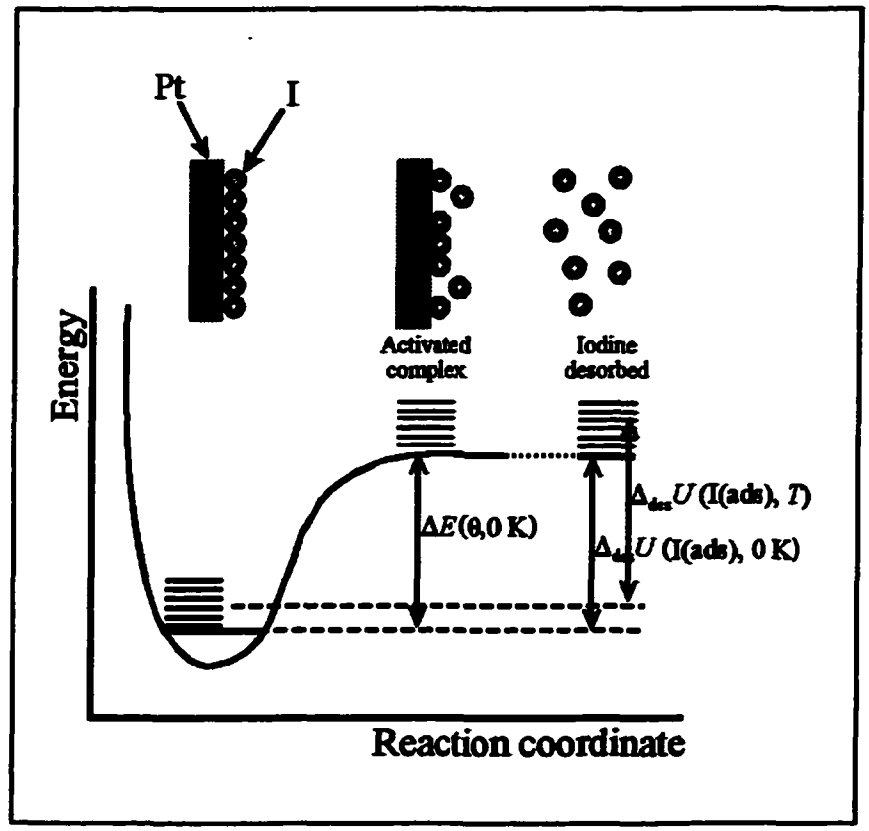

Figure 7.4: Energy diagram for the desorption of iodine from a Pt surface at constant coverage.

this case, the transition state iodine is defined at a position far enough from the surface that the energy is negligibly different from the energy at $r = \infty$. Note that according to some definitions of the transition state, there must be a maximum (with negative curvature) in the reaction co-ordinate, which is not the case here. However, in other definitions, the transition state is the maximum point on the minimum energy path, which would be at $r = \infty$ here. Nevertheless, the exact position of the transition-state is irrelevant in our calculations. In spite of the energies being similar, the entropies of $I^{\ddagger}$ and I(g) are quite different due to differences in translational freedom.

Since the system is composed of a great number of particles, an understanding of the vibrational modes, as well as an evaluation of the rate parameters in the framework of

transition state theory requires the use of statistical thermodynamics.

7.4. Rate of Desorption of Iodine from Pt(111)(√7 x √7)R19.1°-I.

Once a model for desorption of iodine from Pt(111) has been developed, it is possible to interpret the experimental TDS in Fig. (7.1). Iodine desorbing from the Pt(111) follows first order desorption kinetics in the broad peak of the TDS [7.1]. The total rate of desorption (r) is the product of the frequency for motion along the reaction co-ordinate, $\nu_\perp$ (s^{-1}), (perpendicular to the surface), multiplied by the surface concentration of transition-state iodine, $\Gamma_{I^\ddagger}$:

$$r = \nu_\perp \Gamma_{I^\ddagger} = \nu_\perp \Gamma_{max}\, \theta_{I^\ddagger} \tag{5}$$

$\Gamma_{I^\ddagger}$ is defined as the coverage of transition-state, $\theta_{I^\ddagger}$, multiplied by the surface concentration of $I^\ddagger$ at saturation, Γ_{max}.

The rate of the reaction is proportional to the partial pressure of desorbed species (P) at the high pumping speed limit. Hence:

$$P = \alpha\, \nu_\perp \Gamma_{max}\, \theta_{I^\ddagger} \tag{6}$$

where α is a proportionality constant which depends on the pumping system. In the next sections, an analytical expression for $\theta_{I^\ddagger}$ is found. This gives a functional form for the pressure as a function of coverage and temperature (section 7.4.2):

$$P = \alpha \frac{\left(\frac{kT}{h}\right)^3 \frac{1}{\nu_\parallel^{\,2}}}{\exp\left(-\frac{6T^2}{\theta_D^2}\int_0^{\frac{\theta_D}{T}}\left[\frac{x}{2}+\ln\left(1-\exp(-x)\right)\right]x\,dx\right)} \cdot \exp\left(-\frac{\Delta E^\circ(0\text{ K})}{RT}\right)\Gamma_{max}\,\theta\,\exp\left(g\,\theta_{I(ads)}\right) \tag{7}$$

where θ_D is the Debye temperature, defined in section 7.9.2.2. ΔE° (0 K) the standard

apparent activation energy at 0 K and 0 coverage, v_I the vibrational frequency of the activated complex parallel to the surface and *g* an interaction parameter defined in section 7.4.1.2.. Eq. (7) is an improvement over the Arrhenius form. It suggests an appropriate plot whose slope is related to some of the thermodynamic and energetic parameters for the desorption of iodine.

7.4.1. Coverage of the Transition-state Iodine, $\theta_{I^\ddagger}$.

An analytical expression for the coverage of transition state iodine is obtained in this section. The procedure to calculate $\theta_{I^\ddagger}$ is the following: an expression for the free energy of the surface, *A*, is deduced. The chemical potentials of I(ads) and $I^\ddagger$ are derived from the expression for *A* previously calculated. Since I(ads) is at equilibrium with $I^\ddagger$, their chemical potentials are set equal, and the equation is solved for $\theta_{I^\ddagger}$.

7.4.1.1. Analytical Expression of the Free Energy of the Surface, *A*.

From a statistical thermodynamic point of view, the free energy *A* is:

$$A = -kT\ln\left(Q_{total}\right) = -kT\ln\left(W_{config}\, Q_{th}\right) \qquad (8)$$

where Q_{total} is the overall partition function. In the Bragg-Williams approximation, Q_{total} can be split into two components: configurational, W_{config}, and thermal canonical partition function, Q_{th}. These two factors are then calculated as follows.

7.4.1.1.1. Weight of the Configuration.

The weight of the configuration, W_{config}, is defined as the number of possible configurational arrangements of the adsorbed particles on a surface, which mathematically

can be expressed as:

$$W_{config} = \frac{M!}{N_{I(ads)}!N_{I^{\ddagger}}!\left(M - N_{I(ads)} - N_{I^{\ddagger}}\right)!} \tag{9}$$

where M is the total number of sites on the surface, and $N_{I(ads)}$ and $N_{I^{\ddagger}}$ are the number of iodine atoms adsorbed on the surface and in its transition-state respectively. $N_{I(ads)}$ and $N_{I^{\ddagger}}$ can be defined in terms of their respective partial coverages, $\theta_{I(ads)}$ and $\theta_{I^{\ddagger}}$:

$$N_{I(ads)} = M\theta_{I(ads)}, \quad N_{I^{\ddagger}} = M\theta_{I^{\ddagger}} \tag{10}$$

Applying Stirling's approximation (ln x! ≈ x ln x - x) to Eq. (9), and substituting $N_{I(ads)}$ and $N_{I^{\ddagger}}$ in term of their coverages yields:

$$\ln W_{config} = -M\left[\theta_{I(ads)}\ln\left(\theta_{I(ads)}\right) + \theta_{I^{\ddagger}}\ln\left(\theta_{I^{\ddagger}}\right) + \left(1 - \theta_{I(ads)} - \theta_{I^{\ddagger}}\right)\ln\left(1 - \theta_{I(ads)} - \theta_{I^{\ddagger}}\right)\right] \tag{11}$$

7.4.1.1.2. Thermal Canonical Partition Function.

Q_{th} is the thermal canonical partition function. It is associated with the free energy of the surface without the contribution from the configurational entropy. Q_{th} has contributions from the different canonical partition functions, plus an energy term, U_{int} or mean energy of interaction, which describes the nearest neighbor interaction between the adsorbed iodine. Thus:

$$Q_{th} = Q_{I^{\ddagger}}\, Q_{I(ads)} \exp\left(\frac{-U_{int}}{kT}\right) \tag{12}$$

which in terms of the molecular partition functions, q, is:

$$Q_{th} = \left(q_{I^{\ddagger}}\right)^{N_{I^{\ddagger}}} \left(q_{I(ads)}\right)^{N_{I(ads)}} \exp\left(\frac{-U_{int}}{kT}\right) \tag{13}$$

Analytical expressions for the molecular partition functions $q_{I(ads)}$ and $q_{I^{\ddagger}}$ are derived in the appendix of this chapter. For convenience to the reader, they will not be substituted in the

following equations unless necessary.

In Eq. (13), both molecular partition functions are referred to the same energy scale. In order to refer both molecular partition functions to their ground state energies as their respective zero energy, the energy difference between the ground state of adsorbed iodine and excited state (ΔE°(0 K) or standard apparent activation energy at 0 K and 0 coverage, Fig. (7.4)), has to be included[A]:

$$Q_{th} = \left(q_{I^*}\right)^{N_{I^*}} \left(q_{I(ads)}\right)^{N_{I(ads)}} \exp\left(\frac{N_{I(ads)}\,\Delta E^{\circ}(0\text{ K})}{kT}\right) \exp\left(\frac{-U_{int}}{kT}\right) \qquad (14)$$

An expression for U_{int} is still necessary in Eq. (14).

7.4.1.1.2.1. Mean Energy of Interaction, U_{int}.

For a triangular lattice, the energy of interaction may be derived as follows. The probability of interaction between two nearest neighbors is the probability that a site is occupied, times the probability that a close neighbor site is also occupied. Therefore, the probability of interaction is θ^2. As shown in Fig. (7.5), there are 3 lines of interactions per atom in the unit cell of a triangular lattice. Accordingly, the mean number of interactions on a surface is: $3 \times M \times \theta^{2}_{I(ads)}$, where M is the total number of sites. If each of the interactions corresponds to an energy u ($u < 0$ for attractions and $u > 0$ for repulsions), the mean energy of interactions is:

[A] Throught this thesis, the standard state is defined as the standard state at the limit of full coverage on the surface, being full coverage iodine on a Pt(111)($\sqrt{7} \times \sqrt{7}$)R19.1°-I structure. This standard state is then denoted with the superscript (°) after the parameter considered. However, in this chapter, the standard state is defined at the limit of zero coverage, where there are no interactions of the iodine atoms adsorbed. It is then denoted with the superscript (°).

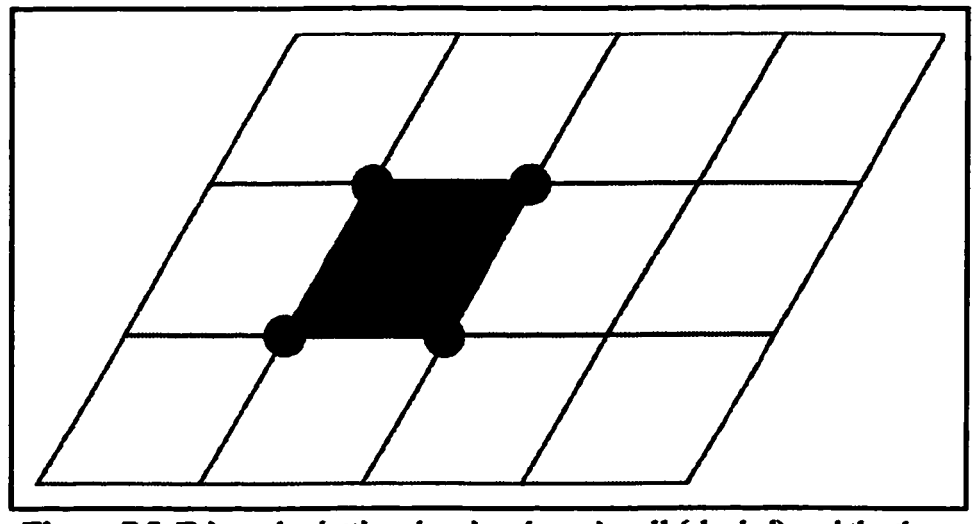

Figure 7.5: Triangular lattice showing the unit cell (shaded) and the three possible lines of interactions per atom within the unit cell.

$$U_{int} = 3u\,M\theta^2_{I(ads)} \tag{15}$$

Substituting U_{int} calculated into Eq. (14) for the thermal canonical partition function yields:

$$Q_{th} = \left(q_{1\phi}\right)^{N_{1\phi}} \left(q_{I(ads)}\right)^{N_{I(ads)}} \exp\left(\frac{N_{I(ads)}\,\Delta E^{\circ}(0\,\mathrm{K})}{kT}\right) \exp\left(\frac{-3u\,M\theta^2_{I(ads)}}{kT}\right) \tag{16}$$

$\ln W$ in Eq.(11), and Q_{th} in Eq. (16) have now been estimated. Substituting them into Eq. (8) for the absolute free energy of the surface, A, and simplifying, gives:

$$\begin{aligned} A = &- kT N_{1\phi} \ln q_{1\phi} - kT N_{I(ads)} \ln q_{I(ads)} - N_{I(ads)} \Delta E^{\circ}(0\,\mathrm{K}) + 3u\,M\theta^2_{I(ads)} \\ &+ kTM\left[\theta_{I(ads)} \ln\left(\theta_{I(ads)}\right) + \theta_{1\phi} \ln\left(\theta_{1\phi}\right) + \left(1 - \theta_{I(ads)} - \theta_{1\phi}\right) \ln\left(1 - \theta_{I(ads)} - \theta_{1\phi}\right)\right] \end{aligned} \tag{17}$$

A more detail analysis of this expression as a function of temperature and coverage is done in section 7.7.

Transforming $N_{I(ads)}$ and $N_{1\phi}$ from Eq. (17) in terms of their partial coverages, Eq. (10), and multiplying per Avogadro's number, N_A, to obtain A per mol:

$$A = -RTM\theta_{I\phi}\ln q_{I(ads)} - RTM\theta_{I(ads)}\ln q_{I(ads)} - M\theta_{I(ads)}\Delta E^{\circ}(0\,K) + 3uMN_A\theta_{I(ads)}^2 + RTM\left[\theta_{I(ads)}\ln\left(\theta_{I(ads)}\right) + \theta_{I\phi}\ln\left(\theta_{I\phi}\right) + \left(1-\theta_{I(ads)}-\theta_{I\phi}\right)\ln\left(1-\theta_{I(ads)}-\theta_{I\phi}\right)\right] \quad (18)$$

7.4.1.2. Chemical Potentials of Adsorbed and Transition State Iodine.

The activation free energy change for the desorption of iodine, $\Delta^{\ddagger}G$ (I(ads)), is the difference between the chemical potential of the transition and the adsorbed states:

$$\Delta^{\ddagger}G(\text{I(ads)}) = \mu_{I\phi} - \mu_{I(ads)} \quad (19)$$

Since the iodine is at equilibrium with its transition-state, $\Delta^{\ddagger}G$ (I(ads)) = 0, Eq. (19) becomes:

$$\mu_{I\phi} = \mu_{I(ads)} \quad (20)$$

The chemical potential of the adsorbed and transition state iodine is defined in terms of the absolute free energy as:

$$\mu_{I\phi} = \left(\frac{\partial A}{\partial N_{I\phi}}\right)_{V,T,N_{I(ads)}} \quad (21)$$

$$\mu_{I(ads)} = \left(\frac{\partial A}{\partial N_{I(ads)}}\right)_{V,T,N_{I\phi}} \quad (22)$$

We can change these partial derivatives according to Eq. (10) to functions of the partial coverages. This gives:

$$\mu_{I\phi} = \left(\frac{\partial A}{\partial N_{I\phi}}\right)_{V,T,N_{I(ads)}} = \left(\frac{\partial A}{\partial \theta_{I\phi}}\cdot\frac{\partial \theta_{I\phi}}{\partial N_{I\phi}}\right)_{V,T,N_{I(ads)}} = \left(\frac{\partial A}{\partial \theta_{I\phi}}\cdot\frac{\partial \frac{N_{I\phi}}{M}}{\partial N_{I\phi}}\right)_{V,T,N_{I(ads)}} = \frac{1}{M}\left(\frac{\partial A}{\partial \theta_{I\phi}}\right)_{V,T,N_{I(ads)}} \quad (23)$$

$$\mu_{I(ads)} = \left(\frac{\partial A}{\partial N_{I(ads)}}\right)_{V,T,N_{I\phi}} = \left(\frac{\partial A}{\partial \theta_{I(ads)}}\cdot\frac{\partial \theta_{I(ads)}}{\partial N_{I(ads)}}\right)_{V,T,N_{I\phi}} = \left(\frac{\partial A}{\partial \theta_{I(ads)}}\cdot\frac{\partial \frac{N_{I(ads)}}{M}}{\partial N_{I(ads)}}\right)_{V,T,N_{I\phi}} = \frac{1}{M}\left(\frac{\partial A}{\partial \theta_{I(ads)}}\right)_{V,T,N_{I\phi}} \quad (24)$$

Substituting A from Eq. (18) into Eq. (23) and (24) yields:

$$\mu_{1\phi} = -RT\ln q_{1\phi} + RT\left[\ln\left(\theta_{1\phi}\right) - \ln\left(1-\theta_{1(ads)}-\theta_{1\phi}\right)\right] \quad (25)$$

$$\mu_{1(ads)} = -RT\ln q_{1(ads)} - \Delta E^{\circ}(0\,\mathrm{K}) + 6uN_A\theta_{1(ads)} + RT\left[\ln\left(\theta_{1(ads)}\right) - \ln\left(1-\theta_{1(ads)}-\theta_{1\phi}\right)\right] \quad (26)$$

Rearranging terms:

$$\mu_{1\phi} = \mu_{1\phi}^{\circ} + RT\ln\left(\frac{\theta_{1\phi}}{1-\theta_{1(ads)}-\theta_{1\phi}}\right) \quad (27)$$

$$\mu_{1(ads)} = \mu_{1(ads)}^{\circ} + RT\ln\left(\left(\frac{\theta_{1(ads)}}{1-\theta_{1(ads)}-\theta_{1\phi}}\right)\exp\left(g\theta_{1(ads)}\right)\right) \quad (28)$$

Where:

$$\mu_{1\phi}^{\circ} = -RT\ln q_{1\phi}, \quad \mu_{1(ads)}^{\circ} = -RT\ln q_{1(ads)} - \Delta E^{\circ}(0\,\mathrm{K}) \text{ and } g = \frac{6uN_A}{RT} \quad (29)$$

Substituting Eq. (27) and (28) into Eq. (20) ($\mu_{\phi} = \mu_{(ads)}$) yields:

$$\mu_{1\phi}^{\circ} + RT\ln\left(\frac{\theta_{1\phi}}{1-\theta_{1(ads)}-\theta_{1\phi}}\right) = \mu_{1(ads)}^{\circ} + RT\ln\left(\left(\frac{\theta_{1(ads)}}{1-\theta_{1(ads)}-\theta_{1\phi}}\right)\exp\left(g\theta_{1(ads)}\right)\right) \quad (30)$$

Eq. (30) can not be solved analytically. We use the software package Maple VI to solve it numerically for $\theta_{1\phi}$ under all reasonable conditions. As justified in section 7.7.1., it is found that:

$$\theta_{1\phi} << \theta_{1(ads)} \;;\; \text{therefore: } \theta_{1\phi} << \theta, \quad \text{where } \theta = \theta_{1(ads)} + \theta_{1\phi} \quad (31)$$

Applying Eq. (31) to the chemical potentials in Eq. (27) and (28) gives:

$$\mu_{1\phi} = \mu_{1\phi}^{\circ} + RT\ln\left(\frac{\theta_{1\phi}}{1-\theta}\right) \quad (32)$$

$$\mu_{I(ads)} = \mu^{\circ}_{I(ads)} + RT\ln\left(\frac{\theta_{I(ads)}}{1-\theta}\exp\left(g\theta_{I(ads)}\right)\right) \tag{33}$$

where the term 1-θ corresponds to the coverage of free sites on the surface.

Substituting Eq. (32) and (33) into Eq. (20):

$$\mu^{\circ}_{I^{\ddagger}} + RT\ln\left(\frac{\theta_{I^{\ddagger}}}{1-\theta}\right) = \mu^{\circ}_{I(ads)} + RT\ln\left(\frac{\theta_{I(ads)}}{1-\theta}\exp\left(g\theta_{I(ads)}\right)\right) \tag{34}$$

and solving analytically Eq. (34) for the coverage of transition-state iodine, after substituting $\mu_{I^{\ddagger}}$ and $\mu_{I(ads)}$ from Eq. (29):

$$\theta_{I^{\ddagger}} = \frac{q_{I^{\ddagger}}}{q_{I(ads)}}\exp\left(-\frac{\Delta E^{\circ}(0\,K)}{RT}\right)\theta\,\exp\left(g\theta_{I(ads)}\right) \tag{35}$$

7.4.2. Total Rate of Reaction for Desorption of I from Pt(111).

After substituting the coverage of transition state iodine from Eq. (35) into Eq. (6), the total rate of the desorption reaction becomes:

$$P = \alpha\,\nu_{\perp}\frac{q_{I^{\ddagger}}}{q_{I(ads)}}\exp\left(-\frac{\Delta E^{\circ}(0\,K)}{RT}\right)\Gamma_{max}\,\theta\,\exp\left(g\theta_{I(ads)}\right) \tag{36}$$

Substituting $q_{I(ads)}$ and $q_{I^{\ddagger}}$ calculated in the appendix of this section in Eq. (36) gives:

$$P = \alpha\,\frac{\left(\frac{kT}{h}\right)^{3}\frac{1}{\nu_{\parallel}^{2}}}{\exp\left(-\frac{6T^{2}}{\theta_{D}^{2}}\int_{0}^{\frac{\theta_{D}}{T}}\left[\frac{x}{2}+\ln\left(1-\exp\left(-x\right)\right)\right]x\,dx\right)}\cdot\exp\left(-\frac{\Delta E^{\circ}(0\,K)}{RT}\right)\Gamma_{max}\,\theta\,\exp\left(g\theta_{I(ads)}\right) \tag{37}$$

where θ_D is defined as the Debye temperature, and $\nu_{\parallel}$ as the vibrational frequency of the transition state iodine parallel to the surface. Taking logarithms and rearranging terms in Eq. (37) yields:

$$\ln\frac{P}{T^3} - \frac{6T^2}{\theta_D^2}\int_0^{\frac{\theta_D}{T}}\left[\frac{x}{2} + \ln\left(1-\exp(-x)\right)\right]x\,dx = \ln\left(\alpha\left(\frac{k}{h}\right)^3\frac{1}{\nu_{\parallel}^2}\Gamma_{max}\,\theta\right) - \frac{\Delta E(\theta,0\text{ K})}{RT} \tag{38}$$

where $\Delta E(\theta,0\text{ K})$ is the apparent activation energy of desorption per mol dependent on coverage at 0 K, and is defined as the energy separation between the ground state energies of $I^{\ddagger}$ and I(ads) at absolute zero at any coverage, Fig (7.4). That is:

$$\Delta E(\theta,0\text{ K}) = \Delta E^{\circ}(0\text{ K}) - RTg\theta_{I(ads)} \tag{39}$$

According to Eq. (39), $\Delta E(0,0\text{ K})$ can be obtained at different coverages with the plot:

$$\ln\frac{P}{T^3} - \frac{6T^2}{\theta_D^2}\int_0^{\frac{\theta_D}{T}}\left[\frac{x}{2} + \ln\left(1-\exp(-x)\right)\right]x\,dx.\ \text{vs.}\ T^{-1} \tag{40}$$

the slope of the line being $-\Delta E(\theta,0\text{ K}) / R$ at each coverage.

7.5. Standard Enthalpy and Gibbs Energy Change of Desorption at the Limit of Full Coverage at 0 K, ($\Delta_{des}H^{\circ}$ (I(ads), 0 K) and $\Delta_{des}G^{\circ}$ (I(ads), 0 K)).

In a similar fashion as in section 7.2 for the classical interpretation of the TDS, the integration of the experimental TDS allows a series of graphs to be drawn using Eq. (40). These are shown in Fig. (7.6). The different slopes indicate a different $\Delta E(\theta,0\text{ K})$. The change of $\Delta E(\theta,0\text{ K})$ with coverage is illustrated in Fig. (7.7).

As seen in Fig. (7.4), at each coverage $\Delta E(\theta,0\text{ K})$ is the same as the internal energy of desorption at the absolute zero $\Delta_{des}U$ (I(ads), 0 K). At absolute zero, there is no entropy component, and PV is negligible; therefore:

$$\begin{aligned}\Delta E(\theta,0\text{ K}) &= \Delta_{des}U\,(\text{I(ads)},0\text{ K}) = \Delta_{des}G\,(\text{I(ads)},0\text{ K}) \\ &= \Delta_{des}H\,(\text{I(ads)},0\text{ K})\end{aligned} \tag{41}$$

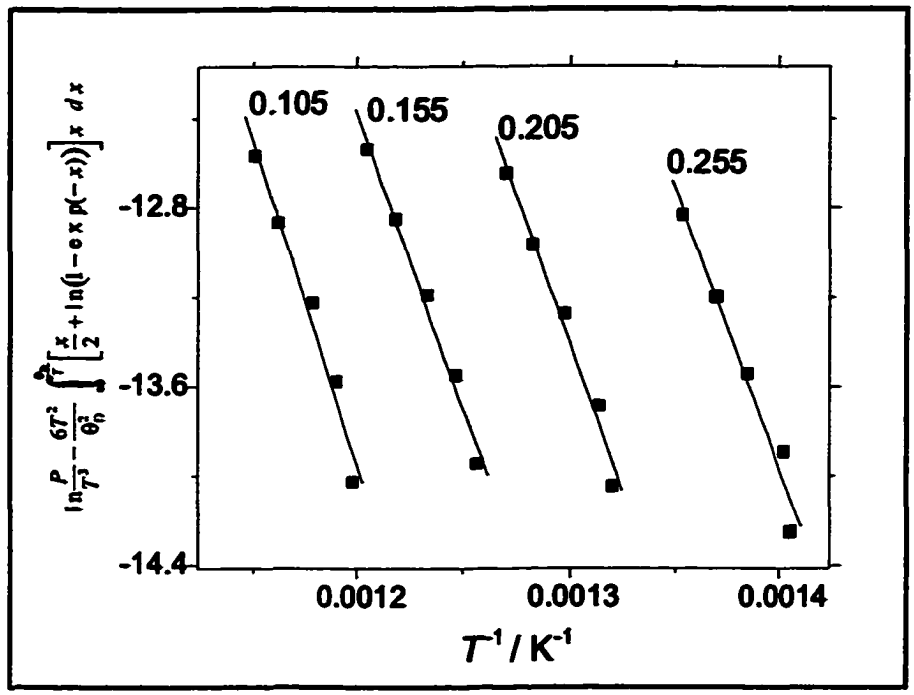

Figure 7.6: Plot for the determination of $\Delta E(\theta,0\ K)$ for different iodine coverages. Each line is labeled with the corresponding coverage.

$\Delta E(\theta,0\ K)$ is equivalent to the standard enthalpy change of reaction at absolute zero, with the standard state defined at the limit of zero coverage. The total standard enthalpy change of desorption of a monolayer of iodine at absolute zero is the integral of the change of $\Delta E(\theta,0\ K)$ with coverage. This makes $\Delta_{des}H^{\circ}$ (I(ads), 0 K) = 210 ± 20 kJ mol^{-1}. The error in $\Delta_{des}H^{\circ}$ (I(ads), 0 K) originates from the error bars in Fig. (7.7).

7.6. $\Delta_{des}H^{\circ}$ (I(ads)), $\Delta_{des}S^{\circ}$ (I(ads)) and $\Delta_{des}G^{\circ}$ (I(ads)).

In the previous section, different thermodynamic parameters for the desorption of iodine from Pt(111) have been calculated. However, these values are referred to the absolute zero. In this section the enthalpy, entropy and Gibbs free energy change of desorption are calculated at room temperature. These parameters are part of the thermodynamic sequence

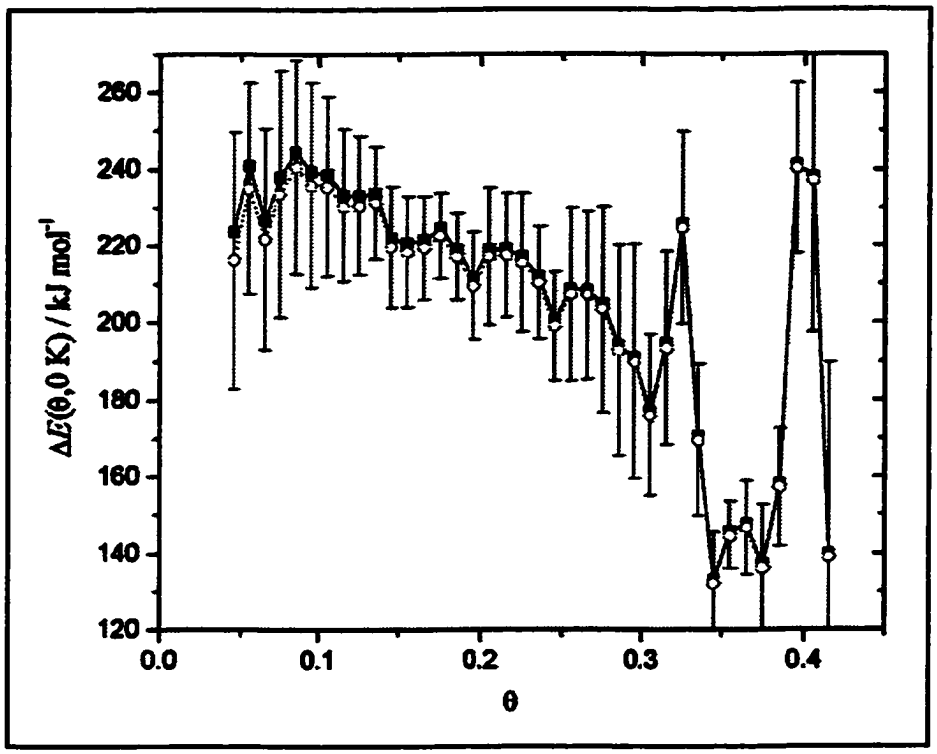

Figure 7.7: Dependence of the apparent activation energy at the absolute zero with coverage (■). The activation energy from the classical interpretation of the TDS, Fig. (7.3), is shown for comparison, (O).

in chapter 5 for the calculation of the thermodynamic parameters of the Pt(111)(3 x 3)-AgI surface compound.

The thermodynamic cycle shown in Fig. (7.8) is used. According to this cycle:

$$\begin{aligned}\Delta_{des}H^{\circ}(\mathrm{I(ads)}) = &-\left(H(\mathrm{I(ads)}, 298.15\ \mathrm{K}) - H(\mathrm{I(ads)}, 0\ \mathrm{K})\right) \\ &+ \Delta_{des}H^{\circ}(\mathrm{I(ads)}, 0\ \mathrm{K}) \\ &+ \left(H(\mathrm{I(g)}, 298.15\ \mathrm{K}) - H(\mathrm{I(g)}, 0\ \mathrm{K})\right)\end{aligned} \tag{42}$$

Similar cycles apply for $\Delta_{des}S^{\circ}$ (I(ads)) and $\Delta_{des}G^{\circ}$ (I(ads)), with relationships equivalent to those in Eq. (42).

In the next three sections $\Delta_{des}H^{\circ}$ (I(ads)), $\Delta_{des}S^{\circ}$ (I(ads)) and $\Delta_{des}G^{\circ}$ (I(ads)) are calculated. To do so, the three terms on the right hand side of Eq. (42) are estimated

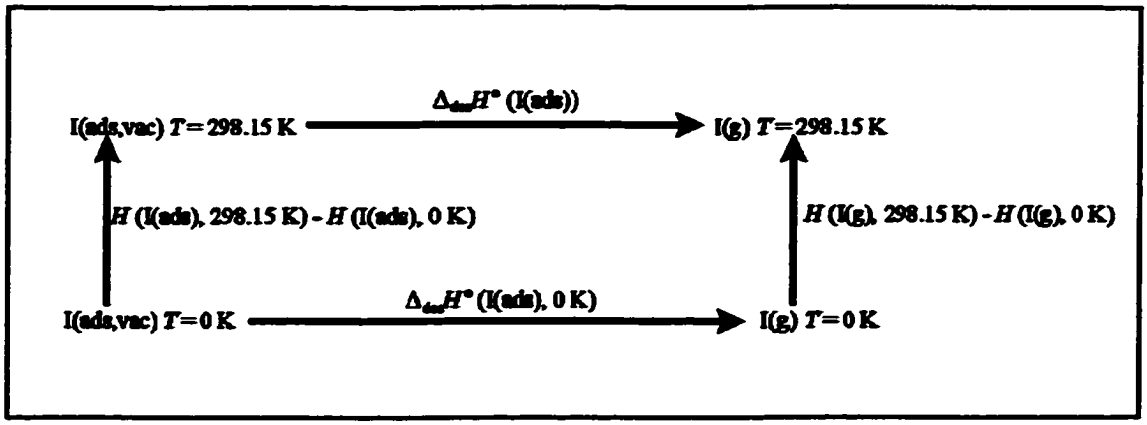

Figure 7.8: Thermodynamic cycle used to calculate $\Delta_{des}H^{\circ}$ (I(ads)).

independently.

7.6.1. Enthalpy Change of Desorption, $\Delta_{des}H^{\circ}$ (I(ads)).

Calculation of the three terms in the right hand side of Eq. (42) gives the enthalpy change of desorption of iodine.

7.6.1.1. (H(I(ads), 298.15 K) - H(I(ads), 0 K))

The adsorbed iodine is heated in this process. Since PV is negligible for a surface process, the change in internal energy ΔU can be approximated to (H(I(ads), 298.15 K) - H(I(ads), 0 K)). As seen in Eq. (43), the internal energy is related to the partition function as:

$$\Delta U = RT^2\left(\frac{\partial \ln q_{I(ads)}}{\partial T}\right) \tag{43}$$

where $q_{I(ads)}$ is calculated in the appendix, Eq. (77). Therefore:

(H(I(ads), 298.15 K) - H(I(ads), 0 K))

$$= RT^2 \frac{\partial}{\partial T}\left(-\frac{6T^2}{\theta_D^2} \int_0^{\frac{\theta_D}{T}} \left[\frac{x}{2} + \ln\left(1 - \exp(-x)\right) \right] x \, dx \right) \qquad (44)$$

This equation is evaluated numerically for $T = 298.15$ K, giving (H(I(ads), 298.15 K) - H(I(ads), 0 K)) = 7.5 ± 0.1 kJ mol^{-1}.

7.6.1.2. $\Delta_{des}H^\circ$ (I(ads), 0 K)

By means of thermal desorption spectroscopy, this value has been estimated in section 7.5 as $\Delta_{des}H^\circ$ (I(ads), 0 K) = 210 ± 20 kJ mol^{-1}.

7.6.1.3. (H(I(g), 298.15 K) - H(I(g), 0 K))

This value is tabulated directly in the NBS tables [7.12], and has a value of 6.1974 $\pm$ 0.0004 kJ mol^{-1}.

7.6.1.4. Total Enthalpy Change of Desorption.

$\Delta_{des}H^\circ$ (I(ads)) can then be calculated by substituting the three elements calculated in sections 7.6.1.1, 7.6.1.2 and 7.6.1.3 in the right hand side of Eq. (42). This gives:

$$\begin{aligned} \Delta_{des}H^\circ(\text{I(ads)}) &= -7.5 \pm 0.1 \text{ kJ mol}^{-1} + 210 \pm 20 \text{ kJ mol}^{-1} + 6.1974 \pm 0.0004 \text{ kJ mol}^{-1} \\ &= 209 \pm 20 \text{ kJ mol}^{-1} \end{aligned} \qquad (45)$$

7.6.2. Entropy Change of Desorption, $\Delta_{des}S^\circ$ (I(ads)).

As in the case of the enthalpy change of desorption, a similar thermodynamic cycle to the one in Fig. (7.8) is used. Since the entropies at 0 K are zero, the cycle simplifies to:

$$\Delta_{des}S^{\circ}(\text{I(ads)}) = S(\text{I(g)}, 298.15\ \text{K}) - S(\text{I(ads)}, 298.15\ \text{K}) \tag{46}$$

The two terms on the right hand side of this equation are evaluated independently in the next sections.

7.6.2.1. *S*(I(g), 298.15 K).

The NBS tables [5.12] lists this entropy as 180.7914 ± 0.0004 J mol^{-1} K^{-1}.

7.6.2.2. *S*(I(ads), 298.15 K).

In terms of the partition function, the entropy change for this reaction is:

$$S = \frac{U - U(0)}{T} + k \ln Q = RT\left(\frac{\partial \ln q_{\text{I(ads)}}}{\partial T}\right)_{V} + R \ln q_{\text{I(ads)}} \tag{47}$$

the entropy change becomes, after substituting the partition function from Eq. (77):

$$\begin{aligned} S(\text{I(ads)}, 298.15\ \text{K}) = RT\frac{\partial}{\partial T}\left(-\frac{6T^2}{\theta_D^2}\int_0^{\frac{\theta_D}{T}}\left[\frac{x}{2} + \ln\left(1 - \exp(-x)\right)\right]x\,dx\right) \\ + R\left(-\frac{6T^2}{\theta_D^2}\int_0^{\frac{\theta_D}{T}}\left[\frac{x}{2} + \ln\left(1 - \exp(-x)\right)\right]x\,dx\right) \end{aligned} \tag{48}$$

taking θ_D as 173 ± 50 K, and evaluating numerically at 298.15 K gives:

$$S(\text{I(ads)}, 298.15\ \text{K}) = 51 \pm 6\ \text{J mol}^{-1}\ \text{K}^{-1} \tag{49}$$

7.6.2.3. Total Entropy Change of Desorption.

The entropy change of desorption is then, after substituting in Eq. (46):

$$\begin{aligned} \Delta_{des}S^{\circ}(\text{I(ads)}) &= 180.7914 \pm 0.0004\ \text{J mol}^{-1}\ \text{K}^{-1} - 51 \pm 6\ \text{J mol}^{-1}\ \text{K}^{-1} \\ &= 130 \pm 6\ \text{J mol}^{-1}\ \text{K}^{-1} \end{aligned} \tag{50}$$

7.6.3. Gibbs Energy Change of Desorption, $\Delta_{des}G^{\circ}$ (I(ads)).

$\Delta_{des}G^{\circ}$ (I(ads)) is calculated by means of the well known thermodynamic relationship:

$$\Delta_{des}G^{\circ}(\mathrm{I(ads)}) = \Delta_{des}H^{\circ}(\mathrm{I(ads)}) - T\,\Delta_{des}S^{\circ}(\mathrm{I(ads)}) \qquad (51)$$

The enthalpy and entropy change of desorption have been calculated previously in sections 7.6.1 and 7.6.2. Therefore, substituting in Eq. (51) yields a Gibbs energy change of desorption rate as follows:

$$\begin{aligned}\Delta_{des}G^{\circ}(\mathrm{I(ads)}) &= 209 \pm 20\ \mathrm{kJ\ mol^{-1}} - 298.15\ \mathrm{K} \times 130 \pm 6\ \mathrm{kJ\ mol^{-1}\ K^{-1}} \\ &= 170 \pm 22\ \mathrm{kJ\ mol^{-1}}\end{aligned} \qquad (52)$$

7.7. Free Energy of the Surface, *A*, Internal Energy of the Surface, *U*, and Interpretation of $\Delta E(\theta,0\ \mathrm{K})$.

The dependence of the different thermodynamic parameters with temperature and iodine coverage are calculated in this section, as well as the real nature of $\Delta E(\theta,0\ \mathrm{K})$. As seen in Fig. (7.7), $\Delta E(0,0\ \mathrm{K})$ decreases from $\Delta E^{\circ}(0\ \mathrm{K}) = 255\ \mathrm{kJ\ mol^{-1}}$ at zero coverage, to 196 kJ mol^{-1} at $\theta = 0.3$. At a coverage 0.33, $\Delta E(\theta,0\ \mathrm{K})$ extrapolates to 190 kJ mol^{-1}. Therefore, the energy difference due to the interactions between $\theta = 0$ and $\theta = 0.33$ is 255 - 190 = 65 kJ mol^{-1}. At a coverage 0.33, each iodine has three I-I bonds per unit cell. Assuming that the maximum coverage on the surface is 0.33, three I-I bonds per iodine atom is the average number of bonds that are broken when all the I are desorbed from the surface. However, TDS accounts for the total number of bonds that are broken during the desorption process, not the average. Each iodine atom has six close neighbors in a triangular lattice at $\theta = 0.33$. When an iodine atom desorbs from the surface at this coverage, six bonds are broken. Therefore, the energy associated with each of these bonds is 65 / 6 kJ mol^{-1} = 11 kJ mol^{-1}. Since $\Delta E(\theta,0\ \mathrm{K})$ decreases at higher coverage, the interactions have to be repulsive, which makes $u = +11$ kJ mol^{-1}.

At coverages higher than 0.33 the plot $\Delta E(\theta,0\ K)$ versus θ begins to fluctuate, Fig. (7.7). This is because different sweep rates are probing different adsorption states and the plots of Eq. (39) are not linear in this coverage range. Hence, the following calculations in this section consider only the coverage range from 0 to 0.33. For the calculations, the coverage is taken as one for full coverage, although referred to the platinum surface the coverage is 0.33 ML. θ = 0.33 ML corresponds with a surface structure Pt(111)($\sqrt{3}$ x $\sqrt{3}$)R30°-I.

7.7.1. Numerical Solution of the Free Energy of the Surface, *A*.

An expression for the free energy of the surface was obtained in section 7.4 as:

$$A = -RTM\theta_{I\phi}\ln q_{I(ads)} - RTM\theta_{I(ads)}\ln q_{I(ads)} - M\theta_{I(ads)}\Delta E^{\circ}(0\ K) + 3uMN_A\theta_{I(ads)}^2 + RTM\left[\theta_{I(ads)}\ln\left(\theta_{I(ads)}\right) + \theta_{I\phi}\ln\left(\theta_{I\phi}\right) + \left(1-\theta_{I(ads)}-\theta_{I\phi}\right)\ln\left(1-\theta_{I(ads)}-\theta_{I\phi}\right)\right] \quad (53)$$

As seen in Eq. (53), A is a function of $\theta_{I(ads)}$ and $\theta_{I\phi}$. In previous sections the approximation $\theta_{I(ads)} >> \theta_{I\phi}$ was used, Eq. (31). However, it is possible to obtain exact numerical values of $\theta_{I(ads)}$ and $\theta_{I\phi}$ as a function of total coverage θ without the use of the previous assumption. This is done applying the following change of variables in Eq. (53):

$$\theta_{I(ads)} = \theta - \theta_{I\phi} \qquad \text{or} \qquad \theta_{I\phi} = \theta - \theta_{I(ads)} \quad (54)$$

The result of this change of variables is two equations for the free energy dependent on θ, and $\theta_{I(ads)}$ or $\theta_{I\phi}$ respectively. These free energies are denoted with the symbols $A(\theta,\theta_{I\phi})$ and $A(\theta,\theta_{I(ads)})$. Since there is always a minimum in the curve of free energy when changing the partial coverages, the partial differential of the free energy at that point will be zero. The partial coverages are then obtained from the numerical solution of the following partial

differential equations:

$$\left(\frac{\partial A(\theta,\theta_{I^{\ddagger}})}{\partial \theta_{I^{\ddagger}}}\right)_{\theta,T}=0, \longrightarrow \text{solution gives } \theta_{I^{\ddagger}} \tag{55}$$

$$\left(\frac{\partial A(\theta,\theta_{I(ads)})}{\partial \theta_{I(ads)}}\right)_{\theta,T}=0, \longrightarrow \text{solution gives } \theta_{I(ads)} \tag{56}$$

After solving numerically Eq. (55) and Eq. (56), the partial coverages of transition-state and adsorbed iodine are obtained. The change of $\theta_{I^{\ddagger}}$ with temperature at different θ is shown in Fig. (7.9). As expected, the coverage of transition-state increases at higher θ and higher temperature. However, $\theta_{I^{\ddagger}}$ is particularly small, which confirms the validity of the

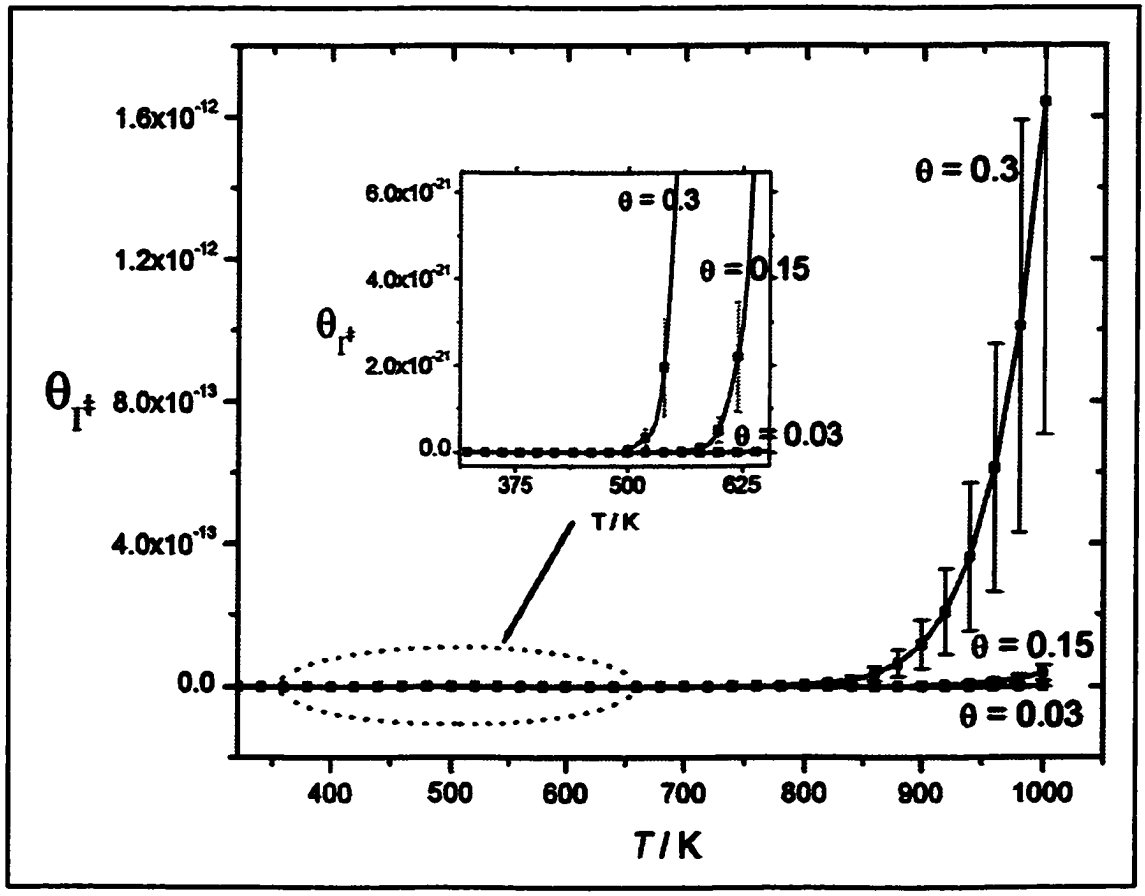

Figure 7.9: Coverage of transition state iodine at different temperatures for several total iodine coverages.

approximation in Eq (31); that is, $\theta_{I(ads)} >> \theta_{I^{\phi}}$, or $\theta \approx \theta_{I(ads)}$.

The exact values of $\theta_{I(ads)}$ and $\theta_{I^{\phi}}$ calculated can then be entered back into Eq. (53) for *A*, for variable values of *T* and θ. Fig. (7.10) shows the free energy of the surface as a function of temperature for different coverages. The Gibbs, *G*, and Helmholtz, *A*, free energy are equal since the *PV* term is negligible. According to this figure, the absolute value of the free energy increases at higher temperatures. This is due to the influence of the partition function of I(ads), which has only a vibrational component. Therefore, the vibrations are more important at higher temperature. As expected, this change is also more pronounced at higher coverages, since the partition function $q_{I(ads)}$ is multiplied by the coverage of the adsorbed iodine.

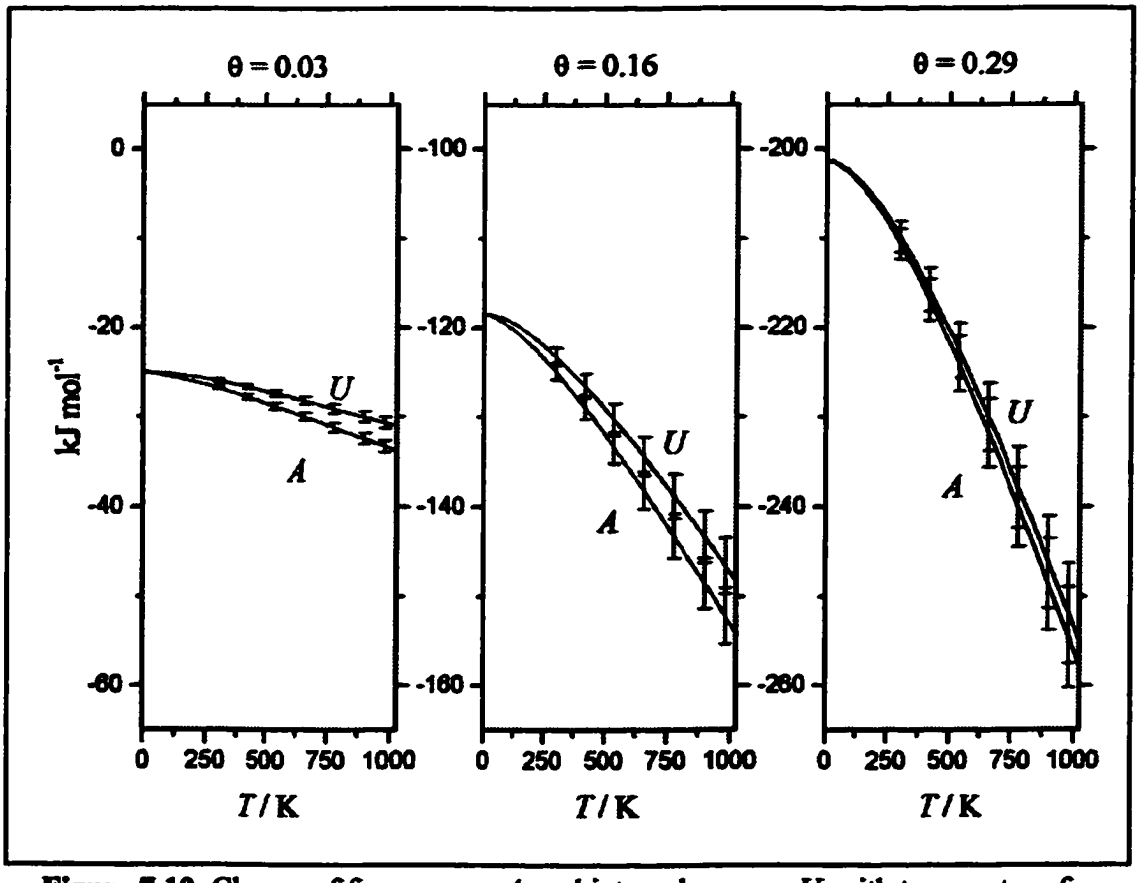

Figure 7.10: Change of free energy, *A*, and internal energy, *U*, with temperature for several iodine coverages.

It is also possible to represent the free energy as a function of coverage for different temperatures, Fig (7.11). The free energy is an extensive property. Therefore, after redefining the energy zero level, it is zero at the limit of zero coverage because there are no adsorbates on the surface. At full coverage ($\theta = 0.33$ ML), and 0 K, the free energy is -221 kJ mol^{-1}. This is consistent with the fact that there are three bonds per iodine in each unit cell, and the energy per bond is estimated as 11 kJ mol^{-1}. Therefore, at full coverage, the free energy per mol of sites is the same as $\Delta E(\theta, 0\ \text{K})$ minus the contribution of the interactions per unit cell, which is three bonds per iodine atom; that is: -255 kJ mol^{-1} + 3×11 kJ mol^{-1} = -222 kJ mol^{-1}.

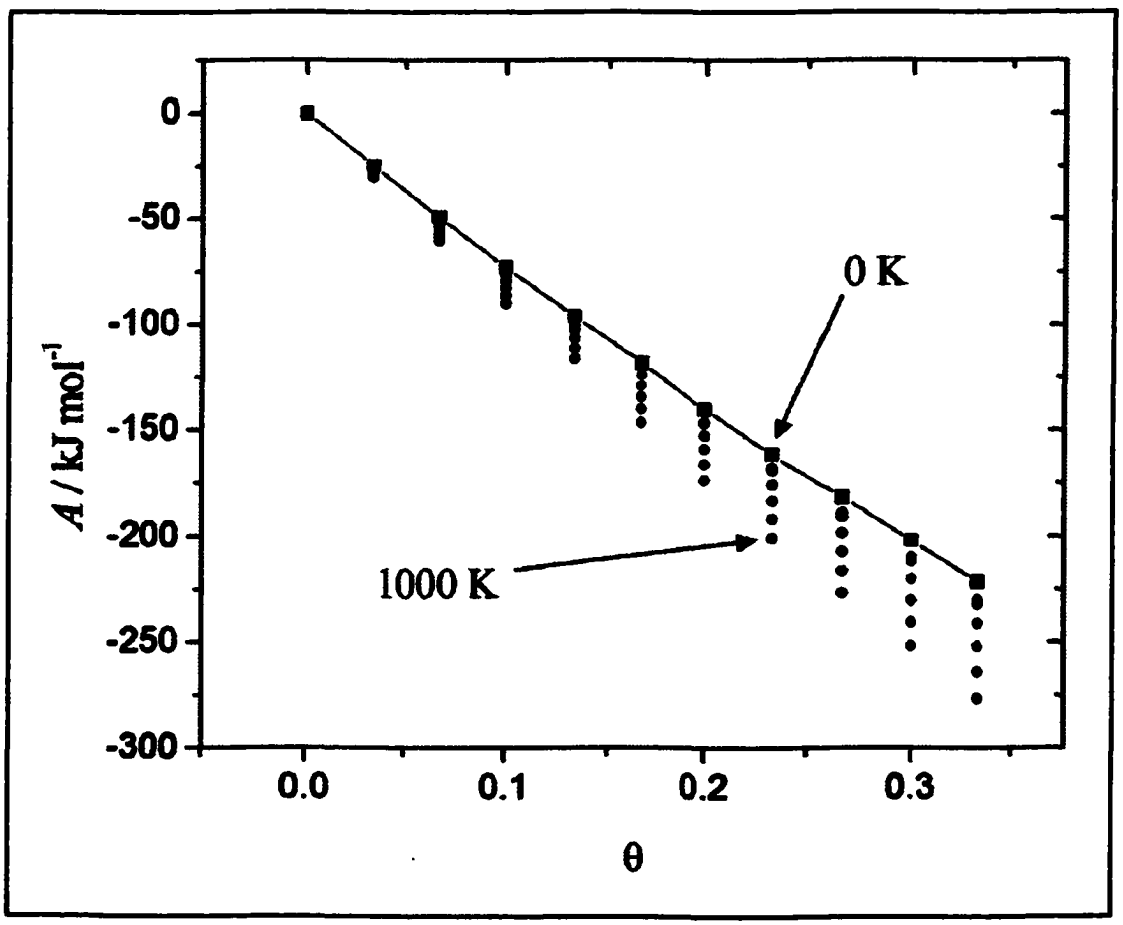

Figure 7.11: Dependence of the free energy *A* of adsorbed iodine with total iodine coverage and temperature.

7.7.2. Internal Energy of the Surface, *U*.

The internal energy is equal to:

$$U = -RTM\theta_{I_2}\ln\left(\left(\frac{kT}{h}\right)^3\frac{1}{v_\perp v_\parallel^2}\right) - RTM\theta_{I(ads)}\ln q_{I(ads)} - M\theta_{I(ads)}\Delta E^\circ(0\,K) + 3uMN_A\theta^2_{I(ads)} \quad (57)$$

The numerical solution of this equation gives the change of internal energy at different temperatures, Fig. (7.10). In this figure, the free energy is also compared with the internal energy. At absolute zero both quantities are the same, since the entropic contribution to the free energy is zero. At higher temperatures, the entropic term increases, which results in a larger difference between the internal and free energy.

7.7.3. ΔE (θ,0 K).

It has been explained how the rate of a reaction in a thermal desorption experiment is proportional to the change in partial pressure of iodine in the system. According to Eq. (6), the rate of desorption of iodine is also proportional to the coverage of the transition-state, which is calculated in Eq. (55). Therefore, ΔE(θ,0 K) can be obtained theoretically with a plot equivalent to the experimental case in section 7.5. After substituting the change in partial pressure (P) with the transition-state coverage, Eq. (38) is linearized by plotting:

$$\ln\frac{\theta_{I_2}}{T^3} - \frac{6T^2}{\theta_D^2}\int_0^{\frac{\theta_D}{T}}\left[\frac{x}{2} + \ln\left(1-\exp(-x)\right)\right]x\,dx. \text{ vs. } T^{-1} \quad (58)$$

where the slope of this plot should still be $-\Delta E(\theta,0\,K)/R$.

The change of ΔE(θ,0 K) obtained is shown in Fig. (7.12), along with the experimental values. The experimental and apparent activation energies appear in close

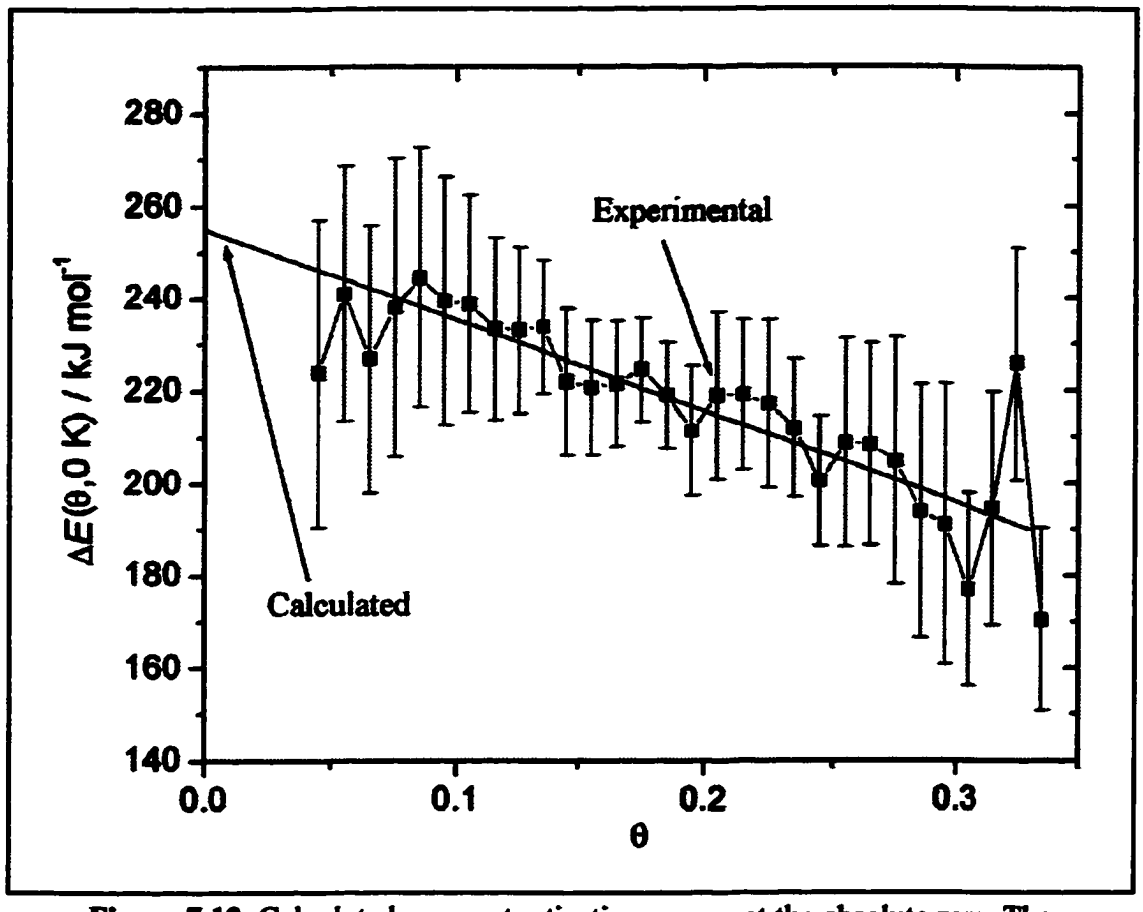

Figure 7.12: Calculated apparent activation energy at the absolute zero. The experimental data points are also included for comparison.

agreement, which confirms the validity of our model for the desorption of iodine.

7.8. TDS Simulations.

Simulations of experimental thermal desorption spectra are attempted in this section to confirm the suitability of the model of desorption proposed. Fig. (7.13) shows the thermal desorption spectra of iodine from Pt(111) for different iodine coverages. These spectra were recorded by Scott Furman at the University of Victoria, [5.1].

Since the partial pressure of desorbed species is equal to the change of iodine coverage with time, Eq. (37) becomes:

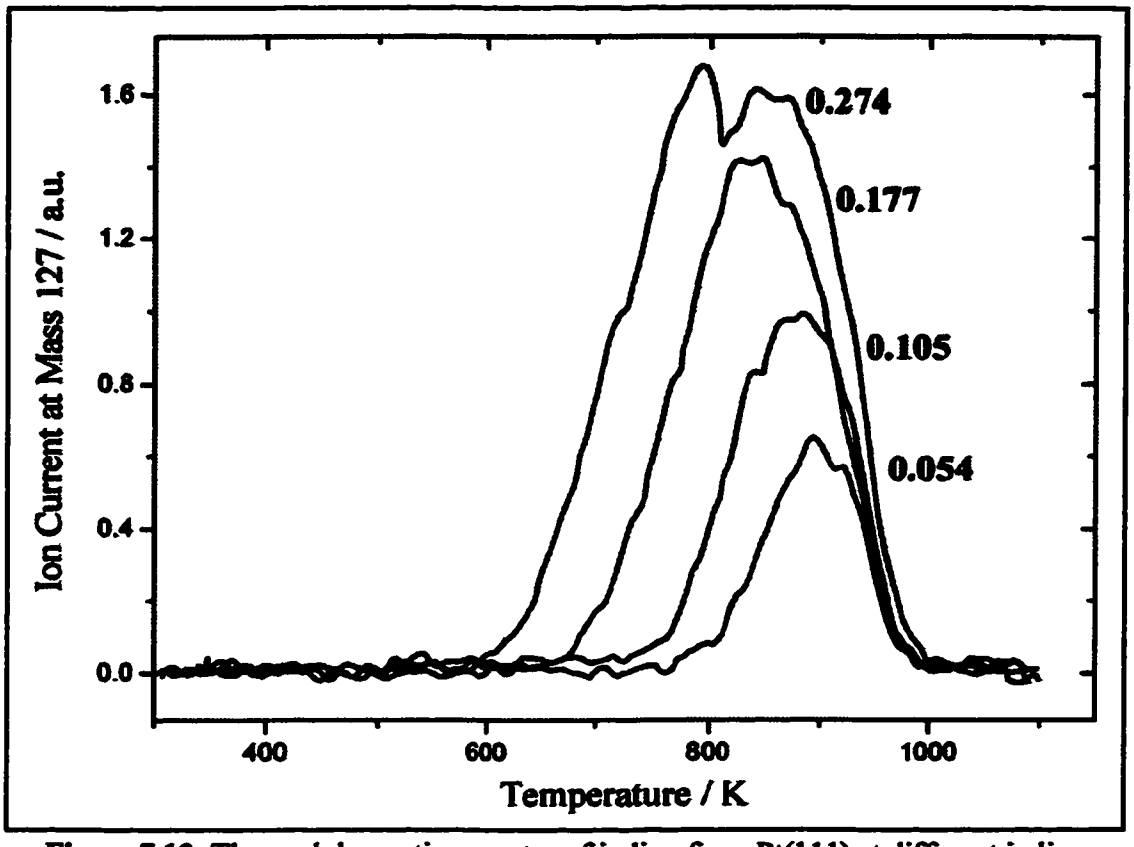

Figure 7.13: Thermal desorption spectra of iodine from Pt(111) at different iodine coverages. Heating rate: 6 K s^{-1}.

$$P = -\alpha\,\Gamma_{max}\frac{d\theta}{dt} = B\,\frac{T^3 \exp\left(-\dfrac{\Delta E°(0\,\mathrm{K})}{RT}\right)\theta\,\exp(g\theta)}{\exp\left(-\dfrac{6T^2}{\theta_D^2}\int_0^{\theta_D/T}\left[\dfrac{x}{2}+\ln\left(1-\exp(-x)\right)\right]x\,dx\right)} \qquad (59)$$

$$\text{where } B = -\alpha\,\frac{k^3\,\Gamma_{max}}{h^3\,\nu_{\parallel}^{\,2}}$$

This differential equation was solved numerically using Gear's method for stiff equations as implemented in the Maple software package. The interaction parameter g has been previously estimated as 65 kJ mol^{-1}, while $\Delta E°(0\,K)$ is estimated as 255 kJ mol^{-1}. Therefore,

the only parameters that need to be adjusted in Eq. (59) are B and the Debye temperature, θ_D. The results of the simulation for values of $B = 3.2 \times 10^6$ K^{-3} s^{-1} and $\theta_D = 200$ K are shown in Fig. (7.14). This figure shows the good agreement between the simulated and experimental TDS at different iodine coverages.

The Debye temperature calculated in these simulations is 200 K. This temperature is within the error of the θ_D proposed in the appendix of 173 ± 50 K. Therefore, no further attempts to refine parameters calculated in previous chapters were undertaken.

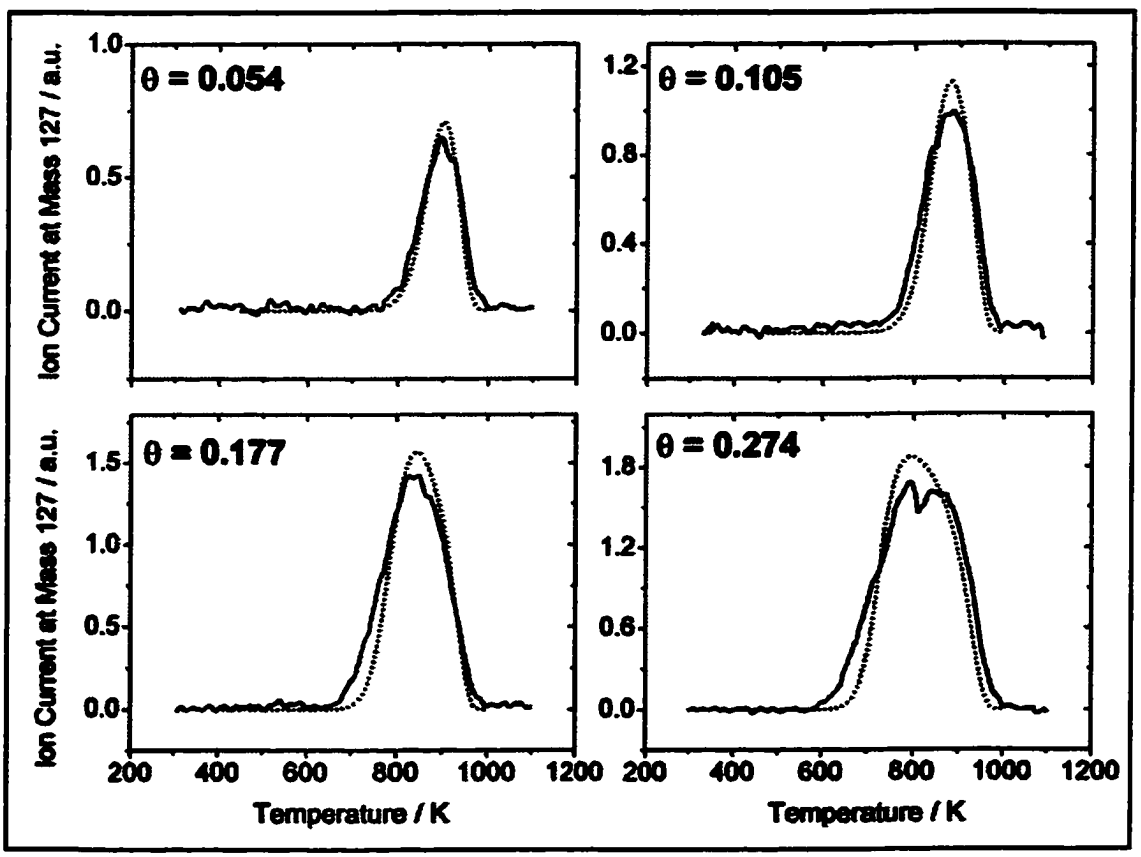

Figure 7.14: (----) Simulated and (—) experimental thermal desorption spectra of iodine from Pt(111) for different iodine coverages. Heating rate: 6 K s^{-1}.

7.9. Appendix. Statistical Thermodynamics.

The molecular partition function, q, gives an indication of the distribution of occupancy of the energy levels of a particle at a certain temperature. It is defined as:

$$q = \sum_i e^{-E_i/kT} \tag{60}$$

where i indexes the molecular energy levels, and E_i is the energy of the i^{th} energy level. The sum is taken over all the states: translational, rotational, vibrational and electronic. Assuming the total energy is a sum of these individual contributions, Eq. (60) can be rewritten as:

$$q = \sum_i e^{-\varepsilon_i^T/kT} \times \sum_i e^{-\varepsilon_i^R/kT} \times \sum_i e^{-\varepsilon_i^V/kT} \times \sum_i e^{-\varepsilon_i^E/kT} = q^T \times q^R \times q^V \times q^E \tag{61}$$

Each mode contributes independently to the overall molecular partition function.

Since the system considers only iodine atoms adsorbed on a surface, the overall partition function does not have any rotational or translational components. The only contribution to the partition function is then the electronic q^E and vibrational partition function q^V:

$$q = q^E \times q^V \tag{62}$$

7.9.1. Partition Function of the Transition-state Iodine.

The difference between the ground state $^2P_{3/2}$ and the $^2P_{1/2}$ state of atomic iodine is $8.2833 \cdot 10^{-20}$ J [7.13]. At the absolute zero $q^E = 4$, and at the highest temperature of the experiment, 1000 K, q^E is:

$$q^{E}_{1000\,K} = \sum_{i} e^{-\varepsilon_i^E/kT} = 4 + 2\cdot e^{-8.2033\cdot10^{-20}\,J/1000\,K} + \ldots \approx 4 \qquad (63)$$

However, it is unclear whether the spins in the transition-state iodine are unpaired, since the activated complex can be assumed still bound to the platinum atoms. This would make the degeneracy of the ground state, g_E, equal to 1, and, therefore, $q = q^V$. For simplicity, we assume $g_E = 1$, although a different value of g_E can be easily accommodated in the equations with a corresponding change in $\nu_\parallel$ without changing the results of the simulations.

I(g) has only three translational degrees of freedom. Treating the Pt surface as rigid, $I^\ddagger$ must also have a total of three degrees of freedom. These are all vibrational: one in the direction of the reaction coordinate with a vibrational frequency $\nu_\perp$, and two degenerate modes in directions parallel to the surface with a vibrational frequency $\nu_\parallel$. The vibrational frequency of the degenerate modes of $I^\ddagger$ is low, and it is assumed to be at least 10 times smaller than for I(ads). Therefore, it is reasonable to treat them in the harmonic approximation.

In the harmonic approximation, the vibrational partition function for these degrees of freedom are expressed as:

$$q^V_{I^\ddagger} = \frac{1}{1-\exp\left(-\frac{h\nu_\perp}{kT}\right)} \cdot \frac{1}{\left(1-\exp\left(-\frac{h\nu_\parallel}{kT}\right)\right)^2} \qquad (64)$$

Since the Pt-$I^\ddagger$ bond is so weak, $h\nu_\perp << kT$. The vibrational modes parallel to the surface can be considered bending modes of the Pt-Pt-$I^\ddagger$ "molecule". Therefore, $\nu_\parallel < \nu_\perp$ and the approximation $h\nu_\parallel << kT$ is also valid. The vibrational partition function is then:

$$q^V_{I^\ddagger} \approx \frac{kT}{h\nu_\perp} \cdot \left(\frac{kT}{h\nu_\parallel}\right)^2 \qquad (65)$$

Since the vibrational partition function is the overall molecular partition function of the transition-state iodine, then:

$$q_{t^\ddagger} = \left(\frac{kT}{h}\right)^3 \frac{1}{\nu_\perp \nu_{||}^2} \tag{66}$$

7.9.2. Partition Function of the Adsorbed Iodine.

In the case of adsorbed iodine, $q = q^V$. The harmonic approximation can not be made directly for individual adsorbed I atoms, since the iodine atoms are close packed and interacting with each other. Instead, cooperative vibrations of the I(ads) lattice must be considered. Quantum theories of lattice heat capacity explain vibrational motions in solids (three dimensions). The two main theories developed to account for this effect are the Einstein and Debye models. In this section, these two models are modified to explain lattice vibrations of surfaces (two dimensions), and the dependence of the heat capacities with temperature is used to assess the validity of each model.

7.9.2.1. Einstein Model.

In the Einstein model, each atom is a discrete oscillator with the vibrational energy levels distributed evenly in energy, $h\nu_E$ being the separation between the levels. All the particles on the surface vibrate independently with the same vibrational frequency, ν_E, Fig. (7.15.a). These three degenerate vibrational motions are explained according to the harmonic oscillator model. The vibrational partition function for a three dimensional harmonic oscillator is given by [7.14]:

$$q^V = \left(1 - \exp\left(-\frac{\theta_E}{T}\right)\right)^{-3} \tag{67}$$

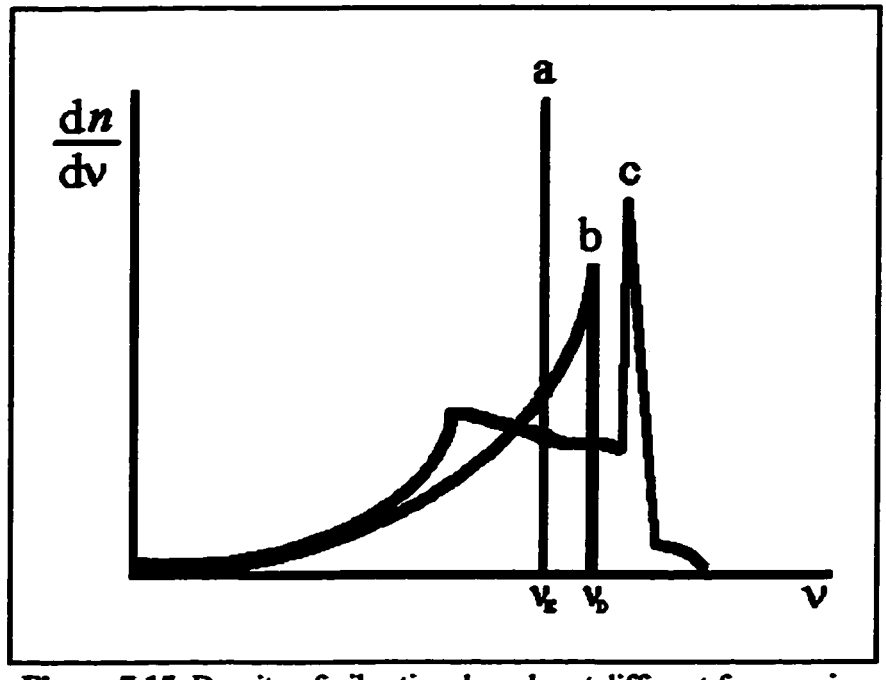

Figure 7.15: Density of vibrational modes at different frequencies for: a) Einstein model, b) Debye model and c) Typical lattice.

θ_E is the Einstein characteristic temperature. It is defined as $\theta_E = h\nu_E/k$, and gives an indication of the stiffness of the lattice. The crystal is more rigid at higher Einstein temperatures. q^V can be approximated to the overall partition function q, Eq. (63), from which the heat capacity, C_v, can be derived:

$$C_V = \left(\frac{\partial U}{\partial T}\right)_V = \frac{\partial}{\partial T}\left[kT^2 \frac{\partial \ln q^N}{\partial T}\right]_V \tag{68}$$

where N is the total number of particles. After substituting q^V for three dimensions from Eq. (67) into Eq. (68), the heat capacity becomes:

$$C_V = 3Nk\left(\frac{\theta_E}{T}\right)^2 \frac{\exp\left(-\frac{\theta_E}{T}\right)}{\left(\exp\left(-\frac{\theta_E}{T}\right)-1\right)^2} \tag{69}$$

The change of the heat capacity with temperature is shown in Fig.(7.16), where there is a poor agreement between the theory and the experimental.

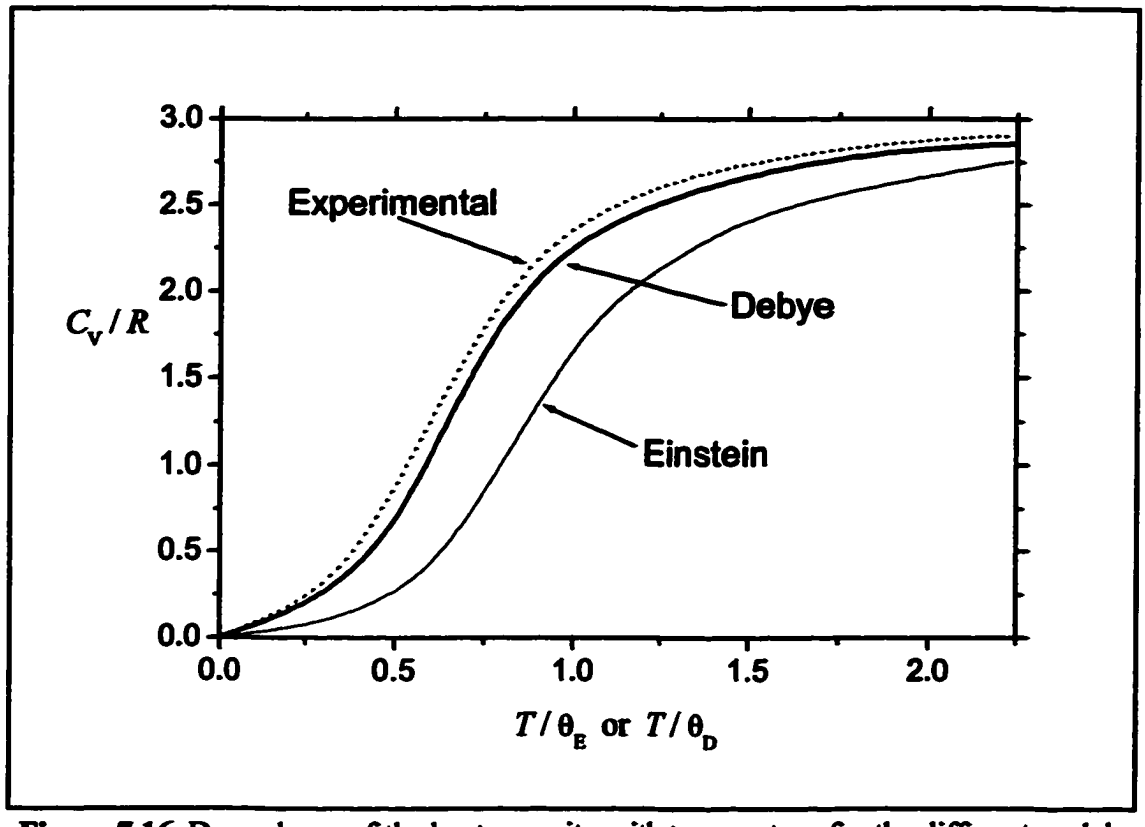

Figure 7.16: Dependence of the heat capacity with temperature for the different models of lattice vibration.

7.9.2.2. Debye Model.

The Debye model is a modification of the Einstein model. In this model the vibrations of the atoms are coupled. Therefore, the vibrations are treated as elastic waves that travel through the crystal. The particles vibrate with a range of frequencies that varies from 0 to a cutoff frequency, ν_D, called the Debye frequency, Fig.(7.15.b), which relates to the Debye temperature, θ_D, by $\theta_D = h \cdot \nu_D / k$. The Debye temperature is a parameter equivalent to θ_E for the Einstein model. θ_D gives an indication of the stiffness of the lattice, being more rigid at higher Debye temperatures. It is also described as the temperature corresponding to the cutoff frequency of the vibrational modes of the Debye model, Fig. (7.15).

According to this model, the vibrational partition function for a solid is [7.15]:

$$q^{v} = \exp\left(- \int_0^{v_0} \frac{f(v)}{N} \left[\frac{hv}{2kT} + \ln\left(1 - \exp\left(- \frac{hv}{kT} \right) \right) \right] dv \right) \tag{70}$$

where the apparent molecular partition function is defined in terms of the canonical partition function, Q, $q = Q^{1/N}$ for N particles. $f(v)$ is the frequency distribution function. It represents the normal vibration spectrum of a solid, with its integral giving the total number of vibrations in a frequency range. $f(v)$ is defined for a three dimensional solid with N particles and $3N$ vibrational modes as [7.14]:

$$f_{3D}(v) = \frac{9 N v^2}{v_D^3} \tag{71}$$

which makes the vibrational partition function in three dimensions:

$$q_{3D}^{v} = \exp\left(- \int_0^{v_0} \frac{9 v^2}{v_D^3} \left[\frac{hv}{2kT} + \ln\left(1 - \exp\left(- \frac{hv}{kT} \right) \right) \right] dv \right) \tag{72}$$

approximating ${q_{3D}}^{v}$ to the overall molecular partition function, and substituting into Eq. (68) gives the heat capacity of the solid. Analytically this is a much more complicated function than in the case of the Einstein model. The behavior of C_v with changing temperature is shown in Fig. (7.16). The results predicted with this theory are in agreement with the experiment, which justifies the use of the Debye model as a valid model for lattice vibrations.

Since adsorbed iodine is a surface compound, the function $f(v)$ from the vibrational partition function has to be defined for a two dimensional surface. For N surface atoms with $3N$ vibrational modes, $f(v)$ is defined as [7.15]:

$$f(v) = \frac{6 N v}{v_D^2} \tag{73}$$

and after substituting in Eq. (70), the vibrational partition function of the surface becomes:

$$q^{V} = \exp\left(- \frac{6}{\nu_D^2} \int_0^{\nu_D} \left[\frac{h\nu}{2kT} + \ln\left(1 - \exp\left(- \frac{h\nu}{kT} \right) \right) \right] \nu \, d\nu \right) \tag{74}$$

It is assumed that the overall partition function for the iodine adsorbed on the surface is then the vibrational partition function from the Debye model. Thus:

$$q_{I(ads)} = \exp\left(- \frac{6}{\nu_D^2} \int_0^{\nu_D} \left[\frac{h\nu}{2kT} + \ln\left(1 - \exp\left(- \frac{h\nu}{kT} \right) \right) \right] \nu \, d\nu \right) \tag{75}$$

We can then change variables in this equation as follows:

$$x = \frac{h\nu}{kT}, \qquad dx = \frac{h}{kT} d\nu, \qquad x_D = \frac{h\nu_D}{kT} = \frac{\theta_D}{T} \tag{76}$$

This change of variables transforms the partition function into:

$$q_{I(ads)} = \exp\left(- \frac{6T^2}{\theta_D^2} \int_0^{\frac{\theta_D}{T}} \left[\frac{x}{2} + \ln\left(1 - \exp\left(- x \right) \right) \right] x \, dx \right) \tag{77}$$

where the only unknown parameter is the Debye temperature. θ_D is now estimated.

7.9.2.1.1. Debye Temperature.

According to the Debye model, at moderate temperatures the mean-square displacement of atoms during the vibrations, $\langle u^2 \rangle$, is inversely proportional to the square of the Debye temperature:

$$\langle u^2 \rangle = \frac{3h^2 T}{m k \theta_D^2} \tag{78}$$

where m is the atomic mass. Assuming that the mean-square displacement of the iodine atoms adsorbed is the same as the platinum atoms on the surface [7.16], then:

$$\theta_{D,I(ads)} = \sqrt{\frac{m_{Pt} \cdot \theta_{D,Pt}^2}{m_I}} \tag{79}$$

Since the desorption of iodine from Pt(111) is a surface process, it is necessary to use the surface Debye temperature, instead of the bulk Debye temperature for a solid. The bulk Debye temperature for platinum has been estimated as 234 ± 10 K [7.17][7.18]. However, there is no consensus about the surface Debye temperature for the Pt(111) face, as several values have been reported. Calculations based on Low Energy Electron Diffraction measurements predict a surface θ_D of 111 ± 10 K [5.17]; theoretical calculations based on different oscillator models report 174 K [5.20]; and calculations based on atomic helium scattering state a value of 145 K [7.19]. They all agree, however, that due to the asymmetry of forces on the surface, the surface Debye temperature is estimated to be 40 to 80% of the bulk Debye temperature [7.20][7.21]. Therefore, since the bulk Debye temperature is estimated as 234 ± 10 K, the surface θ_D for Pt(111) is taken conservatively as 143 ± 42 K. Applying Eq. (79) then gives the surface θ_D for iodine atoms adsorbed on Pt(111) as θ_D = 173 ± 50 K.

7.9.3. Vibrational Frequencies.

The surface Debye temperature for I(ads) is estimated as 173 ± 50 K. According to the Debye model, this corresponds with a vibrational frequency for I(ads) of ν = 120 ± 35 cm^{-1}. It is assumed that the vibrational energy of $I^{\ddagger}$ in the direction of the reaction coordinate is 10 times lower than for I(ads), which makes $\nu_{\perp}$ = 12 cm^{-1}. The vibrational frequency in the direction parallel to the surface is also unknown. However, according to the relationship $\nu_{\parallel} < \nu_{\perp}$, it is assigned conservatively a frequency of $\nu_{\parallel}$ = 8 cm^{-1}.

Chapter 8

Thallium Electrodeposition on Pt(111)(√7 x √7)R19.1°-I.

8.1. Introduction

An understanding of the interaction of anionic species such as iodine on electrodeposition processes might enable an enhancement of the electrocatalytic properties of surfaces. In previous chapters silver adsorption on iodine covered Pt surfaces has been studied. This chapter is the first step in adopting the methodology acquired during the study of the Pt-AgI system to other systems such as Pt-TlI.

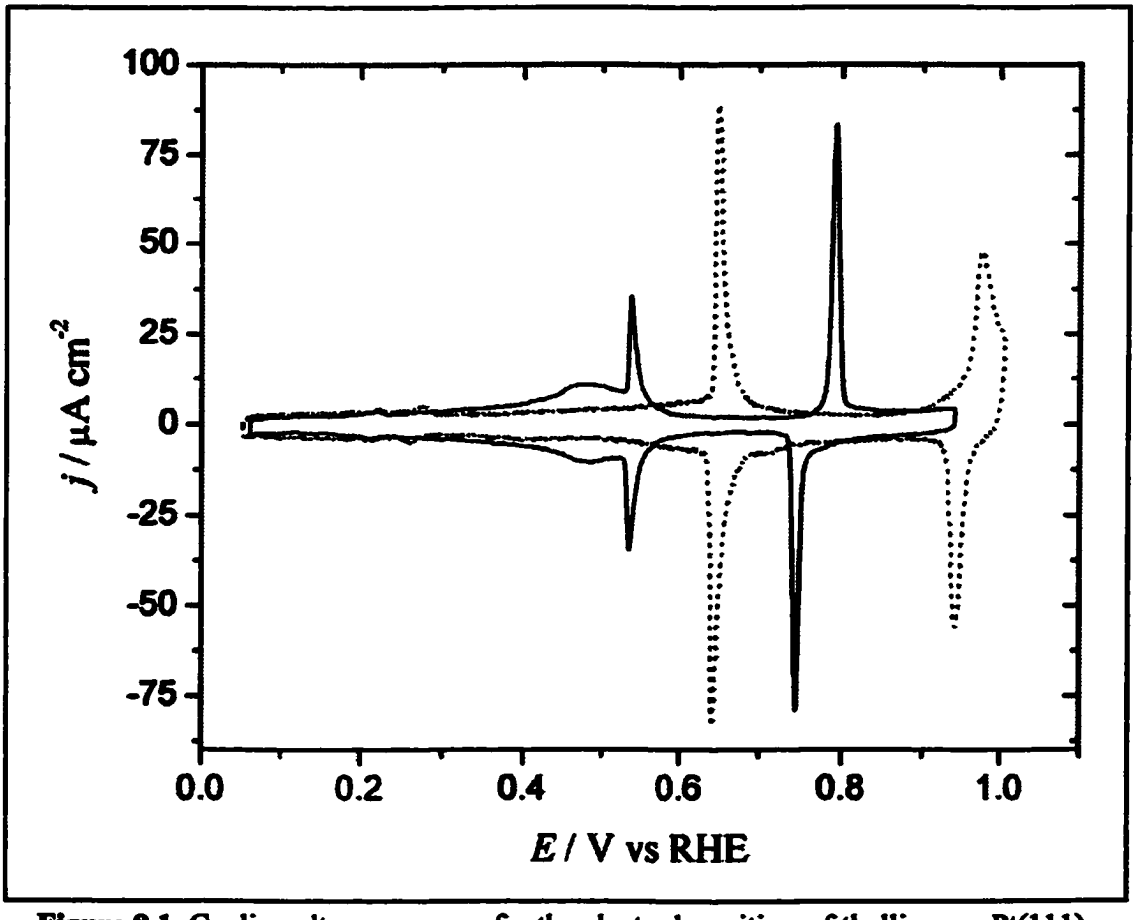

Figure 8.1: Cyclic voltammograms for the electrodeposition of thallium on Pt(111). Sweep rate = 20 mV s^{-1}. $[Tl^+]$ = 1 mM, (—) 0.1 M H_2SO_4, (.....) 0.1 M $HClO_4$.

The cyclic voltammograms for the electrodeposition of Tl^+ on Pt(111) are shown in Fig. (8.1), and agree with voltammograms previously reported [8.1][8.2][8.3]. The voltammogram for Tl^+ deposition in H_2SO_4 resembles the voltammogram for H^+ in sulfuric acid solution, Fig (2.10), in the commonly named "butterfly peak" at + 0.532 V vs RHE[1]. This resemblance has been exploited to acquire a further understanding of one of the traditional problem in electrochemistry, the adsorption of hydrogen on platinum surfaces [8.1]. As well, further research in the area of anion interactions such as HSO_4^- and ClO_4^- on Pt has been accomplished using this system [8.2].

8.2. Cyclic Voltammetry for UPD on Thallium on Pt(111)($\sqrt{7}$ x $\sqrt{7}$)R19.1°-I.

The voltammograms of thallium UPD on Pt(111)($\sqrt{7}$ x $\sqrt{7}$)R19.1°-I in H_2SO_4 and $HClO_4$ solution are shown in Figs. (8.2) and (8.3) respectively. The first sweep of the voltammogram is similar in either H_2SO_4 or $HClO_4$, which shows that electrolyte plays very little role. This sweep shows four cathodic peaks (C1...C4), Fig. (8.2.a and 8.3.a). Sweep-hold experiments around these peaks do not show signs of a NGC mechanism. The peak potentials are calculated by extrapolating to 0 mV s^{-1} from data at different sweep rates. The potentials of these peaks are + 0.408, 0.329, 0.176 and 0.080 V respectively. These peaks are irreversible and disappear in the following cycles. After cycling for at least 30 minutes, all the features of the first cycle of the voltammogram disappear. The new features correspond to the cyclic voltammograms for the deposition of thallium on Pt(111) in the absence of iodine, Fig. (6.1). Accordingly, the iodine desorbs from the surface during the

[1] In this chapter all potentials refer to the RHE.

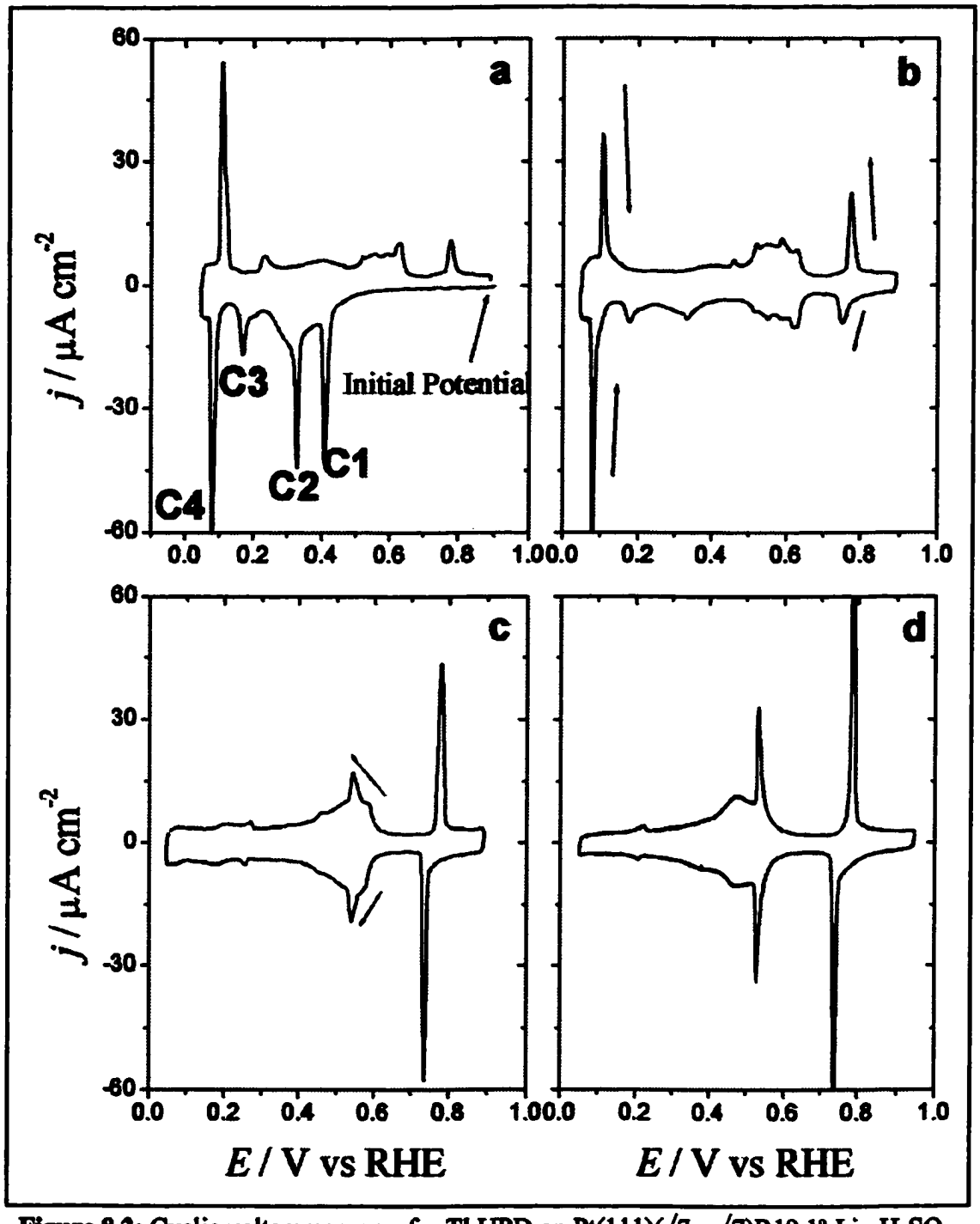

Figure 8.2: Cyclic voltammograms for Tl UPD on Pt(111)($\sqrt{7}$ x $\sqrt{7}$)R19.1°-I in H_2SO_4. $[Tl^+]$ = 1 mM. $[H_2SO_4]$ = 0.1 M. Sweep rate = 20 mV s^{-1}. a) 1st cycle, b) 2nd cycle, c) 5th cycle and d) 50th cycle.

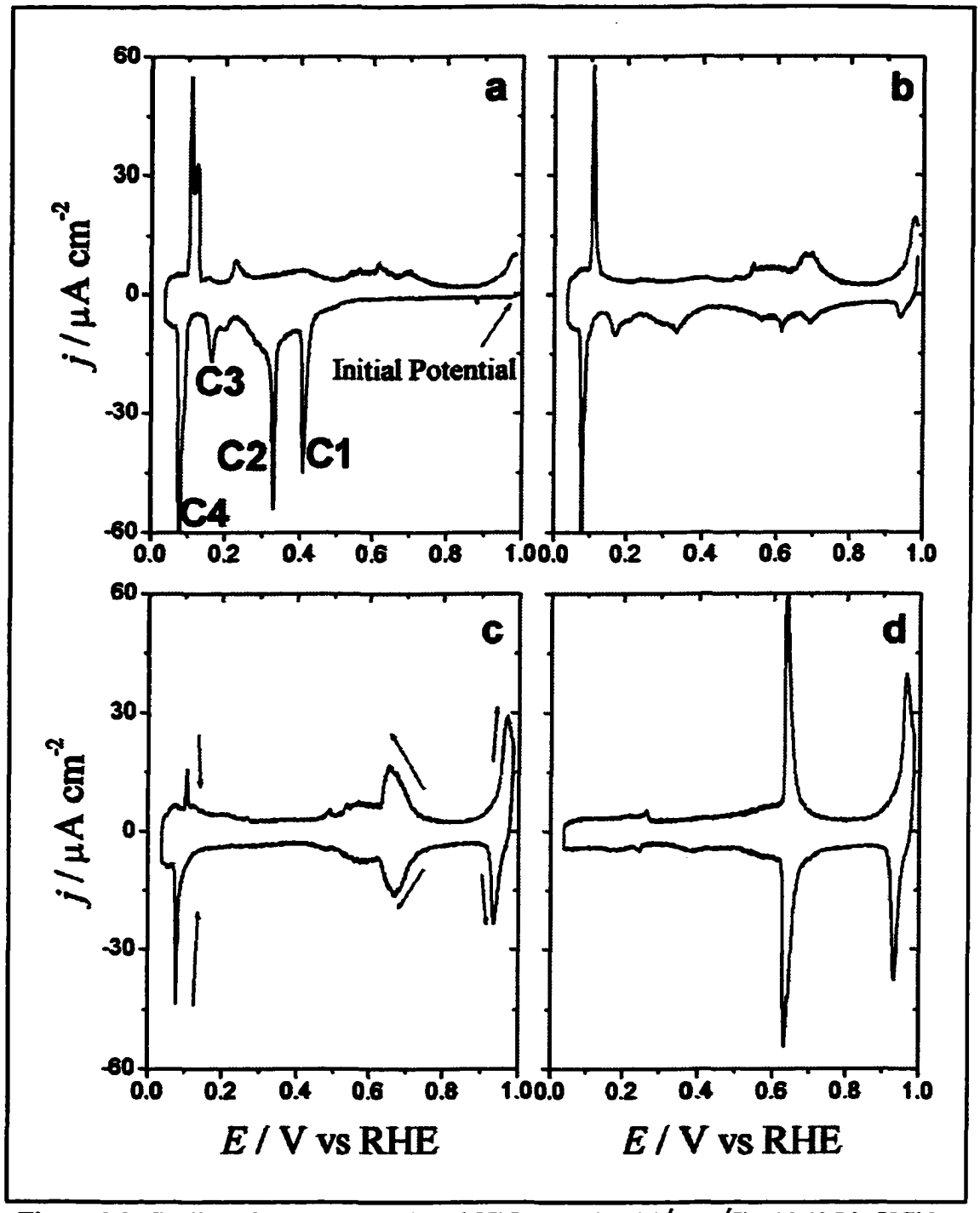

Figure 8.3: Cyclic voltammograms for Tl UPD on Pt(111)($\sqrt{7}$ x $\sqrt{7}$)R19.1°-I in $HClO_4$. $[Tl^+]$ = 1 mM. $[HClO_4]$ = 0.1 M. Sweep rate = 20 mV s^{-1}. a) 1st cycle, b) 2nd cycle, c) 5th cycle and d) 50th cycle.

cycles of Tl UPD on Pt(111)($\sqrt{7}$ x $\sqrt{7}$)R19.1°-I, giving a clean and ordered Pt(111) surface. This surface does not suffer reconstruction during the electrodeposition.

In order to estimate how much thallium is deposited on the surface, it is necessary to determine in what form the iodine is released from the surface, e.g. I_2, TlI, TlI_2^-. A sweep-hold experiment is suitable for this estimation, Fig. (8.4). Starting from the Pt(111)($\sqrt{7}$ x $\sqrt{7}$)R19.1°-I at + 0.9 V, the potential is swept in the negative direction down to + 0.05 V. At this point, the potential is held for as long as it is required to completely remove the iodine from the surface, namely, 3 minutes, Fig. (8.4.a). The following cycles after holding the potential are then the UPD of thallium on bare Pt(111), Fig. (8.4.b).

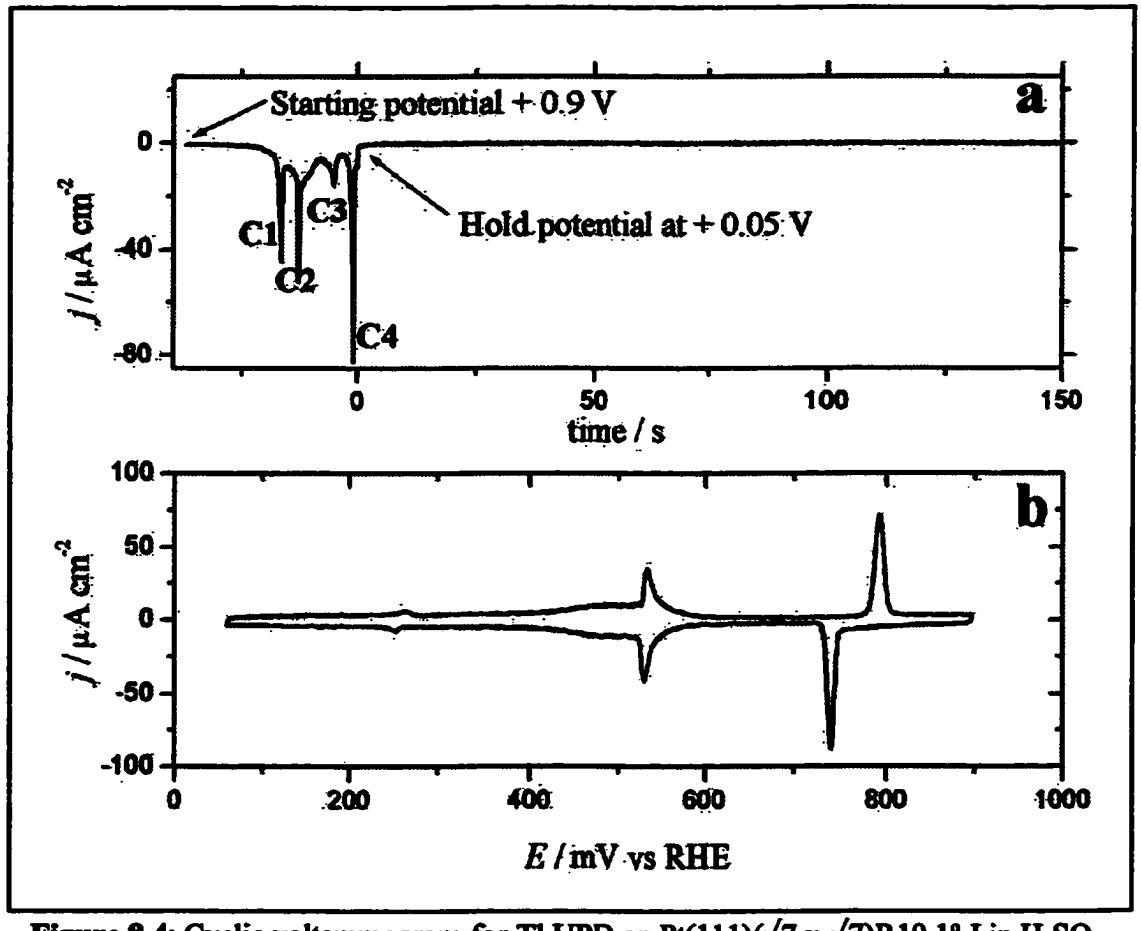

Figure 8.4: Cyclic voltammogram for Tl UPD on Pt(111)($\sqrt{7}$ x $\sqrt{7}$)R19.1°-I in H_2SO_4. $[Tl^+]$ = 1 mM. $[H_2SO_4]$ = 0.1 M. Sweep rate = 20 mV s^{-1}. a) Sweep-hold experiment for the first sweep, b) Following cycles.

Integration of the voltammogram in Fig. (8.4.a) gives the charge that passes through the electrode during the UPD process. The charge is 270 $\mu C\ cm^{-2}$, including the charge that passed during the time the potential was held at + 0.05 V, and corrected for double layer charging. The double-layer charging baseline Fig. (8.5), was obtained from impedance measurements, as discussed in more detail in the next section.

After holding the potential at the end of the first cathodic sweep, the surface is free of iodine. At this potential the thallium has a close-packed hexagonal structure [8.2][8.4].

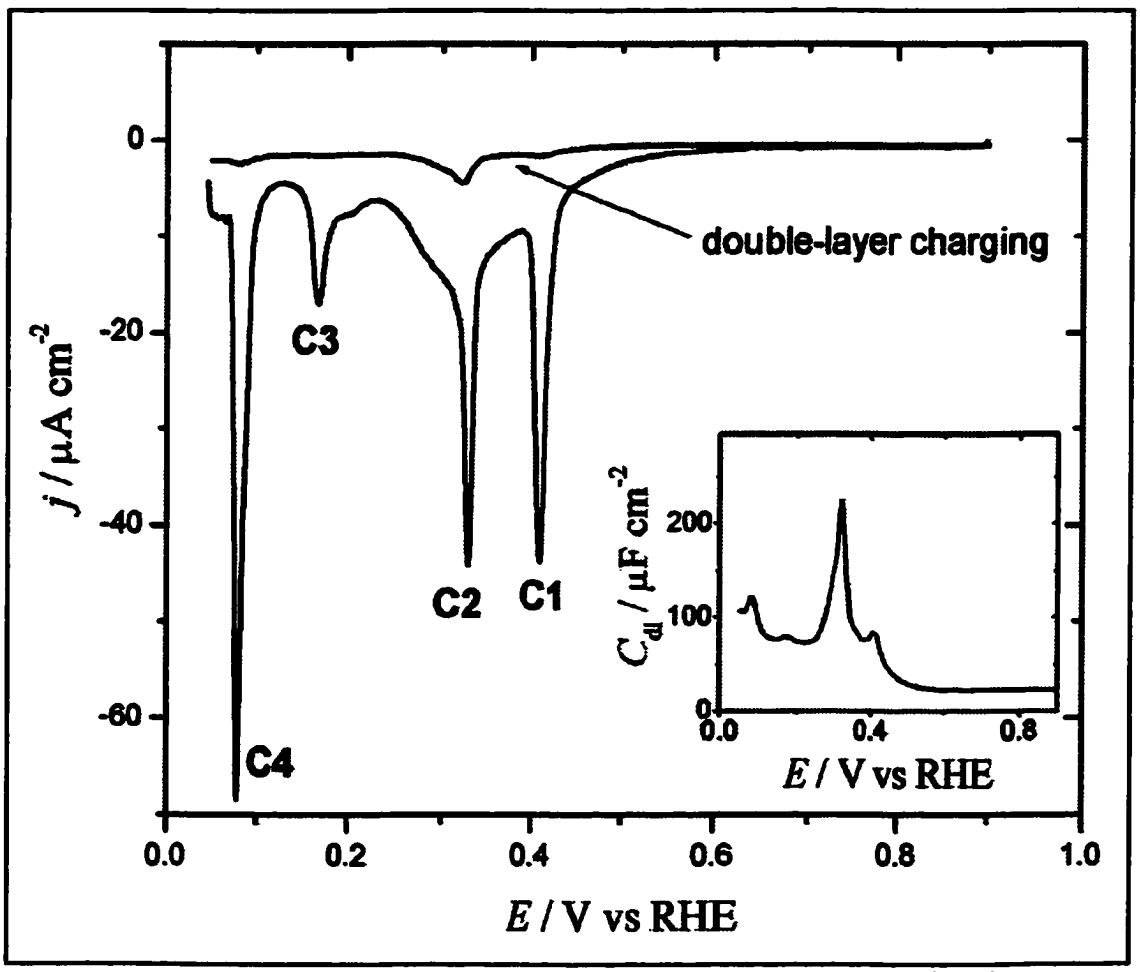

Figure 8.5: First cycle of the cyclic voltammogram for Tl UPD on Pt(111)($\sqrt{7}$ x $\sqrt{7}$)R19.1°-I in H_2SO_4, together with the baseline for the double layer charging obtained with single frequency A.C. voltammetry: 0.5 mV rms, 2000 Hz. Insert: Double layer capacitance for the first sweep. $[Tl^+] = 1$ mM. $[H_2SO_4] = 0.1$ M. Sweep rate = 20 mV s^{-1}.

The maximum coverage for a close-packed hexagonal phase of Tl corresponds to 0.66 ML, in agreement with the Tl coverage measured with Surface X-ray Scattering (SXS) in H_2SO_4 at + 0.1 V [8.2]. Assuming that thallium and iodine desorb as TlI, the difference between the total coverage for the thallium deposited, 270 $\mu C\ cm^{-2}$ or 1.12 ML, and the coverage of the remaining thallium at the end of the cycle, 0.66 ML, corresponds to how much thallium came off the surface at the same time as the iodine desorption, i.e., the equivalent of 1.12 - 0.66 = 0.46 monolayers.

A ($\sqrt{7}$ x $\sqrt{7}$)R19.1°-I surface structure on Pt(111) corresponds with a coverage of 0.43 of a monolayer. This coverage matches the coverage of thallium desorbed from the surface. Therefore, it is reasonable to assume that the same amount of iodine and thallium come off the surface during the time the iodine desorbs. Whether the species released is Tl-I or Tl^+, I^- is still unknown.

In the following sections of this chapter, an attempt is made to explain some of the features of the voltammogram, Fig. (8.2.a and 8.3.a), focusing primarily on the first deposition peak.

8.2.1. A.C. Impedance and Integration Baselines.

The exact value of the integration charge of the voltammogram is critical in order to assign different surface structures to the processes associated with each peak of the voltammogram. Subtracting the charge associated with the charging of the double layer from the total charge of the voltammogram gives the charge due only to the faradaic process. The traditional way for obtaining the baseline is a linear extrapolation of the region of potential where there is no faradaic process. However, a straight baseline in the

voltammograms implies a constant double layer capacitance, despite the phase transformations and changes on the surface. This seems unlikely; therefore, a calculation of the double layer capacitance is required.

As explained in section 2.3.2, the change of C_{dl} with potential was calculated by means of either single frequency A.C. voltammetry, fitting the results to the equivalent circuit:

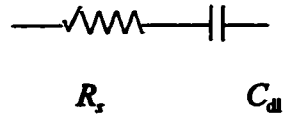

(1)

or multi-frequency A.C. voltammetry, and fitting the results to the equivalent circuit:

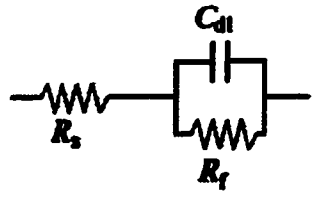

(2)

Fig. (8.5) shows the C_{dl} obtained with single frequency A.C. voltammetry for the first sweep of Tl electrodeposition on Pt(111)($\sqrt{7}$ x $\sqrt{7}$)R19.1°-I. Some of the peaks of the C_{dl} seem to track the main features of the cyclic voltammogram. This suggests a relationship between C_{dl} and the faradaic resistance, R_f.

A relationship between C_{dl} and the faradaic current is contrary to the classical interpretation of double layer capacitance, where C_{dl} is independent of any faradaic process [8.5][8.6][8.7][8.8]. However, correlations of C_{dl} with the faradaic process have been observed for other systems such as Pt oxidation [8.9][8.10], and hydrogen UPD on several

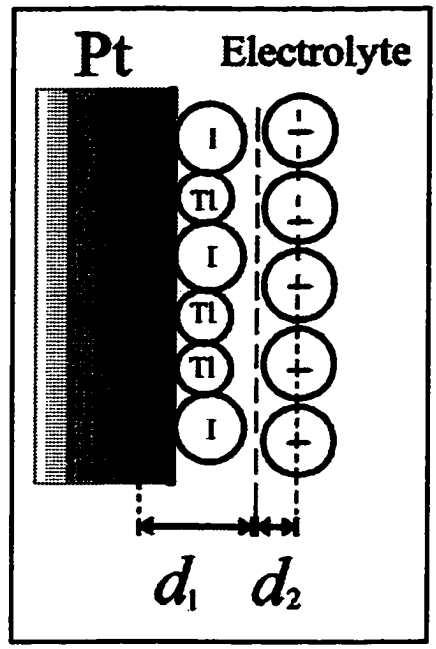

Figure 8.6: Simple double layer model.

Pt single crystals [8.11]. We suggest, therefore, that under certain conditions there is an interdependence between C_{dl} and R_f, which plays a bigger role for the electrochemical reaction than is commonly assumed. Further research is needed in this area to assert the true nature, and for what type of processes this relationship is significant.

A certain dependence of the double layer capacitance with the rate of the faradaic process, however, can be explained with the help of a simple model of the double layer. Consider the interface as a layer of uncharged Tl and I adsorbed on the Pt surface, Fig. (8.6). From Gauss' law, the potential drop at the interface is:

$$\Delta V = \frac{\sigma d_1}{\varepsilon_1(\Gamma)} + \frac{\sigma d_2}{\varepsilon_2} \qquad (3)$$

where σ is the charge at the surface of the electrode and d_1 and d_2 are the distances of the layers shown in Fig. (8.6). $\varepsilon_1(\Gamma)$ and ε_2 are the permittivities of the Tl-I layer and electrolyte

respectively. Since the structure of the Tl-I layer changes during the different peaks in the voltammogram, the permittivity in this layer can be assumed dependent on the surface concentration of Tl and I on the surface (Γ).

The double layer capacitance is then:

$$C_{dl} = \frac{d\sigma}{d\Delta V} = \frac{1}{\frac{d_1}{\varepsilon_1(\Gamma)} + \frac{d_2}{\varepsilon_2}} \qquad (4)$$

Therefore, a change in $\varepsilon_1(\Gamma)$ due to adsorption of Tl on the surface brings a change of double layer capacitance. It is possible that under certain conditions during an electrochemical reaction, $\varepsilon_1(\Gamma)$ changes in a certain way that makes C_{dl} track the peaks in the voltammogram.

Another important feature of the C_{dl} shown in Fig. (8.5) are the high values of capacitance in the potential region of the deposition peaks C1 to C4. Traditionally, it is assumed that C_{dl} ranges from 10 to 40 μF cm^{-2}. However, high values of C_{dl} have been also previously reported for systems such as hydrogen UPD on Pt(111) in neutral solution [8.12], or Tl UPD on Ag(100) and Ag(110) [8.13].

The existence of fast processes that take place faster or at the same time scale as the charging of the double layer could explain high apparent values of C_{dl}. However, the R_s calculated would have a contribution from the fast process, since the equivalent circuit used for the fitting would not be the one shown in equation (1). This would make R_s track the different peaks of the voltammogram. Fig. (8.7) shows the same C_{dl} from Fig. (8.5), together with R_s. One of the features of this figure is that R_s does not track the voltammogram. On the other hand, in this experiment R_s varies from 7.1 to 7.5 Ω cm^2 at different potentials, which seems too small a change to explain the presence of a fast process. Therefore, that fact that R_s does not track the peaks of the voltammogram, and the small change of R_s with

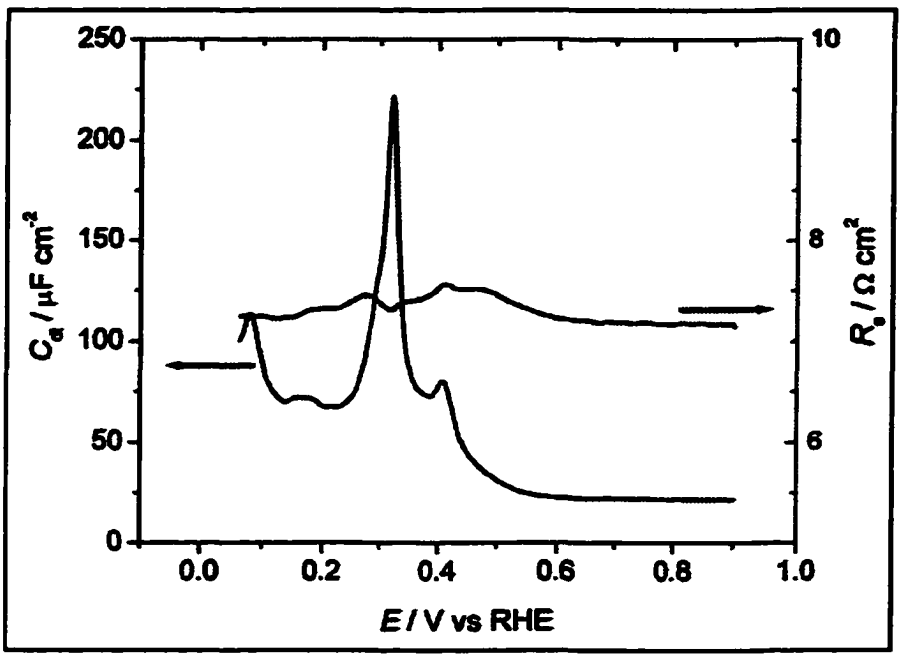

Figure 8.7: C_{dl} and R_s for the same conditions as in Fig. (8.5).

potential suggests that the measured C_{dl} is due only to the capacitance of the double layer.

8.3. Peak C1: First Cathodic Peak for the UPD of Tl on Pt(111)(√7 x √7)R19.1°-I.

Starting from a Pt(111)(√7 x √7)R19.1°-I structure, the cyclic voltammogram around the first deposition peak at different sweep rates is shown in Fig. (8.8). The decrease of the C1 peak is slower at higher sweep rates, which is the characteristic behavior of an irreversible process. The disappearance of the C1 peak correlates with the appearance of a new set of double peaks, C11 and C12, at + 0.608 and + 0.544 V respectively. These potentials were calculated after extrapolating the peak potentials for several sweep rates to 0 mV s^{-1}, after the peaks C11 and C12 were fully developed, Fig. (8.9). These peaks, C1, C11 and C12, do not show NGC mechanism, and are independent of the electrolyte, $HClO_4$ or H_2SO_4, which excludes any type of electrolyte effect.

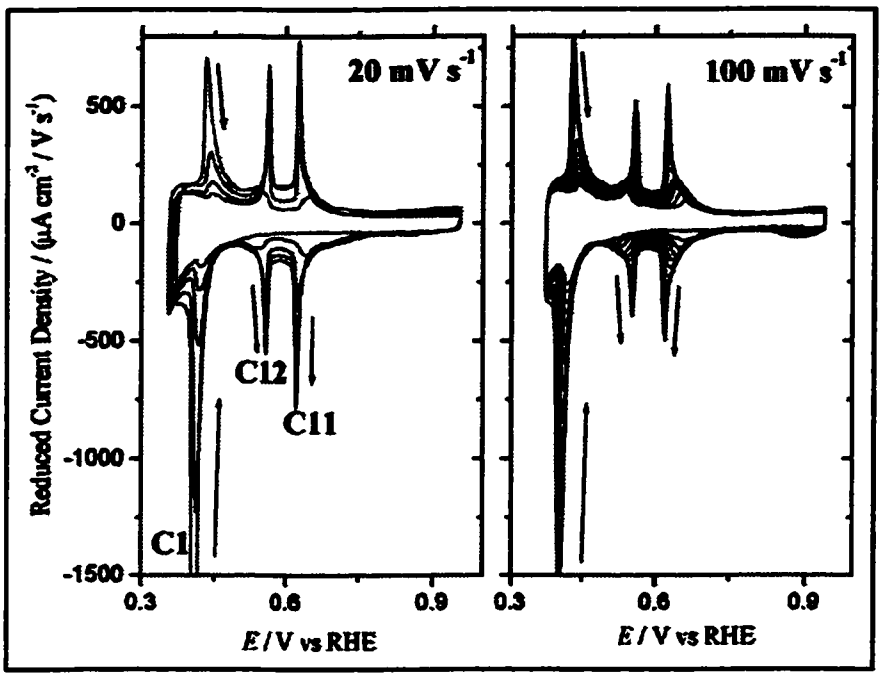

Figure 8.8: Successive cycles around peak C1 for Tl UPD on Pt(111)($\sqrt{7}$ x $\sqrt{7}$)R19.1°-I at two sweep rates. $[Tl^+] = 1$ mM. $[H_2SO_4] = 0.1$ M.

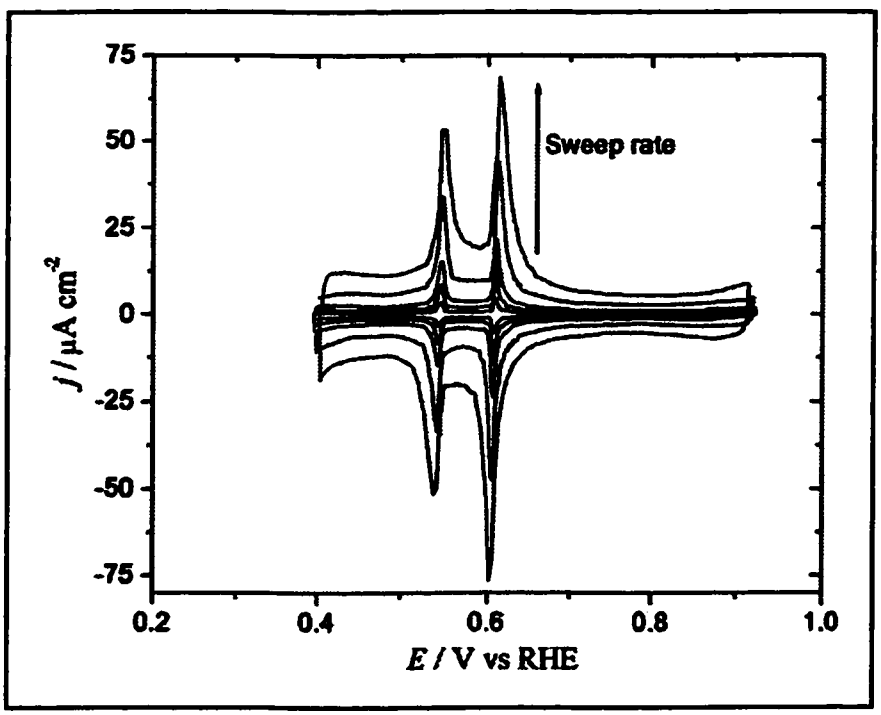

Figure 8.9: Cyclic voltammogram for the peaks C11 and C12 for Tl UPD on Pt(111)($\sqrt{7}$ x $\sqrt{7}$)R19.1°-I. Sweep rates: 5, 10, 20, 50 and 100 mV s^{-1}. $[Tl^+] = 1$ mM. $[H_2SO_4] = 0.1$ M.

Since the process under the peak C1 is irreversible, a sweep-hold experiment is suitable to calculate the charge of the peak. The potential was swept from + 0.9 V down to a potential immediately after the C1 deposition peak, and held at + 0.4 V for one minute, before being swept back again, Fig. (8.10). At this point, the C1 peak has disappeared from the voltammogram, and the new set of peaks C11 and C12 is fully developed. These two peaks will be explained in the following sections.

The total charge that passes through the peak C1 after subtracting the double layer charging is 51 $\mu C\ cm^{-2}$. The charge that passes during the time the potential is held is 14 $\mu C\ cm^{-2}$. The total charge is then 65 $\mu C\ cm^{-2}$. These charges may be explained with the help of

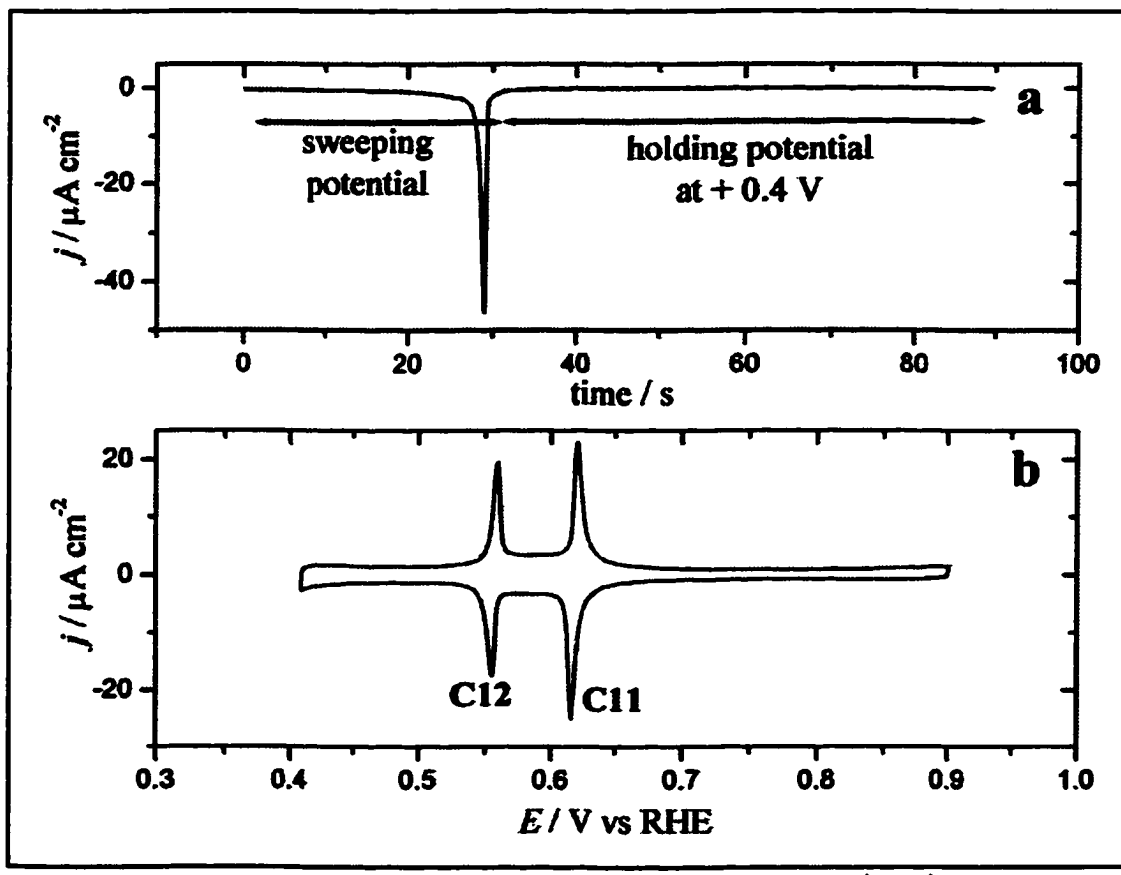

Figure 8.10: a) Sweep-hold experiment for Tl UPD on Pt(111)($\sqrt{7}$ x $\sqrt{7}$)R19.1°-I in H_2SO_4 around peak C1, b) Following cycles after holding potential. $[Tl^+] = 1$ mM, $[H_2SO_4] = 0.1$ M. Sweep rate = 20 mV s^{-1}.

the cyclic voltammogram for the electrodeposition of Tl on Pt(111)(3x3)-I, Fig. (8.11), similar to the voltammogram for Tl deposition in I^- solution [8.4]. As explained in chapter 4, the Pt(111)(3x3)-I structure forms spontaneously by dipping the Pt(111) surface into an I^- solution. As seen in Fig. (8.11), although the potentials are slightly different, + 0.399, 0.324, 0.160 and 0.086 V for the peaks C1, C2, C3 and C4 respectively, the main features of the reduction sweep are similar to the first sweep of the voltammogram of Pt(111)($\sqrt{7}$ x $\sqrt{7}$)R19.1°-I in Tl^+ solution, Fig. (8.2.a). However, the voltammogram is reversible and reproducible from cycle to cycle. This indicates that no iodine desorbs from the surface during the electrodeposition of thallium on Pt(111)(3x3)-I.

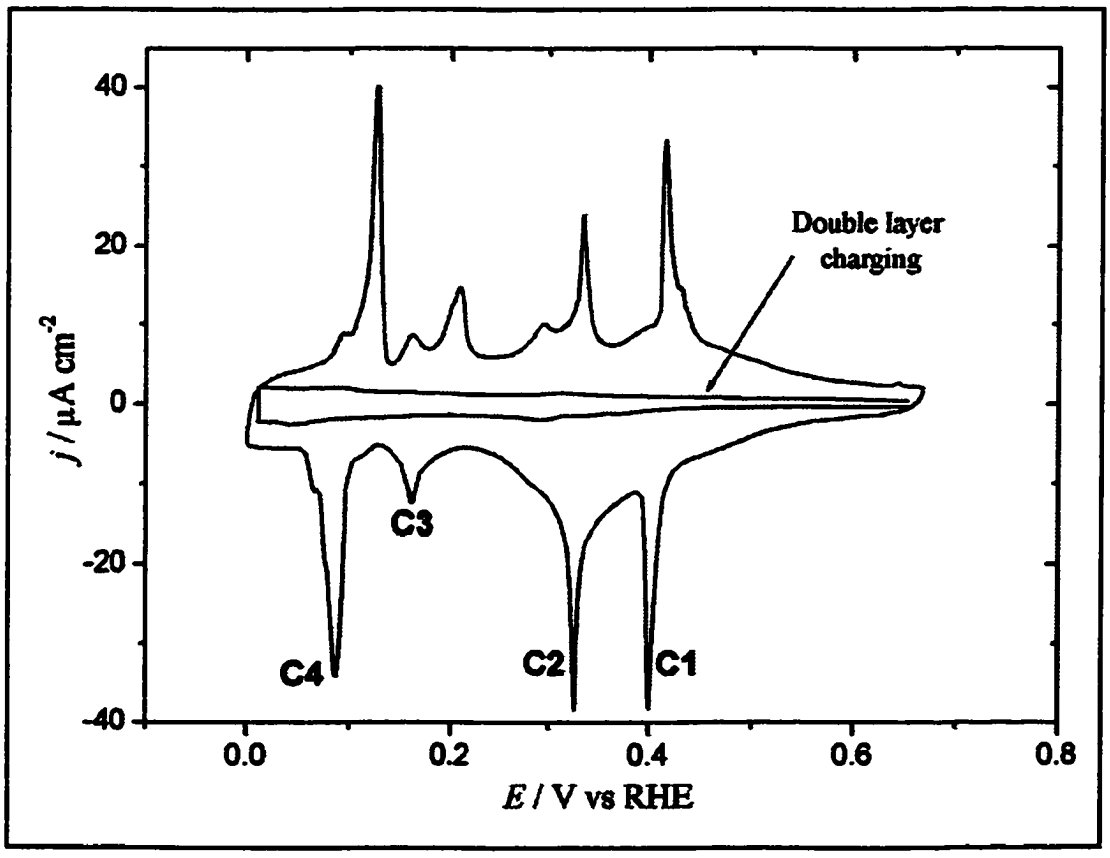

Figure 8.11: Cyclic voltammogram for Tl UPD on Pt(111)(3 x 3)-I in H_2SO_4, together with the baseline due to double layer charging obtained with A.C. voltammetry: Modulated signal: 0.5 mV rms, 2000 Hz.
$[Tl^+] = 1$ mM, $[H_2SO_4] = 0.1$ M. Sweep rate = 20 mV s^{-1}.

The charge under the peak C1 for the Pt(111)($\sqrt{7}$ x $\sqrt{7}$)R19.1°-I surface is 51 μC cm^{-2}, while for the Pt(111)(3 x 3)-I it is 54 μC cm^{-2}. These charges correspond with 0.211 ML and 0.224 ML respectively. The coverage for two atoms in a (3 x 3) structure is 0.224 ML. We propose that the first deposition peak is the deposition of two thallium atoms per unit cell in a (3 x 3) structure, independently of whether the iodine layer has a ($\sqrt{7}$ x $\sqrt{7}$)R19.1° or (3 x 3) structure. This is consistent with the fact that Tl-Tl interactions are more important than Tl-I interaction. Whether the thallium deposits on top or underneath the iodine layer is still unknown.

In section 8.4, an explanation for the appearance of the new set of peaks is proposed, as well as surface structures corresponding with the different regions of the voltammogram.

8.3.1. Cohesive Gibbs Energy Change of the Pt(111)-Tl-I Structure Formed in the First Deposition Peak C1.

For convenience, in this section the Pt(111)-(3 x 3)-I-Tl structure formed in the peak C1 of the voltammogram is called as Pt(111)-Tl-I. We can calculate a rough estimate of some of the thermodynamic parameters of this structure applying the equivalent thermodynamic sequence to that in chapter 5. The thermodynamic sequence is shown in Fig. (8.12).

The following equation for the calculation of the cohesive Gibbs energy change of the Pt(111)-Tl-I is obtained applying the sequence in Fig. (8.12):

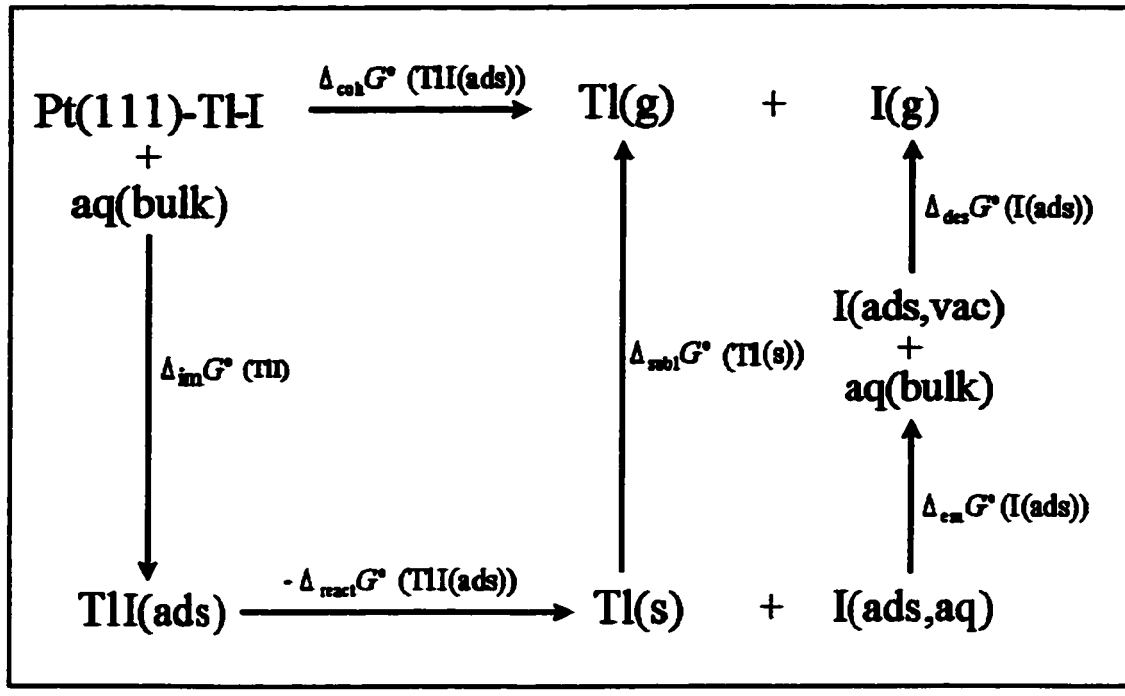

Figure 8.12: Thermodynamic sequence corresponding with the cohesion of Pt(111)-Tl-I. The symbols are equivalent to the ones in Fig. (5.1).

$$\Delta_{coh}G^{\circ}(\mathrm{TlI(ads)}) = \Delta_{im}G^{\circ}(\mathrm{TlI}) - \Delta_{react}G^{\circ}(\mathrm{TlI(ads)}) + \Delta_{subl}G^{\circ}(\mathrm{Tl(s)}) + \Delta_{em}G^{\circ}(\mathrm{I(ads)}) + \Delta_{des}G^{\circ}(\mathrm{AgI(ads)}) \quad (5)$$

It was determined in chapter 5 for the Pt-Ag-I system that the Gibbs free energy change of immersion is the same order of magnitude but of different sign to the Gibbs free energy change of emersion, and each of them is small. According to this, we make the approximation for Pt-Tl-I:

$$\Delta_{im}G^{\circ}(\mathrm{TlI}) \approx -\Delta_{em}G^{\circ}(\mathrm{I(ads)}) \quad (6)$$

The reaction for the C1 peak is:

$$(\sqrt{7} \times \sqrt{7})\mathrm{R19.1^{\circ}\text{-}I(ads)} + \mathrm{Tl^{+}(aq)} + \mathrm{e^{-}} \rightarrow \mathrm{Pt\text{-}Tl\text{-}I(ads)} \quad (7)$$

The measured reversible potential of C1 relative to an $Tl|Tl^{+}$ electrode in the same solution is the cell potential for the reaction which is the sum of reaction (7) and the reaction

$Tl \rightarrow Tl^+ + e^-$; that is:

$$Tl(s) + (\sqrt{7} \times \sqrt{7})R19.1°\text{-}I(ads) \rightarrow Pt\text{-}Tl\text{-}I(ads) \quad (8)$$

which is the reaction that allows the calculation of $\Delta_{react}G°(TlI(ads))$ for the second stage of the thermodynamic sequence in Fig. (8.12). Since all species are in their standard states, the reversible potential of C1/A1 versus $Tl|Tl^+$ is $E°$ for reaction (8). We use the following conversion to refer this potential *vs* $Tl|Tl^+$ (1 mM in 0.1 M H_2SO_4) at room temperature:

$$E_{Tl^+|Tl} - E_{H^+|H_2} = E°_{Tl^+|Tl} + \frac{RT}{F}\ln\frac{\gamma_{Tl^+}m_{Tl^+}}{\gamma_{H^+}m_{H^+}} = -0.4546\ V \quad (9)$$

taking the activity coefficients of H^+ and Tl^+ in 0.1 M H_2SO_4 to be the same, and taking the ratio of their molalities as the experimental value of 100.

As in the case of the Pt-Ag-I system, we assume that the best estimate of $E°$ is the extrapolation of the peak to the baseline. Accordingly, $E°$ for reaction (8) is $+0.877\ V_{Tl|Tl^+}$. Multiplying $E°$ by $-F$ gives the free energy change as $\Delta_{react}G°(TlI(ads)) = -84 \pm 0.3\ kJ\ mol^{-1}$.

$\Delta_{subl}G°(Tl(s))$ is tabulated as $+147.41 \pm 0.04\ J\ mol^{-1}$ [8.14], and $\Delta_{des}G°(I(ads))$ was calculated in chapter 7 as $+170 \pm 22\ kJ\ mol^{-1}$.

Substituting the Gibbs free energy changes previously calculated in the right hand side of equation (5) gives $\Delta_{coh}G°(TlI(ads)) = +401 \pm 22\ kJ\ mol^{-1}$.

8.4. Set of Double Peaks C11 and C12.

As explained above, it is proposed that the first deposition peak C1 corresponds with the deposition of a Tl adlayer in a (3 x 3) structure. This structure is stable when it matches the structure of the iodine adlayer deposited on the Pt(111), explaining the reversibility of the voltammogram for Tl deposition on Pt(111)(3 x 3)-I. However, since there is a mismatch

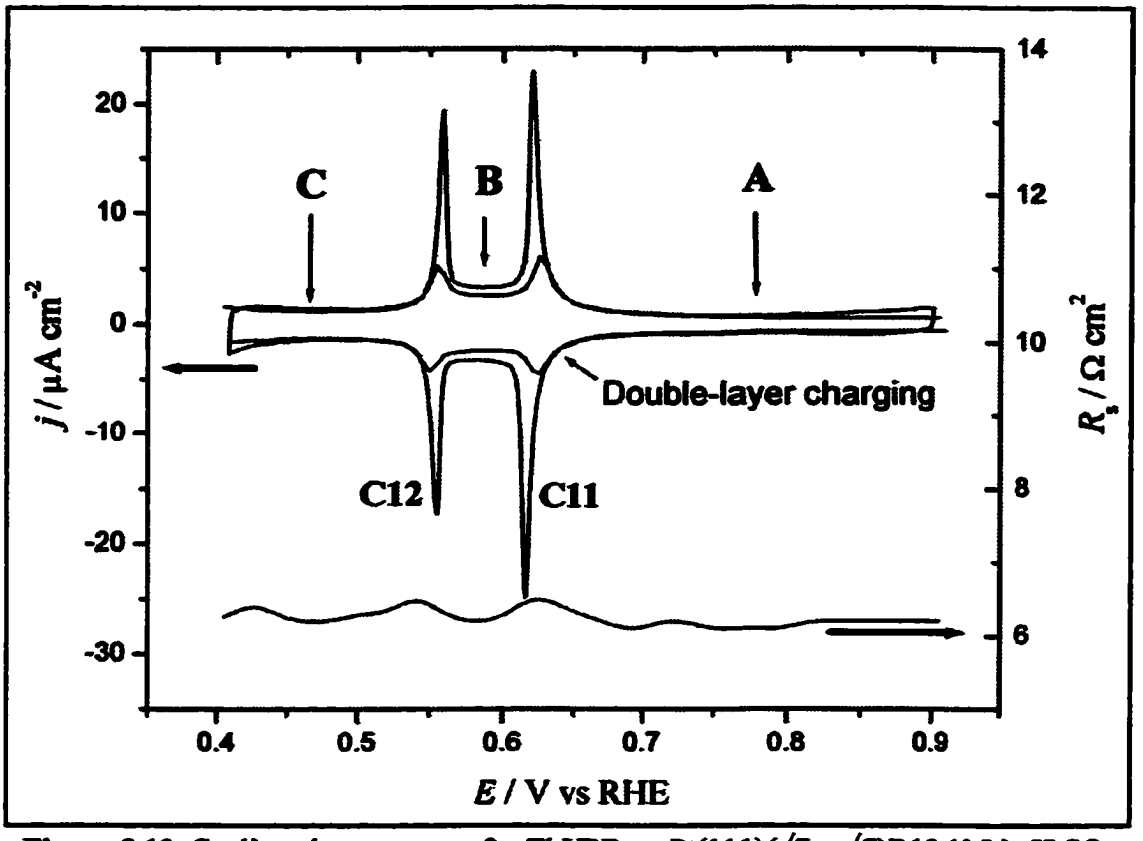

Figure 8.13: Cyclic voltammogram for Tl UPD on Pt(111)($\sqrt{7}$ x $\sqrt{7}$)R19.1°-I in H_2SO_4 after holding potential for 1 minute after peak C1. Double layer charging and R_s obtained with A.C. voltammetry at different frequencies: 3Hz to 50 kHz, modulated signal 0.5 mV rms. $[Tl^+] = 1$ mM. $[H_2SO_4] = 0.1$ M. Sweep rate = 20 mV s^{-1}.

between the (3 x 3) Tl adlayer and the($\sqrt{7}$ x $\sqrt{7}$)R19.1° structure of the iodine, the Tl-I layer undergoes an slow irreversible process which changes its structure, changing all the features of the voltammogram, Fig. (8.8). The new voltammogram can be divided in three distinct regions, A, B and C, Fig. (8.13). Integration of the deposition peaks after subtraction of the double layer charging gives a charge for the peak C11 of 11 μC cm^{-2}, and 8 μC cm^{-2} for the peak C12. The total cathodic charge for the C11 and C12 peaks is therefore 19 μC cm^{-2}, equivalent to 0.08 monolayers. The narrowness and reversibility of the peaks C11 and C12 imply that these peaks are due to surface processes, and that regions A, B and C correspond

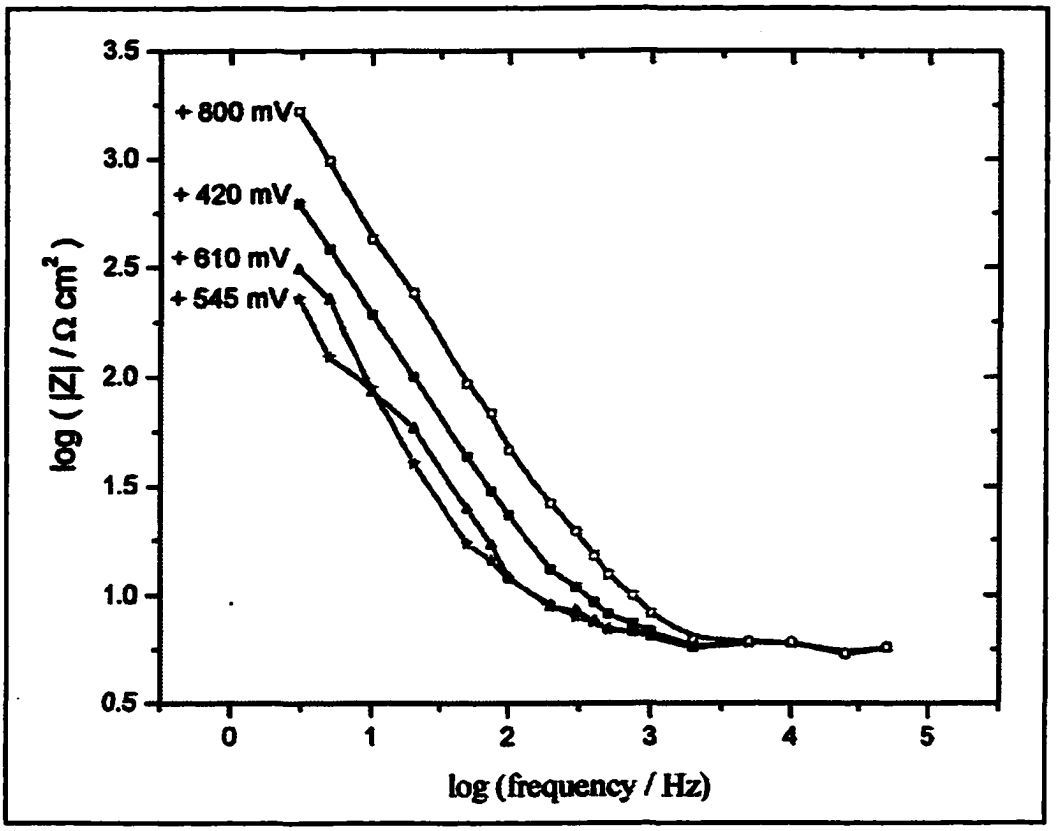

Figure 8.14: Bode plot at different potentials of the voltammogram shown in Fig. (8.13) for frequencies from 3 Hz to 50 kHz.

to well ordered surface adlayers.

Fig. (8.13) shows also the change of C_{dl} and R_s with potential in the voltammogram. As explained in the previous section, the small change of R_s with potential in Fig. (8.13) implies that there are no faster processes at the same time scale of the charging of the double layer. We can make the Bode plot at different potentials to support this argument. Fig. (8.14) shows the Bode plot at different potentials corresponding with the voltammogram in Fig. (8.13). log (|Z|) is constant at high frequencies. The constant value of log (|Z|) at high frequencies is an indication that the only processes involved at this frequency range is the double layer charging.

8.4.1. Thallium Coverage.

It is possible to estimate the thallium coverage through the three peaks of the voltammogram in Fig. (8.13) using Auger electron spectroscopy. A coverage of 0.66 ML of Tl is obtained by cyclic voltammetry for Tl UPD on Pt(111) for a final potential of 0.1 V, Fig. (8.1), [8.1][8.2]. The thallium coverages calculated with AES were referenced to the intensity of the Tl peak at 89 eV at the known coverage of 0.66 ML, Fig. (8.15.X). AES does not show the presence of Tl on the surface in region A of the voltammogram, Fig.

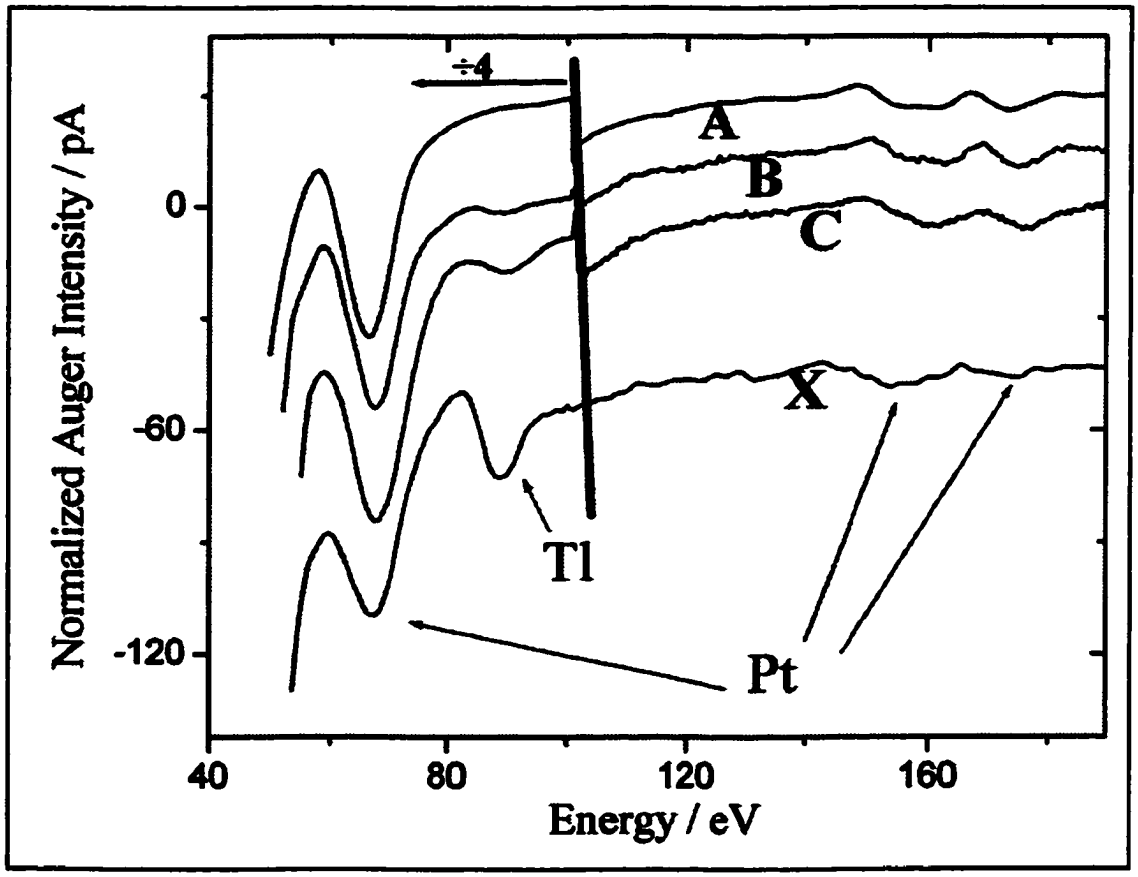

Figure 8.15: Auger spectra for the regions A, B and C of the voltammogram for Tl deposition on Pt(111) covered with iodine after rearrangement of the Pt(111)($\sqrt{7}$ x $\sqrt{7}$)R19.1°-I structure. X: calibration Auger spectra. Spectra shifted for clarity. Beam current = 10μA.

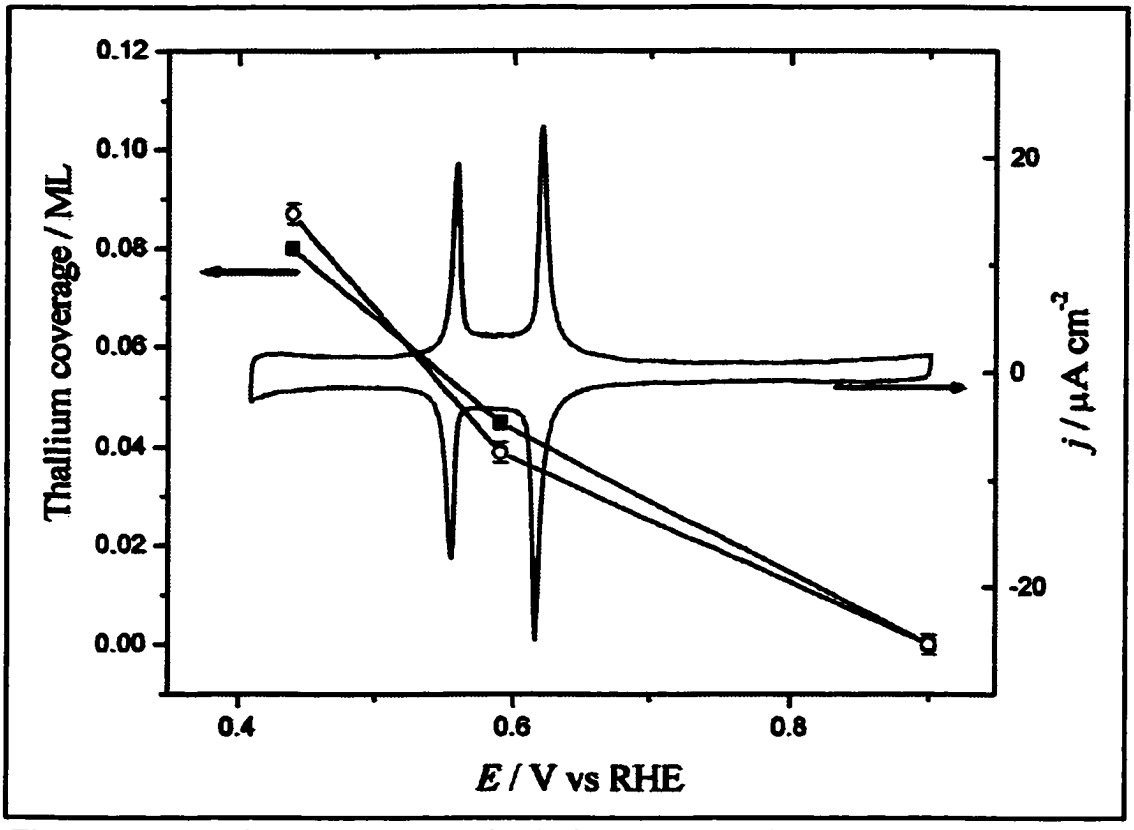

Figure 8.16: Thallium coverages obtained with: ○) AES and ■) integration of the cyclic voltammogram for Tl UPD on Pt(111)($\sqrt{7}$ x $\sqrt{7}$)R19.1°-I in H_2SO_4 after holding potential for 1 minute after peak C1 (also shown).
$[H_2SO_4] = 0.1$ M, $[Tl^+] = 1$ mM. Sweep rate = 20 mV s^{-1}

(8.15.A). 11 μC cm^{-2} for the cathodic peak C11 is equivalent to 0.045 monolayers of thallium in region B of the voltammogram. This agrees with the thallium coverage obtained with Auger spectroscopy: 0.039 ± 0.002, Fig. (8.15.B). The coverage obtained for region C of the voltammogram by coulometric measurements is 0.08, while for Auger spectroscopy is 0.087 ± 0.002, Fig. (8.15.C). The results for the different estimates of the coverage of thallium in the three regions of the voltammogram are shown in Fig. (8.16).

8.4.2. Iodine Coverage.

The total charge under the cathodic peak C1 is 65 μC cm^{-2}. Therefore, the equivalent

of 65 - 19 = 46 $\mu C\ cm^{-2}$ of Tl comes off the surface during the irreversible rearrangement process. This charge corresponds to 0.19 monolayers of Tl desorbed, assuming one electron per atom. Accepting that one iodine atom desorbs per thallium atom, the remaining iodine coverage after the rearrangement process is 0.42 - 0.19 = 0.23 monolayers (0.42 being the iodine coverage for the initial Pt(111)($\sqrt{7}$ x $\sqrt{7}$)R19.1°-I).

The desorption of iodine from the surface can be further assessed by charge measurements of iodine oxidation. This reaction corresponds to the five electron process:

$$Pt(111)\text{-}I + 3H_2O \rightarrow Pt(111) + IO_3^- + 6H^+ + 5e- \qquad (10)$$

The peak for iodine oxidation from the surface occurs at + 1.3 V under the conditions studied. Oxidation of Tl^+ to Tl^{3+} in solution starts at +1.2 V. Therefore, due to the overlap of the oxidation peaks, the oxidation of iodine has to be carried out in a different electrochemical cell than the cell where the thallium is deposited. The electrode is transferred after the deposition and rearrangement of the Tl-I layer to a different electrochemical cell with the same electrolyte but without Tl^+. The breaking of the electrode-electrolyte meniscus from the solution which contains Tl^+ is done at a potential +0.9 V, which is a potential corresponding with region A of the voltammogram, Fig. (8.13), where there is no Tl adsorbed on the surface. The immersion potential in the cell with no Tl^+ is also controlled at + 0.9 V, and immersion is followed by sweeping anodically in order to oxidize all the iodine from the surface, Fig. (8.17). The potential is held for one minute after the iodine oxidation peak to assure the complete oxidation of the iodine layer. The total charge that passes during the iodine oxidation also contains the charge for the oxidation of the bare platinum. Therefore, the total charge has to be corrected by subtraction of the charge for the reduction of the platinum oxide.

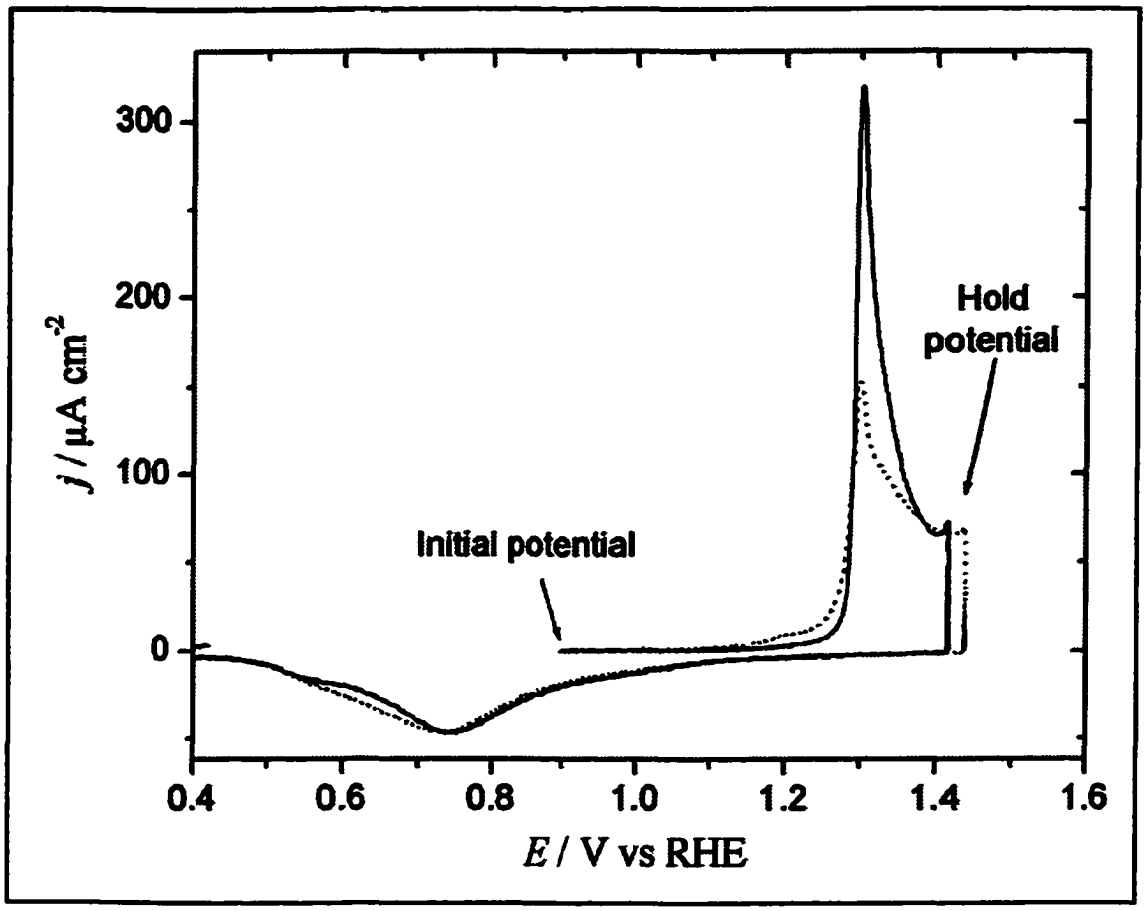

Figure 8.17: Iodine oxidation voltammograms, (——) without deposition of Tl, (.....) after Tl deposition. 20 mV s^{-1}, $[H_2SO_4] = 0.1$ M.

The oxidation charge for Pt(111)(√7 x √7)R19.1°-I without Tl deposition after correction for the Pt oxidation is 520 μC cm^{-2}. This charge corresponds to a five electron process with 104 μC cm^{-2} per electron, or 0.43 of a monolayer, as compared with 0.428 for an ideal (√7 x √7)R19.1° surface structure. The agreement of these charges gives us confidence in the validity of the experiment.

After deposition of Tl and development of the peaks C11 and C12, the oxidation charge of iodine is 330 μC cm^{-2}, which corresponds to 66 μC cm^{-2} per electron. This charge is equivalent to 0.27 monolayers, as compared with 0.23 monolayers previously proposed obtained by charge measurements of Tl deposition along the peaks C11 and C12. The two

measurements are in good agreement, which indicates the desorption of one iodine atom per thallium during the rearrangement process of the Tl-I adlayer.

8.4.3. Surface Structures, LEED analysis.

An attempt to assign different surface structures to the three regions of the voltammogram in Fig. (8.13) was made using the ultra-high vacuum techniques available in our laboratory. As previously explained, the experiment involves transferring the crystal from the high-pressure chamber to the main chamber of the UHV system after Tl electrodeposition and breaking of the crystal-electrolyte meniscus. Therefore, the first step is the measurement of the open-circuit potential, in order to ensure that the surface structure does not change during the transfer. Unfortunately, there is a gradual change of the open potential, Fig. (8.18). This stabilizes at + 1.15 V, at a more negative potential than that corresponding for the oxidation of I from the surface. It is worth noting how the open-circuit potential changes gradually along the potential range, except at potentials corresponding with the peaks C11 and C12 in the voltammogram, Fig. (8.18). At these potentials the open-circuit potential is stable for a few seconds, and then changes again.

According to the change of the open-circuit potential, it is possible that the surface structure rearranges after breaking the contact between the crystal and the solution. Care was taken breaking the meniscus and transferring the crystal from the high-pressure chamber to the analysis chamber after the electrochemical experiment. After the transfer, AES did not detect traces of electrolyte on the surface. Therefore, the crystal is assumed to be free of the double layer after the meniscus is broken. Since for emersion potentials corresponding with each the three regions of the voltammogram the LEED diffraction

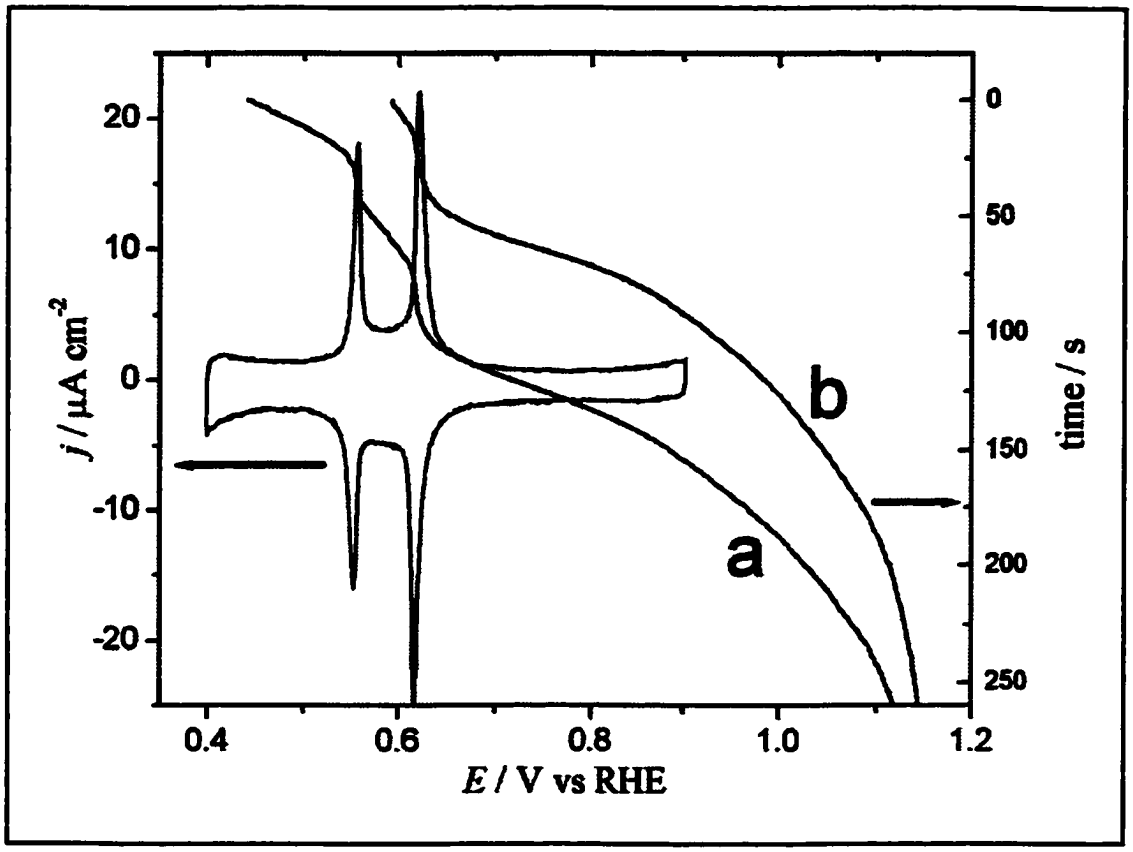

Figure 8.18: a and b) Open-circuit potential starting at two different potentials, together with the cyclic voltammogram for Tl deposition on iodine modified Pt(111) surface. 20 mV s^{-1}, $[H_2SO_4] = 0.1$ M, $[Tl^+] = 1$ mM.

patterns are different and reproducible[2], it is reasonable to assume that the different surface structures do not change once the crystal has been removed from the solution.

However, we have to be careful when analyzing the surface structures obtained with LEED. The transfer of the crystal until the LEED measurement took from 10 to 15 minutes. It is possible that during that time the original surface structures systematically evolved to the ones detected by LEED. In-situ electrochemical surface techniques would be necessary

---

2 Three experiments were made to measure region C of the voltammogram with emersion potentials at + 400, + 388 and + 385 mV, three experiments for region B with emersion potentials at + 590, + 592 and + 575 mV, and two experiments for region C with emersion potentials at + 815 and + 727 mV.

in order to ascertain the nature of the surface structures in the different regions of the voltammogram.

8.4.3.1. Region C: LEED Pattern and Surface Structure.

The region C of the voltammogram corresponds with more negative potentials than the peak C12. At these potentials, the LEED pattern is as shown in Fig. (8.19). This LEED pattern is interpreted as the diffraction pattern for a Pt(111)$\begin{bmatrix} 4 & 0 \\ 3 & 6 \end{bmatrix}$-TlI surface structure, which is a rectangular superlattice on top of the hexagonal (111). The rectangular $\begin{bmatrix} 4 & 0 \\ 3 & 6 \end{bmatrix}$ unit cell is shown in Fig. (8.20).

The position of the Tl and I atoms on the Pt(111) surface is unknown unless a full dynamical LEED analysis of the diffraction beams is undertaken. However, the LEED pattern in Fig. (8.19) shows systematic absences, which enable us to propose a specific surface structure. Systematic absences are absences of diffraction spots in the LEED pattern

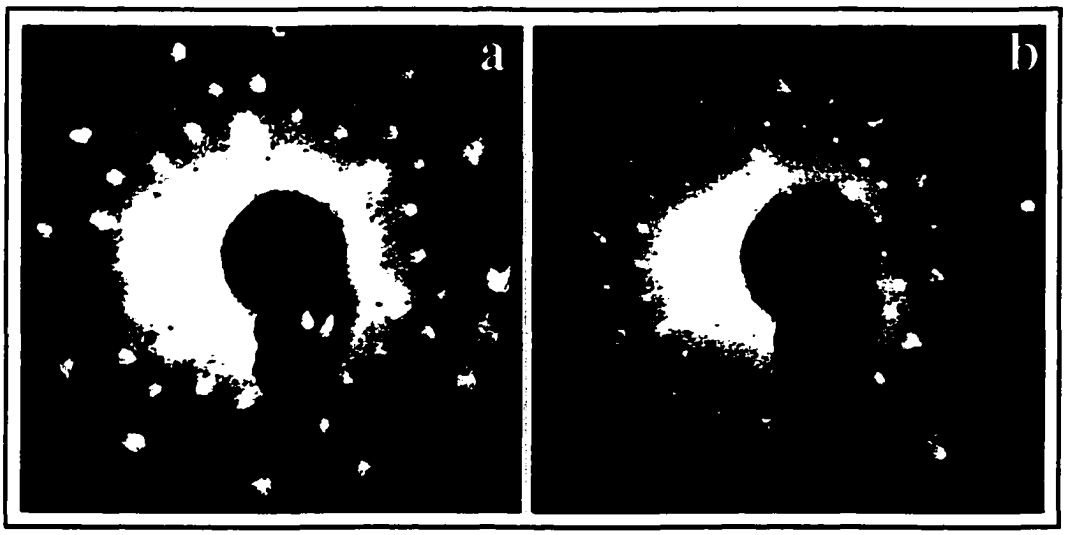

Figure 8.19: LEED patterns at a) 35 and b) 70 eV of a platinum surface corresponding with region C of the voltammogram.

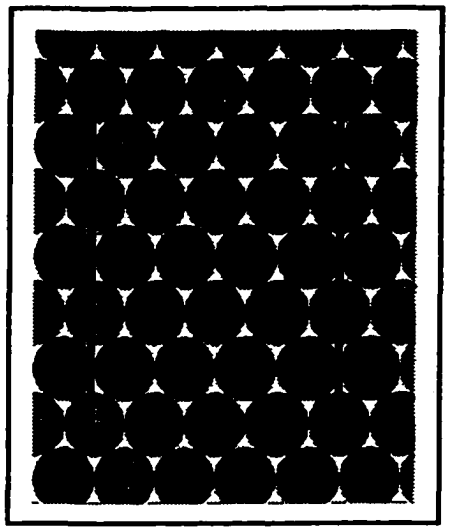

Figure 8.20: Pt(111)$\begin{bmatrix} 4 & 0 \\ 3 & 6 \end{bmatrix}$ unit cell.

due to the existence of special symmetries in the unit cell.

Fig. (8.21.a) shows the LEED pattern calculated for the $\begin{bmatrix} 4 & 0 \\ 3 & 6 \end{bmatrix}$ unit cell on a (111) substrate, using the computer pattern simulator LEEDpat 1.0 [8.15]. The real LEED pattern

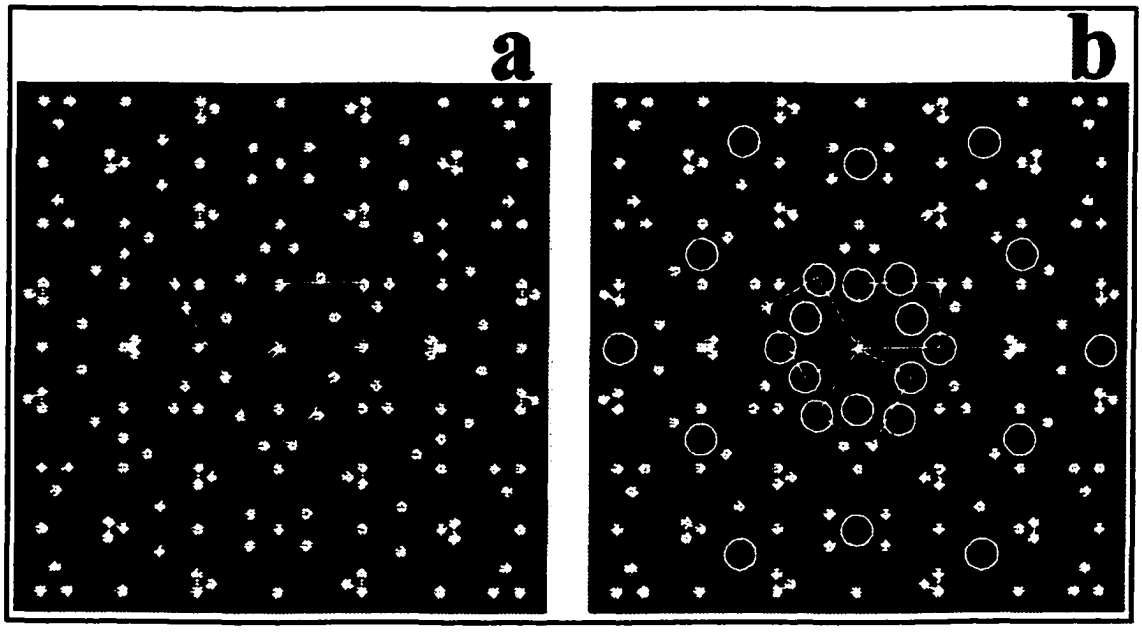

Figure 8.21: Computer simulation of the LEED pattern for a $\begin{bmatrix} 4 & 0 \\ 3 & 6 \end{bmatrix}$ structure on a (111) surface showing the three domains of the unit cell, a) for no special symmetry of the lattice, b) for p2gg symmetry of the lattice and the systematic absences (circles).

shows systematic absences for the whole energy range in the h0 direction for h = 1n, 3n.., and 0k for k = 1n, 3n..., for each of the three rotational domains, Fig. (8.21.b). These absences imply a p2gg symmetry of the superlattice, Fig. (8.22). However, a p2gg symmetry of the superlattice is incompatible with the p3m1 symmetry of the Pt(111) substrate. This suggests that the systematic absences are instead real diffraction spots, although too faint to be detected with our electron optics.

While the first platinum layer is compatible with p2gg symmetry of the superlattice, the incompatibility arises for the differences between the first and second platinum layer. It is reasonable to assume that the influence of the second Pt layer in the intensity of the diffraction spots is smaller than the first Pt layer. Therefore, although the superlattice does not have true p2gg symmetry, in this context it approximates that symmetry.

It was calculated in the previous section that in this region of the voltammogram the

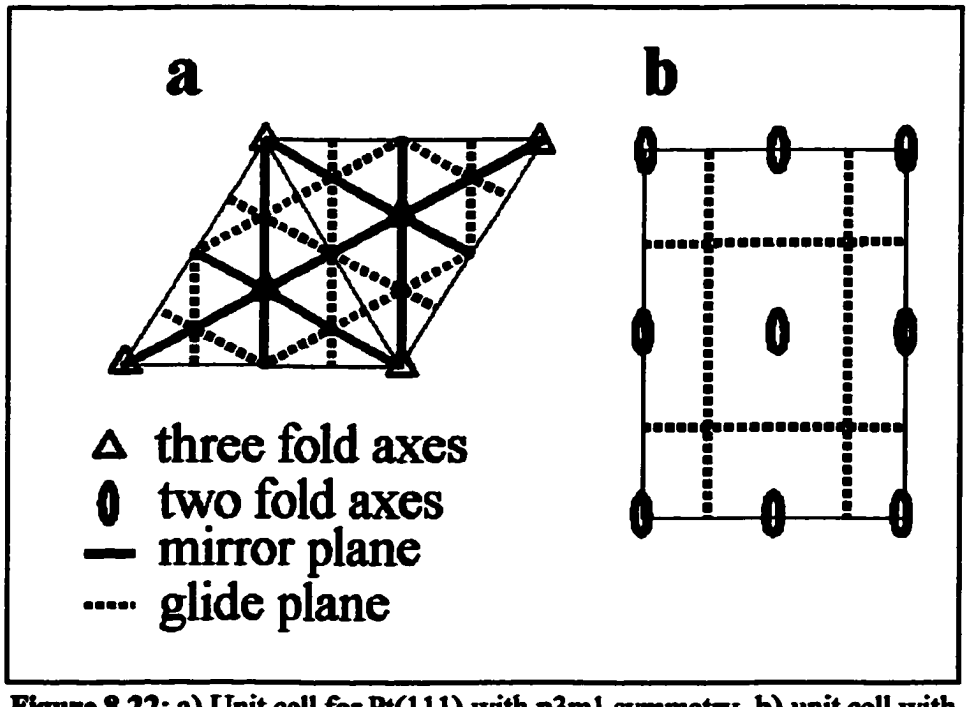

Figure 8.22: a) Unit cell for Pt(111) with p3m1 symmetry, b) unit cell with p2gg symmetry.

thallium coverage is 0.08 ML, and 0.23 ML for iodine. This accounts for three times more iodine than thallium on the surface. Assuming one electron per thallium atom adsorbed, 0.08 ML is equivalent to 2 thallium atoms per Pt(111)$\begin{bmatrix} 4 & 0 \\ 3 & 6 \end{bmatrix}$ unit cell. A coverage of 0.23 ML for iodine correlates then to 6 iodine atoms per Pt(111)$\begin{bmatrix} 4 & 0 \\ 3 & 6 \end{bmatrix}$ unit cell. According to the suggested symmetry of the unit cell, and the number of Tl and I atoms in it, only one surface structure appears reasonable, that of Fig. (8.23).

In this surface structure, the two thallium atoms per unit cell occupy 2-fold sites. There are two types of iodine atoms: four of the iodine atoms per unit cell are adsorbed on displaced atop sites, while the other two are in 2-fold sites. The position of the second platinum layer relative to the first platinum layer is unknown.

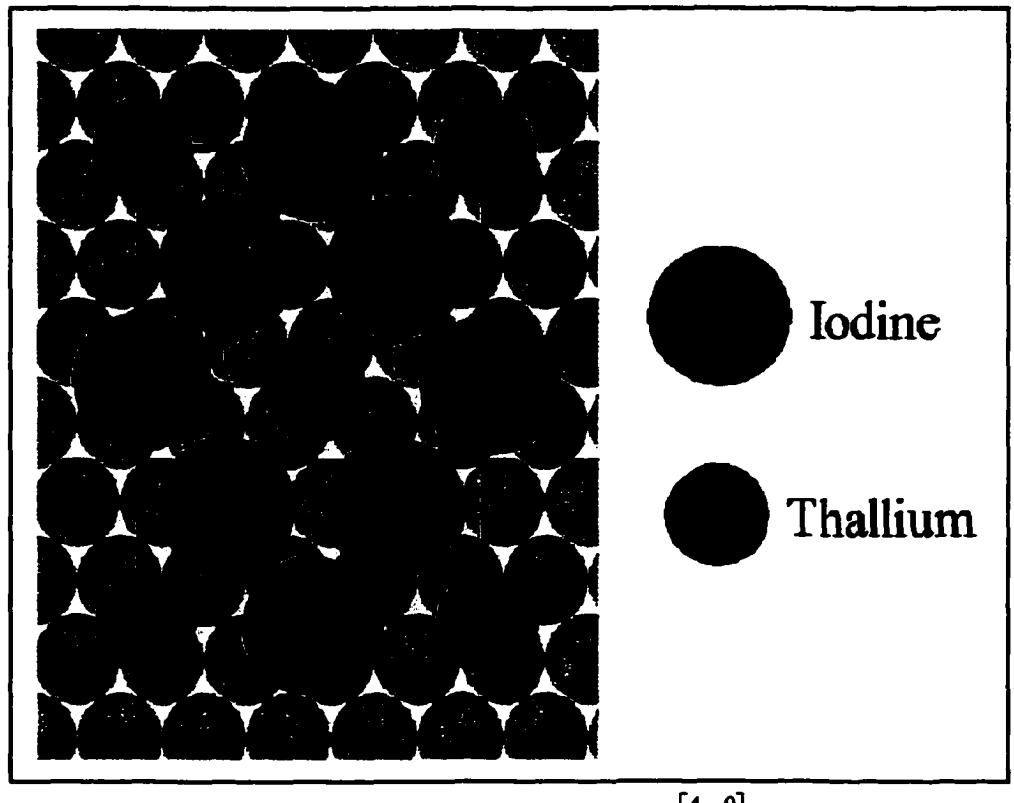

Figure 8.23: Proposed structure for the Pt(111))$\begin{bmatrix} 4 & 0 \\ 3 & 6 \end{bmatrix}$-TlI structure.

8.4.3.2. Region B: LEED Pattern and Surface Structure.

Region B in the voltammogram is at potentials between the C11 and C12 deposition peaks. The LEED pattern of this region is shown in Fig. (8.24). This pattern is a mixture of ($\sqrt{7}$ x $\sqrt{7}$)R19.1° and ($\sqrt{3}$ x $\sqrt{3}$)R30° structures, which correlates with patches of the two surface structures on top of the platinum surface. The unit cells for these structures are shown in Fig. (8.25).

Region A of the voltammogram has a low coverage Pt(111)($\sqrt{7}$ x $\sqrt{7}$)R19.1°-I (see below in the text). Therefore, it seems reasonable that the patches of the surface in this region of the voltammogram with a ($\sqrt{7}$ x $\sqrt{7}$)R19.1° LEED pattern correspond to the same surface structure. The ($\sqrt{3}$ x $\sqrt{3}$)R30° pattern correlates then with patches of Pt(111)($\sqrt{3}$ x $\sqrt{3}$)R30°-TlI on the crystal.

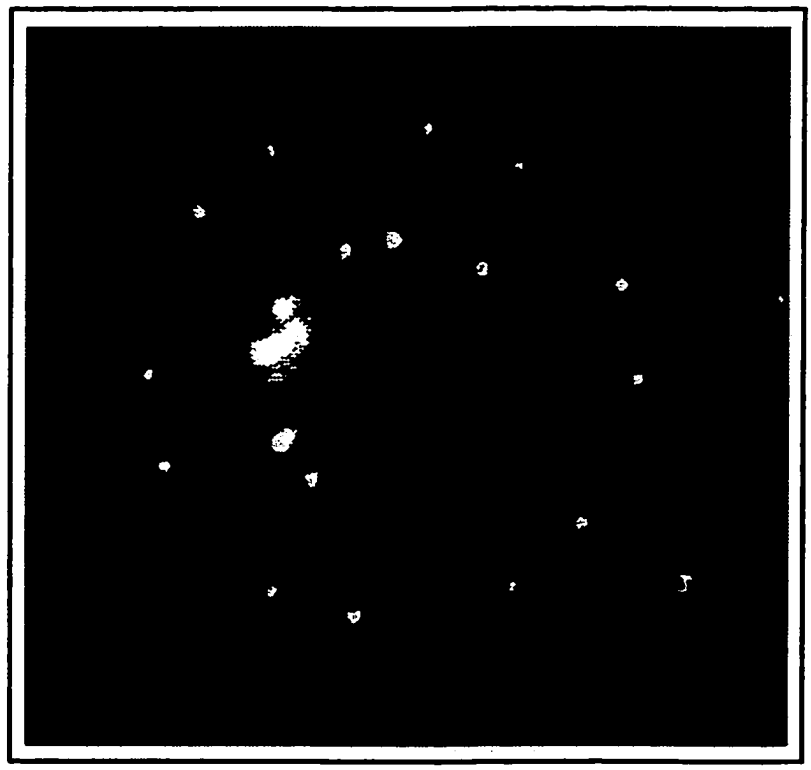

Figure 8.24: LEED pattern at 73 eV of a platinum surface corresponding with region B of the voltammogram.

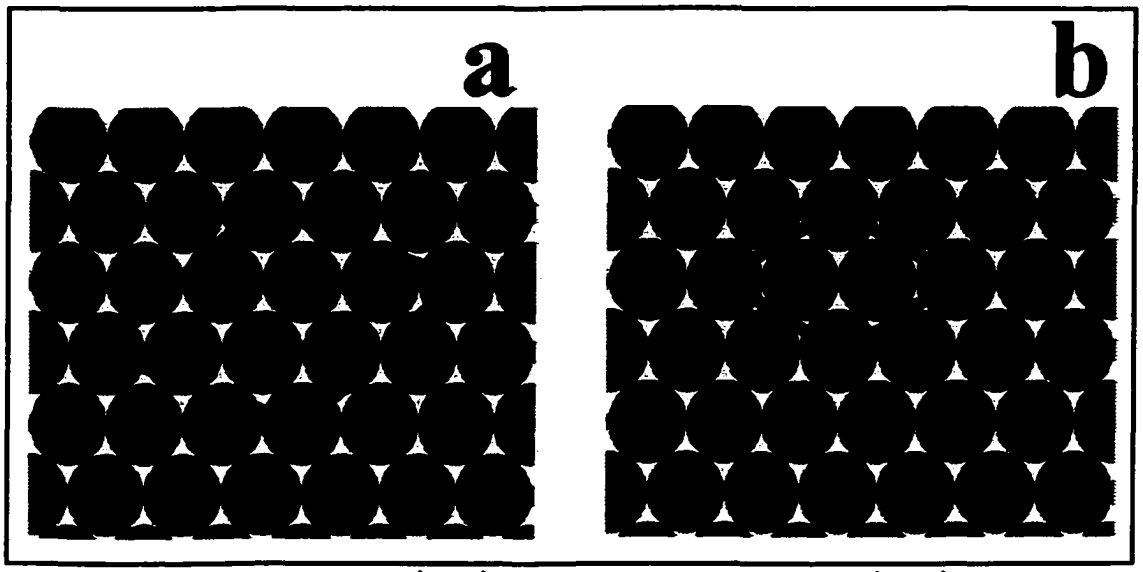

Figure 8.25: a) Pt(111)(√7 x √7)R19.1° unit cell, b) Pt(111)(√3 x √3)R30°.

8.4.3.3. Region A: LEED Pattern and Surface Structure.

This region of the voltammogram corresponds with potentials more anodic than the C11 peak. Auger spectroscopy shows no thallium adsorbed on the surface, Fig. (8.15.A). The LEED pattern corresponds with a Pt(111)(√7 x √7)R19.1° structure. The iodine coverage was calculated in section 8.4.2. from subtraction of thallium charges to the initial iodine coverage as 0.23 ML (1.6 iodine atoms per (√7 x √7)R19.1° unit cell), and from charges of iodine oxidation as 0.27 ML (1.9 iodine atoms per (√7 x √7)R19.1° unit cell).

According to the iodine coverage, the LEED pattern can be explained as islands of Pt(111)(√7 x √7)R19.1°-I with a local iodine coverage of 0.43 ML, and bare patches of Pt(111) on the rest of the surface. This explanation seems unlikely, since the voltammogram would reflect two deposition peaks: one for Tl deposition on Pt(111)(√7 x √7)R19.1°-I and another one for Tl deposition on Pt(111).

A different explanation of the iodine coverage considers a Pt(111)(√7 x √7)R19.1°-I with two iodine atoms per unit cell. However, a Pt(111)(√7 x √7)R19.1°-I structure with two

iodine atoms per unit cell has not been reported in the literature.

8.5. Peak C2: Second Cathodic Peak for the UPD of Tl on Pt(111)(√7 x √7)R19.1°-I.

Without holding the potential after the peak C1, the cyclic voltammogram for Tl electrodeposition on Pt(111)(√7 x √7)R19.1°-I has a second deposition peak at + 0.328 V, Fig. (8.26). The shape of this peak, excepting the cathodic shoulder, is similar to the first deposition peak. The charges are similar as well, 52 μC cm^{-2} and 51 μC cm^{-2} for peaks C2 and C1 respectively.

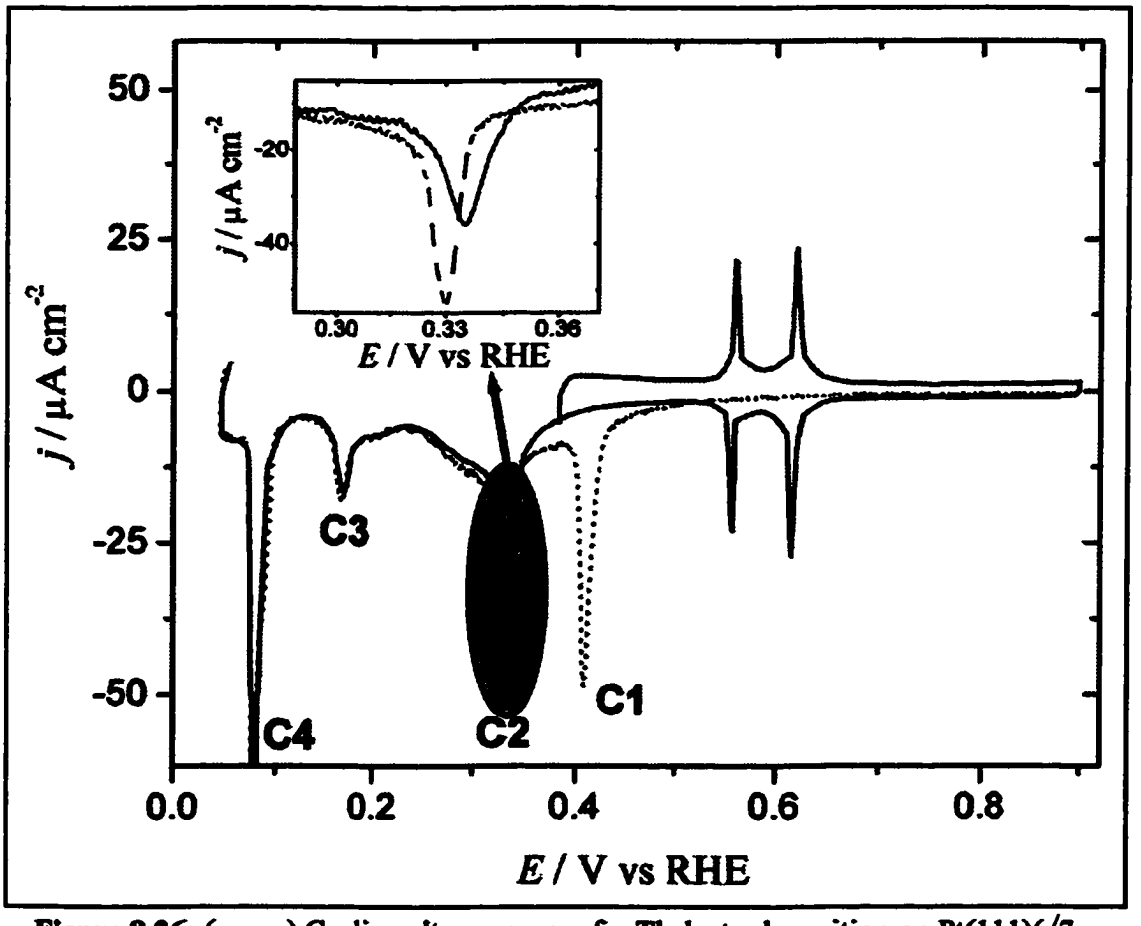

Figure 8.26: (.....) Cyclic voltammogram for Tl electrodeposition on Pt(111)(√7 x √7)R19.1°-I, (——) after holding the potential at + 0.395 V, allowing the formation of the peaks C11 and C12. $[Tl^+]$ = 1 mM. $[H_2SO_4]$ = 0.1 M. Sweep rate = 20 mV s^{-1}.

The shape and charge of the C2 peak are also similar for electrodeposition of Tl on Pt(111)(3 x 3)-I, Fig. (8.11). In the latter case the peak potential is at + 0.324 V, and the charge is 54 $\mu C\ cm^{-2}$. Therefore, it seems reasonable to assume that the peak C2 corresponds with the deposition of another two thallium atoms per (3 x 3) unit cell, on the previously modified Pt(111)($\sqrt{7}$ x $\sqrt{7}$)R19.1°-I with an adlayer of two thallium atoms per (3 x 3) unit cell during the peak C1.

If this is the case, the deposition process corresponding with the peak C2 depends on the state of the surface prior to the peak C2. Fig. (8.26) shows how the potential of the peak C2 shifts anodically from + 0.329 to + 0.336 V, and the charge decreases from 52 to 42 $\mu C\ cm^{-2}$, when the surface has been allowed to rearrange and develop the peaks C11 and C12. 42 $\mu C\ cm^{-2}$ for the C2 peak on the modified surface is equivalent to 0.17 ML. The surface structure immediately before the peak C2 is Pt(111)$\begin{bmatrix} 4 & 0 \\ 3 & 6 \end{bmatrix}$-2Tl-6I. 0.17 ML suggests the deposition of another two Tl atoms per $\begin{bmatrix} 4 & 0 \\ 3 & 6 \end{bmatrix}$ unit cell on the Pt(111)$\begin{bmatrix} 4 & 0 \\ 3 & 6 \end{bmatrix}$-2Tl-6I surface structure.

8.5.1. Cathodic Shoulder of the Deposition Peak C2.

Fig. (8.27) shows the first four cycles of the voltammetry for Tl deposition on Pt(111)($\sqrt{7}$ x $\sqrt{7}$)R19.1°-I in H_2SO_4. During the first cycle the peak C1 disappears and the peaks C11 and C12 are developed. In the following cycles the peak C2, its cathodic shoulder and the peaks C11 and C12 decrease irreversibly, enhancing new features in the voltammogram. These new features are different for $HClO_4$ as electrolyte, Fig. (8.28). Thus, the irreversible processes associated with the peak C2 are electrolyte dependent.

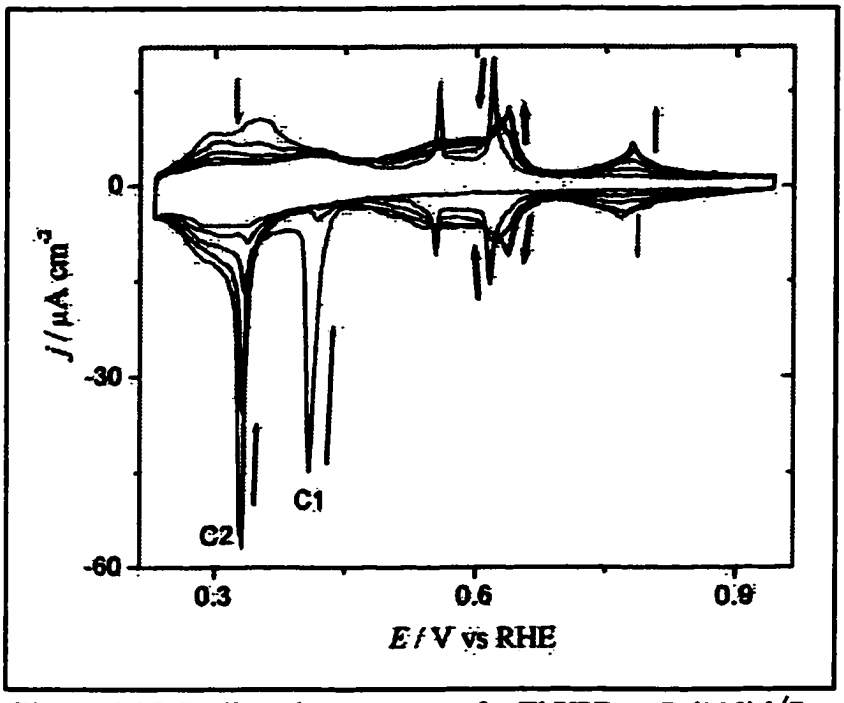

Figure 8.27 Cyclic voltammograms for Tl UPD on Pt(111)(√7 x √7)R19.1°-I in H_2SO_4 sweeping back after peak C2. $[Tl^+] = 1$ mM. $[H_2SO_4] = 0.1$ M. Sweep rate = 20 mV s-1.

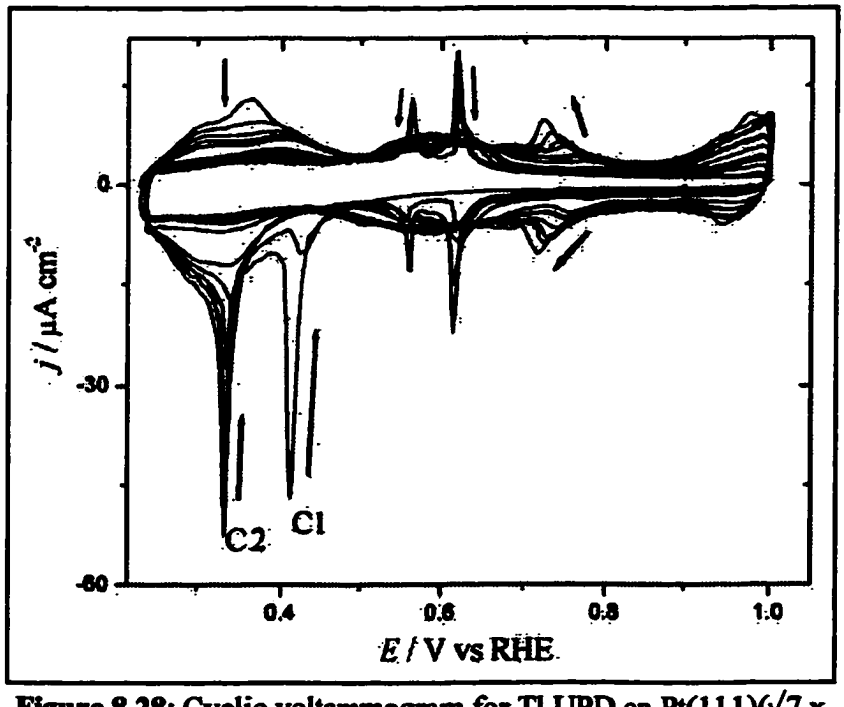

Figure 8.28: Cyclic voltammogram for Tl UPD on Pt(111)(√7 x √7)R19.1°-I in $HClO_4$ sweeping back after peak C2. $[Tl^+] = 1$ mM. $[HClO_4] = 0.1$ M. Sweep rate = 20 mV s^{-1}.

It is more convenient to perform a sweep-hold experiment in order to study the final steady-state voltammogram after the irreversible process in peak C2. Fig. (8.29) and (8.30) show the cyclic voltammograms in both H_2SO_4 and $HClO_4$, after holding the potential at several potentials in the peak C2 and its cathodic shoulder.

In H_2SO_4 solution, there is a new peak with its maximum at + 0.637 V, together with a set of peaks centered at + 0.775 V. The latter peak is assigned to Tl UPD on bare Pt(111), since the voltammogram on Pt(111), Fig. (8.1), shows a peak at the same potential. Accordingly, either patches of the platinum surface are free from iodine, or the iodine coverage is too low on the surface to alter the Tl deposition during the irreversible process in peak C2.

Thallium deposition on Pt(111) in H_2SO_4 has the so called "butterfly" peak at + 0.533 V, Fig. (8.1). This has been assigned to adsorption/desorption and long-range interactions between bisulfate ions with Tl adatoms on Pt(111) [8.2][8.16]. At more negative potentials than + 0.533 V the surface is covered with thallium. In the region between + 0.533 and + 0.775 V the surface is covered with a Tl-bisulfate adlayer. Due to the similar shape of the peak at + 0.533 V for Tl UPD on Pt(111) with the peak at + 0.637 V for Pt(111) covered with iodine, Fig. (8.29), the latter peak is also assigned to bisulfate adsorption from the electrolyte.

Quantification of the amount of iodine desorbed is questionable by electrochemical methods, due to the overlapping of three different adsorption/desorption reactions: thallium, iodine and bisulfate. Therefore, no attempt to interpret the charges was made.

The cyclic voltammogram in $HClO_4$ solution for Tl deposition on Pt(111) has a peak at + 0.642 V and a set of peaks centered at + 0.959 V, Fig. (8.1). These have been

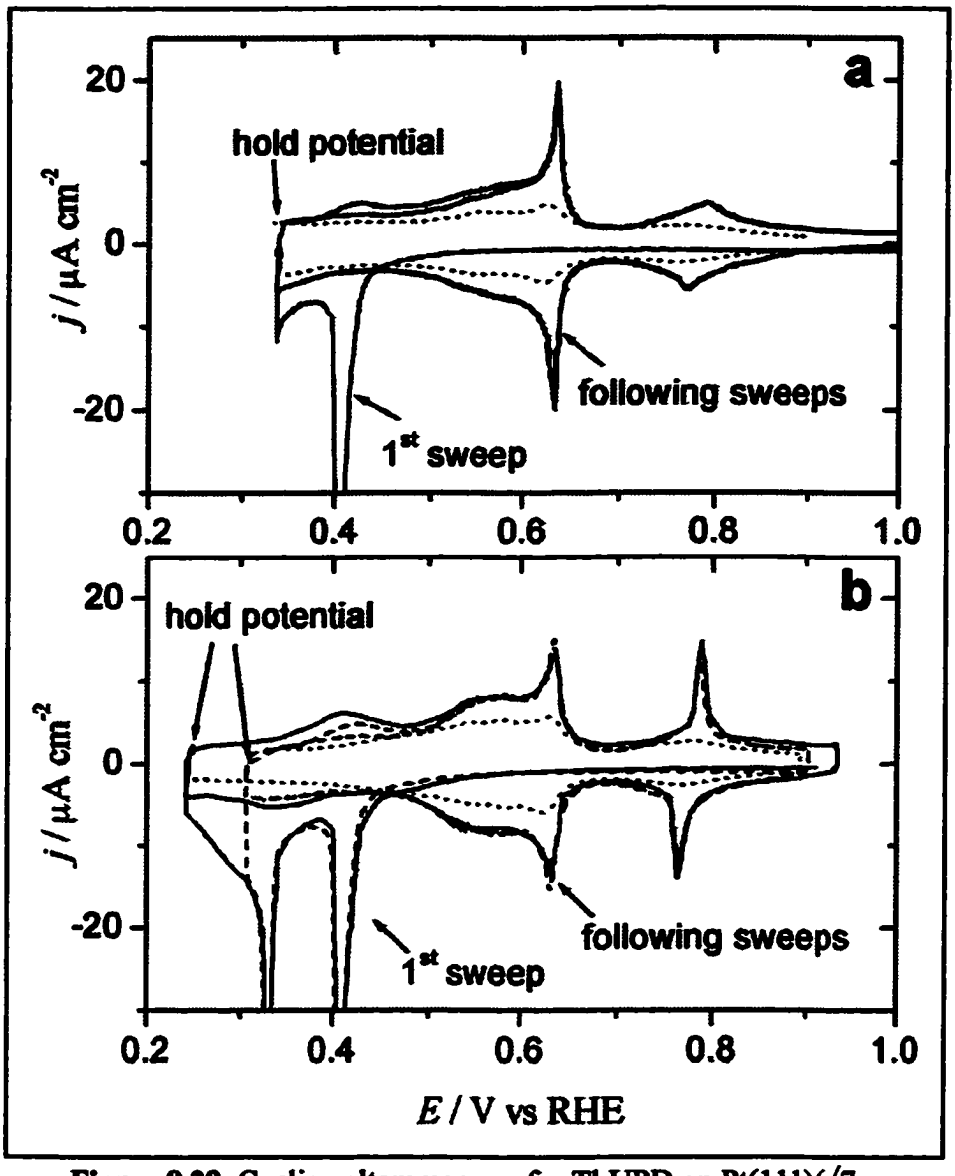

Figure 8.29: Cyclic voltammogram for Tl UPD on Pt(111)(√7 x √7)R19.1°-I in H_2SO_4. a) holding potential one minute at the beginning of peak C2, b) holding potential for 1 minute in the cathodic shoulder of peak C2 at several potentials.
(.....) double layer charging. $[Tl^+] = 1$ mM. $[H_2SO_4] = 0.1$ M. Sweep rate $= 20$ mV s^{-1}.

tentatively assigned to Tl deposition on Pt(111), [8.2]. For Tl deposition on Pt(111)(√7 x √7)R19.1°-I, after holding the potential at different points of the peak C2, a peak with the

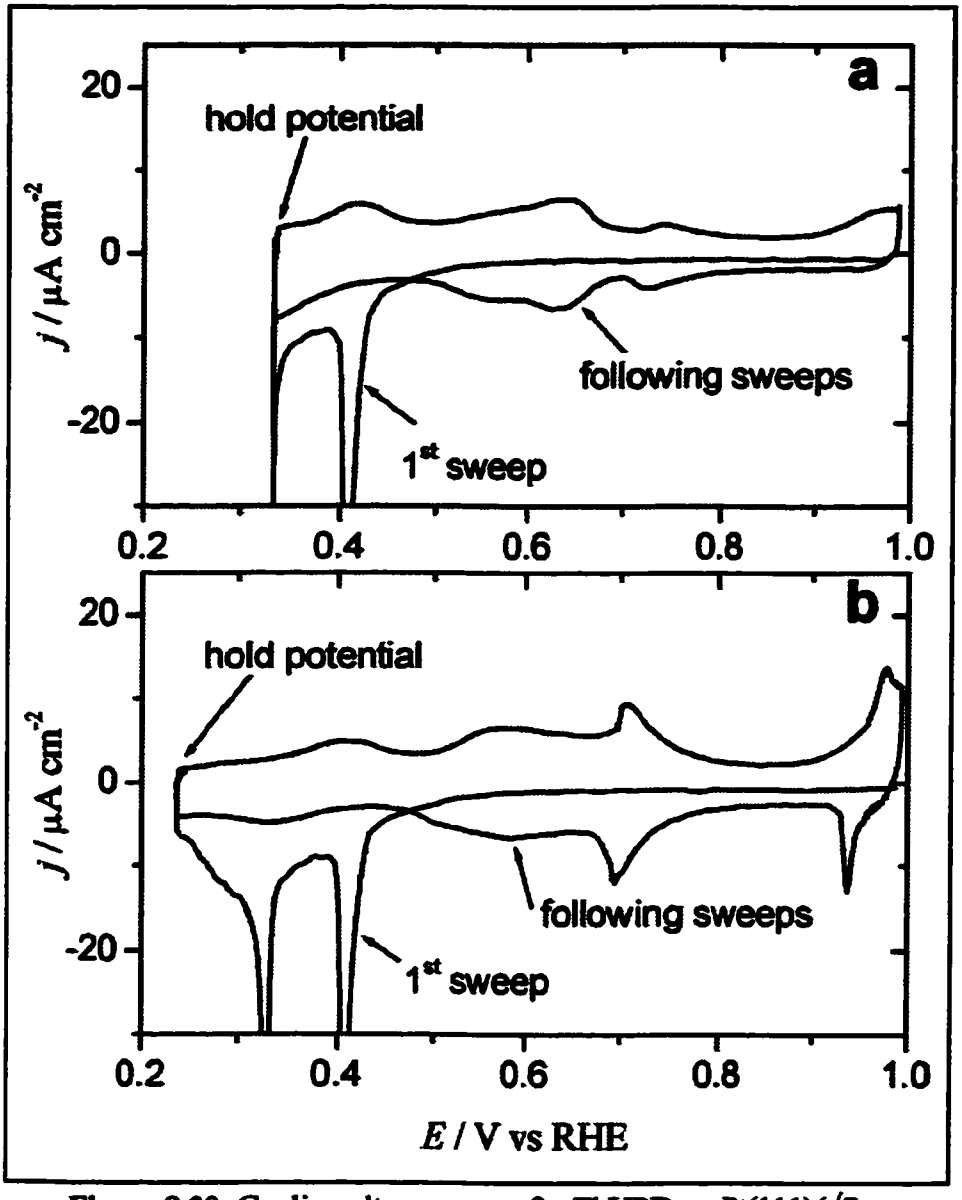

Figure 8.30: Cyclic voltammogram for Tl UPD on Pt(111)(√7 x √7)R19.1°-I in $HClO_4$. a) holding potential one minute at the beginning of peak C2, b) holding potential for 1 minute after peak C2. $[Tl^+] = 1$ mM. $[HClO_4] = 0.1$ M. Sweep rate = 20 mV s^{-1}.

maximum at + 0.696 V and a set of peaks centered at + 0.957 V develops, Fig. (8.30). Comparing with Tl on bare Pt(111), these peaks correspond with Tl UPD. As in the case of H_2SO_4 solution, this implies that either patches of bare platinum, or a low iodine coverage remains on the surface during the Tl deposition process. This point can be depicted more

clearly by continuing the voltammogram down to + 0 V, Fig. (8.31), which, as noted above, produces desorption of iodine from cycle to cycle. The features of the voltammogram evolve slowly from cycle to cycle until reaching the voltammogram for Tl electrodeposition on Pt(111). This indicates that the peak at + 0.642 V in $HClO_4$ indeed corresponds to Tl electrodeposition.

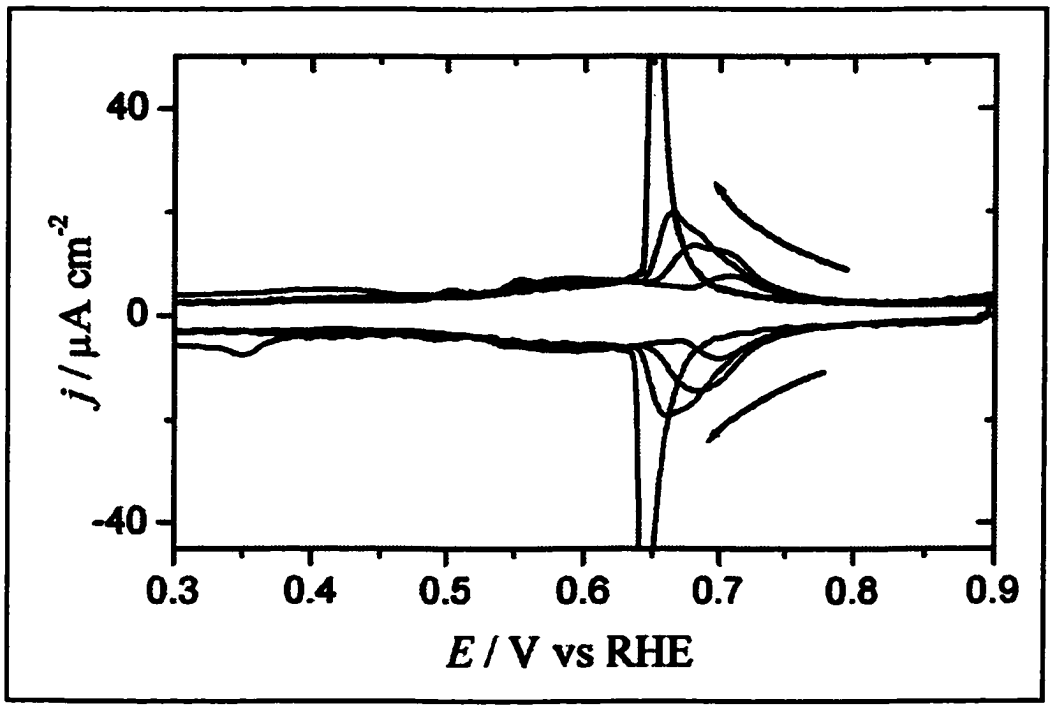

Figure 8.31: 2nd and following cycles for the voltammogram for Tl UPD on Pt(111)(√7 x √7)R19.1°-I in $HClO_4$. $[Tl^+]$ = 1 mM. $[HClO_4]$ = 0.1 M. Sweep rate = 20 mV s^{-1}.

Chapter 9

Conclusion.

In this thesis we have investigated Ag and Tl-iodine adlayers on Pt single crystal surfaces. We focussed the research primarily on the Pt-Ag-I system, and specifically on the Pt(111)(3 x 3)-AgI surface structure. This surface compound is formed during the initial stage of the UPD of Ag on Pt(111)($\sqrt{7}$ x $\sqrt{7}$)R19.1°-I after deposition of 4/9 monolayers of Ag.

A crystallographic analysis is reported in chapter 3 using LEED in the tensor LEED approach. The Pt(111)(3 x 3)-AgI structure approximates a two-layer slice of bulk AgI cut parallel to its (111) plane, with the Ag UPD atoms in direct contact with the Pt(111) surface. No significant corrugation is found for either the I layer or the Ag layer. This, together with the fact that Ag deposition is not site specific with respect to Pt, implies that the Ag:I interactions are more important than Pt:Ag.

A systematic study of the electrodeposition process for different orientations of the Pt substrate is done in chapter 4. It is found that the initial deposition occurs on the terraces; hence, the step sites are not the most reactive. The deposition around the steps is disordered, while on the terraces it is ordered for terraces larger than the length of a Pt(111)(3 x 3)-AgI unit cell. The minimum length of the terrace ensures that the Ag deposits with at least one (3 x 3)-AgI local unit cell. This confirms that Ag-I interactions are more important than Pt-Ag interactions.

A further understanding of the Pt(111)(3 x 3)-AgI structure is obtained in chapter 5 using a thermodynamic sequence to calculate some of its fundamental thermodynamic

parameters. This sequence is completed in chapter 6 with study of the temperature dependence of the electrodeposition process. The process is thermodynamically controlled, which enables the calculation of several of the thermodynamic parameters of the UPD process.

One of the stages of the thermodynamic sequence involves the desorption of iodine from the platinum surface. In chapter 7 we apply statistical thermodynamics to propose a model of desorption. In this model the iodine goes through a transition state with similar energy as the desorbed iodine, although the entropies are quite different. The model is tested with the simulation of thermal desorption spectra.

With the thermodynamic sequence in chapter 5 the formation free energy and enthalpy for the surface compound Pt(111)(3 x 3)Ag-I were calculated as:

$\Delta_{for}G^{o}$(AgI(ads) = -146 ± 23 kJ mol^{-1}.

$\Delta_{for}H^{o}$(AgI(ads)) = -139 ± 22 kJ mol^{-1}.

and the cohesive free energy and enthalpy are:

$\Delta_{coh}G^{o}$(AgI(ads) = +462 ± 24 kJ mol^{-1}.

$\Delta_{coh}H^{o}$(AgI(ads)) = +531 ± 22 kJ mol^{-1}.

To gain insight into the nature of the bonding, we may consider the cohesive enthalpy for Pt(111)(3 x 3)-AgI assuming a pure covalent bond between Ag and I, and a metallic bond between Pt and Ag.

9.1. Energy of the Ag-I bond in Pt(111)(3 x 3)-AgI.

The energy per Ag-I bond is estimated using thermochemical data from the NBS

tables [9.1]. The experimental enthalpy change for the reaction representing homolytic dissociation of the lattice is:

$$AgI(s) \rightarrow Ag(g) + I(g) \quad \Delta_{coh}H^{\circ}(AgI(s)) = +453.23\ kJ\ mol^{-1} \tag{1}$$

Since AgI has the zinc blende structure, each I atom bonds tetrahedrally to four Ag atoms. The total energy per bond is therefore:

$$\Delta_{coh}H^{\circ}(Ag\text{-}I(s)) = +\frac{453.23}{4} = +113.30\ kJ\ mol^{-1} \tag{2}$$

The bond energy for each of the Ag-I bonds in the Pt(111)(3 x 3)-AgI structure is obtained applying the correlation between the bond order and bond energy [9.2]:

$$\Delta H_s = \Delta H_b\, n^p \tag{3}$$

where ΔH_s is the bond energy of Ag-I in the Pt(111)(3 x 3)-AgI structure, ΔH_b the bond energy of the Ag-I bond in bulk and p an empirical parameter that we approximate to 1. n is the bond order of AgI in the Pt(111)(3 x 3)-AgI structure relative to AgI bulk, and was estimated in chapter 3 as 1.46. According to Eq. (3), the total energy per bond is $\Delta_{coh}H^{\circ}$(Ag-I(s)) = + 165.5 kJ mol^{-1}.

As explained in chapter 3, there are four iodine atoms per Pt(111)(3 x 3)-AgI unit cell, and each of them bonds to three silver atoms. The total energy of these twelve bonds in the unit cell, Fig. (9.1), may be estimated as:

$$\Delta H^{\circ}(Ag\text{-}I) = +165.5 \times 12 = +1985.0\ kJ\ mol^{-1} \tag{4}$$

9.2. Energy of the Pt-Ag bond in Pt(111)(3 x 3)-AgI.

The energy per Pt-Ag bond is calculated following Pauling's approximation. This approximation requires the energy for Pt-Pt and Ag-Ag bonds, which are obtained from the

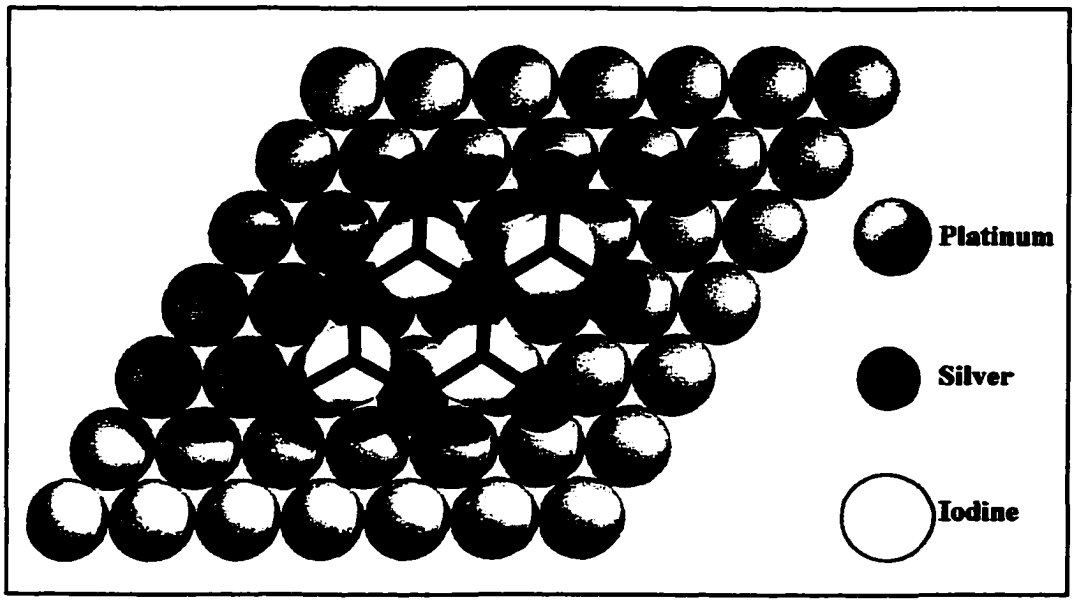

Figure 9.1: Pt(111)(3 x 3)-AgI structure showing the 12 Ag-I bonds per unit cell.

sublimation enthalpies:

$$\begin{aligned} &Pt(s) \rightarrow Pt(g) \quad \Delta H^{\circ}(Pt) = +\,565.3\ kJ\ mol^{-1} \\ &Ag(s) \rightarrow Ag(g) \quad \Delta H^{\circ}(Ag) = +\,284.5\ kJ\ mol^{-1} \end{aligned} \tag{5}$$

The coordination number in the fcc crystal structure for Pt or Ag is twelve. Therefore, there are six bonds per Pt or Ag in the unit cell of either structure. The energy per Pt-Pt and Ag-Ag bond is therefore:

$$\begin{aligned} \Delta H^{\circ}(Pt) &= +\frac{565.3}{6} = +\,94.2\ kJ\ mol^{-1} \\ \Delta H^{\circ}(Ag) &= +\frac{284.5}{6} = +\,47.4\ kJ\ mol^{-1} \end{aligned} \tag{6}$$

The energy of the Pt-Ag bond is assumed to be the arithmetic mean of the bond energies for Pt and Ag, with a correction for the difference of electronegativities, according to the relation [9.3]:

$$\Delta H^{\circ}(PtAg) = \frac{1}{2}\left[\Delta H^{\circ}(Pt) + \Delta H^{\circ}(Ag)\right] + 96\left(x_{Pt} - x_{Ag}\right)^2 = +\,82.5\ kJ\ mol^{-1} \tag{7}$$

where x_{Pt} and x_{Ag} are the electronegativities of Pt and Ag (2.28 and 1.93 respectively).

Of the four Ag atoms per Pt(111)(3 x 3)-AgI unit cell, one is in a three fold site with respect to Pt and three are in a displaced atop site, Fig. (9.2). The bond energy calculated corresponds to energy of the Pt-Ag bond for Ag in a three fold position, with a bond length of 2.82 Å. As explained in chapter 3, this bond length is close to expectation from the sum of metallic radii (2.83 Å), and to the bond length for bulk AgI in the zinc blende structure (2.81 Å). Each of the other three Ag atoms in a displaced atop site are bonded to one Pt with one Pt-Ag bond length of 2.48 Å, and two other Pt-Ag bonds of length 3.11 Å, Fig. (9.2). We consider the 3-fold Pt-Ag bond of 2.82 Å as normal, then the 2.48 Å bonds are compressed and the 3.11 Å bonds are stretched.

We can calculate the bond energy of these two different types of Pt-Ag bonds assuming the Morse approximation for the energy of a diatomic molecule as a function of the interatomic distance. According to this approximation, the energy of the Pt-Ag molecule is:

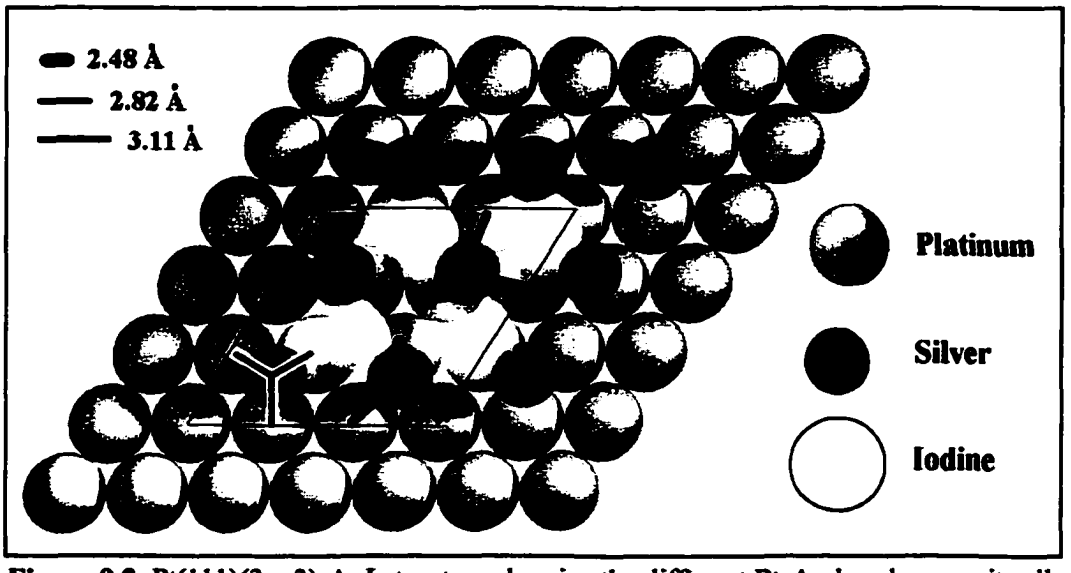

Figure 9.2: Pt(111)(3 x 3)-AgI structure showing the different Pt-Ag bonds per unit cell.

$$\Delta H = D_e \left(1 - e^{-(R-R_e)\sqrt{\frac{k}{2D_e}}} \right)^2 \qquad (8)$$

where R is the Pt-Ag distance, R_e the Pt-Ag equilibrium distance (2.82 Å), and D_e is the energy of dissociation, calculated as 82.5 kJ mol^{-1}. k is the force constant of the bond. It can be approximated as 125 N m^{-1} with an empirical correlation for diatomic molecules that combine atoms of the 4th and 5th rows of the periodic table[9.2][9.4].

According to Eq. (8), the bond energy of a Pt-Ag bond of 2.48 Å is -11.4 kJ mol^{-1}, and for a Pt-Ag bond length of 3.11 Å is 64.9 kJ mol^{-1}. The total energy per unit cell of the Pt-Ag bonds is the sum of the energies of all the bonds:

$$\Delta H^{\circ}(\text{Pt-Ag}) = +82.5 \times 3 + 64.9 \times 6 + (-11.4) \times 3 = +602.7 \text{ kJ mol}^{-1} \qquad (9)$$

9.3. Total Cohesive Enthalpy of Pt(111)(3 x 3)-AgI.

The total cohesive energy of the unit cell is the sum of the Ag-I and Pt-Ag bond enthalpies calculated in Eq. (5) and (10):

$$\Delta H^{\circ}(\text{Pt-Ag-I})_{cell} = +1985.0 + 602.7 = +2587.7 \text{ kJ mol}^{-1} \qquad (10)$$

Experimentally, $\Delta_{coh}H^{\circ}$ (AgI(ads)) obtained is per mole of iodine. Therefore, since there are four iodine atoms per unit cell, the theoretical cohesive energy per mole of iodine is:

$$\Delta H^{\circ}(\text{Pt-Ag-I}) = \frac{2587.7}{4} = +646.9 \text{ kJ mol}^{-1} \qquad (11)$$

where the contributions of the Pt-Ag and Ag-I bonds energies to ΔH° (Pt-Ag-I) are 23 and 77 % respectively.

Considering the simplicity of the model, there is a relative good agreement (< 20%)

between the theoretical cohesive energy and the experimental $\Delta_{coh}H^{\circ}$ (AgI(ads)) of 531 ± 22 kJ mol^{-1}, calculated in chapter 5 from the enthalpy change of reaction:

$$AgI(ads) \rightarrow I(g) + Ag(g) \qquad (12)$$

The four iodine atoms in a Pt(111)(3 x 3)-AgI unit cell are above the Ag layer in well defined three fold positions. This directionality is caused by the predominantly covalent Ag-I bond. The metallic character of the Pt-Ag accounts then for its non-directionality, as seen for three of the Ag atoms per unit cell in ill-defined displaced atop sites with respect to Pt. The different contributions of the Pt-Ag and Ag-I bonds to the total cohesive energy (23 *vs* 77%) explain the greater importance of the Ag-I interactions over the Pt-Ag interactions, as deduced in chapters 3 and 4.

The study of thallium electrodeposition on Pt(111)($\sqrt{7}$ x $\sqrt{7}$)R19.1°-I is still in the first stages of completion. The study of this system is much more complicated than for Ag-I. The reason is the irreversibility of the processes, and desorption of iodine during the thallium deposition. An explanation for the processes that take place in the first electrodeposition peak has been proposed. The thallium deposits initially with a (3 x 3) structure on top of the Pt(111) surface covered with iodine, regardless of the structure of the iodine adlayer. It is estimated that the cohesive Gibbs energy change of this surface compound is 401 ± 22 kJ mol^{-1}. This surface compound undergoes an irreversible phase change to a Pt(111)$\begin{bmatrix} 4 & 0 \\ 3 & 6 \end{bmatrix}$-TlI structure, involving the desorption of Tl and I. Further analysis of this surface structure, including the temperature dependence of the electrodeposition process, is needed. This will enable the calculation of the parameters that determine the stability of the different surface compounds, as well as the reasons of the desorption of I during the electrodeposition process.

Literature Cited

[1.1] J.X. Wang, I.K. Robinson, J.E. DeVilbiss, R.R. Adzic, The Journal of Physical Chemistry B, **104** (2000) 7951.

[1.2] J.X. Wang, I.K. Robinson, R.R. Adzic, Surface Science, **412/413** (1998) 374.

[1.3] R.R. Adzic, J.X. Wang, The Journal of Physical Chemistry B, **102** (1998) 6305.

[1.4] F. Möller, O.M. Magnussen, R.J. Behm, Electrochimica Acta, **40** (1995) 1259.

[1.5] F. Möller, O.M. Magnussen, R.J. Behm, Physical Review B, **51** (1995) 2484.

[1.6] J.H. White, H.D. Abruña, Journal of Physical Chemistry, **94** (1990) 894.

[1.7] J.E. Harris, M.P. Soriaga, Electrochimica Acta, **34** (1989) 1387.

[1.8] J.E. Harris, M.E. Bothwell, J.F. Rodriguez, M.P. Soriaga, J.L. Stickney, Journal of Physical Chemistry, **93** (1989) 2610.

[1.9] N.C. Gibson, P.M. Saville and D.A. Harrington, Journal of Electroanalytical Chemistry, **318** (1991) 271.

[1.10] F. El Omar, R. Durand, R. Faure, Journal of Electroanalytical Chemistry, **160** (1984) 385.

[1.11] M.T. Paffett, C.T. Campbell, T.N. Taylor, Langmuir, **1** (1985) 741.

[1.12] A.M. Bittner, Journal of Electroanalytical Chemistry, **431** (1997) 51.

[1.13] B.P. Costa, J. Canullo, D.V. Moll, R.C. Salvarezza, M.C. Giordano, A.J. Arvia, Journal of Electroanalytical Chemistry, **244** (1988) 261.

[1.14] L.H. Mascaro, M.C. Santos, S.A.S. Machado, L.A. Avaca, Journal of the Chemical Society, Faraday Transactions, **93** (1997) 3999.

[1.15] A. Vaskevich, E. Gileadi, Journal of Electroanalytical Chemistry, **442** (1998) 147.

[1.16] A.T Hubbard, J.L. Stickney, S.D. Rosasco, M.P. Soriaga and D. Song, Journal of Electroanalytical Chemistry, **150** (1983) 165.

[1.17] J.L. Stickney, S.D. Rosasco, D. Song, M.P. Soriaga and A.T. Hubbard, Surface Science, **130** (1983) 326.

[1.18] A. Wieckowski, B.C. Schardt, S.D. Rosasco, J.L. Stickney and A.T. Hubbard, Surface Science, **146** (1984) 115.

[1.19] T. Solomun, B.C. Schardt, S.D. Rosasco, A. Wieckowski, J. Stickney and A.T. Hubbard, Journal of Electroanalytical Chemistry,**176** (1984) 309.

[1.20] D.G. Frank, O.M.R. Chyan, T. Golden and A.T. Hubbard, Journal of Physical Chemistry, **98** (1994) 1895.

[1.21] N. Shinotsuka, K. Sashikata and K. Itaya, Surface Science, **335** (1995) 75.

[1.22] A.T. Hubbard, J.L. Stickney, S.D. Rosasco, M.P. Soriaga and D.Song, Journal of Electroanalytical Chemistry, **150** (1983) 165.

[1.23] N. Shinotsuka, K. Sashikata, K. Itaya, Surface Science, **335** (1995) 75.

[1.24] M. Labayen, E. Herrero, J.M. Feliu, D.A. Harrington, Journal of Electroanalytical Chemistry, **488** (2000) 32.

[1.25] J.L. Stickney, S.D. Rosasco, D. Song, M.P. Soriaga and A.T. Hubbard, Surface Science, **130** (1983) 326.

[1.26] M. Labayen, D.A. Harrington, M. Saidy, K.A.R. Mitchell, Surface Science, **490** (2001) 256.

[2.1] S.A. Furman, "Surface Chemistry of Iodine on Pt(111)", Ph.D thesis (University of Victoria) 1998.

[2.2] S.A. Furman, D.A. Harrington, Journal of Vacuum Science and Technology, **A14** (1996) 256.

[2.3] J. Clavilier, J. Ganon. M. Petit, Journal of Electroanalytical Chemistry, **265** (1989) 231.

[2.4] J. Clavilier, K. Achi, A. Rodes, Chemical Physics, **141** (1990) 1.

[2.5] D.A. Harrington, Journal of Electroanalytical Chemistry, **355** (1993) 21.

[2.6] M.E. van der Geest, N.J. Dangerfield, D.A. Harrington, Journal of Electroanalytical Chemistry, **420** (1997) 89.

[2.7] J. Clavilier, D. Armand, S.G. Sun, M. Petit, Journal of Electroanalytical Chemistry, **205** (1986) 267.

[2.8] J. Clavilier, M. Wasberg, M. Petit, L.H. Klein, Journal of Electroanalytical Chemistry, **374** (1994) 123.

[2.9] N. Shinotsuka, K. Sashikata, K. Itaya, Surface Science, **335** (1995) 75.

[2.10] J. Clavilier, K. Achi, M. Petit, A. Rodes, M.A. Zamakhchari, Journal of Electroanalytical Chemistry, **295** (1990) 333.

[2.11] R. Gomez, J. Clavilier, Journal of Electroanalytical Chemistry, **354** (1993) 189.

[2.12] E. Herrero, J.M. Orts, A. Aldaz, J.M. Feliu, Surface Science, **440** (1999) 259.

[2.13] F. Lu, G.N. Salaita, H. Baltruschat and A.T. Hubbard, Journal of Electroanalytical Chemistry, **222** (1987) 305.

[2.14] D.D. Wagman, W.H. Evans, V.B. Parker, R.H. Schumm, I. Halow, S.M. Bailey, K.L. Churney and R.L. Nutall, Journal of Physical Chemistry, Reference Data, **11** (1982) Supplement 2.

[3.1] A.T. Hubbard, J.L. Stickney, S.D. Rosasco, M.P. Soriaga and D.Song, Journal of Electroanalytical Chemistry, **150** (1983) 165.

[3.2] J.L. Stickney, S.D. Rosasco, D. Song, M.P. Soriaga and A.T. Hubbard, Surface Science, **130** (1983) 326.

[3.3] A. Wieckowski, B.C. Schardt, S.D. Rosasco, J.L. Stickney, and A.T. Hubbard, Surface Science, **146** (1984) 115.

[3.4] J.D.H. Donnay, Ed., Crystal Data: Determinative Tables, 2nd Ed., American Crystallographic Association, Washington, D.C., 1963, p. 841.

[3.5] M. Saidy, K.A.R. Mitchell, S.A. Furman, M. Labayen and D.A. Harrington, Surface Review and Letters, **6** (1999) 871.

[3.6] M. Labayen, D.A. Harrington, M. Saidy, K.A.R. Mitchell, Surface Science, **490** (2001) 256.

[3.7] P.J. Rous, M.A. Van Hove, G.A. Somorjai, Surface Science, **226** (1990) 15.

[3.8] M.A. Van Hove, W. Moritz, H. Over, P.J. Rous, A. Wander, A. Barbieri, N. Materer, U. Starke, G.A. Somorjai, Surface Science. Rep. **19** (1993) 191.

[3.9] A. Wander, M.A. Van Hove, G.A. Somorjai, Physical Review Letters, **67** (1991) 626.

[3.10] P.C. Wong, M.Y. Zhou, K.C. Hui, K.A.R. Mitchell, Surface Science, **163** (1985) 172.

[3.11] J.B. Pendry. Journal of Physics C, **13** (1980) 937.

[3.12] G. Ertl, J. Küppers, "Low Energy Electrons and Surface Chemistry", VCH, Germany, (1974).

[3.13] M.J. Moore, J.S. Kasper, Journal of Chemical Physics, **48** (1968) 2446.

[3.14] K.A.R. Mitchell, S.A. Schlatter, R.N.S. Sodhi, Canadian Journal of Chemistry, **64** (1986) 1435.

[3.15] L.C. Pauling, "Nature of the Chemical Bond", 3rd ed. Cornell University Press, Ithaca, NY, USA, (1960).

[4.1] J.L. Stickney, S.D. Rosasco, B.C. Schardt, and A.T. Hubbard, Journal of Physical Chemistry, **88** (1984) 251.

[4.2] A. Wieckowski, S.D. Rosasco, B.C. Schardt, J.L. Stickney, A.T. Hubbard, Inorganic Chemistry, **23** (1984) 565.

[4.3] W.L. DeSimone and J.J. McBreen, Langmuir, **11** (1995) 4428.

[4.4] M. Labayen, E. Herrero, J.M. Feliu, D.A. Harrington, Journal of Electroanalytical Chemistry, **488** (2000) 32.

[4.5] T. Solomun, B.C. Schardt, S.D. Rosasco, A. Wieckowski, J. Stickney and A.T. Hubbard, Journal of Electroanalytical Chemistry, **176** (1984) 309.

[4.6] F. Lu, G.N. Salaita, H. Baltruschat, A.T. Hubbard, Journal of Electroanalytical Chemistry, **222** (1987) 305.

[4.7] J.L. Stickney, S.D. Rosasco, D. Song, M.P. Soriaga and A.T. Hubbard, Surface Science, **130** (1983) 326.

[4.8] A. Hamelin and J. Lipkowski, Journal of Electroanalytical Chemistry, **171** (1984) 317.

[4.9] L.J. Buller, E. Herrero, R. Gomez, J.M. Feliu. H.D. Abruna, Journal of the Chemical Society, Faraday Transactions, **21** (1996) 3757.

[4.10] C. Nishihara, H. Nozoye, Journal of Electroanalytical Chemistry, **386** (1995) 139.

[4.11] A. Wieckowski, B.C. Schardt, S.D. Rosasco, J.L. Stickney and A.T. Hubbard,

Surface Science, **146** (1984) 115.

[5.1] A. Wieckowski, B.C. Schardt, S.D. Rosasco, J.L. Stickney and A.T. Hubbard, Surface Science, **146** (1984) 115.

[5.2] T. Solomun, B.C. Schardt, S.D. Rosasco, A. Wieckowski, J. Stickney and A.T. Hubbard, Journal of Electroanalytical Chemistry, **176** (1984) 309.

[5.3] J.L. Stickney, S.D. Rosasco, B.C. Schardt, and A.T. Hubbard, Journal of Physical Chemistry, **88** (1984) 251.

[5.4] A.W. Adamson, "Physical Chemistry of Surfaces", 5th Ed. John Wiley & Sons, Inc., NY, USA, (1990).

[5.5] T. Young, Philosophical Transactions of the Royal Society of London, **95** (1805) 65.

[5.6] W.V. Kayser, Journal of Colloid and Interface Science, **56** (1976) 622.

[5.7] D.D. Wagman, W.H. Evans, V.B. Parker, R.H. Schumm, I. Halow, S.M. Bailey, K.L. Churney, R.L. Nuttall, Journal of Physical Chemistry, Reference Data, **11** (Suppl. 2) (1982) 2-52, 2-160.

[5.8] F. Lu, G.N. Salaita, H. Baltruschat, A.T. Hubbard, Journal of Electroanalytical Chemistry, **222** (1987) 305.

[5.9] J.L. Stickney, S.D. Rosasco, D. Song, M.P. Soriaga and A.T. Hubbard, Surface Science, **130** (1983) 326.

[6.1] M. Labayen, E. Herrero, J.M. Feliu, D.A. Harrington, Journal of Electroanalytical Chemistry, **488** (2000) 32.

[6.2] N. Shinotsuka, K. Sashikata, K. Itaya, Surface Science, **335** (1995) 75.

[6.3] A.T. Hubbard, J.L. Stickney, S.D. Rosasco, M.P. Soriaga and D.Song, Journal of Electroanalytical Chemistry, **150** (1983) 165.

[6.4] T. Solomun, B.C. Schardt, S.D. Rosasco, A. Wieckowski, J. Stickney and A.T. Hubbard, Journal of Electroanalytical Chemistry,**176** (1984) 309.

[6.5] J.L. Stickney, S.D. Rosasco, D. Song, M.P. Soriaga and A.T. Hubbard, Surface Science, **130** (1983) 326.

[6.6] A. Wieckowski, B.C. Schardt, S.D. Rosasco, J.L. Stickney, and A.T. Hubbard, Surface Science, **146** (1984) 115.

[6.7] N.C. Gibson, P.M. Saville and D.A. Harrington, Journal of Electroanalytical Chemistry, **318** (1991) 271.

[6.8] D.D. Wagman, W.H. Evans, V.B. Parker, R.H. Schumm, I. Halow, S.M. Bailey, K.L. Churney, R.L. Nuttall, Journal of Physical Chemistry, Reference Data, **11** (Suppl. 2) (1982) 2-52, 2-160.

[6.9] Y. Sawatari, T. Sueoka, Y. Singaya, M. Ito, Y. Osamura, Spectrochimica Acta, **50** (1994) 1555.

[6.10] M.J. Weaver, Langmuir, **14** (1998) 3932.

[6.11] U.W. Hamm, D. Kramer, R.S. Zhai, K.M. Kolb, Journal of Electroanalytical Chemistry, **414** (1996) 85.

[6.12] V.A. Benderskii, G.I. Velichko, Journal of Electroanalytical Chemistry, **140** (1982) 1.

[6.13] V.A. Benderskii, S.D. Babenko, A.G. Krivenko, Journal of Electroanalytical Chemistry, **86** (1978) 223.

[6.14] L.I. Korshunov, Y.M. Zolovitskii, V.A. Benderskii, Electrokhimiya, **4** (1968) 499.

[6.15] V.A. Benderskii, A.M. Brodskii, G.I. Velichko, L.I. Daikhin, Electrokhimiya, **23** (1987) 435.

[7.1] S.A. Furman, "Surface Chemistry of Iodine on Pt(111)", Ph.D thesis (University of Victoria) 1998.

[7.2] V.P. Zhdanov, Journal of Physical Chemistry, **114** (2001) 4746.

[7.3] A.V. Myshlyavtsev, V.P. Zhdanov, Chemical Physics Letters, **162** (1989) 43.

[7.4] J.L. Sales, G. Zgrablich, V.P. Zhdanov, Surface Science, **209** (1989) 208.

[7.5] S.H. Payne, J. Zhang, H.J. Kreuzer, Surface Science, **264** (1992) 185.

[7.6] H.J. Kreuzer, Z. Jun, S.H. Payne, W.Nichtl-Pecher, L. Hammer, K. Müller, Surface Science, **303** (1994) 1.

[7.7] S.H. Payne, H.J. Kreuzer, Surface Science, **222** (1989) 404.

[7.8] H.J. Kreuzer, Surface Science, **231** (1990) 213.

[7.9] J.A.W. Elliott, C.A. Ward, Journal of Chemical Physics, **106** (1997) 5677.

[7.10] C.A. Ward, R.D. Findlay, M. Rizk, Journal of Chemical Physics, **76** (1982) 5599.

[7.11] G.S. Hammond, Journal of the American Chemical Society, **77** (1955) 334.

[7.12] D.D. Wagman, W.H. Evans, V.B. Parker, R.H. Schumm, I. Halow, S.M. Bailey, K.L. Churney, R.L. Nuttall, Journal of Physical and Chemical Reference Data, **11** (Suppl. 2) (1982) 2-52, 2-160.

[7.13] W.A. de Jong, L. Visscher, W.C. Nieuwpoort, Journal of Chemistry Physics, **107** (1997) 9046.

[7.14] M.C. Gupta, "Statistical Thermodynamics", John Wiley and Sons, Wiley Eastern Limited, New Delhi, India, 1990.

[7.15] G.A. Somorjai, "Introduction to surface chemistry and catalysis", John Wiley and Sons, New York, USA, 1994.

[7.16] M.A. Van Hove, W.H. Weinberg, C.-M. Chan, "Low-Energy Electron Diffraction: Experiment, Theory and Structural Determination", Springer Series in Surface Sciences, Berlin, Germany, 1986.

[7.17] H.B. Lyon, G.A. Somorjai, Journal of Chemical Physics, **44** (1966) 3707.

[7.18] N. Materer, U. Starke, A. Barbieri, R. Doll, K. Heinz, M.A. Van Hove, G.A. Somorjai, Surface Science, **325** (1995) 207.

[7.19] W.H. Weinberg, Journal of Chemical Physics, **57** (1972) 5463.

[7.20] D.P. Jackson, Surface Science, **43** (1974) 431.

[7.21] C. Waldfried, D.N. McIlroy, J. Zhang, P.A. Dowben, G.A. Katrich, E.W. Plummer, Surface Science, **363** (1996) 296.

[8.1] J. Clavilier, J-P. Ganon, M. Petit, Journal of Electroanalytical Chemistry, **265** (1989) 231.

[8.2] R.R. Adzic, J.X. Wang, O.M. Magnussen, B.M. Ocko, The Journal of Physical Chemistry, **100** (1996) 14721.

[8.3] I. Oda, Y. Shingaya, H. Matsumoto, M. Ito, Journal of Electroanalytical Chemistry, **409** (1996) 95.

[8.4] D.R. Wheeler, J.X. Wang, R.R. Adzic, Journal of Electroanalytical Chemistry, **387** (1995) 115.

[8.5] R. Parsons, Canadian Journal of Chemistry, **59** (1981) 1898.

[8.6] P. Delahay, G.G. Susbielbes, The Journal of Physical Chemistry, **70** (1966) 3150.

[8.7] K. Holub, G. Tessari, P. Delahay, The Journal of Physical Chemistry, **71** (1967) 2612.

[8.8] P. Delahay, K. Holub, Journal of Electroanalytical Chemistry, **16** (1968) 131.

[8.9] M.E. van der Geest, N.J. Dangerfield and D.A. Harrington, Journal of Electroanalytical Chemistry, **420** (1997) 89.

[8.10] M.W. Breiter, Journal of Electroanalytical Chemistry, **38** (1964) 7.

[8.11] S. Morin, H. Dumont, B.E. Conway, Journal of Electroanalytical Chemistry, **412** (1996) 39.

[8.12] T. Pajkossy, D.M. Kolb, Electrochimica Acta, **46** (2001) 3063.

[8.13] M. Klimmeck, K. Juttner, Electrochimica Acta, **27** (1982) 83.

[8.14] D.D. Wagman, W.H. Evans, V.B. Parker, R.H. Schumm, I. Halow, S.M. Bailey, K.L. Churney, R.L. Nuttall, Journal of Physical and Chemical Reference Data, **11** (Suppl. 2) (1982) 2-52, 2-160.

[8.15] K. Hermann, M.A. Van Hove (LBL), Lawrence Berkeley National Laboratory, Berkeley, and University of California, Davis, USA. http://electron.lbl.gov/vanhove/vanhove.html

[8.16] S.A. Furman, "Surface Chemistry of Iodine on Pt(111)", Ph.D thesis (University of Victoria) 1998.

[8.17] N.S. Marinkovic, W.R. Fawcett, J.X. Wang, R.R. Adzic, Journal of Physical Chemistry, **99** (1995) 17490.

[9.1] D.D. Wagman, W.H. Evans, V.B. Parker, R.H. Schumm, I. Halow, S.M. Bailey, K.L. Churney, R.L. Nuttall, Journal of Physical Chemistry, Reference Data, **11** (Suppl. 2) (1982) 2-52, 2-160.

[9.2] H.S Johnston, "Gas Phase Reaction Rate Theory", The Ronald Press Company, N Y, USA,1966.

[9.3] L.C. Pauling, "Nature of the Chemical Bond", 3rd ed. Cornell University Press, Ithaca, NY, USA, 1960.

[9.4] J. Waser, L. Pauling, Journal of Chemical Physics, 18 (1950) 747.